Improving the quasi-dynamic test method for low-temperature solar thermal collectors

Juan Manuel Rodríguez Muñoz

Postgraduate program in Energy Engineering
Facultad de Ingeniería
Universidad de la República

Montevideo – Uruguay
August of 2025

Improving the quasi-dynamic test method for low-temperature solar thermal collectors

Juan Manuel Rodríguez Muñoz

Doctorate's Thesis submitted to the Postgraduate Program in Energy Engineering, Facultad de Ingeniería of the Universidad de la República, as part of the necessary requirements for obtaining the title of Doctor in Energy Engineering.

Director:
Ph.D. Prof. Italo Bove

Co-advisor:
Ph.D. Prof. Rodrigo Alonso Suárez

Academic director:
Ph.D. Prof. Italo Bove

Montevideo – Uruguay
August of 2025

Rodríguez Muñoz, Juan Manuel

Improving the quasi-dynamic test method for low-temperature solar thermal collectors / Juan Manuel Rodríguez Muñoz. - Montevideo: Universidad de la República, Facultad de Ingeniería, 2025.

XIX, 186 p. 29, 7cm.

Director:

Italo Bove

Co-advisor:

Rodrigo Alonso Suárez

Academic director:

Italo Bove

Tesis de Doctorado – Universidad de la República, Program in Energy Engineering, 2025.

Bibliography: p. 133 – 139.

1. Colectores solares térmicos, 2. ISO 9806, 3. Ensayos en condiciones cuasi-dinámicas, 4. Modificador por ángulo de incidencia, 5. Identificación de parámetros dinámica. I. Bove, Italo, *et al.* II. Universidad de la República, Postgraduate Program in Energy Engineering. III. Title

MEMBERS OF THE THESIS DEFENSE COURT

Ph.D. Fabienne Sallaberry

Ph.D. Jorge Facão

Ph.D. Prof. Octavio García Valladares

Ph.D. Prof. José Cataldo

Ph.D. Prof. Pedro Curto

Montevideo – Uruguay
August of 2025

Agradecimientos

Agradezco en primer lugar a los integrantes del proyecto BECS: Ignacio Texeira, Rodrigo Alonso Suárez, Roberto Iurato, Javier Capeche y Andrés Monetta. Su trabajo dedicado hizo posible desarrollar una infraestructura de alta calidad, que permitió la creación de una nueva área de I+D en el LES, en la cual se enmarca esta tesis. Tambien agradezco a Gonzalo Abal por haber impulsado y apoyado institucionalmente la realizacion de este proyecto. Asimismo, agradezco a Francisco Guimaraens, quien se incorporó al proyecto cuando el BECS ya estaba en operación, pero cuya labor en la realización de los ensayos fue fundamental para la culminación de este trabajo.

En segundo lugar, agradezco a la Dirección Nacional de Energía por apoyar el lineamiento estratégico de construir el BECS con recursos locales, lo que permitió un conocimiento detallado de las instalaciones y facilitó la implementación de las metodologías de ensayo SST y QDT. Igualmente, agradezco al PTB de Alemania por organizar la intercomparación de laboratorios de ensayos de colectores solares en Latinoamérica, actividad que posibilitó la validación de dichas metodologías y brindó certeza sobre el trabajo realizado posteriormente. También agradezco a la Comisión Sectorial de Investigación Científica de la Universidad de la República por financiar la beca doctoral que usufructué antes de incorporarme al Régimen de Dedicación Total.

Mi más profundo agradecimiento a mis directores de tesis, por la confianza y la orientación a lo largo de estos años. Sus innumerables consejos me han ayudado enormemente a crecer tanto a nivel profesional como personal. Ha sido un verdadero placer realizar este proceso de formación con su acompañamiento. Extiendo también mi reconocimiento a mis compañeros del Laboratorio de Energía Solar y del Departamento de Física del Centro Universitario Regional Litoral Norte, por el excelente clima laboral y el compañerismo.

Finalmente, quiero mencionar que esta tesis marca el cierre de un proceso de formación de 16 años, iniciado en 2010 al comenzar mis estudios en

la Facultad de Ingeniería. A lo largo de este período, he vivido numerosas experiencias, tanto buenas como malas, que han contribuido a mi desarrollo personal y profesional. Sin embargo, en todo este tiempo siempre conté con el incondicional apoyo de mi familia, sin el cual esta tesis no hubiese sido posible. Les agradezco profundamente y dedico esta tesis a ellos.

ABSTRACT

Solar thermal energy systems (STES) are an alternative to fossil fuels for heat production in the residential and industrial sectors, contributing to the reduction of greenhouse gas emissions. Solar thermal collectors, which are responsible for capturing and transferring solar energy to a fluid, are the central components of these systems. To promote the use of STES, it is essential to ensure the quality and thermal performance of collectors, which is achieved through standardized procedures such as those described in ISO 9806:2017, one of the most widely used standards worldwide for this purpose.

In Uruguay, the promotion of STES was declared a national interest in 2009, and in 2013, an agreement was signed between the Ministry of Industry, Energy and Mining (MIEM) and the University of the Republic (UdelaR) to create the Solar Heaters Test Bank (BECS, from its name in Spanish). Its purpose is to carry out thermal performance tests on solar thermal collectors and factory-made solar water heaters in accordance with ISO standards, with the aim of homologation, supporting innovation by national companies, and promoting research. For these tests, the ISO 9806:2017 standard is used for solar collectors, which contemplates two methodologies for thermal performance test: steady state testing (SST) and quasi-dynamic testing (QDT).

This thesis aims to enhance the thermal performance testing procedures established in ISO 9806:2017 for low-temperature collectors, particularly the QDT method, consolidating the BECS infrastructure as a recognized research platform. These improvements enhance the reliability and applicability of the methodology, providing a more robust framework for evaluating the thermal performance of low-temperature solar collectors. Specifically, the primary contributions were the improved experimental characterization of the incidence angle modifier for the direct and diffuse components, and the enhanced modelling of transient effects in the QDT method. A more detailed description of these contributions is provided below.

With respect to the beam component of the IAM, a new model was developed and validated for flat plate (FPC) and heat pipe evacuated tube (ETC-HP) collectors. This model can therefore be applied to uniaxial and biaxial

IAM collectors. It demonstrated greater accuracy and consistency with the SST method than existing models. For the diffuse component, two alternative models were proposed: one based on global isotropic diffuse irradiance (an extension of the SST approach) and the other distinguishing between contributions from the sky and the ground. In both cases, the associated parameters are estimated by integrating the IAM for the direct component. Both models showed better agreement with the SST, the former being preferred for its simplicity, as the latter requires an additional measurement related to the diffuse irradiance reflected by the ground. In addition, transient modeling was improved by implementing a Dynamic Parameter Identification (DPI) algorithm, which outperformed the traditional Multiple Linear Regression (MLR) method in accuracy and demonstrated a lower sensitivity to averaging time. Both diffuse IAM models and the DPI procedure showed advantages for the two technologies addressed in this thesis, FPC and ETC-HP, although the improvements were more significant in the latter case.

Finally, the thesis includes secondary scientific contributions, which are described below. To facilitate the implementation of the aforementioned primary contribution, a MATLAB tool was developed to integrate all the proposed models. Additionally, improvements were made to the measurement of diffuse solar irradiance on an inclined plane, which is necessary for the implementation of the QDT method. To this end, a new correction model for horizontal diffuse irradiance measurements with a shadow band was developed, alongside experimental characterization of the albedo of the BECS environment, and a comparison of different models. Although the thesis focuses primarily on the QDT method, it also proposes an enhancement to the SST method through a refined procedure for converting SST parameters into QDT parameters. This new procedure incorporates the effect of the diffuse fraction into the standard conversion process, thus improving the consistency between the two methods.

Keywords:
Solar thermal collectors, ISO 9806, Quasi dynamic test method, Incident angle modifier, Dynamic parameter identification.

RESUMEN

La energía solar térmica (EST) es una alternativa a los combustibles fósiles para la producción de calor en los sectores residencial e industrial, contribuyendo a la reducción de las emisiones de gases de efecto invernadero. Los colectores solares térmicos, responsables de captar y transferir la energía solar a un fluido, son el componente central de estos sistemas. Para fomentar el uso de la EST, es fundamental garantizar la calidad y el desempeño térmico de los colectores, lo que se logra mediante procedimientos estandarizados como los descritos en la norma ISO 9806:2017, una de las más utilizadas a nivel mundial para este propósito.

En Uruguay, la promoción de la EST fue declarada de interés nacional en 2009, y en 2013 se firmó un acuerdo entre el Ministerio de Industria, Energía y Minería (MIEM) y la Universidad de la República (UdelaR) para crear el Banco de Ensayos de Calentadores Solares (BECS). Su objetivo es realizar ensayos de desempeño térmico en colectores solares y sistemas solares prefabricados para calentamiento de agua, conforme a la normativa ISO, con fines de homologación, apoyo a la innovación de empresas nacionales y fomento de la investigación. Para los ensayos de colectores solares se emplea la norma ISO 9806:2017, que contempla dos metodologías: ensayo en estado estacionario (SST) y ensayo en condiciones cuasi-dinámicas (QDT).

Esta tesis tiene como objetivo mejorar los procedimientos de ensayo de desempeño térmico establecidos en la norma ISO 9806:2017 para colectores de baja temperatura, particularmente el método QDT, consolidando la infraestructura del BECS como una plataforma de investigación reconocida. Estas mejoras incrementan la confiabilidad y la aplicabilidad de la metodología, proporcionando un marco más sólido para la evaluación del desempeño térmico de colectores solares de baja temperatura. En particular, las principales contribuciones fueron la mejora en la caracterización experimental del modificador del ángulo de incidencia (IAM) para las componentes directa y difusa, y el mejoramiento del modelado de los efectos transitorios en el método QDT. Una descripción más detallada de estas contribuciones se presenta a continuación.

Con respecto a la componente directa del IAM, se desarrolló y validó un

nuevo modelo para colectores planos (FPC) y colectores de tubos evacuados con heat pipe (ETC-HP), siendo por lo tanto aplicable tanto a colectores con IAM uniaxial como biaxial. Este modelo presentó una mayor precisión y una mejor consistencia con el método SST en comparación con los modelos existentes. Para la componente difusa, se propusieron dos modelos alternativos: uno basado en la irradiancia global difusa isotrópica (una extensión del enfoque SST) y otro que distingue entre las contribuciones del cielo y del suelo. En ambos casos, los parámetros asociados se estiman a partir de la integración del IAM para la componente directa. Ambos modelos mostraron una mejor concordancia con el SST, siendo preferido el primero por su simplicidad, ya que el segundo requiere una medición adicional relacionada con la irradiancia difusa reflejada por el suelo. Además, el modelado transitorio se mejoró mediante la implementación de un algoritmo de Identificación Dinámica de Parámetros (DPI), que superó en precisión al método tradicional de Regresión Lineal Múltiple (MLR) y mostró menor sensibilidad al tiempo de promediado. Tanto los modelos de IAM difuso como el procedimiento DPI presentaron ventajas para ambas tecnologías analizadas en esta tesis, FPC y ETC-HP, aunque las mejoras fueron más significativas en este último caso.

Finalmente, la tesis incluye contribuciones científicas secundarias, que se describen a continuación. Para facilitar la implementación de las contribuciones principales mencionadas, se desarrolló una herramienta en MATLAB que integra todos los modelos propuestos. Asimismo, se introdujeron mejoras en la medición de la irradiancia solar difusa en plano inclinado, necesaria para la aplicación del método QDT. Para ello, se desarrolló un nuevo modelo de corrección para mediciones de irradiancia difusa horizontal con banda de sombra, junto con la caracterización experimental del albedo en el entorno del BECS. Si bien la tesis se centra principalmente en el método QDT, también propone una mejora al método SST mediante un procedimiento mejorado para la conversión de parámetros SST a parámetros QDT. Este nuevo procedimiento incorpora el efecto de la fracción difusa en el proceso de conversión estándar, mejorando así la consistencia entre ambos métodos.

Palabras claves:
Colectores solares térmicos, ISO 9806, Ensayos en condiciones cuasi-

dinámicas, Modificador por ángulo de incidencia, Identificación de parámetros dinámica.

Contents

Chapter 1

Introduction

1.1. Brief global energy outlook

The increase in greenhouse gas emissions has led to a progressive increase in the global average temperature. This has resulted in an intensification and increase in the frequency of extreme weather events, as well as changes in precipitation patterns and climate dynamics, a phenomenon known as climate change. These changes have an adverse effect on various human activities, such as agriculture, livestock farming, fuel supply, and contribute to the increased spread of disease (Arnell et al., 2019).

Approximately three-quarters of these emissions originate in the energy sector (IEA, 2024; Ritchie et al., 2020), where demand is constantly increasing due to economic and demographic development. However, significant reductions in these emissions can be achieved through various strategies, such as the substitution of fossil fuels with those that have a lower carbon content, the integration of renewable energies into the energy mix, carbon capture and storage, the improvement of energy efficiency, and the reduction of the final energy demand. In this context, solar thermal energy is a promising alternative to fossil fuels for heating and cooling purposes.

Solar thermal energy systems (STES) is the use of solar energy to heat a fluid. This requires the integration of various devices, each with a specific function, such as solar energy capture and conversion, storage, etc. (Duffie and Beckman, 2006). Solar thermal collectors are the key component of these systems, as they capture solar energy and transfer it to heat fluids. These collectors can be classified according to the temperature at which they are

used, which ranges as follows: low, medium, and high. Alternatively, they can be classified according to the fluid used, which can be either water or air, among others. Low-temperature collectors are used primarily for domestic hot water (DHW), whereas medium and high temperature collectors are used primarily to generate heat for industrial processes and produce electricity.

Low-temperature water collectors can be divided into two main categories: covered and uncovered. This thesis focuses on covered collectors. Covered collectors account for 94 % of the installed capacity in the world, with flat plate and evacuated tube technologies being the most common (IEA-SCH, 2024). However, the distribution of installed capacity for these technologies varies significantly by region. In China, for example, evacuated tube technology dominates the market with a share of 87 %. In Europe and the MENA region (Middle East Europe and North Africa), flat plate collectors account for 79 % and 92 % of the installed capacity, respectively. In Latin America, flat plate collectors are the most common technology, followed by uncovered collectors, with 53 % and 38 %, respectively. Evacuated tube technology is not widely used in this part of the world.

The installed capacity of solar collectors has grown significantly in the past decade worldwide. This growth has slowed in recent years for various reasons (IEA-SCH, 2024). For example, other technologies, such as heat pumps, have entered the DHW market, which are highly efficient and competitive. Their presence in the market has increased in recent years and is expected to continue to increase (IEA, 2022). However, STES has started to gain ground in other markets, such as district heating, a system that distributes heat to several homes from a central location, and industrial applications. In summary, STES remains an important option for decarbonizing the energy sector.

In order to increase the participation of STES in the global energy matrix, it is crucial to test collectors to ensure the quality of the commercialized equipment in terms of both durability and thermal performance. The ISO-9806 (2017) standard is the most widely used worldwide for testing solar thermal collectors (Fischer et al., 2004; Fischer et al., 2006; Hofer et al., 2015; Janotte et al., 2009; Kratzenberg et al., 2006; Osório and Carvalho, 2014; Rodríguez-Muñoz et al., 2020; Rojas et al., 2008; Zambolin and Del Col, 2010). Covers both qualification testing (material durability) and thermal performance testing. Although it was originally developed for flat-plate and uncovered collectors, it was later extended to other low-temperature collector technologies,

such as evacuated tube collectors, and then to medium and high-temperature collectors, including parabolic trough concentrators and Fresnel-type concentrators, as evidenced by the above references.

For thermal performance testing, the standard proposes a generic thermodynamic model that can be adapted according to technology. This model can be used to predict the useful power produced by a collector under different meteorological and operational conditions, enabling the design of STES installations. This model has a set of characteristic parameters that must be determined experimentally for each collector. The standard proposes two methods to determine these parameters: the first under steady state conditions (SST — Steady State Testing) and the second under quasi-dynamic conditions (QDT — Quasi-Dynamic Testing). The thermodynamic model used in each case differs slightly, primarily in its treatment of diffuse solar radiation. However, the standard provides a procedure for converting the parameters from one model to another.

1.2. Solar thermal energy in Uruguay

In Uruguay, a long-term energy policy was approved in 2008 (MIEM-DNE, 2008), focusing on the diversification of the energy matrix through the promotion of local renewable energy sources. Regarding STE, in 2009 Law No. 18.585, better known as the Solar Law, was enacted, declaring research, development, and training in the use of solar thermal energy to be of national interest. The law aimed to expand the installed capacity of solar water heaters for domestic hot water production in the residential and service sectors, including hotels, healthcare facilities and sports clubs. This initiative required the development of local infrastructure to certify the quality and thermal performance of the equipment marketed in the country.

In this sense, the first precedent was a project carried out at the Faculty of Engineering between 2010 and 2011, aiming to build local solar thermal testing capacities in Uruguay. Led by the Fluid Mechanics and Environmental Engineering Institute, this work generated valuable knowledge on developing such capacities using local resources. Following this experience, between 2013 and 2018, the Solar Heater Test Bank (Banco de Ensayos de Calentadores Solares, BECS) was established through an agreement between the Ministry of Industry, Energy and Mining (MIEM) and the University of the Republic (UdelaR).

This infrastructure strengthened quality assurance in the STES sector by testing the thermal performance of solar thermal collectors and factory-made solar water heaters. These tests were carried out according to current ISO standards; for solar thermal collectors, the ISO-9806 (2017) standard was adopted.

I joined the BECS project in 2014 as an engineering assistant and became the technical engineer responsible in 2016. In 2019, I led BECS's participation in a laboratory intercomparison in Latin America organized by the German Metrological Institute (PTB), which validated the implementation of SST and QDT methodologies for flat plate collectors at BECS. This activity strengthened the local testing infrastructure and marked the culmination of nearly a decade of development in this field (Fischer, 2020).

These activities were included in my Master's thesis, during which I identified areas for improvement in the testing standard, such as the conversion of SST-QDT parameters, optical efficiency and dynamic modelling. The thesis document is available at Rodríguez-Muñoz (2021) and has led to the following scientific publications: Rodríguez-Muñoz et al. (2020, 2021a).

Building on these previous activities, this thesis focuses on improving the thermal performance testing of low-temperature solar collectors, with a particular emphasis on the QDT method. The following section reviews the historical development and current state of the SST and QDT test methods. It discusses their respective advantages and disadvantages, as well as the strategies implemented to address their limitations. This analysis provides a framework for understanding the scientific contributions of this thesis.

1.3. State of the art of solar collector performance testing

The first method to be developed was the SST, which was initially introduced by the American Society of Heating, Refrigerating and Air Conditioning Engineers (ASHRAE) in 1977, through the first version of the ASHRAE 93 testing standard. Years later, in 1994, this method was adopted and adapted by the International Organization for Standardization (ISO), resulting in the first version of ISO 9806. This testing method incorporates several decades of research in the field (Hill and Streed, 1976; Hottel and Whillier, 1955; Hottel and Woertz, 1942; Whillier, 1953) and was widely adopted by laboratories

in the United States and European countries (IEA-SHC, 1979; Streed et al., 1979). Even today, it remains the most commonly used testing method.

This test method proposes a thermodynamic model for the collector, whose parameters are determined separately through the execution of three subtests: efficiency tests, where the optical efficiency at normal incidence and thermal loss factors are determined; incidence angle modifier test, where the dependency of optical efficiency on the incidence angle is determined; and thermal capacity test, where the dynamic characteristics of the collector are determined, including thermal capacity and time constant. All subtests require strict conditions of a clear sky and high stability in the fluid entering the collector (i.e. temperature and flow rate). These strict conditions make this method robust and reliable. However, stable and long-persistent clear-sky conditions are difficult to achieve in some countries and regions because of local weather patterns.

To overcome this limitation, two approaches emerged as a possible solution. The first involved conducting tests indoors using a solar irradiance simulator. This option was incorporated into the aforementioned testing standards. However, such installations are costly and do not allow the incidence angle modifier to be determined, which means that a complete characterization of the collector is not possible.

The second approach involved modifying the testing method to enable operation under transient conditions, thus allowing tests to be conducted under variable sky conditions. This resulted in the development of the QDT testing method. This methodology achieved significant support in Europe during the 1980s and 1990s, particularly in countries with variable solar resources. Several testing methods were proposed during this period (Amer et al., 1998a; Amer et al., 1998b; Bosanac et al., 1994; Emery and Rogers, 1984; Muschaweck and Spirkl, 1993; Perers, 1993; Perers, 1997; Prapas et al., 1988; Rogers, 1981; Rönnelid et al., 1997; Wang et al., 1987), all of which relied on thermodynamic models similar to SST but with modifications to account for dynamic effects. These methods determine all parameters simultaneously using a set of experimental data, which includes both clear and cloudy sky conditions. The primary differences lie in the techniques used to calculate the model parameters, such as linear and nonlinear regression or Laplace transformation.

Among all these works, the studies by Perers (1993) and Perers (1997) stand out for the reasons described below. Firstly, the thermodynamic model

is general, which makes it applicable to both low-temperature collectors with and without covers. Secondly, it proposes a differentiated modelling approach for the incidence angle modifier that takes into account the different components of solar irradiance: direct and diffuse. This step was crucial for enabling the testing under cloudy sky conditions. Finally, the author suggests estimating the dynamic term using finite differences and treating that variable as an independent one within a linear regression algorithm as a strategy to handle transient effects. This procedure, commonly known as MLR (multilinear regression), simplified the parameter identification process, facilitating the subsequent adoption of the method by other laboratories.

These works laid the foundation for the current QDT method. In this regard, the EN 12975 standard was introduced in 2000, marking the first time that this method was included alongside the traditional SST. It was subsequently adopted in ISO 9806 and the ASHRAE 93 standard. It should be noted that the latest version of the European standard has become a requirement, referring to ISO 9806. In the latest version of ISO 9806, the thermodynamic model proposed for this method is quite general, making it applicable not only to low-temperature collectors but also to medium and high-temperature collectors. The applicability of this method under cloudy sky conditions led to its adoption by several laboratories around the world (Fischer et al., 2004; Fischer et al., 2006; Hofer et al., 2015; Janotte et al., 2009; Kratzenberg et al., 2006; Osório and Carvalho, 2014; Rodríguez-Muñoz et al., 2020; Rojas et al., 2008; Zambolin and Del Col, 2010), expanding their testing capacity compared to the SST method.

However, the QDT method has certain drawbacks that can be categorized into two main areas: challenges related to the IAM for both the direct and diffuse components of solar irradiance, and those related to the dynamic modelling of the collector.

With regard to the IAM for the beam direction, K_b, this parameter is actually a function of the angle of incidence. The scientific literature offers a variety of empirical functions for the QDT method, each with a set of parameters that must be determined from experimental data derived from tests. In my Master's thesis, we showed that the model typically recommended for flat-plate collectors (Souka and Safwat, 1966) does not adequately describe the experimental data. Other options were analyzed, but none stood out for their performance (Osório and Carvalho, 2014; Sallaberry et al., 2011; Zambolin and

Del Col, 2012). A similar problem occurs with evacuated tube technologies; several empirical functions are available, but there is no consensus on which performs better. As a result, test users have to select an empirical function for each technology based on their experience. This is considered to be a research gap, since a general model that can be applied to all technologies would be desirable. This would make the method more robust, as it would be less dependent on the tester and ensure good performance in all cases.

Regarding diffuse IAM, both the SST and QDT test methods in ISO 9806:2017 use the same approach: modelling diffuse solar irradiance globally using a single parameter, K_d, which remains constant for a given collector. The two test methods differ in how this parameter is estimated. In the SST method, K_d is derived indirectly from K_b, which is determined experimentally by a specific sub-test, as previously mentioned. Specifically, K_d is estimated by integrating and weighting the previously determined K_b function over the angle observed by the collector, under the assumption of an isotropic diffuse solar irradiance sky distribution. In contrast, the QDT method determines K_d directly from the experimental data, taking into account some anisotropic effects in the solar irradiance distribution. This results in a clear difference in the treatment of K_d between the two methods, resulting in discrepancies that have been experimentally demonstrated (Kovács et al., 2011; Osório and Carvalho, 2014; Rodríguez-Muñoz, 2021).

In this sense, Kovács et al. (2011) analyzed the effect of the diffuse fraction on the parameter conversion from SST to QDT, a variable normally neglected, since SST tests are typically performed under low diffuse fraction conditions. The authors showed that in the case of evacuated tube collectors, this variable becomes significant even within the range allowed by the standard. However, further research in this area could help reduce discrepancies between the two testing methods. For example, further enhancement of the parameter conversion from SST to QDT could be achieved, as well as analyzing an alternative diffuse IAM approach for the QDT test method.

Regarding the issue of dynamic modelling, it is well known that MLR results depend on the averaging time used for the experimental data (Fahr et al., 2018). Although the standard suggests an averaging time of 30 seconds, it is known that short averaging times can cause difficulties in the parameter identification process. Typically, data averaging times of 5 to 10 minutes are used, giving results similar to those of the SST method. The optimum

averaging time for the best results depends on the collector technology, which makes this procedure less robust. Ideally, a single averaging time applicable to all technologies would improve the reproducibility of the test method, or a method whose results are not so dependent on this variable.

In addition, the QDT method has shown excellent results for flat plate collectors; however, extending its application to evacuated tube collectors with heat pipes has proven challenging (Osório and Carvalho, 2014; QAiST, 2012). These collectors have significantly larger time constants compared to flat plate collectors, making it difficult for the traditional MLR approach to accurately describe transient effects and complicating the identification of some parameters.

Furthermore, although the QDT method allows testing under variable sky conditions, it still requires the fluid entering the collector to remain stable. This requirement naturally complicates the applicability of the method in operational installations (in-situ testing). Interest in this area of research has grown in recent years due to the increasing need to ensure that installations perform as expected according to their design (Fahr et al., 2019), as part of the quality infrastructure in countries promoting STES.

In response to these problems, several alternative transient test methods have been developed (Fahr et al., 2018; Hofer et al., 2015; Kong et al., 2012, 2015; Xu, 2009; Xu et al., 2013). These methods introduce modifications to improve the accuracy of determining characteristic parameters under quasi-dynamic conditions and enable their application in-situ in some cases. Specifically, they improve the thermodynamic model used in the QDT method by incorporating multi-node models and/or suggesting different ways of identifying parameters than MLR, such as dynamic parameter identification or Laplace transformation. Nevertheless, these studies have mainly focused on the application of these methods to specific types of collectors. Although they have the potential to be extended to other technologies, this remains a research gap.

1.4. About this thesis

The main objective of this thesis is to improve the thermal performance test method described in the ISO-9806 (2017) standard, with particular emphasis on the QDT method. In this context, a series of tests were carried out on flat plate collectors (FPC) and evacuated tube collectors with heat pipes (ETC-

HP), using both test methods, on the BECS platform of the Solar Energy Laboratory of the Universidad de la República (LES, for its name in spanish, http://les.edu.uy/), located in the city of Salto, Uruguay (latitude=31.28° S, longitude=57.92° W). The experimental data obtained from these tests were processed using the standard methodology to establish a reference framework, and then also analyzed using alternative approaches to address the research gaps identified in the previous section (IAM modelling and dynamic modelling). This process resulted in a series of scientific contributions, which are summarised below.

(a) **Enhanced experimental characterization of IAM for direct solar irradiance in the QDT method:** a new empirical correlation was developed to improve IAM modelling within the QDT framework. Designed for broad applicability, the model is suitable for various solar collector technologies, including flat plate and evacuated tube collectors. It was experimentally validated and benchmarked against existing correlations, demonstrating superior accuracy and consistency across a wide range of incidence angles.

(b) **Improved characterization of IAM for diffuse solar irradiance:** two major contributions were made, one for each testing method. For the SST method, an improved parameter conversion procedure from SST to QDT was proposed, incorporating the diffuse fraction into the process. This led to more realistic estimates that align better with those obtained using the QDT method. For the QDT method, two alternative models for K_d were evaluated, both producing results more consistent with SST. In addition, a cost-benefit analysis was performed regarding the inclusion of an additional measurement for ground-reflected diffuse irradiance.

(c) **Development of Dynamic Parameter Identification (DPI) for the application of the QDT method to low-temperature collectors:** a specific implementation of the DPI procedure was developed within the standardized QDT framework, and its performance was assessed against the standard MLR procedure. The results demonstrated that DPI outperforms MLR, showing lower sensitivity to the averaging time of the experimental data and providing more accurate estimates of the useful power output of solar collectors.

(d) **Development of a parameter identification tool for the QDT**

method: a MATLAB program was developed to perform parameter identification within the QDT framework. This tool integrates all the proposed developments related to IAM modelling and dynamic parameter identification. This facilitates the reproduction of these improvements and the implementation of the QDT method in general.

(e) **Improvements in diffuse solar irradiance measurements:** given the importance of diffuse irradiance measurements on inclined surfaces for QDT testing and the models developed in item (b), specific efforts were made to improve their accuracy. A new correction factor was proposed for horizontal diffuse irradiance measurements obtained with a shadow band. Additionally, the ground albedo on the BECS platform was experimentally characterized to improve the estimation of the ground-reflected diffuse irradiance.

These contributions improve the reliability and applicability of the QDT method, providing a more robust framework for evaluating the performance of low-temperature solar thermal collectors. These improvements have also resulted in the publication of four articles in high-impact international journals in the field of renewable energy (Rodríguez-Muñoz et al., 2021b, 2024, 2025, 2026). These articles constitute the core of this thesis.

This thesis is therefore structured as follows. Chapter 2 provides a review of the aforementioned articles, presented in order of publication. It highlights the specific contributions of the author of this thesis, explaining how these align with and contribute to the objectives of the thesis and its interrelation. Chapter 3 presents the main conclusions and outlines directions for future work, and Chapter 4 contains the full preprints of the articles.

In addition, two complementary articles were published during the development of this thesis, focusing primarily on point (e): improvements in the measurement of diffuse solar irradiance (Rodríguez-Muñoz et al., 2021c; Rodríguez-Muñoz et al., 2023). Although this topic is indirectly related to QDT testing, as it deals with diffuse solar irradiance measurements rather than the QDT method itself, these papers are relevant in the broader context of solar energy research. For this reason, these articles have been included as appendices.

Chapter 2

Papers review

This chapter provides a review of the four articles that form the core of this thesis. These articles are presented in the order they were published. This chapter highlights the scientific contributions, as well as the articles' connection to the thesis's overall objectives. The complete references are provided below in the same order, including links to the published online versions of the articles.

- Rodríguez-Muñoz, J. M., Bove, I., and Alonso-Suárez, R. (2021b). Novel incident angle modifier model for quasi-dynamic testing of flat plate solar thermal collectors. *Solar Energy*, *224*, 112–124. https://doi.org/https://doi.org/10.1016/j.solener.2021.05.026
- Rodríguez-Muñoz, J. M., Bove, I., and Alonso-Suárez, R. (2024). Improving the experimental estimation of the incident angle modifier of evacuated tube solar collectors with heat pipes. *Renewable Energy*, *235*, 121240. https://doi.org/https://doi.org/10.1016/j.renene.2024.121240
- Rodríguez-Muñoz, J. M., Bove, I., Alonso-Suárez, R., and Galione, P. A. (2025). On the choice of the parameter identification procedure in quasi-dynamic testing of low-temperature solar collectors. *Renewable Energy*, *247*, 122931. https://doi.org/https://doi.org/10.1016/j.renene.2025.122931
- Rodríguez-Muñoz, J. M., Bove, I., and Alonso-Suárez, R. (2026). Experimental characterization of the diffuse incident angle modifier of solar thermal collectors: Improving consistency between test methods. *Renewable Energy*, *256*, 123912. https://doi.org/https://doi.org/10.1016/j.renene.2025.123912

Regarding my personal contributions, the CRediT author statement from

Elsevier was used as a reference, which can be consulted here. In general, in all the articles I contributed to Conceptualization, Methodology, Software, Validation, Formal Analysis, Investigation, Resources, Data Curation, Writing – Original Draft, Writing – Review & Editing, Visualization and the coordination of the thermal performance tests. The thesis supervisors contributed to Writing – Original Draft, Supervision, Investigation, and Formal Analysis, and in the first article also to Methodology and Visualization (paper 1, 5 and 6). As expected, the involvement of the supervisors' decreased with time, in line with my progress during the doctoral program and consistent with the expected development of my research autonomy.

2.1. Paper 1: Novel incident angle modifier model for quasi-dynamic testing of flat plate solar thermal collectors.

As mentioned in the introduction, the scientific literature provides different models for the direct IAM that can be used within the QDT framework. Each model comes with a set of parameters that must be determined from experimental test data. In my Master's thesis, I demonstrated that the model generally recommended for flat-plate collectors (Souka and Safwat, 1966) does not accurately reflect the experimental data within certain ranges of the incidence angle. Other alternatives were analyzed, but none showed outstanding performance (Osório and Carvalho, 2014; Sallaberry et al., 2011; Zambolin and Del Col, 2012).

A similar issue arises with evacuated tube technologies, where multiple models have been used but no consensus has been reached on the most suitable one. Consequently, test users must select one for each technology based on their experience. We identify this as a research gap: a general model that can be applied to all technologies would improve the robustness of the QDT method by reducing dependence on the tester while ensuring good performance.

The limitations described above motivated this article, which represented an initial step toward developing a general model to characterize IAM for direct radiation, K_b. Specifically, this paper proposes a novel model for the QDT method of flat-plate solar collectors that is based on the approach commonly used in the SST method. This novel model works by discretising the full

range of incidence angles into smaller sub-intervals and modelling $K_b(\theta)$ as a piecewise linear function within each interval. For example, for an angle step of 10°, the model parameters are $K_b(10°), K_b(20°), \ldots, K_b(80°)$, where each $K_b(\theta_i)$ represents the value of the modifier at node θ_i. For all collector types, boundary conditions are imposed such that $K_b(0°) = 1$ and $K_b(90°) = 0$, thereby fixing the values of the first and last nodes.

Its applicability was experimentally demonstrated using a specific flat-plate collector; a dataset was used to calibrate the parameters, and a separate dataset was used to evaluate the performance of the model. Compared to other commonly used IAM models, this new approach demonstrated improved accuracy across a wide range of incidence angles.

2.2. Paper 2: Improving the experimental estimation of the incident angle modifier of evacuated tube solar collectors with heat pipes.

This paper focuses on enhancing the IAM estimation for evacuated tube solar collectors with heat pipes, covering both diffuse and beam IAM, as well as the QDT and SST methods.

With regard to the QDT method, the novel model previously proposed for flat-plate collectors is extended for the first time to evacuated tube collectors with heat pipes (ETC-HP). Although this work primarily focuses on ETC-HP collectors, the results are applicable to evacuated tubes, in general. Thus, this paper represents a step forward in demonstrating the general applicability of the model.

The determination of the IAM of the beam for the ETC technology is particularly challenging, given its bidirectional dependence, that is, the function K_b depends on two incidence angles: θ_L and θ_T. These angles correspond to the projections of the beam radiation onto two orthogonal planes: one parallel to the longitudinal axis of the tubes and the other in the transverse direction. A significant simplification was introduced by McIntire (1982), who proposed the factorization of the IAM into two independent components. This method expresses K_b as the product of two univariate functions: one dependent on

θ_L and the other on θ_T, that is, $K_b = K_{bL} \times K_{bT}$. In this formulation, K_{bL} represents the IAM evaluated at $(\theta_L, 0)$, and K_{bT} at $(0, \theta_T)$. Building on this factorization, the extension of the empirical model proposed in the previous article involves applying the same discretization scheme to both K_{bL} and K_{bT}. This strategy allows for an independent and accurate characterization of each component of the IAM.

Given the particularities of this technology (biaxial IAM), a dedicated MATLAB tool was developed for parameter identification (i.e., determining the model's parameters), which facilitates reproducibility by other testing laboratories. The program employs a constrained nonlinear regression algorithm to compute and report the values of the characteristic parameters. The constraints are designed to ensure convergence toward physically meaningful values. The tool also reports the associated uncertainties and t-statistics (i.e., the ratio between the parameter estimate and its standard error). For the parameter a_2, the upper and lower bounds can be set arbitrarily, allowing it to be fixed at zero if a negative estimate is obtained or if a positive estimate is accompanied by a t-statistic below 2 (in such a case, both bounds should be set to zero). Additionally, the program allows users to define the angular step for the IAM model, used in the discretization of the function K_b (with a default value of 10°). It is important to note that the tool does not evaluate the quality of the experimental data or verify compliance with ISO 9806 requirements; these aspects must be ensured prior to use. Nevertheless, the tool provides recommended graphs to help assess data variability.

Another research gap addressed by this article is the compatibility of test results between SST and QDT, an issue previously diagnosed in (Kovács et al., 2011; Osório and Carvalho, 2014). It proposes an improved parameter conversion method from SST parameters to QDT parameters, and vice versa, which incorporates the diffuse fraction into the standard procedure. This enhancement increases the accuracy of both diffuse and beam IAM estimates and helps to reduce discrepancies between testing methods. In paper 4, the discrepancies in the diffuse IAM are further analyzed, and alternative modelling approaches for this parameter in the QDT method are proposed, further improving the compatibility between testing methods.

The proposed improvements were experimentally implemented on two ETC-HP collectors, representing the first tests of this technology on the BECS platform. As a result, specific adjustments to the platform were required to en-

sure the proper implementation of test methods for this particular technology. In this context, some tests had to be repeated. During this process, critical aspects were identified and guidelines were outlined in the article to facilitate the implementation of SST and QDT test methods for this type of collector, constituting another scientific contribution.

2.3. Paper 3: On the choice of the parameter identification procedure in quasi-dynamic testing of low-temperature solar collectors.

In Rodríguez-Muñoz et al. (2025), research gaps related to transient modelling of solar thermal collectors and parameter identification within the QDT test method are addressed. As mentioned in the introduction, although the traditional MLR procedure is widely used due to its simplicity, it has certain limitations: it is sensitive to the data averaging interval and presents specific challenges when applied to ETC-HP collector tests.

To overcome these shortcomings, this paper explores the DPI procedure in greater depth as an alternative to the traditional MLR method. Although this approach was previously proposed by other authors for flat-plate collectors under transient test conditions, this paper presents its specific implementation within the QDT framework for both FPC and ETC-HP collectors. In this context, the procedure was implemented in a MATLAB environment and validated against the traditional MLR approach and SST results using experimental data from two solar thermal collectors, one of each type. The principal scientific contributions of this work are the specific implementation and validation of the procedure within the standardized framework, together with its demonstrated advantages over the MLR method. These advantages are described below.

First, through sensitivity analysis and comparison with MLR results, it is shown that the DPI method exhibits less variability with respect to data averaging time. While the MLR method requires a specific averaging time for each collector type, the DPI procedure allows for a broader range of values without compromising accuracy. Moreover, the DPI approach effectively handles

high-resolution data and outperforms MLR in terms of useful power estimation precision and, consequently, parameter uncertainty. Furthermore, it is shown that the DPI procedure provides more reliable results for IAM determination in ETC-HP collectors and enables a reduction in test duration by shortening the required measurement sequences.

The main drawback of the DPI procedure is its more complex implementation, as it requires nonlinear regression algorithms coupled with numerical methods for solving differential equations. To address this, a dedicated MATLAB tool was developed, building upon the one introduced in the previous section; therefore, this paper introduces its second version. This tool enables users to select either the MLR or DPI procedure. For the latter, it also allows users to select the simulation time step. A 30-second simulation time step is set as the default, as this is considered a good compromise between precision and program execution time (shorter time steps increase precision but also computational cost due to the larger data volume).

2.4. Paper 4: Experimental characterization of the diffuse incident angle modifier of solar thermal collectors: improving consistency between test methods.

The issues related to IAM for diffuse solar irradiance identified in my master's thesis gave rise to two lines of research, some of which led to the development of this paper.

Initially, it was considered that the problem could be associated with the uncertainty of measuring diffuse solar irradiance on an inclined plane during QDT testing. In the BECS, the diffuse irradiance is performed indirectly: the global irradiance on the inclined plane is measured directly, along with the global and diffuse irradiance on the horizontal plane. Using these last two measurements, direct normal irradiance (DNI) is inferred via the closure relationship. The DNI is then projected onto the inclined plane to obtain the direct irradiance on that surface. Finally, by subtracting the direct from the global irradiance on the inclined plane, the title diffuse component is estimated.

The diffuse irradiance on the horizontal plane is measured using a shadow

band, which blocks the direct solar irradiance. However, it also blocks part of the diffuse irradiance, and therefore the measurement must be corrected. This correction is commonly made under the assumption that the diffuse irradiance is isotropic, a simplification that introduces a systematic negative bias (Batlles et al., 1995). This bias can lead to an underestimation of diffuse IAM during QDT testing, which could explain the difference in the diffuse IAM parameter between the testing methods. Consequently, a research was carried out to improve the correction factor, which is presented in Rodríguez-Muñoz et al. (2021c) and included in the Appendix A.1 of this thesis (paper 5).

In Rodríguez-Muñoz et al. (2021c), several correction methods were evaluated to account for the anisotropic nature of diffuse irradiance. The study showed that adapting these methods to local conditions significantly improves the accuracy of the measurement. Nine known models for the Pampa Húmeda region were tested, both in their original form and with local adjustments. A new model, based on the parameterization of the Battle method (Batlles et al., 1995), was also proposed and showed the best overall performance under various sky conditions.

Subsequent to the aforementioned paper, the improved model was implemented within the QDT framework. However, no significant improvement was observed with regard to diffuse IAM. A slight difference was found in the beam IAM values at high incidence angles. Although minimal, it suggests some relevance of diffuse solar irradiance measurements in the identification of these parameters, even under clear-sky conditions, where its influence is typically assumed to be low.

These studies provided motivation and direction for further work to improve the modelling of this parameter, both in the context of the SST and QDT test methods. Regarding the SST, an improved procedure was proposed to convert the IAM parameters obtained from the SST to the format required by the QDT. This procedure is described in Section 2.2 and was published in Rodríguez-Muñoz et al. (2024) (paper 2).

Finally, for the QDT method, and within the scope of the work presented in Rodríguez-Muñoz et al. (2026) (paper 4), two alternative models for diffuse IAM were introduced and experimentally evaluated using data from both a flat-plate collector and an evacuated tube collector, thus covering different technologies. Model 1 extends the SST diffuse IAM model to the QDT framework, treating diffuse irradiance as a single global component. Model 2, on

the other hand, separates the contributions of sky and ground-reflected diffuse irradiance, requiring an additional solar measurement (i.e., ground-reflected diffuse irradiance). Both models had previously been proposed by other authors (Bosanac et al., 1994; Carvalho et al., 2009); however, this paper presents their specific implementation within the framework of standardized testing procedures. In addition, a conversion parameter from SST to QDT is proposed for Model 2.

It is important to note that the implementation of Model 2 required the estimation of ground-reflected diffuse solar irradiance. To this end, in the article a method for estimating this component was proposed, which involved characterizing the ground albedo around the BECS platform. This characterization led to a separate publication Rodríguez-Muñoz et al. (2023), which is also included as an Appendix A.1 in this thesis (paper 6).

The comparison was conducted using the improvements introduced in the previous papers (papers 1 to 3 and paper 5), providing a more robust reference framework for evaluating diffuse IAM models. The results showed that both proposed models enhance the consistency between test methods. Given the minimal performance differences between them, Model 1 is recommended due to its simpler implementation.

To facilitate the implementation of these models, they were incorporated into the previously mentioned MATLAB tool, resulting in the third and latest version to date. This version includes all the improvements related to the QDT testing proposed within the framework of this thesis.

Additionally, this work demonstrates the application of the improved parameter conversion procedure proposed in paper 2 (Rodríguez-Muñoz et al., 2024), showing that the combination of both contributions helps to further reduce the discrepancies between the two test methods.

Chapter 3

Conclusions and future work

3.1. Conclusions

This thesis proposes a set of improvements to quasi-dynamic testing (QDT) for low-temperature solar thermal collectors, including flat plate collectors (FPC) and evacuated tube collectors with heat pipes (ETC-HP). These improvements encompass both optical efficiency and transient modelling, and have enhanced the reliability and applicability of the QDT method, providing a more robust framework for evaluating the performance of low-temperature solar thermal collectors. These advancements have led to the publication of four articles in high-impact international journals in the field of renewable energy, which constitute the core of this thesis. A summary of these improvements is presented below.

First, a novel IAM model for the beam component of solar irradiance was proposed and successfully applied to one FPC and two ETC-HP collectors, demonstrating its adaptability to different technologies, particularly to both uniaxial and biaxial IAM configurations. Moreover, its superiority over other available models was experimentally verified. Given its strong performance and broad applicability across various technologies, as well as its consistency with the SST method (as it is an extension of this approach), we consider it a promising model for general use within the standard testing framework.

Second, the characterization of the IAM for the diffuse component of solar irradiance was improved, enhancing the consistency with the results obtained from the SST method. For the QDT approach, two alternative models were proposed to the one currently included in the standard. The first is an ex-

tension of the model used in the SST, treating diffuse irradiance as globally isotropic. The second model treats diffuse irradiance from the sky and the ground separately, which requires an additional solar measurement. In both cases, diffuse irradiance was considered isotropic, and the associated parameters were estimated by integrating the beam IAM. Both models proved to be better options than the one currently included in the standard, as they yielded power output estimates that were more consistent with those from the SST. Given the additional measurement required by Model 2, we consider Model 1 the preferable option, as it offers comparable performance while being simpler to implement.

Along the same lines, although this thesis focuses primarily on the QDT method, an improvement related to the SST testing approach has also been proposed. Specifically, a refined procedure was developed to convert the SST parameters to QDT parameters. This method incorporates the modelling of the diffuse fraction, which becomes relevant at high incidence angles, even under clear-sky conditions, providing more realistic and consistent results compared to those obtained through QDT. The conversion procedure covers all parameters associated with optical efficiency, including IAMs for both the direct and diffuse components.

In addition to IAM, improvements regarding the transient model and parameter identification in the QDT method were addressed. Specifically, the use of the Dynamic Parameter Identification (DPI) procedure was explored as an alternative to the traditional Multiple Linear Regression (MLR) method. Although MLR is widely used due to its ease of implementation, it presents well-known limitations, such as variability of results depending on the averaging time of the experimental data.

In this regard, a DPI algorithm was implemented within the standardized QDT framework for both FPC and ETC collectors, and its superiority over the traditional MLR method was experimentally demonstrated. First, through sensitivity analysis and comparison with MLR results, it was shown that the DPI method exhibits less variability with respect to data averaging time. Although the MLR method requires a specific averaging time for each collector type, the DPI procedure allows for a broader range of averaging times without compromising accuracy. Moreover, the DPI approach effectively handles high-resolution data, outperforming MLR in terms of the precision of useful power estimation and parameter uncertainty.

However, it is important to note that these improvements increase the complexity of parameter identification. To facilitate the incorporation of these enhancements, as well as the reproduction of QDT tests in general, a MATLAB tool was developed throughout the thesis and articles production. This tool enables parameter identification by reporting parameter values along with their uncertainties. It integrates the previously mentioned beam IAM model and enables the angular discretization step to be set. Additionally, it includes three diffuse IAM models (the standard model and the two proposed alternatives) and offers the option to use either the MLR or DPI method for parameter identification.

As a complementary contribution, this work also addressed improving diffuse solar irradiance measurements with sadow bands, which are essential for the implementation of the QDT method. In this regard, a new model was proposed for the correction factor of the shadow band in horizontal diffuse irradiance measurements. This model was compared with other existing models, which demonstrated superior overall performance under various sky conditions. In addition, the albedo of the ground surrounding the BECS platform was characterized and different models for this variable were analyzed. These studies resulted in two articles, which are included in the appendix section.

3.2. Future work

The completion of this thesis marks the consolidation of the BECS infrastructure as a research platform, with a research line aimed at improving testing methodologies and supporting the national development of solar equipment. The following areas have been identified as potential directions for future research.

- With regard to evacuated tube collectors, alternative angular domains have recently been proposed to represent the IAM of the beam for this type of geometry. These approaches offer advantages in terms of physical interpretation and, in some technologies, even demonstrate improved performance (Chen et al., 2023; Hertel et al., 2015). In this context, evaluating these domains within the QDT framework is a relevant topic for future work, particularly when compared to the angular domain currently in use. In addition, significant differences were found in the estimation

of parameter a_5 for this ETC-HP technology, differences between the testing methods and with the estimation of this parameter by weighting the heat capacity of the different materials that make up the collector. Although the implementation of the DPI procedure has helped to reduce the differences, there is still work to be done, such as evaluating the application of other thermodynamic models for this technology.

- The nonlinear regression algorithm implemented for parameter identification required an alternative method to estimate parameter uncertainty, as the one suggested by the standard was not applicable. The linearization method was chosen because it offers a good balance between precision and ease of implementation. However, this method only accounts for the statistical error associated with the regression (Type A) and does not include the uncertainty of the measurements themselves (Type B). In this regard, other methods that account for the uncertainty of measurement are available (Rodrigues et al., 2024; Zirkel-Hofer et al., 2018), although they involve significantly higher computational costs. Exploring these methods and optimizing computational resources represents another potential area for future work.
- This thesis focuses on FPC and ETC-HP collectors, as they are the most widely used technologies, both globally and nationally. However, there are other types of solar collector that are relevant in the market, and extending the improvements developed in this thesis to those technologies represents an important line of future work. For example, unglazed collectors, collectors for medium-temperature applications such as compound parabolic concentrators (CPC), and high-temperature collectors. This is considered a crucial step to facilitate the incorporation of the proposed improvements, ensuring that the testing methods remain applicable across a wide range of technologies.
- The QDT method has made it possible to conduct testing in more flexible conditions, thereby increasing the testing capacity of outdoor laboratories in locations with variable cloud conditions. However, it requires some stability in the fluid entering the collector, which limits its use in real installations. As a future work direction, exploring the application and/or extension of the QDT method to real in-situ installations is considered valuable, since in-situ performance measurement of collectors is an increasingly recognized need (Fahr et al., 2019; Tschopp et al., 2017).

The development of the DPI procedure will facilitate this process as it offers greater flexibility in the thermodynamic model, allowing, for example, discretization of the model along the fluid flow direction to better handle temperature variations at the collector inlet.

- Finally, while all previous work has focused on collector testing, future efforts are expected to extend this line of research to other solar components, such as factory-made solar water heaters and thermal storage tanks. The first medium-term objective is to extend the DPI algorithm to enable the dynamic testing of factory-made solar water heaters in accordance with ISO-9459-5 (2007). This is necessary because the current tool is based on closed-source code, which makes it difficult for testing laboratories to implement (Almeida et al., 2014).

Chapter 4

Full papers

4.1. Paper 1

Novel incident angle modifier model for quasi-dynamic testing of flat plate solar thermal collectors

J. M. Rodríguez-Muñoz[a,*], I. Bove[b], R. Alonso-Suárez[b]

[a] *Laboratorio de Energía Solar, Centro Universitario Regional Litoral Norte, Av. L. Batlle Berres km 508, Salto, Uruguay*
[b] *Laboratorio de Energía Solar, Instituto de Física, Facultad de Ingeniería, J. H. y Reissig 565, Montevideo, Uruguay*

Abstract

There are two accepted standard methodologies to characterize the performance of solar thermal collectors: Steady-State Testing (SST) and Quasi-Dynamic Testing (QDT). This last methodology requires a model for the Incident Angle Modifier (IAM). In this article a new model for the IAM is presented to be used in the quasi-dynamic testing of Flat Plate Collectors (FPC), inspired in the interpolation procedure indicated by the ISO-9806 (2017) standard for SST. The model considers the IAM as a continuous and piecewise linear function and uses its nodes values at each 10° as adjustable parameters. The model's performance is compared against four other widely-used pre-existing models, being more precise and showing a better overall agreement in the whole incident angle's range. It is observed that the proposal is also more reliable, as it has a lower sensitivity to experimental data variability. This second characteristic allows to reduce test's duration because it eliminates the ISO-9806 (2017) requirement of testing the collector in the morning and afternoon, in a balanced manner. Although the specific implementation of this work is for FPC, the model can be extended to other solar collector technologies as it has the ability to represent the IAM variability for all incident angles.

Keywords: Flat plate collectors, incident angle modifier, quasi-dynamic testing, ISO 9806 standard.

1. Introduction

The energy efficiency test of solar thermal collectors allows to determine the main parameters of their thermodynamic behavior. The models resulting from this characterization can be used to estimate the useful energy that the equipment will produce in annual or monthly terms, typically, from simulations of higher temporal resolution (hourly or 10-minute) that take meteorological and utilization data as input for the location and specific application. The ISO-9806 (2017) standard is one of the most used to characterize the thermal performance of solar collectors since it covers a wide variety of technologies: uncovered collectors, flat plate, vacuum tubes, concentrating collectors, etc. This standard admits two test methodologies: one in

*Corresp. author: J. M. Rodríguez-Muñoz, jrodrigue@fing.edu.uy

Steady State Testing (SST), where a high stability of the system forces is required (flow rate and temperature at the inlet, solar irradiance, wind speed, etc.), and the other in Quasi-Dynamic Testing (QDT), in which the stability conditions are more flexible. In various publications the equivalence between both methodologies has been shown, to cite a few: Fischer et al. (2004), Kratzenberg et al. (2006), Rojas et al. (2008), García de Jalón et al. (2011), Osório & Carvalho (2014), Rodríguez-Muñoz et al. (2020).

This work focuses on the modeling of the Incident Angle Modifier (IAM, see its definition in Section 2) for the QDT methodology. This methodology requires the collector to experience various operating conditions during the test time. This variability in operating conditions is achieved by varying the inlet flow temperature and exposing the collector to operate under different sky conditions (clear sky, partially cloudy sky, and completely overcast sky). The determination of all characteristic parameters of the collector is done simultaneously by using Multi-Linear Regression (MLR). There are previous works in which non-linear regression techniques and dynamic simulations have been used together to determine these parameters (Muschaweck & Spirkl, 1993), although their use is not widespread. In either case, whether linear or nonlinear regression is used, a model must be chosen for the IAM. This quantity is usually modeled as an empirical function of the incident angle, θ, and the expression takes the form of an adjustable parameterization. If the adjustment of the parameters is done through multi-linear regression, then the IAM model used must be linear with respect to the parameters.

Several empirical models have been proposed for the IAM. The ISO-9806 (2017) standard suggest one method in particular, known as Ambrosetti function. Its utilization for an standard QDT requires a non linear regression algorithm and has not been reported yet, aside the work of Muschaweck & Spirkl (1993) in which a dynamic in-situ testing is used. Another model, widely-used for Flat Plate Collectors (FPC) with one cover, is that of Souka & Safwat (1966), which has a single adjustable parameter through linear regression. Two improved variations of this model were proposed by incorporating a second adjustable parameter, a linear model (Kalogirou, 2004) and a non-linear model (Tesfamichael & Wäckelgård, 2000), whose use extends to FPC with two covers. Perers (1997) proposed a piecewise model that assumes a constant IAM value for each incident angle interval, and thus, there is an adjustable parameter for each defined interval. This model was initially tested for FPC and has the disadvantage that if there are large IAM variations within a certain interval, then the error of the model in that interval will also be large. This model has also been successfully used in flat collectors with CPC reflectors (Rönnelid et al., 1997). For vacuum tube collectors the problem is more complex as the IAM is a function of two incident angles: θ_L and θ_T. An important simplification to this problem was introduced by McIntire (1982), which consists in factoring the IAM, that is, writing it as the product of two functions, one dependent on θ_L and the other on θ_T. Osório & Carvalho (2014) uses this simplification to test vacuum tube collectors with the QDT method, using the Souka & Safwat model for the θ_L dependent function and the Perers model for the θ_T dependent function. Zambolin & Del Col (2012), considering the large variation of the θ_T dependent function and that

the Perers model does not fit quite well, proposed a generalization of the Souka & Safwat model for this component by adding 3 adjustable coefficients (4 in total). For concentrating collectors, some specific IAM empirical models were developed (Kalogirou, 2004; Eck et al., 2014), which can be used for linear QDT as they are linear with respect to their parameters. In the SST it is valid to determine the IAM for certain incident angles (which we shall call nodes), and then linearly interpolate between them. In this sense, the ISO-9806 (2017) standard proposes an equation to perform this interpolation.

This article presents a new model for the IAM to be used in the QDT of FPC using multi-linear regression. The model consists in building the IAM up by a continuous and piecewise linear function. For this, the interpolation equation provided by the ISO-9806 (2017) standard for SST is generalized as a model (parametrization) for the QDT case, using the eight inner node values as adjustable parameters. This changes fundamentally the way this equation is used, as for the SST case it is just a way to linearly interpolate between directly measured IAM data at given incident angles, and for this proposal it is used as IAM model whose parameters are determined by linear regression at the same time with the other collector's parameters. This model can be seen as an improvement of the Perers model, given that both models have some similarities, such as, for example, that the range of incident angles must be partitioned and that dummy functions must be used to adjust the parameters to the experimental data. These dummy functions are such that they take the value of 1 if a certain variable belongs to a category and 0 if not. The main advantage of the proposed model compared to the previous ones is that it is more precise, in particular, in the intervals of incident angles where the IAM presents large variations. This property makes the model an attractive choice to be used in the testing of vacuum tube solar collectors, which have a more complex IAM. Another advantage of the novel model is that it is more reliable against experimental uncertainty, since its parameters are not very sensitive to variations in the measurements. Furthermore, we think that the proposed model can eliminate the requirement of the ISO-9806 (2017) standard to have measurements before and after solar noon, which increases the duration of the tests. This article shows the implementation of this new model and validates it for a reference FPC. Using a set of independent data, its performance is evaluated, and the sensitivity of the characteristic parameters against the variation of the experimental data is analyzed. The performance of this model is compared with that of the ISO-9806 (2017); Souka & Safwat (1966); Kalogirou (2004); Perers (1997) models. The use of the Kalogirou model for the QDT methodology has not yet been analyzed in the literature, which is another contribution of this work.

This article is organized as follows. Section 2 describes the thermal model presented in the ISO-9806 (2017) standard for quasi-dynamic testing of low temperature solar collectors with cover (flat plate collectors are included in this category) and shows the implementation of the different IAM models (parameter identification procedure). Section 3 describes the test facility, the measurements taken, and the adjustment and evaluation methodology of the different models. Section 4 presents and discusses the results. Finally, Section 5 summarizes the main conclusions of this work.

2. Collector model and parameter identification procedure

This section describes the thermal model used in the quasi-dynamic testing of FPC, the different incidence angle modifier models and the parameter identification procedure.

2.1. Model for quasi-dynamic testing

The thermal model considered by the quasi-dynamic method of the ISO-9806 (2017) standard is quite general and can be applied to different technologies of thermal solar collectors. The standard provides criteria on how to use the model in each case, that is, which terms can be omitted in the general equation depending on the solar collector technology. Eq. (1) shows the suggested model for low temperature collectors with cover,

$$\frac{\dot{Q}_u}{A_G} = \eta_{0,b}\left[K_b\left(\theta\right)\ G_{bt} + K_d\ G_{dt}\right] - a_1\left(\vartheta_m - \vartheta_a\right) - a_2\left(\vartheta_m - \vartheta_a\right)^2 - \frac{C}{A_G}\frac{d\vartheta_m}{dt}, \tag{1}$$

where G_{bt} and G_{dt} are the direct and diffuse solar irradiance on the collector plane, respectively, and the parameters that characterize the thermal behavior of the collector are: $\eta_{0,b}$, K_b, K_d, a_1, a_2 and C. The meaning and unit of each parameter, including A_G, are indicated in nomenclature list.

The $\eta_{0,b}$ peak efficiency corresponds to the product of the efficiency factor and the optical efficiency of the collector at normal incidence, that is, $\eta_{0,b} = F'\left(\tau\alpha\right)_n$. It should be noted that, for uniformity with other articles and textbooks, the nomenclature used in this work is not exactly the one used by ISO-9806 (2017) standard for the QDT, however, the parameters have the same meaning. All the characteristic parameters of the collector are assumed to be constant except for the incident angle modifier for direct solar irradiance (K_b), which is modeled as a function of the incident angle.

2.2. Incident angle modifier (IAM)

The incident angle modifier for direct solar irradiance is defined as the ratio between the peak efficiency at a given incident angle, $\eta_b(\theta)$, and the peak efficiency at normal incidence to the collector plane ($\theta = 0°$), $\eta_{0,b}$:

$$K_b\left(\theta\right) = \frac{\eta_b(\theta)}{\eta_{0,b}}. \tag{2}$$

In the case of FPC, K_b is a function dependent only on the incident angle θ (univariate function). In this article, five models for this function are considered.

The first model is given in Eq. (3) and corresponds to the one suggested by the standard ISO-9806 (2017). This model has a single adjustable parameter, n, which has a non linear dependency with the IAM, and so,

must be determined by non linear regression for QDT. The rest of the models considered in this work are linear with respect to their parameters, which can be determined by a simple linear regression.

$$K_b(\theta) = 1 - \tan^n(\theta/2). \tag{3}$$

The second model is given in Eq. (4) and corresponds to the Souka & Safwat (1966) model. This model has a single adjustable parameter, b_0, and has been widely-used in the quasi-dynamic testing of FPC (Fischer et al., 2004; Kratzenberg et al., 2006; Rojas et al., 2008; Kong et al., 2012; Osório & Carvalho, 2014; Rodríguez-Muñoz et al., 2020).

$$K_b(\theta) = 1 - b_0 \left(\frac{1}{\cos\theta} - 1 \right). \tag{4}$$

The third model is that of Kalogirou (2004), represented by Eq. (5). This model incorporates an additional quadratic term in the variable $(1/\cos\theta - 1)$ and the adjustable parameters are b_1 and b_2.

$$K_b(\theta) = 1 - b_1 \left(\frac{1}{\cos\theta} - 1 \right) - b_2 \left(\frac{1}{\cos\theta} - 1 \right)^2. \tag{5}$$

These three models (ISO-9806, Souka & Safwat and Kalogirou) require that the experimental data (samples) are obtained in a distributed manner throughout the range of variation of the incident angle, ideally, in a uniform manner. Otherwise, the adjustment of the parameters may be biased for one angle range or another, affecting the representativeness of the model throughout the IAM range.

The fourth considered model corresponds to that of Perers (1997), also known as the extended MLR or angle-by-angle method. Like the second model, the model of Perers is widely-used (Rönnelid et al., 1997; Kong et al., 2012; Zambolin & Del Col, 2012; Osório & Carvalho, 2014). As previously mentioned in the introduction, this model consists of a piecewise constant function for incident angle intervals. For example, if a 10° step is used, the adjustable parameters will be $K_b(0° \to 10°), K_b(20° \to 30°), \ldots, K_b(80° \to 90°)$, where $K_b(\theta_i \to \theta_{i+1})$ is the value of K_b (constant) in the interval from θ_i to θ_{i+1}. When there are large variations in K_b, small intervals should be defined to reduce the error of the method. This may result in a large set of experimental data being required, since sufficient data must be available in each of the defined intervals. It should be noted that for the $K_b(\theta_i \to \theta_{i+1})$ value to be similar to the real K_b value at the midpoint of each interval, one must have an approximately uniform distribution of experimental data in each one, and the intervals length must be taken as small enough that a linear behavior can be assumed within them. If within an interval, K_b does not behave in a linear way or the distribution of the samples is not uniform, then this desirable property will not be obtained.

The models described above were selected by their relevance and are used here as reference level to compare the performance of the proposed model. Model 1 is non linear, so it implies a more complex computational implementation than the others, but it is suggested as a reference by the ISO-9806 (2017) for

SST, so it is considered in the comparison although its utilization has not been reported for the standard QDT. Model 2 and 4 are linear, hence simpler to implement, and are widely-used for QDT. Model 3 is an improvement of Model 2 that adds a linear second order term, and its implementation does not represent an extra complexity. This model has also not been tested yet for QDT.

The last model is the one proposed in this work. This model consists in dividing the incident angle range into sub-intervals and assume a piecewise linear function into them. For example, if a 10° step is used, the adjustable parameters will be $K_b(10°), K_b(20°), \ldots, K_b(80°)$, where $K_b(\theta_i)$ corresponds to the K_b value in the θ_i angle (or node). It is imposed for the first and last parameter, respectively, that $K_b(0°) = 1$ and $K_b(90°) = 0$. In the same way as the Perers model, the smaller the angular step, the smaller the model error and the greater the experimental data requirement. The main advantage of this method compared to the previous one is that for the same angular step, a better fit is obtained in the intervals where there are large K_b variations. Another advantage is that, although it is recommended, it is not strictly necessary that the distribution of experimental data in each defined interval to be uniform. The implementation of this proposal requires a little more elaboration than that of the previous linear models, and is described in the next subsection along with the rest of the models.

2.3. Parameter identification procedure

The IAM models described in the previous section can be classified into two groups: (i) linear models and (ii) non linear models. Models from 2 to 5 (Souka & Safwat, Kalogirou, Perers and the novel model) belong to the first group and model 1 (ISO-9806, 2017) to the second. This section describes the parameter identification procedure used for each model, according to their classification. In both cases the measured variables correspond to 5-minutes temporal averages of 10 seconds samples.

2.3.1. Linear IAM models

The parameter identification of Eq. (1) for the linear IAM models is performed by multi-linear regression (MLR). This is done by implementing for each model the standard linear least mean square algorithm with multiple variables. The implementation of the Souka & Safwat model is described in detail in Kratzenberg et al. (2006). Since K_b depends linearly on its only parameter (b_0), the adjustment can be made linearly in terms of the variable $(1/\cos\theta - 1)$. The implementation of the second model is an extension of the first one, adding the independent variable $(1/\cos\theta - 1)^2$ to the linear regression model, so its implementation does not vary significantly. The implementation of the third model is explained in Perers (1997). The adjustment of the Perers model is done through the use of dummy functions. Specifically, a dummy function is applied for each incident angle interval, defined usually by a 10° spacing, and each of these variables will adopt the value of 1 if the incident angle is included in it and 0 if not. Then the parameter adjustment problem can

be written as a multi-linear regression, using these functions as variables associated with each adjustable parameter.

The implementation of the proposed model is as follow. If an angular step of 10° is chosen and the K_b values at the nodes are known, 0°, 10°, 20°,..., 90°, then the K_b value for any θ angle can be expressed as:

$$K_b(\theta) = \left[K_b\left(\left\lfloor \frac{\theta}{10} \right\rfloor 10\right)\left(\left\lfloor \frac{\theta+10}{10} \right\rfloor - \frac{\theta}{10}\right) + K_b\left(\left\lfloor \frac{\theta}{10} \right\rfloor 10 + 10\right)\left(\frac{\theta}{10} - \left\lfloor \frac{\theta}{10} \right\rfloor\right)\right], \tag{6}$$

where the open square brackets indicate to round up to the previous lower natural number. An advantage of this formulation is that it allows to set the ends of the IAM at physically appropriate values, if $K_b(0°) = 1$ and $K_b(90°) = 0$ are set. This equation corresponds to equation 27 of the ISO-9806 (2017) standard, and is given there for SST as a way to interpolate the IAM data, measured at given incident angles. Therefore, as given by the standard, this simple two-points line determination is not a model itself. Here, in the following paragraphs, it is shown how to include this expression into Eq. (1) to create an IAM model with the nodes $K_b(10°), \ldots, K_b(80°)$ as adjustable parameters. In this way, these parameters are adjusted by linear regression jointly with the other collector's parameters, identically to the other models' formulations.

Applying Eq. (6) to each of the intervals (0°→10°, 10°→20°,..., 80°→90°), the term $K_b\ G_{bt}$ of Eq. (1) can be easily written as follows:

$$\begin{aligned} K_b\ G_{bt} =& K_b(0°)\ G_{bt}(0°, 10°)\left(\frac{10-\theta}{10}\right) \\ &+ \sum_{\substack{\phi=10° \\ \text{steps}=10°}}^{80°} K_b(\phi)\left[G_{bt}(\phi-10°, \phi)\left(\frac{\theta-(\phi-10°)}{10}\right) + G_{bt}(\phi, \phi+10°)\left(\frac{(\phi+10°)-\theta}{10}\right)\right] \\ &+ K_b(90°)\ G_{bt}(80°, 90°)\left(\frac{\theta-80}{10}\right), \end{aligned} \tag{7}$$

where the notation $G_{bt}(\phi_1, \phi_2)$, with ϕ_1 and ϕ_2 as two generic angles that satisfy $\phi_2 > \phi_1$, means that $G_{bt} = G_{bt}(\theta)$ if θ belongs to the interval (ϕ_1, ϕ_2), and that $G_{bt} = 0$ otherwise. This function, $G_{bt}(\phi_1, \phi_2)$, can also be seen as a term-by-term product between the vector of measurements G_{bt} and a dummy function that is 1 if θ belongs to the interval (ϕ_1, ϕ_2) or 0 if otherwise. Then, substituting Eq. (7) in Eq. (1), the useful power produced by the collector can be expressed as follows:

$$\begin{aligned} \frac{\dot{Q}_u}{A_G} = \eta_{0,b}\Bigg\{ & K_b(0°)\ G_{bt}(0°, 10°)\left(\frac{10-\theta}{10}\right) \\ &+ \sum_{\substack{\phi=10° \\ \text{steps}=10°}}^{80°} K_b(\phi)\left[G_{bt}(\phi-10°, \phi)\left(\frac{\theta-(\phi-10°)}{10}\right) + G_{bt}(\phi, \phi+10°)\left(\frac{(\phi+10°)-\theta}{10}\right)\right] \\ &+ K_b(90°)\ G_{bt}(80°, 90°)\left(\frac{\theta-80}{10}\right)\Bigg\} + \eta_{0,b} K_d\ G_{dt} - a_1\left(\vartheta_m - \vartheta_a\right) - a_2\left(\vartheta_m - \vartheta_a\right)^2 - \frac{C}{A_G}\frac{d\vartheta_m}{dt}. \end{aligned} \tag{8}$$

For the application of the multi-linear regression algorithm, Eq. (8) must be written linearly in terms of its parameters, that is, in the form of $y = \sum_{i=1}^{n} p_i x_i$, where y is the dependent variable, x_i are the independent variables (n in total) and p_i are the parameters to be determined. Thus, the useful power produced by the collector per unit area is defined as the dependent variable ($y = \dot{Q}_u / A_G$) and the independent variables and the coefficients to be determined are listed below:

- $x_1 = G_{bt}(0°, 10°)\left(\frac{10-\theta}{10}\right)$, $p_1 = \eta_{0,b}$,
- $x_2 = \left[G_{bt}(0°, 10°)\left(\frac{\theta}{10}\right) + G_{bt}(10°, 20°)\left(\frac{20-\theta}{10}\right)\right]$, $p_2 = \eta_{0,b}\ K_b(10°)$,
- $x_3 = \left[G_{bt}(10°, 20°)\left(\frac{\theta-10}{10}\right) + G_{bt}(20°, 30°)\left(\frac{30-\theta}{10}\right)\right]$, $p_3 = \eta_{0,b}\ K_b(20°)$,
- $x_4 = \left[G_{bt}(20°, 30°)\left(\frac{\theta-20}{10}\right) + G_{bt}(30°, 40°)\left(\frac{40-\theta}{10}\right)\right]$, $p_4 = \eta_{0,b}\ K_b(30°)$,
- $x_5 = \left[G_{bt}(30°, 40°)\left(\frac{\theta-30}{10}\right) + G_{bt}(40°, 50°)\left(\frac{50-\theta}{10}\right)\right]$, $p_5 = \eta_{0,b}\ K_b(40°)$,
- $x_6 = \left[G_{bt}(40°, 50°)\left(\frac{\theta-40}{10}\right) + G_{bt}(50°, 60°)\left(\frac{60-\theta}{10}\right)\right]$, $p_6 = \eta_{0,b}\ K_b(50°)$,
- $x_7 = \left[G_{bt}(50°, 60°)\left(\frac{\theta-50}{10}\right) + G_{bt}(60°, 70°)\left(\frac{70-\theta}{10}\right)\right]$, $p_7 = \eta_{0,b}\ K_b(60°)$,
- $x_8 = \left[G_{bt}(60°, 70°)\left(\frac{\theta-60}{10}\right) + G_{bt}(70°, 80°)\left(\frac{80-\theta}{10}\right)\right]$, $p_8 = \eta_{0,b}\ K_b(70°)$,
- $x_9 = \left[G_{bt}(70°, 80°)\left(\frac{\theta-70}{10}\right) + G_{bt}(80°, 90°)\left(\frac{90-\theta}{10}\right)\right]$, $p_9 = \eta_{0,b}\ K_b(80°)$,
- $x_{10} = G_{dt}$, $p_{10} = \eta_{0,b}\ K_d$,
- $x_{11} = -(\vartheta_m - \vartheta_a)$, $p_{11} = a_1$,
- $x_{12} = -(\vartheta_m - \vartheta_a)^2$, $p_{12} = a_2$,
- $x_{13} = -\frac{d\vartheta_m}{dt}$, $p_{13} = C/A_G$.

It shall be noted that the values of $K_b(0°)$ and $K_b(90°)$ are not included in the regression problem, since they are imposed at $K_b(0°) = 1$ and $K_b(90°) = 0$. From this point onwards, the problem is solved like any other multiple linear regression problem. The determination of the parameters $p_1, p_2, \ldots, p_{13}$ and the calculation of their respective uncertainties can be consulted in textbooks, for example Quarteroni et al. (2000). The solution of the least mean square algorithm for multiple variables is:

$$p = (X^T X)^{-1} X^T y, \tag{9}$$

where p is a vector containing the parameters' values and X is a matrix with the x_i variables as columns. The uncertainty for each parameter is derived from the covariance matrix, whose detailed calculation can be consulted in Kratzenberg et al. (2006). This is the same procedure that is applied for the parameters' determination in the other linear models. An script (for matlab) that allows to calculate the model's parameters and uncertainty is provided in http://les.edu.uy/RDpub/RBA_model_training.m.

2.3.2. Non linear IAM model

The parameters identification for model 1 is performed by a non linear least mean square algorithm with multiple variables. There are several ways to address the problem. The procedure used in this work is to linearize the function y^* (estimation of the y variable) around an operating point p_0 as follows:

$$y^*(p) \approx y^*(p_0) + J(p_0)\,(p - p_0)\,, \tag{10}$$

where $J(p_0)$ is the Jacobian matrix of the function $y^*(p)$ evaluated at p_0. The elements of this matrix can be estimated numerically using centered finite differences. Then the problem can be solved iteratively using Eq. (9), substituting the matrix X with $J(p_0)$ and the vector y with $y^*(p_0) - y$. This algorithm is known as Newton's iterative method (Quarteroni et al., 2000). The uncertainty of the parameters can be estimated analogously to the linear case. It is recalled that, as in the previous section (linear models), the temporal derivative of the mean temperature of the fluid ($d\vartheta_m/dt$) is estimated by finite differences using the experimental data and is treated as an independent variable in the regression algorithm.

3. Experimental data and methodology

This section describes the test facility, the measurements performed and the methodology for evaluating the models.

3.1. Test facility

The measurements were taken at the Solar Heaters Test Platform (BECS) of the Solar Energy Laboratory (LES, http://les.edu.uy/) of the Universidad de la República (UdelaR) located near the city of Salto (Latitude=31.28° S, Longitude=57.92° W), Uruguay. This test facility was designed by researchers from this laboratory based on the pre-existing platform of the National Renewable Energy Center (CENER) in Spain. Recently, the BECS participated in a Latin American inter-comparison of test laboratories organized by the PTB (Physikalisch-Technische Bundesanstalt), the German Metrological Institute, an activity in which the platform obtained the best qualification for almost all tests and just one minor observation in the determination of a secondary variable (Fischer, 2020).

A flat plate solar thermal collector with a gross area of 2.02 m^2 was used for this work, which was the reference collector also used in the aforementioned inter-comparison of test laboratories. The measurements were made between November 17th and December 18th, 2019. Some of these measurements were also used for the inter-comparison. The collector was mounted on a mobile tracker as shown in Figure 1. The horizontal tilt of this tracker can be manually adjusted between 5° and 85°, and the azimuth can be adjusted manually or automatically with a 2-minute time step between −90° and 90°.

Figure 1: Assembly of the collector on the solar tracker of the test bank.

Figure 2 shows a simplified diagram of the thermo-hydraulic installation of the BECS. It has three independent circuits: (1) the primary circuit or collector circuit, in green, (2) the heating circuit, in red, and (3) the cooling circuit, in blue. The pipe's black sections close to the solar collector in the primary circuit correspond to flexible pipes that can be seen in Figure 1. The temperature control at the collector inlet (primary circuit) is done in two stages. First, the hot fluid at the collector outlet must be cooled, a process that is done by the heat exchanger IC1. The fluid is then precisely heated to match the required inlet temperature (set by the operator) through the heat exchanger IC2. The cooling circuit uses water at 10 °C that comes from an electric water chiller and the heating circuit uses hot water that comes from the 30 litre electric water heater. Each circuit has a circulation pump (B1, B2 and B3) and a manually regulated valve (VR1, VR2 and VR3). These valves are used to roughly set the flow in each circuit. The manually regulated valve VR4 is used to regulate the temperature of the fluid at the inlet of the IC1 heat exchanger, which mixes the hot return and the cold water at 10 °C. The flow rates in the three circuits are precisely regulated by electro-pneumatic valves (V51, V52 and V53), commanded by PID controllers (indicated by the dotted line). The entire control system was developed locally using a S7-1200 Siemens PLC. The diagram also indicates the location of the water temperature sensors (T_1, T_2, T_3, ϑ_i y ϑ_o), the ambient temperature sensor (ϑ_a), the global horizontal (G_h) and titled plane (G_t) irradiance sensors, the horizontal diffuse irradiance sensor (G_{dh}), the wind measurement (v) and the wind forcer (WG).

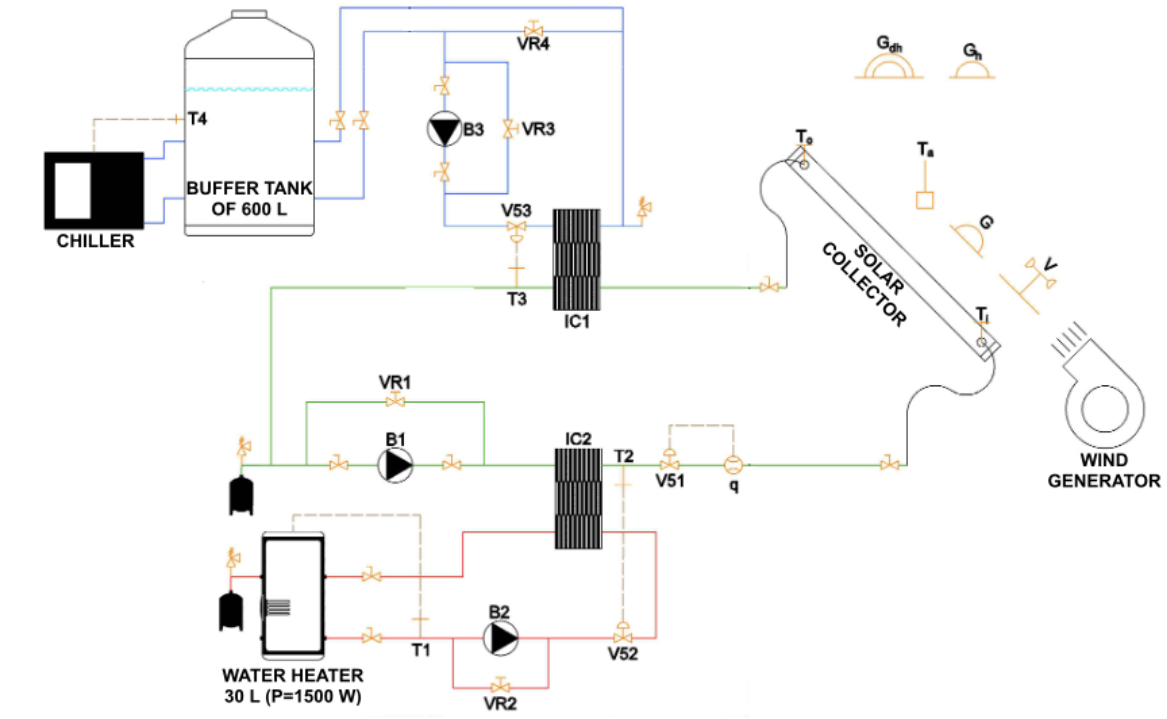

Figure 2: Thermo-hydraulic installation diagram.

To measure the temperature at the input and output of the collector (ϑ_i and ϑ_o), a 3 wire PT100 with 4-20 mA transmitters from Herten company were used. These sensors were calibrated at LES using a calibrated thermal bath and calibrated reference thermometers, reporting a standard uncertainty (P67, $k = 1$) of 0.02 °C. Ambient temperature (ϑ_a) was recorded with a Honeywell 2-wire PT1000 sensor also calibrated at LES with a standard uncertainty of 0.02 °C. The flow measurement (q) was performed with an Endress & Hauser electromagnetic flowmeter with a standard uncertainty of 0.5 % of the measurement. The wind speed parallel to the collector plane (v) was measured with an NGR cup anemometer with a standard uncertainty of 0.25 m/s. The global irradiance in the collector plane (G_t) was measured with a Kipp & Zonen CMP10 pyranometer. The global irradiance in the horizontal plane (G_h) was measured with a Kipp & Zonen CMP11 pyranometer and the diffuse irradiance in the horizontal plane (G_{dh}) with a Kipp & Zonen CMP6 pyranometer mounted with a shadow band from the same manufacturer. All the pyranometers used are spectrally flat (ISO-9060, 2018), being Class A for the global irradiance measurements (G_h and

G_t) and Class B for the diffuse irradiance measurement (G_{dh}). The diffuse irradiance measurement (with shadow band) was corrected with the expression provided by the manufacturer (Drummond, 1956). These pyranometers are calibrated annually at the LES according to the ISO-9847 (1992) standard against a Kipp & Zonen CMP22 secondary standard that is kept traceable to the world radiometric reference at the World Radiation Center in Davos, Switzerland. All measurements were recorded every 10 seconds using a Fischer Scientific DT85 datalogger. The G_{bt} direct irradiance in the collector plane was estimated from the G_h and G_{dh} with the following procedure. First, the direct normal irradiance (DNI, G_b) was calculated using the closure relation $G_h = G_b \cos\theta_z + G_{dh}$, where $\cos\theta_z$ is the cosine of the solar zenith angle. Then, the G_{bt} was calculated from the DNI, by multiplying with the cosine of the incident angle, θ.

3.2. Measured sequences

The tests were performed according to the ISO-9806 (2017) standard. During the tests, a wind speed of 3 m/s (spatial average) was imposed along the collector plane by using the air forcers shown in Figure 1. The fluid flow was set at 2.4 l/min and the tracker inclination angle was set at 45°. The azimuth was adjusted manually or automatically depending on the day type. The day types correspond to specific test sequences defined by the ISO-9806 (2017) standard and there are 4 different day types in total. Each of these sequences (day type) must have a duration of at least 3 hours and may be made up of several non-consecutive sub-sequences of at least 30 minutes each. The procedure and the purpose of each day type is described in the next paragraph. In all cases, before the measurement period, the collector was put through a conditioning period of 15 minutes at the corresponding test temperature. This period was not included in the models' parameter identification.

From the tests carried out, 16 different measurement sub-sequences were obtained; 11 of these sub-sequences were used to adjust the models and the remaining 5 were used for validation. The main characteristics of the training sub-sequences are shown in Table 1. This table shows the date and time of the test, the inlet temperature ϑ_i (average and maximum variability), the flow q (average and maximum variability), the average of the difference $\vartheta_m - \vartheta_a$, the diffuse fraction at the collector's plane $f_d^* = G_{dt}/G_t$ (range of variation) and the incident angle θ (range of variation). All the sequences meet the requirements for temperature and flow stability at the collector's inlet established in the ISO-9806 (2017) standard for the QDT methodology (variability less than $\pm 1\,^{\circ}\mathrm{C}$ and 2 %, respectively). The day type 1 sequence is made up of the sub-sequences $1a - 1e$. These series were obtained under clear sky conditions and during the tests an inlet temperature was set such that the mean temperature of the fluid was close to ambient temperature, that is, $\vartheta_m \simeq \vartheta_a$. These sequences (day type 1) are mostly used to determine $\eta_{0,b}$ and the IAM parameters. During sub-sequence $1a$, the solar tracker was configured so that it follows the position of the Sun in azimuth to obtain small incident angles ($\theta \leq 11.3°$). For sequences $1b - 1e$, the tracker was oriented North (fixed position) to obtain greater incident angles. Series $1b$ and $1c$ were measured before solar noon and series $1d$

and $1e$ after solar noon. The standard requires data measured before and after solar noon in approximately the same amount for large incident angles. The rest of the training sub-sequences (from $2a$ to $4b$) were obtained with azimuthal tracking to work in conditions close to those of normal incidence ($K_b \simeq 1$). This is not a requirement of the standard but it was done to achieve a greater decoupling of the independent variables and thus improve the parameter identification. Sub-sequences $2a$ and $2b$ were performed at an intermediate temperature and under variable sky conditions. The high variability of the diffuse fraction f_d^* in these sub-sequences accounts for this. These sub-sequences from day type 2 are useful to better identify the C and K_d parameters. The day type 3 and day type 4 sequences are mainly used to identify the thermal loss factors: a_1 and a_2. Sub-sequences $3a$ and $3b$ were performed at an intermediate temperature and in clear sky conditions. Sub-sequences $4a$ and $4b$ were performed at high temperature and in clear sky conditions.

Table 1: Description of the different measurement sub-sequences for model training.

Day type	Sub sec.	Date	Time	# data points	ϑ_i (°C)	q (l/min)	$\vartheta_m - \vartheta_a$ (°C)	f_d^*	θ (°)
1	1a	24/11	09:05-10:15	14	18.21(0.14)	2.39(0.7 %)	0.60	≤ 0.128	≤ 11.3
	1b	19/12	08:50-11:10	28	26.35(0.13)	2.39(0.9 %)	1.38	≤ 0.171	44.3-69.0
	1c	22/11	10:50-11:40	10	28.23(0.10)	2.39(0.7 %)	1.09	≤ 0.274	37.3-43.4
	1d	24/11	13:50-14:55	13	26.23(0.30)	2.39(0.7 %)	0.87	≤ 0.145	37.4-48.2
	1e	24/11	15:20-16:30	14	26.72(0.10)	2.39(0.9 %)	-0.32	≤ 0.195	52.2-65.0
2	2a	19/11	11:15-13:50	31	47.88(0.18)	2.39(0.7 %)	17.90	0.50-1.03	≤ 33.8
	2b	18/11	14:50-16:55	25	64.37(0.18)	2.39(1.0 %)	31.40	0.29-1.02	≤ 11.9
3	3a	17/11	15:05-16:40	19	49.74(0.19)	2.39(0.9 %)	20.10	≤ 0.117	≤ 10.4
	3b	28/11	09:35-11:35	24	65.29(0.12)	2.39(0.8 %)	41.74	≤ 0.105	≤ 27.5
4	4a	20/11	14:10-16:50	32	81.01(0.12)	2.39(1.0 %)	48.40	≤ 0.145	≤ 18.0
	4b	18/12	08:40-10:00	16	85.55(0.23)	2.39(0.8 %)	61.30	≤ 0.110	≤ 9.9

The main characteristics of the validation sub-sequences are shown in Table 2. These sub-sequences were obtained according to the day type 1 procedure (in clear sky conditions and with $\vartheta_m \simeq \vartheta_a$). This was done to reduce the effect of the parameters not linked to the IAM (K_d, a_1, a_2 and C) in the validation and thus focus on the effect that the different IAM models have on the collector performance (useful power). All validation sub-sequences were performed with the solar collector facing North (fixed position) to obtain large incident angles in the morning and in the afternoon. The $1f - 1h$ sub-sequences were performed before solar noon and the $1i - 1j$ sub-sequences after solar noon. As shown in Section 4, the relevant variations in IAM occur in the region of large incident angles ($\theta \gtrsim 40°$), for which the models are expected to provide a solution. For this reason, the focus is to evaluate the performance of the models in this range of angles.

Table 2: Description of the different measurement sequences for validation of the models.

Day type	Sub sec.	Date	Time	# data points	ϑ_i (°C)	q (l/min)	$\vartheta_m - \vartheta_a$ (°C)	f_d^*	θ (°)
	1f	6/12	08:25-09:45	16	24.06(0.73)	2.39(0.7 %)	2.6	≤ 0.206	58.3-71.3
	1g	6/12	9:50-10:55	13	26.36(0.62)	2.39(0.7 %)	3.3	≤ 0.132	44.2-68.3
1	1h	6/12	10:55-11:30	7	28.84(0.77)	2.39(0.9 %)	5.2	≤ 0.106	41.4-43.9
	1i	9/12	12:55-14:20	17	32.75(0.08)	2.39(0.8 %)	4.3	≤ 0.150	36.9-42.6
	1j	9/12	14:20-16:50	29	34.21(0.10)	2.39(0.7 %)	3.0	≤ 0.222	44.2-68.3

To obtain a day type 1 sequences, it is sufficient to measure the useful power from approximately normal incidence ($\theta \simeq 0°$) to angles greater than 60°. In this case, both the training sub-sequences and the validation sub-sequences were measured up to a 70° angle. useful power measurements in the presence of angles greater than 70° are associated with a high uncertainty, since in these conditions the collector works with a small temperature difference between its inlet and outlet due to the IAM adopting a very small value (close to zero). For the purposes of conducting annual performance simulations, it is considered acceptable to perform a linear approximation of the IAM in the range of 70° and 90°, with $K_b(90°) = 0$. The data series are available in http://les.edu.uy/RDpub/IAM_experimental_data.rar.

3.3. Performance evaluation

As mentioned in the previous section, the sub-sequences of Table 1 were used for model training, that is, to determine the characteristic parameters of each model. Then, with the parameters calculated in the previous step, the useful power produced by the collector was estimated for the sub-sequences of Table 2, in order to compare it with the experimental useful power. For these sub-sequences ($1f - 1j$), the Mean Bias Error (MBE) and the Root Mean Square Error (RMSE), in useful power per unit area, were calculated as shown in the following equations:

$$\text{MBE} = \frac{1}{N}\sum_{i=1}^{N}\left(\frac{\dot{Q}^*_{u,i}}{A_G} - \frac{\dot{Q}_{u,i}}{A_G}\right), \qquad \text{RMSE} = \sqrt{\frac{1}{N}\sum_{i=1}^{N}\left(\frac{\dot{Q}^*_{u,i}}{A_G} - \frac{\dot{Q}_{u,i}}{A_G}\right)^2}, \tag{11}$$

where N is the amount of data samples, $\dot{Q}^*_u$ is the estimated useful power (predicted with Eq. (1)) and $\dot{Q}_u$ is the experimental useful power. As a way of summarizing the information obtained by the MBE and the RMSE metrics into a single indicator, a third performance indicator was calculated, which consists of a combination of the previous ones (Combine Performance Indicator - CPI). This metric is shown in Eq. (12) and is similar to the one used in Gueymard (2012); Abal et al. (2017).

$$\text{CPI} = \frac{|\text{MBE}| + \text{RMSE}}{2}. \tag{12}$$

4. Results

4.1. Parameter identification

Table 3 shows the parameters value for the different considered models. These parameters were obtained from the experimental sub-sequences of Table 1 by linear or non linear regression as described in Subsection 2.3. Table 3 also shows the uncertainty of each parameter and the t-ratio. The t-ratio is the ratio between the value and its uncertainty, and is used to evaluate the statistical significance of a parameter. The parameter $K_b(80° \rightarrow 90°)$ of model 4 and the parameter $K_b(80°)$ of model 5 were omitted from this table because the experimental measurements reach up to 70°. Furthermore, in the case of model 4, $K_b(0° \rightarrow 10°) = 1$ was imposed and for this reason this parameter is also omitted. For FPC and others the IAM is always less than unity (Duffie & Beckman, 1991). In the case of models 4 and 5, the experimental uncertainty can lead to the IAM adopting values slightly higher than this limit (Perers, 1997; Kong et al., 2012). To avoid this behavior, the physical constraint $K_b(\theta) \leq 1$ for all θ was imposed for these models.

It is common that different tests on the same collector arise to different a_1 and a_2 values. However, this differences tend to compensate between both parameters, that is, the higher the a_1 value, the lower the a_2 value and vice versa. This behavior can be seen in Fischer et al. (2004); García de Jalón et al. (2011); Osório & Carvalho (2014). For this reason it is not convenient to directly compare the value of these parameters separately. It is better to compare the combined effect through the global loss factor$a(\Delta\vartheta)$, which can be calculated as follows: $a(\Delta\vartheta) = a_1 + a_2\Delta\vartheta$, where the temperature difference is $\Delta\vartheta = \vartheta_m - \vartheta_a$. It is usual to use the loss factor combined to a temperature difference of 50 °C for this kind of collector. The value of this parameter, $a(50\,°\mathrm{C}) = a_{50}$, is also shown in Table 3. This parameter was the one used in the test laboratory inter-comparison mentioned in Subsection 3.1 (Fischer, 2020).

The ISO-9806 (2017) standard establishes that a parameter has been correctly identified (statistically significant) if the t-ratio is greater than 3. Table 3 shows that in all cases a t-ratio greater than this value was obtained except for the case of the b_1 parameter of the Kalogirou model, where a value of 1.5 was obtained. According to the standard, this suggests that this parameter can be omitted from the model in this case, and that it is possible for this collector to use a model that consists only of the second-order term without significant loss of performance. Table 3 particularly highlights the high t-ratio of the parameters associated with IAM models 4 and 5, being in all cases higher than those of models 1, 2 and 3 (n, b_0, b_1 y b_2). It is observed that the value of the parameters $\eta_{0,b}$, K_d, a_{50} and C/A_G, common to the 5 models, are very close to each other, with differences of less than ±3 %.

Table 3: Value, uncertainty and t-ratio of the characteristic parameters of each of the considered models. Units for the parameters are indicated in the nomenclature list at the end of the article.

Model 1 ISO-9806 (2017)				Model 2 Souka & Safwat (1966)				Model 3 Kalogirou (2004)			
param.	value	uncert.	t-ratio	param.	value	uncert.	t-ratio	param.	value	uncert.	t-ratio
$\eta_{0,b}$	0.721	0.001	1030	$\eta_{0,b}$	0.725	0.001	515	$\eta_{0,b}$	0.718	0.001	665
K_d	0.971	0.003	303	K_d	0.973	0.006	163	K_d	0.967	0.005	201
n	3.811	0.036	107	b_0	0.121	0.005	26	b_1	0.0121	0.0082	1.5
a_1	4.155	0.060	69	a_1	4.311	0.144	38	b_2	0.106	0.007	15
a_2	0.084	0.0010	8	a_2	0.0074	0.0020	4	a_1	4.051	0.081	50
a_{50}	4.575	0.078	58	a_{50}	4.681	0.151	31	a_2	0.0101	0.0052	8
C/A_G	10919	304	36	C/A_G	11029	581	19	a_{50}	4.556	0.272	43
								C/A_G	10730	406	27

Model 4 Perers (1997)				Model 5 (this work)			
param.	value	uncert.	t-ratio	param.	value	uncert.	t-ratio
$\eta_{0,b}$	0.714	0.001	562	$\eta_{0,b}$	0.716	0.001	581
K_d	0.976	0.005	187	K_d	0.975	0.004	229
$K_b(10^\circ \rightarrow 20^\circ)$	1.000	0.003	401	$K_b(10^\circ)$	1.000	0.003	391
$K_b(20^\circ \rightarrow 30^\circ)$	1.000	0.004	293	$K_b(20^\circ)$	1.000	0.003	364
$K_b(30^\circ \rightarrow 40^\circ)$	0.994	0.005	221	$K_b(30^\circ)$	1.000	0.006	158
$K_b(40^\circ \rightarrow 50^\circ)$	0.990	0.003	287	$K_b(40^\circ)$	0.998	0.003	331
$K_b(50^\circ \rightarrow 60^\circ)$	0.921	0.004	234	$K_b(50^\circ)$	0.962	0.003	276
$K_b(60^\circ \rightarrow 70^\circ)$	0.823	0.006	137	$K_b(60^\circ)$	0.882	0.004	202
a_1	4.249	0.108	40	$K_b(70^\circ)$	0.714	0.012	62
a_2	0.0070	0.0018	4	a_1	4.210	0.076	55
a_{50}	4.599	0.140	33	a_2	0.0076	0.0013	6
C/A_G	10967	472	24	a_{50}	4.590	0.100	46
				C/A_G	10791	338	33

To compare the different IAM models with each other, K_b was calculated as a function of θ in the range $0^\circ - 70^\circ$ for each model. The resulting models are shown in Figure 3. It is evident that the collector used has a very good optical performance since K_b is close to unity in the range of 0° to 40°. In this range ($0^\circ - 40^\circ$), the different IAM models have values that are very similar to each other, with the maximum difference between them being less than 3 %. In contrast, K_b changes more abruptly in the range between 40° and 70°, where the largest discrepancies are observed between the models. The largest difference occurs at node 70°

and corresponds to 33 %.

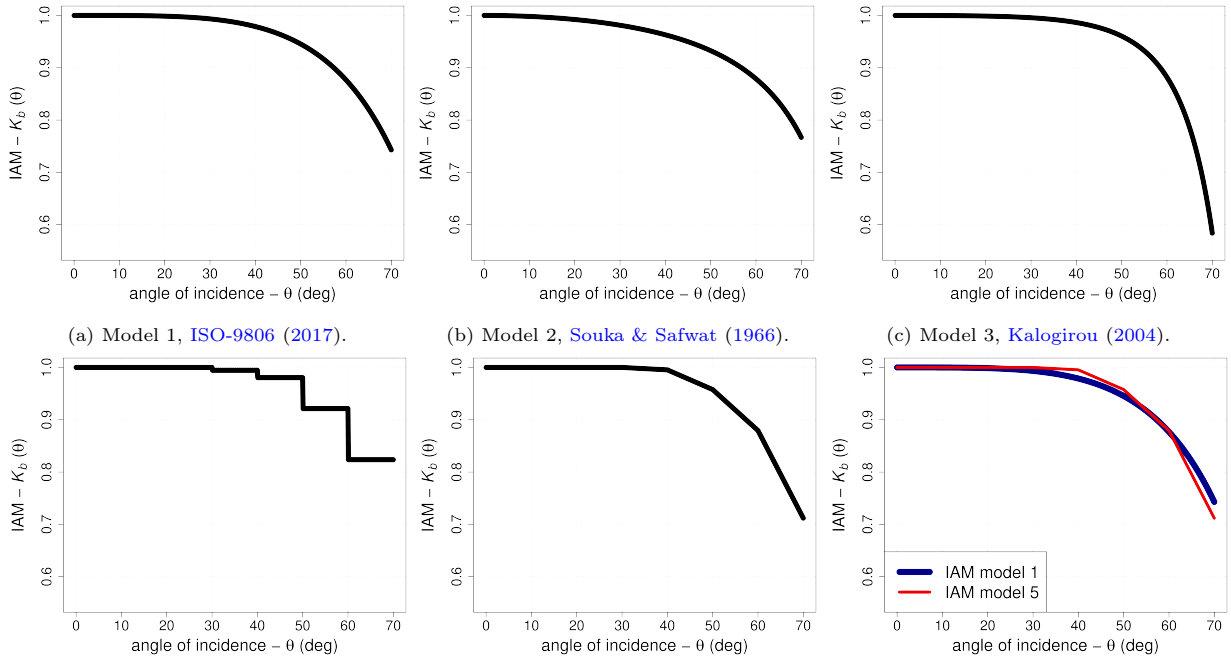

(a) Model 1, ISO-9806 (2017). (b) Model 2, Souka & Safwat (1966). (c) Model 3, Kalogirou (2004).

(d) Model 4 Perers (1997). (e) Model 5, (this work). (f) Comparison between models 1 and 5.

Figure 3: $K_b(\theta)$ graph as a function of the θ incident angle for each model. Figure (f) shows the comparison between the novel model and the one suggested by the ISO-9806 (2017); model 1 (blue) and 5 (red). The parameters of the corresponding models are those of Table 3. The data for these plots can be accessed in http://les.edu.uy/RDpub/IAM_Fig3_data.zip.

4.2. Performance of IAM models

Table 4 shows the performance indicators (MBE, RMSE and CPI) for each model, using the sub-sequences $1f-1g$ for their validation (see Table 2). The indicators are calculated for the θ interval between 40° and 70°, since this is the range where the higher K_b variations occur. Indicators are also provided for the $40°-50°$, $50°-60°$ and $60°-70°$ sub-intervals. The models were classified according to the global performance metric (CPI) in each interval (ranking: from 1 to 5). At the end of this table, the amount of data in each sub-interval is presented and it can be seen that the data is approximately uniformly distributed (about one third of the data is in each sub-interval). Figure 4 shows the scatter plots between the estimated useful power vs. experimental useful power (black dots), both per unit area, for each IAM model. The perfect agreement line $x = y$ (in red) is included in the graphs to help interpret the results. Note that higher values of useful power per unit area are associated with lower incident angles and vice versa.

The model 1 presents a CPI of 6.6 W/m^2 in the global $40°-70°$ range, thus ranking third in terms of performance. When observing the MBE discriminated by intervals, this model underestimates the experimental data (MBE < 0) in the $40°-50°$ and $50°-60°$ sub-intervals, and overestimates it (MBE > 0) in the

Table 4: Performance of the different models for the $1f - 1j$ sequences.

Model	Indicator	Incident angle θ			
		$40° - 50°$	$50° - 60°$	$60° - 70°$	$40° - 70°$
Model 1	MBE (W/m^2)	-8.7	-7.1	2.5	**-4.7**
ISO-9806 (2017)	RMSE (W/m^2)	9.8	8.5	7.0	**8.6**
	CPI (W/m^2)	9.2	7.8	4.7	**6.6**
	Rank	4	3	1	**3**
Model 2	MBE (W/m^2)	-13.4	-7.9	7.3	**-5.3**
Souka & Safwat (1966)	RMSE (W/m^2)	14.2	9.8	10.4	**11.8**
	CPI (W/m^2)	13.8	8.9	8.9	**8.5**
	Rank	5	4	4	**5**
Model 3	MBE (W/m^2)	-4.9	-2.9	-8.3	**-5.3**
Kalogirou (2004)	RMSE (W/m^2)	6.6	5.0	10.4	**7.6**
	CPI (W/m^2)	5.7	3.9	9.4	**6.5**
	Rank	3	1	5	**2**
Model 4	MBE (W/m^2)	-3.5	-8.6	-0.5	**-4.2**
Perers (1997)	RMSE (W/m^2)	7.1	13.8	15.7	**12.5**
	CPI (W/m^2)	5.3	11.2	8.1	**8.3**
	Rank	1	5	3	**4**
Model 5	MBE (W/m^2)	-4.7	-6.9	-3.9	**-5.2**
(this work)	RMSE (W/m^2)	6.5	7.8	6.6	**7.0**
	CPI (W/m^2)	5.6	7.3	5.2	**6.1**
	Rank	2	2	2	**1**
amount of data per bin		23(37.7 %)	19(31.1 %)	19(31.1 %)	**61(100%)**

$60° - 70°$ sub-interval. This behavior can be seen in Figure 4a. Although this model is in the third place in the global ranking, close to the second one, in the $40° - 50°$ sub-interval it presents a poor performance (rank 4). Model 2 presents a CPI of 8.5 W/m^2 in the $40° - 70°$ range, thus ranking last in terms of performance. When observing the MBE discriminated by intervals, this model present a similar bias behavior that model 1 as it underestimates the experimental data in the $40° - 50°$ and $50° - 60°$ sub-intervals, and overestimates in the $60° - 70°$ sub-interval, but in a greater extent. The model 2 not only presents the worst overall performance, but also provides a weak performance in discriminated sub-intervals, ranking almost last for all of them. The model 3 presents a CPI of 6.5 W/m^2 in the $40° - 70°$ range and ranks second. When looking at the indicators discriminated by sub-intervals, a good performance is observed in the first two ($40° - 50°$ and

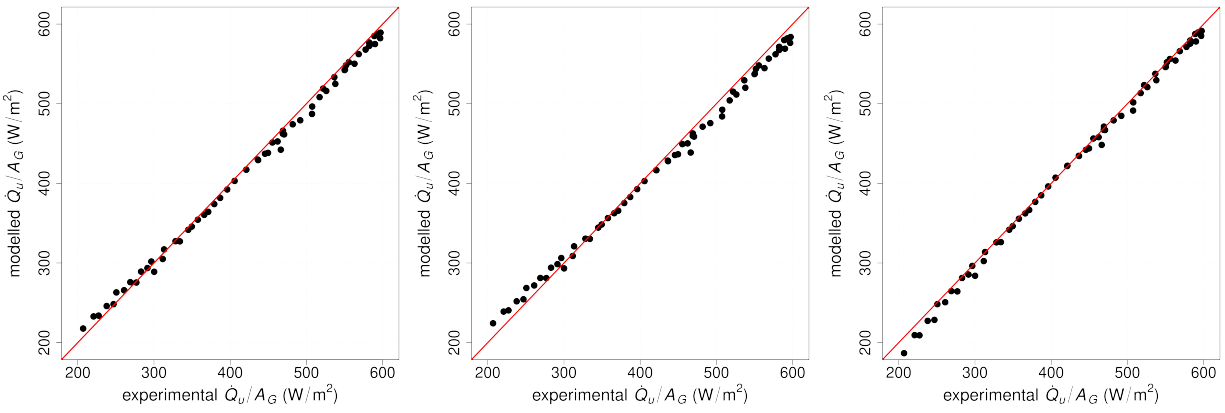

(a) Model 1, ISO-9806 (2017). (b) Model 2, Souka & Safwat (1966). (c) Model 3, Kalogirou (2004).

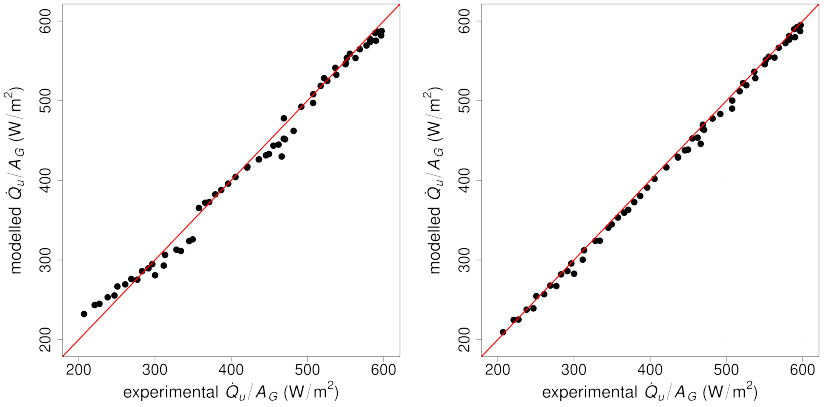

(d) Model 4 Perers (1997). (e) Model 5 (this work).

Figure 4: Scatter plots of estimated vs. experimental useful power (points), both per unit area. The perfect agreement line is shown in red to help interpret the data. The data for this plot can be accessed in http://les.edu.uy/RDpub/Qu_Fig4_data.zip.

$50° - 60°$) but a poor performance is observed in the last. If the b_1 parameter of this model is set to zero and the parameter identification is performed again, omitting the variable associated with this parameter, the performance of the model improves a little in the first sub-interval, but the overall performance ($40° - 70°$ range) does not change significantly, retaining its position in the global ranking (second place). This is in agreement with the t-ratio observed for the b_1 parameter in Table 3. The b_1 parameter of this model is, in effect, removable for this collector, leaving a second order model in the variable $(1/\cos\theta - 1)$ that has a better performance than model 2. The model 4 presents a CPI of 8.3 W/m^2 in the $40° - 70°$ range and is located in fourth place, very close to model 2. This model presents a very good performance in the first interval but it downgrades significantly in the following ones. In Figure 4d the effect of the discontinuities in the model (typical of a constant piecewise function) can be observed at 50° and 60° angles. This same figure shows the reason why this model has a high RMSE and a low MBE. In all the model's sub-intervals there is a region where the model underestimates and another region where the model overestimates. These

differences tend to compensate for the MBE, but the squared differences are not compensated, resulting in a high RMSE value. Finally, the model 5 presents a CPI of 6.1 W/m^2 in the $40° - 70°$ range and is ranked in the first place, showing a better performance in comparison with models 1 and 3 and significantly better in comparison to models 2 and 4 (CPI is reduced by 6 % and 27 % in respect to the former and latter ones). The model 5 has also a very good performance in all considered sub-ranges of incident angles, ranked as 2 in each sub-interval, showing an homogeneous behavior. Figure 4e provides evidence of this good performance. It is also highlighted that in the last interval $(60° - 70°)$, the new model has a significantly lower CPI than the other linear models (models 2, 3 and 4), with a reduction of 35 %. In this last interval the performance of the novel model is only improved by the non linear model 1. However, in the first sub-interval $(40° - 50°)$, model 5 outperforms importantly model 1, with a CPI reduction of 39 %.

In sum, three groups of models can be roughly distinguished: (i) the models 2 and 4 with a CPI of $\simeq 8.5\,W/m^2$, (ii) the models 1 and 3, with a CPI of $\simeq 6.5\,W/m^2$, and (iii) the proposed model, which achieves the lowest CPI of $\simeq 6.0\,W/m^2$. The models in the (i) and (ii) categories may have a good performance in one sub-interval but typically underperform in at least one them due to a worse modelling of the overall IAM behavior. On the contrary, model 5 has not this drawback, being its performance homogeneous across the $40° - 70°$ incident angles range. Also, being linear, its implementation is simple, therefore it is also the best choice considering the accuracy-simplicity tradeoff.

If a smaller angular step is used for models 4 and 5, for example of 5° instead of 10°, the conclusions do not change. The overall performance of model 4 improves, but fails to exceed that of model 5 with an angular step of 10°. Furthermore, model 4 with 5° resolution continues to show large RMSE values in the range $(60° - 70°)$. Ideally, if the angular resolution is lowered enough, the performance of models 4 and 5 should converge to the same value. However, reducing the angular step in practice presents difficulties because obtaining an adequate amount of data for each interval depends on the Sun's apparent path at the test location and the averaging time of the data. On the other hand, reducing the angular resolution requires the addition of more parameters (associated with more independent variables) in the piecewise linear regression models, which makes the parameter identification procedure more complex and more experimental data are required. A resolution of 10° for model 5 allows the IAM to be adequately characterized with a low level of error, it is feasible in practice and it allows keeping the number of independent variables limited.

4.3. Sensitivity to measured data

In this section, the sensitivity of the IAM models to the variability of the input data is evaluated, that is, how much the parameters of the models vary when considering different training sets. For this, by using the sub-sequences of Table 1 and 2 together, 8 different data sets were defined, from A to H. Table 5 shows the composition of the different data sets, indicating the sub-sequences from Table 1 and 2 that constitute each set. All the sets in this table are composed of the same data sub-sequences for day type 2, day type 3

and day type 4, differing only in the sequences for day type 1. One of the requirements of ISO-9806 (2017) is that data sets must contain measurements before and after solar noon (balanced data set). In this sense, the sets from A to D are sets that meet this requirement. Sets E to H do not meet this requirement; sets E and F have measurements only before solar noon and sets G and H only after. All sets include the sub-sequence 1a, which is not relevant if it was taken before or after solar noon because azimuthal tracking was carried out during this sub-sequence. This sub-sequence is important to correctly determine the $\eta_{o,b}$ parameter, since it comprises small incident angles, so it was included in all sets.

Table 5: Composition of the different data sets for sensitivity analysis.

Data set	Sequences		Balanced	# data
name	day type 1	day type 2, 3 and 4	data set	points
A	$1a, 1b, 1c, 1d, 1e$	$2a, 2b, 3a, 3b, 4a, 4b$	yes	226
B	$1a, 1b, 1c, 1i, 1j$	$2a, 2b, 3a, 3b, 4a, 4b$	yes	245
C	$1a, 1f, 1g, 1h, 1d, 1e$	$2a, 2b, 3a, 3b, 4a, 4b$	yes	224
D	$1a, 1f, 1g, 1h, 1i, 1j$	$2a, 2b, 3a, 3b, 4a, 4b$	yes	243
E	$1a, 1b, 1c$	$2a, 2b, 3a, 3b, 4a, 4b$	no	199
F	$1a, 1f, 1g, 1h$	$2a, 2b, 3a, 3b, 4a, 4b$	no	197
G	$1a, 1d, 1e$	$2a, 2b, 3a, 3b, 4a, 4b$	no	188
H	$1a, 1i, 1j$	$2a, 2b, 3a, 3b, 4a, 4b$	no	207

The purpose of the sets from E to H is to evaluate the relevance of the balanced set requirement in the standard when using the different IAM models. The elimination of this requirement allows the reduction of the testing time. The last column of Table 5 indicates the amount of data that each data set contains. We shall recall that each point corresponds to an average in 5 minutes. The ABCD sets have 235 points on average, which is equivalent to ∼19.5 hours of testing, while the EFGH sequences have 198 data points on average, which is equivalent to ∼16.5 hours of testing and represents a reduction of 3 hours within testing (∼15%) with respect to the duration of the ABCD sets.

The sensitivity analysis was done as follows. First, the characteristic parameters for each of the data sets in Table 5 (from A to H) were determined. Then, for each parameter the average of the ABCD sets was determined. These averages were taken as the reference values for the parameters, as the sets from A to D comply with the standard. The variability of each parameter was calculated, for the ABCD and EFGH groups, as the maximum between: (1) the maximum value found in the sets minus the reference value and (2) the reference value minus the minimum value found in the sets. The relative variability was calculated as the found variability divided by the reference value and expressed as a percentage. Table 6 shows the results of this analysis for the 4 models. In the last two rows, for each model, the average and the standard deviation of the relative variability of all the parameters is presented, excluding for this calculation the a_{50}

parameter, which is not a parameter obtained directly from the models.

Table 6: Sensitivity analysis results. Units for the parameters are indicated in the nomenclature list at the end of the article.

Model 1 ISO-9806 (2017)				Model 2 Souka & Safwat (1966)				Model 3 Kalogirou (2004)			
param.	mean ABCD	var. ABCD	var. EFGH	param.	mean ABCD	var. ABCD	var. EFGH	param.	mean ABCD	var. ABCD	var. EFGH
$\eta_{0,b}$	0.721	0.1 %	0.3 %	$\eta_{0,b}$	0.726	0.1 %	0.6 %	$\eta_{0,b}$	0.718	0.0 %	0.1 %
K_d	0.967	0.4 %	0.3 %	K_d	0.967	0.6 %	0.7 %	K_d	0.964	0.4 %	0.3 %
n	3.811	2.6 %	4.4 %	b_0	0.117	3.6 %	13.6 %	b_1	0.009	49 %	281 %
a_1	4.122	1.5 %	1.9 %	a_1	4.226	2.1 %	5.1 %	b_2	0.097	12 %	37.4 %
a_2	0.0097	13.0 %	9.7 %	a_2	0.0092	19.1 %	27.5 %	a_1	3.987	2.0 %	0.9 %
a_{50}	4.605	0.6 %	0.8 %	a_{50}	4.685	0.5 %	2.2 %	a_2	0.0110	12.1 %	7.1 %
C/A_G	10602	4.0 %	2.7 %	C/A_G	10648	4.2 %	4.1 %	a_{50}	4.546	0.3 %	0.4 %
mean var.		3.2 %	2.9 %	mean var.		4.4 %	7.7 %	C/A_G	10615	3.5 %	2.9 %
std var.		4.5 %	3.4 %	std var.		6.8 %	9.8 %	mean var.		9.8 %	41.3 %
								std var.		16.5 %	97.7 %

Model 4 Perers (1997)				Model 5 (this work)			
param.	mean ABCD	var. ABCD	var. EFGH	param.	mean ABCD	var. ABCD	var. EFGH
$\eta_{0,b}$	0.716	0.3 %	0.2 %	$\eta_{0,b}$	0.715	0.0 %	0.0 %
K_d	0.973	0.3 %	1.0 %	K_d	0.975	0.2 %	0.3 %
$K_b(10° \to 20°)$	1.008	0.1 %	0.1 %	$K_b(10°)$	1.004	0.1 %	0.1 %
$K_b(20° \to 30°)$	1.013	0.1 %	0.1 %	$K_b(20°)$	1.016	0.1 %	0.1 %
$K_b(30° \to 40°)$	0.997	0.4 %	8.5 %	$K_b(30°)$	1.012	0.3 %	0.4 %
$K_b(40° \to 50°)$	0.985	0.5 %	0.7 %	$K_b(40°)$	0.999	0.3 %	0.8 %
$K_b(50° \to 60°)$	0.933	1.3 %	1.8 %	$K_b(50°)$	0.971	0.9 %	1.2 %
$K_b(60° \to 70°)$	0.828	1.3 %	1.6 %	$K_b(60°)$	0.891	1.1 %	1.7 %
a_1	4.153	2.5 %	3.0 %	$K_b(70°)$	0.717	2.3 %	3.2 %
a_2	0.0086	20.1 %	23.0 %	a_1	4.139	2.9 %	1.9 %
a_{50}	4.583	0.4 %	0.5 %	a_2	0.0086	15.8 %	12.3 %
C/A_G	10626	4.8 %	3.3 %	a_{50}	4.566	1.2 %	0.5 %
mean var.		2.7 %	3.7 %	C/A_G	10675	2.9 %	2.7 %
std var.		5.7 %	6.5 %	mean var.		2.2 %	1.9 %
				std var.		4.2 %	3.3 %

When the ABCD data sets are considered, it is observed that models 1, 2, 4 and 5 show low variability

in all parameters except for a_2. In the case of model 3, a low variability is observed in the parameters $\eta_{0,b}$, K_d, a_1 and C/A_G, but a high variability is observed in the parameters a_2, b_1 and b_2. It should be noted that although in all cases there is a high variability of the a_2 parameter, this variability tends to be compensated by that of a_1 and ultimately the global loss coefficient, a_{50}, varies little.

When the EFGH data sets are considered, a behavior similar to the previous one is observed but there is a notable increase in the variability of the following parameters: b_0 (model 2), b_1 and b_2 (model 3), and $K_b(30^\circ \rightarrow 40^\circ)$ (model 4). In the case of the b_1 parameter, which presents a notorious high variability, it happens that some sets (FGH) result in a negative value for it, and the sign change with respect to the reference value (average of ABCD, $b_1 > 0$) and its small value causes the high relative variability. Even if the parameter b_1 is not taken into account, that is, if the variable associated with this parameter is omitted in the parameter identification, the variability of b_2 continues to be large in both cases, whether the ABCD or EFGH sets are considered. In the case of the $K_b(30^\circ \rightarrow 40^\circ)$ parameter, the dynamic effects are not being compensated correctly as the determination of this parameter is mainly determined through the $2a$ subsequence (see Table 1), which belongs to the day type 2 and is associated with high sky variability (and thus high variability of $d\vartheta_m/dt$). In model 1, an increase in the variability of n parameter is observed. Finally, in model 5, no significant increase in variability is observed in any of the parameters when considering the ABCD sets against the EFGH sets. In average terms, a general increase in the variability of the parameters is observed in linear models 2, 3 and 4 when moving from one set to another, being the Perers model the least affected of these 3 (see last rows of Table 6). In the case of model 1 and 5, the average variability even decreases slightly when moving from a balanced set to an unbalanced one, being the models less affected by a change in the adjustment sequences.

In short, it is seen that models 1 and 5 are the most reliable to use as they are less sensitive to variations in the input data. In addition, this models can be implemented by using data sets containing measurements only before or after solar noon. In fact, the novel proposal shows the lowest variability of the models tested here and, being of $\simeq 2\%$, it further enables to reduce the testing times by considering only morning or afternoon data series. The model 3 is the most sensitive and it is not recommended to use it with unbalanced data sets (morning or afternoon data only). The model 2 also shows the same limitation, in a lesser extent, but it is also not recommended in this sense. The model 4, although a good overall variability is observed, it has an important increased variability in one of its main parameters. To summarize, the reliability ranking against variations in the input data of the analyzed models is, from highest to lowest: model 5, model 1, model 4, model 2 and model 3.

5. Conclusions

In this work, a new linear IAM model was proposed to be used for QDT of flat plate solar collectors under the ISO-9806 (2017) standard. The performance of this model was evaluated and compared with that of four other models available in the literature. This include two linear models widely-used for QDT (Souka & Safwat, 1966; Perers, 1997), another linear model not tested yet for QDT (Kalogirou, 2004) and the non linear model suggested by the ISO-9806 (2017) standard for SST. For the comparison, a data set was used to train the models and an independent data set was used to evaluate them. The tests and measurements were performed according to ISO-9806 (2017) standard. The comparison showed that the proposed model (with a resolution of 10°) presents a very good performance in the entire range of incidence angles, outperforming in overall all the others models (even if the Perers model is used with an increased angular resolution of 5°). The proposed model also has a balanced behavior in all incident angles sub-intervals, with homogeneous metrics across them, ranking second in each one. This is not observed for the other models, that typically fail to represent at least one sub-range. This is a remarkable property of the novel model, which describes better the IAM behavior in its whole range without misrepresenting, in particular, large incident angles in where the IAM variations are greater. We also think that this property makes the model a good choice to be used in the testing of solar thermal collectors with more complex IAM behavior, such as vacuum tube collectors, which is part of our current work. The proposed model, being linear, is simple to employ for QDT, thus can be implemented, for instance, in a standard spreadsheet in the same way as the other widely-used linear models, but with higher accuracy.

On the other hand, the variability of the models' parameters was analyzed against the variation of the input data set (sensitivity analysis). This analysis showed that the proposed model is the most reliable as the parameters of this model are less sensitive to variations in the input data. It was shown that the proposed model can be used with unbalanced data sets (not symmetric with respect to solar noon) without loss of performance in the determination of its parameters, that is, by using sets only containing data obtained in the morning or in the afternoon. This property allows to reduce the time of the tests. Further case studies of this property are required, accounting for different climates, to give this observation a more general scope.

The use of the Kalogirou (2004) and Ambrosetti (ISO-9806, 2017) models have not been reported yet for the standard QDT methodology and were included in this work. Both models showed a fair overall performance in the $40° - 70°$ range, and are indeed good choices for QDT. However, both of them present difficulties in representing at least one of the incident angles sub-ranges. The sensitivity analysis showed that Kalogirou model is sensitive to the variability of the training data and that its utilization with unbalanced data sets is not recommended. So, it is possible to use this model for QDT, provided that this observation is taken into account.

Acknowledgments

The authors would like to thank the Ministerio de Industria, Energía y Minería (MIEM, Uruguay), especially its Dirección Nacional de Energía (DNE), the Fideicomiso Uruguayo de Ahorro y Eficiencia Energética (Fudaee, Uruguay) and the Corporación Nacional para el Desarrollo (CND, Uruguay), for having provided financial and logistical support for the development of the BECS facility and for having promoted this project with local capacities. The authors are also grateful to the PTB of Germany for promoting and financing the inter-laboratory on efficiency test of solar collectors, which has given us technical certainty about our local testing capabilities.

Nomenclature

Symbol	Definition	Units
A_G	gross collector area	m^2
a_1	first order thermal loss factor	W/m^2K
a_2	second order thermal loss factor	W/m^2K^2
a_{50}	global thermal loss factor at $(\vartheta_m - \vartheta_a) = 50\,°C$	W/m^2K
b_0	adjustable parameter of the Souka & Safwat	-
b_1, b_2	adjustable parameters of the Kalogirou	-
C	collector thermal capacity	$J\,K^{-1}$
CPC	compound parabolic concentrators	-
CPI	combine performance indicator	W/m^2
DNI	direct normal irradiance	W/m^2
f_d^*	diffuse fraction in the plane of the collector	-
FPC	flat plate collector	-
G_h	global solar irradiance at an horizontal plane	W/m^2
G_b	direct normal irradiance	W/m^2
G_{dh}	diffuse solar irradiance at an horizontal plane	W/m^2
G_t	global solar irradiance at the collector plane	W/m^2
G_{bt}	direct solar irradiance at the collector plane	W/m^2
G_{dt}	diffuse solar irradiance at the collector plane	W/m^2
IAM	incident angle modifier	-
K_b	incidence angle modifier for direct solar irradiance	-
K_d	incidence angle modifier for diffuse solar irradiance	-
MBE	mean bias error	W/m^2
MLR	multi-linear regression	-
n	adjustable parameter of the ISO-9806	-
$\dot{Q}_u$	useful power produced by the collector	W
QDT	quasi-dynamic testing	-
SST	steady state testing	-
RMSE	root mean square error	W/m^2
ϑ_i	fluid temperature at the collector inlet	°C
ϑ_o	fluid temperature at the collector outlet	°C
ϑ_m	mean temperature of the fluid passing through the collector	°C
ϑ_a	ambient air temperature	°C
$\eta_{0,b}$	collector peak efficiency referred to direct solar irradiance	-
θ	incidence angle of direct solar irradiance in the collector plane	deg
θ_z	solar zenith angle	deg

References

Abal, G., Aicardi, D., Alonso Suárez, R., & Laguarda, A. (2017). Performance of empirical models for diffuse fraction in uruguay. *Solar Energy*, *141*, 166 – 181. URL: http://www.sciencedirect.com/science/article/pii/S0038092X1630562X. doi:https://doi.org/10.1016/j.solener.2016.11.030.

Drummond, A. J. (1956). On the measurement of sky radiation. *Archiv für Meteorologie, Geophysik und Bioklimatologie, Serie B*, *7*, 413 – 436. URL: https://link.springer.com/article/10.1007%2FBF02242969. doi:https://doi.org/10.1007/BF02242969.

Duffie, J. A., & Beckman, W. A. (1991). *Solar engineering of thermal processes*. John Wiley & Sons.

Eck, M., Hirsch, T., Feldhoff, J., Kretschmann, D., Dersch, J., Morales, A. G., Gonzalez-Martinez, L., Bachelier, C., Platzer, W., Riffelmann, K.-J., & Wagner, M. (2014). Guidelines for csp yield analysis – optical losses of line focusing systems; definitions, sensitivity analysis and modeling approaches. *Energy Procedia*, *49*, 1318 – 1327. URL: http://www.sciencedirect.com/science/article/pii/S1876610214005955. doi:https://doi.org/10.1016/j.egypro.2014.03.141. Proceedings of the SolarPACES 2013 International Conference.

Fischer, S. (2020). *Quality Infrastructure for Energy Efficiency and Renewable Energy in Latin America and the Caribbean, Report # 95309*. Report Intituto Metrológico Aleman - PTB. URL: http://les.edu.uy/report/Expert_Report-RR-Test_R1.pdf.

Fischer, S., Heidemann, W., Müller-Steinhagen, H., Perers, B., Bergquist, P., & Hellström, B. (2004). Collector test method under quasi-dynamic conditions according to the european standard en 12975-2. *Solar Energy*, *76*, 117 – 123. URL: http://www.sciencedirect.com/science/article/pii/S0038092X03002901. doi:https://doi.org/10.1016/j.solener.2003.07.021.

Gueymard, C. A. (2012). Clear-sky irradiance predictions for solar resource mapping and large-scale applications: Improved validation methodology and detailed performance analysis of 18 broadband radiative models. *Solar Energy*, *86*, 2145 – 2169. URL: http://www.sciencedirect.com/science/article/pii/S0038092X11004221. doi:https://doi.org/10.1016/j.solener.2011.11.011. Progress in Solar Energy 3.

ISO-9060 (2018). *Solar energy — Specification and classification of instruments for measuring hemispherical solar and direct solar radiation*. Standard International Organization of Standarization Switzerland.

ISO-9806 (2017). *Solar Energy – Solar thermal collectors – Test methods*. Standard International Organization of Standarization Switzerland.

ISO-9847 (1992). *Solar Energy – Calibration of field pyranometers by comparison to a reference pyranometer*. Standard International Organization of Standarization Switzerland.

García de Jalón, A., Sallaberry, F., Olano, X., , Mateu, E., Astiz, R., Ezcurra, M., & Ramíres, L. (2011). Comprarison of thermal efficiency curves of solar collectors tested in outdoor conditions. In *Proceedings of ISES World Congress 2011*. URL: http://proceedings.ises.org/paper/eurosun2010/eurosun2010-0269-Sallaberry.pdf.

Kalogirou, S. A. (2004). Solar thermal collectors and applications. *Progress in Energy and Combustion Science*, *30*, 231 – 295. URL: http://www.sciencedirect.com/science/article/pii/S0360128504000103. doi:https://doi.org/10.1016/j.pecs.2004.02.001.

Kong, W., Wang, Z., Fan, J., Bacher, P., Perers, B., Chen, Z., & Furbo, S. (2012). An improved dynamic test method for solar collectors. *Solar Energy*, *86*, 1838 – 1848. URL: http://www.sciencedirect.com/science/article/pii/S0038092X12001077. doi:https://doi.org/10.1016/j.solener.2012.03.002.

Kratzenberg, M., Beyer, H., & Colle, S. (2006). Uncertainty calculation applied to different regression methods in the quasi-dynamic collector test. *Solar Energy*, *80*, 1453 – 1462. URL: http://www.sciencedirect.com/science/article/pii/S0038092X06000880. doi:https://doi.org/10.1016/j.solener.2006.03.010.

McIntire, W. R. (1982). Factored approximations for biaxial incident angle modifiers. *Solar Energy*, *29*, 315 – 322. URL: http://www.sciencedirect.com/science/article/pii/0038092X82902468. doi:https://doi.org/10.1016/0038-092X(82)90246-8.

591 Muschaweck, J., & Spirkl, W. (1993). Dynamic solar collector performance testing. *Solar Energy Materials and Solar Cells*, *30*,
592 95 – 105. URL: http://www.sciencedirect.com/science/article/pii/092702489390011Q. doi:https://doi.org/10.1016/
593 0927-0248(93)90011-Q.
594 Osório, T., & Carvalho, M. J. (2014). Testing of solar thermal collectors under transient conditions. *Solar Energy*, *104*,
595 71 – 81. URL: http://www.sciencedirect.com/science/article/pii/S0038092X14000851. doi:https://doi.org/10.1016/
596 j.solener.2014.01.048. Solar heating and cooling.
597 Perers, B. (1997). An improved dynamic solar collector test method for determination of non-linear optical and thermal
598 characteristics with multiple regression. *Solar Energy*, *59*, 163 – 178. URL: http://www.sciencedirect.com/science/
599 article/pii/S0038092X97001473. doi:https://doi.org/10.1016/S0038-092X(97)00147-3.
600 Quarteroni, A., Sacco, R., & Saleri, F. (2000). *Numerical Mathematics*. Springer.
601 Rodríguez-Muñoz, J. M., Monetta, A., Bove, I., & Alonso-Suárez, R. (2020). Ensayo cuasi-dinámico de colectores solares de
602 placa plana en uruguay de acuerdo a la norma iso 9806:2017. *ENERLAC. Revista de energía de Latinoamérica y el Caribe*,
603 *4*, 10–26. URL: http://enerlac.olade.org/index.php/ENERLAC/article/view/142.
604 Rojas, D., Beermann, J., Klein, S., & Reindl, D. (2008). Thermal performance testing of flat-plate collectors. *Solar Energy*,
605 *82*, 746 – 757. URL: http://www.sciencedirect.com/science/article/pii/S0038092X08000352. doi:https://doi.org/10.
606 1016/j.solener.2008.02.001.
607 Rönnelid, M., Perers, B., & Karlsson, B. (1997). On the factorisation of incidence angle modifiers for cpc collectors. *Solar*
608 *Energy*, *59*, 281 – 286. URL: http://www.sciencedirect.com/science/article/pii/S0038092X97000169. doi:https://doi.
609 org/10.1016/S0038-092X(97)00016-9. Selected Proceeding of ISES 1995: Solar World Congress. Part IV.
610 Souka, A., & Safwat, H. (1966). Determination of the optimum orientations for the double-exposure, flat-plate collector and its
611 reflectors. *Solar Energy*, *10*, 170 – 174. URL: http://www.sciencedirect.com/science/article/pii/0038092X66900041.
612 doi:https://doi.org/10.1016/0038-092X(66)90004-1.
613 Tesfamichael, T., & Wäckelgård, E. (2000). Angular solar absorptance and incident angle modifier of selective absorbers
614 for solar thermal collectors. *Solar Energy*, *68*, 335 – 341. URL: http://www.sciencedirect.com/science/article/pii/
615 S0038092X00000293. doi:https://doi.org/10.1016/S0038-092X(00)00029-3.
616 Zambolin, E., & Del Col, D. (2012). An improved procedure for the experimental characterization of optical efficiency in
617 evacuated tube solar collectors. *Renewable Energy*, *43*, 37 – 46. URL: http://www.sciencedirect.com/science/article/
618 pii/S0960148111006136. doi:https://doi.org/10.1016/j.renene.2011.11.011.

4.2. Paper 2

Improving the experimental estimation of the incident angle modifier of evacuated tube solar collectors with heat pipes

J. M. Rodríguez-Muñoz[a,*], I. Bove[b], R. Alonso-Suárez[a,b]

[a] *Laboratorio de Energía Solar, Departamento de Física del Litoral, CENUR Litoral Norte, Universidad de la República*
[b] *Laboratorio de Energía Solar, Instituto de Física, Facultad de Ingeniería, Universidad de la República*

Abstract

This article focuses on the thermal performance testing of evacuated tube solar collectors with heat pipes (ETC-HP) using the ISO 9806:2017 standard test methods: Steady-state testing (SST) and Quasi-dynamic testing (QDT). The main objective of this work is to improve the experimental estimation of the incident angle modifier (IAM) for these types of solar collectors in both test methods. For the QDT method, a novel model for the IAM is presented and validated against SST results. This IAM model, recently developed for flat plate collectors under the SST framework, has demonstrated superior performance compared to other available models. This study marks its first application to ETC-HP technology, showcasing its adaptability across different technologies and test methods. While this work primarily focuses on ETC-HP collectors, the results are applicable to evacuated tubes in general. Thus, the generality of this model and its consistency with the SST method make it suitable for implementation in test standards as a general-purpose model. Regarding the SST method, and aiming to enhance consistency between testing methods, an improved parameter conversion from SST to QDT is also proposed, reducing IAM differences between test methods by 1 to 19 percentage points, with greater improvement at higher incidence angles.

Keywords: Solar thermal collector, incident angle modifier, evacuated tube, ISO 9806 standard.

1. Introduction

Solar thermal systems are used for a variety of applications including domestic hot water, heating and cooling of buildings, heat generation for industrial processes and electricity generation. Solar thermal collectors are the main component of these systems, capturing solar energy and transferring it to a working fluid; therefore, the thermodynamic characterisation of these devices is very important. This characterisation is usually carried out by means of standardised tests, being the ISO-9806 (2017) standard one of the most widely used in the world. Although there are other standards (ASHRAE-93, 2014; EN-12975, 2022), they all present a high degree of similarity, reason why they can be considered equivalent to each other (Rojas et al.,

*Corresp. author: J. M. Rodríguez-Muñoz, jrodrigue@fing.edu.uy

List of Symbols

$\dot{Q}_u$	Useful power produced by the collector, W.	f_d	Diffuse fraction, G_{dt}/G_t.
$\eta_{0,b}$	Collector peak efficiency referred to direct solar irradiance.	G_{bt}	Direct solar irradiance on collector plane, Wm^{-2}.
$\eta_{0,hem}$	Collector peak efficiency referred to global solar irradiance.	G_{dt}	Diffuse solar irradiance on collector plane, Wm^{-2}.
θ	Incidence angle.	G_t	Global solar irradiance on collector plane, Wm^{-2}.
θ_L	Longitudinal angle of incidence.	K_b	Incidence angle modifier for direct solar irradiance.
θ_T	Transversal angle of incidence.	K_d	Incidence angle modifier for diffuse solar irradiance.
ϑ_a	Ambient air temperature, °C.	K_{bL}	Incidence angle modifier in the longitudinal plane.
ϑ_i	Collector inlet temperature, °C.	K_{bT}	Incidence angle modifier in the transversal plane.
ϑ_m	Mean temperature of heat transfer fluid, °C.	K_{hem}	Incidence angle modifier for global solar irradiance.
ϑ_o	Collector outlet temperature, °C.	q	Volumetric flow rate, $\mathrm{L\,min}^{-1}$.
a_1	Heat loss coefficient, $\mathrm{W/m^2K}$.	u	Surrounding air speed, $\mathrm{m\,s}^{-1}$.
a_2	Temperature dependence of the heat loss coefficient, $\mathrm{W/m^2K^2}$.		
a_5	Effective thermal capacity, $\mathrm{J/Km^2}$.		
A_G	Gross area of collector, m^2.		

2008). In fact, the latest version of the (EN-12975, 2022) standard has become a requirements standard from now on, referring to ISO-9806 (2017).

The ISO-9806 (2017) standard was initially developed for flat plate collectors and uncovered collectors. It was later extended to other low temperature collector technologies, such as evacuated tube collectors, then to medium and high temperature collectors; parabolic trough concentrators and Fresnel-type concentrators (Fischer et al., 2006; Janotte et al., 2009; Hofer et al., 2015). The ability of this standard to adapt to different technologies is one of its main strengths. In this sense, the standard proposes a generic thermodynamic model, adaptable according to the technology, which makes it possible to predict the useful power produced by a collector under different meteorological and usage conditions. This model has a set of characteristic parameters that must be determined experimentally for each collector. To determine them, the standard proposes two methods: the first one in steady state conditions (SST - Steady State Testing) and the second one in quasi-dynamic conditions (QDT - Quasy-Dynamic Testing). The thermodynamic model used in each case is slightly different, mostly related to the treatment of diffuse solar irradiance. However, the standard provides a procedure for converting the parameters from one model to another.

The SST method was the first to be developed and is still the most widely used. However, its implementation requires strict clear sky conditions to achieve steady state, which is a limitation for outdoor

laboratories in climates with variable cloud cover. This limitation motivated the development of the second method, QDT, which requires the test to be performed under varying cloud conditions. The QDT is then more flexible than the SST in terms of variability requirements and incorporates transient phenomena and diffuse solar irradiance modelling. This methodology is widely accepted worldwide and has been adopted by laboratories in Europe (Fischer et al., 2004; García de Jalón et al., 2011; Osório & Carvalho, 2014; Zambolin & Del Col, 2012), the United States (Rojas et al., 2008) and Latin America (Kratzenberg et al., 2006; Rodríguez-Muñoz et al., 2020). Many of these works show compatibility with the SST methodology. The advantage of the QDT method over the SST is the number of annual tests that can be obtained under outdoor conditions in variable cloud cover weather. In particular, in a previous study (Rodríguez-Muñoz et al., 2020), we evaluated the applicability of this methodology for a flat-plate collector in the Pampa Húmeda region of South America (SESA, Southeastern South America). This analysis showed that the QDT methodology can achieve more than twice as many annual tests as the SST methodology in this region.

However, the QDT method has some drawbacks. For example, results vary depending on the averaging time used for the experimental data. Furthermore, some difficulties have been reported when trying to extend this methodology to evacuated tube collectors with heat pipes (QAiST, 2012; Osório & Carvalho, 2014). This type of collector has a very large time constant compared to other technologies, such as flat plate collectors, and the QDT method has difficulty in describing the temperature variations at the collector outlet. This makes it difficult to determine some characteristic parameters of evacuated tube collectors, particularly those related to the angle of incidence modifier. Although this topic has been studied and there are specific experimental guidelines for determining the IAM for this type of collector (QAiST, 2012), the implementation of QDT tests and the accurate determination of the IAM remains a challenge. In this sense, the nonlinearity of the IAM in these types of collectors makes the problem even more complicated. Furthermore, some discrepancies have been reported between the angle of incidence modifier for diffuse solar irradiance obtained by one methodology and another (Kovács et al., 2011), suggesting that the modelling of this parameter and the conversion of SST to QDT parameters can be improved.

In response to the above problems, several alternatives have been proposed. On the one hand, improved transient test methods have been developed (Kong et al., 2012, 2015; Xu et al., 2012, 2013; Hofer et al., 2015). These methods address some of the drawbacks of the traditional QDT method and, in particular, improve the modeling of the transient behavior of solar collectors. Nevertheless, these studies have focused on the application of these methods to a specific type of collector, and the extension of these techniques to ETC-HP collectors remains an open task. On the other hand, specifically regarding the determination of the IAM, several models for ETC collectors have been proposed within the framework of the traditional QDT method (Souka & Safwat, 1966; Sallaberry et al., 2011; Zambolin & Del Col, 2012; Osório & Carvalho, 2014). These models improve the IAM modeling for this type of collector while retaining the advantages of the traditional QDT method, such as its applicability to a wide range of technologies. While all of the

aforementioned proposals are valuable, none of them stand out significantly in terms of performance. It is noteworthy that while the test standard proposes an IAM model for collectors with uniaxial IAM, known as the Ambrosetti function, no proposal is made for collectors with biaxial IAM, such as ETC collectors.

Finally, it is important to note that the ISO-9806 (2017) standard is currently under review. This review period offers a valuable opportunity to propose potential improvements and solutions to the aforementioned problems, including those suggested in this article, which are detailed in the following section.

1.1. Article's contribution

This work improves the experimental estimation of the IAM of ETC-HP technology, proposing modifications in both SST and QDT methods, which are described as follows.

For the QDT method, a novel model for IAM is presented and validated against the SST results. This IAM model was recently developed for flat plate collectors under the SST framework (Rodríguez-Muñoz et al., 2021b) and demonstrated superior performance compared to other available models (Souka & Safwat, 1966; Perers, 1997; Kalogirou, 2004). The present study represents its extension to the ETC-HP technology, demonstrating its applicability across different technologies and test methods, particularly in adapting to the more complex geometry of evacuated tubes, i.e., biaxial IAM. While this work focuses on ETC-HP collectors, the results can be extrapolated to evacuated tubes in general. In this sense, the generality of this model and its consistency with the SST method make it suitable for implementation in test standards as a general purpose model. In addition, the effect of using different averaging times on the experimental data is analysed and the most appropriate value for this variable is determined by comparison with results obtained using the SST method. This optimisation improves the accuracy of the IAM as well as the other characteristic parameters.

On the other hand, regarding the SST method, an enhanced parameter conversion procedure from SST to QDT is proposed. This method incorporates the diffuse fraction into the standard procedure, providing enhanced results for the IAM of the SST method and improving the compatibility between testing methodologies. All these previous analyses, including QDT and SST method, are demonstrated experimentally using the test data of two solar collectors of this type (ETC-HP).

Finally, this work provides some complementary contributions to the field. It identifies overlooked challenges in extending the QDT method to ETC-HP technology, attributed to its slow thermal response. In this respect, the data acquisition procedure of the QDT method for this type of collector and its subsequent processing are described in detail and guidelines are provided to improve the reliability of the results, complementing existing work in this field (QAiST, 2012). Furthermore, a free and documented parameter identification software is provided, using a constrained nonlinear regression algorithm. Currently, there are no freely available implementations of the QDT test, regardless of its optimisation methodology (linear or nonlinear). This availability not only provides a tool for testing laboratories, but also improves the

reproducibility and validation of scientific work in the field. It is emphasized that this software is intended for general use with low-temperature glazed solar collectors, including both flat plate and evacuated tube technologies, that is, collectors with both uniaxial and biaxial IAM.

1.2. Article's outline

This article is organised as follows. In the following section, Section 2, the thermodynamic model of the ISO-9806 (2017) standard for low-temperature covered solar collectors is briefly described, along with the new IAM model for the QDT method. The test procedure and parameter identification algorithm are also described in this section. While the description covers both methods, it places particular emphasis on the QDT method and provides guidelines to improve the reliability of the results. Section 3 describes the test platform, the collectors tested and the measurements. Section 4 presents the results of both methods, including an analysis of the averaging time for the QDT method, and introduces the novel parameter conversion procedure (SST to QDT). Finally, Section 5 summarises the main conclusions of the work.

2. Methodology

This section describes the thermodynamic model used for each test method, including the novel IAM model for the QDT method, and the standard parameter conversion from SST to QDT model. Additionally, it includes a detailed description of the test procedure and the parameter identification algorithm for the QDT method.

2.1. QDT model and parameters

As mentioned in the introduction, the thermodynamics considered by the quasi-dynamic method of the ISO-9806 (2017) standard has a wide application and can be applied to different technologies of thermal solar collectors. The standard provides criteria on how to use the model for each case, specifying which terms can be omitted in the general equation depending on the solar collector technology. The suggested model for low-temperature collectors with cover is shown in Eq. (1),

$$\frac{\dot{Q}_u}{A_G} = \eta_{0,b}\left[K_b\left(\theta\right)\ G_{bt} + K_d\ G_{dt}\right] - a_1\left(\vartheta_m - \vartheta_a\right) - a_2\left(\vartheta_m - \vartheta_a\right)^2 - a_5\frac{d\vartheta_m}{dt}, \tag{1}$$

where $\dot{Q}_u$ is the useful power produced by the collector, G_{bt} and G_{dt} are the direct and diffuse solar irradiance on the collector plane, respectively, ϑ_m the average temperature of the fluid passing through the collector (average between the inlet and outlet temperatures), ϑ_a the ambient temperature, and the parameters that characterize the thermal behavior of the collector are: $\eta_{0,b}$, K_b, K_d, a_1, a_2 and a_5. The first parameter is the optical efficiency of the collector at normal incidence referred to direct solar irradiance, a_1 and a_2 are the thermal loss factors, a_5 is the effective thermal capacity divided by the total area of the collector (A_G), and K_b and K_d are the incident angle modifiers (IAM – Incident Angle Modifier) for the direct and diffuse

solar irradiance, respectively. All parameters are constant except for IAM for direct solar irradiance, K_b, which varies in relation to the angle of incidence of the direct beam, θ.

A novel parameterization for the QDT test of flat plate collectors was proposed and assessed in a previous study (Rodríguez-Muñoz et al., 2021b). This parameterization involves dividing the incident angle range into smaller intervals and assuming a piecewise linear function within each interval, taking the nodal values of the IAM as parameters to be determined. For instance, if a 10° interval is employed, the adjustable parameters would be $K_b(10°), K_b(20°), \ldots, K_b(80°)$, where $K_b(\theta_i)$ represents the K_b value at the angle θ_i (or node). Then the K_b value for any θ angle can be expressed as:

$$K_b(\theta) = \left[K_b \left(\left\lfloor \frac{\theta}{10} \right\rfloor 10 \right) \left(\left\lfloor \frac{\theta + 10}{10} \right\rfloor - \frac{\theta}{10} \right) + K_b \left(\left\lfloor \frac{\theta}{10} \right\rfloor 10 + 10 \right) \left(\frac{\theta}{10} - \left\lfloor \frac{\theta}{10} \right\rfloor \right) \right], \tag{2}$$

where the open square brackets indicate to round up to the previous lower natural number. For all types of collectors it is mandated that $K_b(0°) = 1$ and $K_b(90°) = 0$ for the first and last parameters, respectively.

In Rodríguez-Muñoz et al. (2021b), it is shown how to integrate this equation into the QDT testing of flat plate collectors, and how to determine the nodal values using multilinear regression. This approach exhibited superior performance across a wide range of angles of incidence compared to other models (Souka & Safwat, 1966; Perers, 1997; Kalogirou, 2004; ISO-9806, 2017).

When dealing with evacuated tube collectors, the situation becomes more intricate, as K_b is a function of two angles of incidence, θ_L and θ_T, which correspond to the angles projected onto two perpendicular planes; one longitudinally along the tube axis and the other transversely across the tube, respectively. A significant simplification for this issue was introduced by McIntire (1982), involving the factorization of the IAM. This factorization expresses the IAM as the product of two distinct functions: one reliant on θ_L and the other on θ_T, denoted as $K_b = K_{bL} \times K_{bT}$. K_{bL} signifies K_b calculated at $(\theta_L, 0)$ and K_{bT} signifies K_b calculated at $(0, \theta_T)$. This assumption is widely accepted and commonly applied in tests involving this type of collector (Osório & Carvalho, 2014; Zambolin & Del Col, 2012). Typically, the parameterizations used to describe the IAM of flat plate collectors are applied to each IAM component of ETC technology.

In the present study, the same factorization assumption was adopted, and the recently proposed parameterization by Rodríguez-Muñoz et al. (2021b) for flat plate collectors was utilized for each IAM component of the ETC. To be more precise, the discretization process of Rodríguez-Muñoz et al. was applied to both the functions K_{bL} and K_{bT}. However, in this case, integrating this model into QDT testing is more complex, and the procedure used in this work is detailed in Subsection 2.5.

This article marks the first application of this parameterization for evacuated tube collectors with heat pipes, highlighting its generality across different technologies, particularly its applicability to collectors with biaxial IAM. As mentioned earlier, this model outperforms those currently available; therefore, the implementation of this model improves the accuracy of the IAM estimation for ETC.

2.2. SST model and parameters

The SST implementation provides the baseline reference for comparison with the enhanced QDT methods. For the SST methodology, the classical simpler model is used that deals globally with solar radiation, making the following substitution,

$$\eta_{0,hem} K_{hem} G_t = \eta_{0,b} \left[K_b(\theta) \; G_{bt} + K_d \; G_{dt} \right]. \tag{3}$$

This equation is considered valid under clear sky conditions, which are the conditions for conducting the SST test ($G_t > 700\,\mathrm{W/m^2}$ and a diffuse fraction less than 30 %, as specified by the standard). This substitution results in the following model,

$$\frac{\dot{Q}_u}{A_G} = \eta_{0,hem} K_{hem} G_t - a_1 (\vartheta_m - \vartheta_a) - a_2 (\vartheta_m - \vartheta_a)^2 - a_5 \frac{d\vartheta_m}{dt}, \tag{4}$$

where G_t is the global solar irradiance at the collector plane, and the parameters $\eta_{0,hem}$ and K_{hem} correspond respectively to the optical efficiency at normal incidence and the angle of incidence modifier, both related to the global solar irradiance. It is worth noting that in the SST model, the parameter C is commonly used to characterise the effective thermal capacity of the collector. However, in order to maintain homogeneity, a_5 was chosen instead. The relationship between C and a_5 is given by $a_5 = C/A_G$.

2.3. Conversion between SST and QDT

Annex B of ISO-9806 provides a procedure for estimating the parameters $\eta_{0,b}$, K_b and K_d from $\eta_{0,hem}$ and K_{hem}, and the reverse procedure, which is outlined below. The parameter K_d is calculated by averaging and normalising K_b over the solid angle seen by the collector, as shown in Eq. (5):

$$K_d = \frac{\int_0^{\pi/2} \int_0^{\pi/2} K_b(\theta, \gamma) \cos(\theta) \sin(\gamma) \, d\theta d\gamma}{\int_0^{\pi/2} \int_0^{\pi/2} \cos(\theta) \sin(\gamma) \, d\theta d\gamma}. \tag{5}$$

For this calculation, clear sky conditions are assumed as well as an isotropic distribution for diffuse solar irradiance. It is pointed out that the SST is done under clear sky conditions, as we mentioned before, conditions where the solar irradiance can be neglected and $K_{hem} = K_b$ can be reasonably assumed).

The ISO-9806 (2017) standard suggests performing this integral as a summation, discretising the integration domain by squares of 10° side, the approach used in this work. The parameter $\eta_{0,b}$ is then calculated from Eq. (3) assuming normal incidence and a diffuse fraction of 15 % in the plane of the collector, which is a reasonable assumption for SST conditions.

However, since there are differences in the IAM estimation between the SST and QDT methods, an improved parameter conversion method is proposed in this work, which, together with its advantages over the standard procedure, are presented in Subsection 4.4.

2.4. Test procedures

Table 1 shows the conditions required for each test method and for each variable, including the allowed variability. These conditions must be met by the measurements recorded during the test in order to be used for parameter identification. In particular, the SST methodology imposes more rigorous requirements, both in terms of the required values and their allowed variation. Conversely, the QDT methodology requires the representation of different weather conditions during the test. In the following subsection, a brief overview of both test methods is presented, with particular emphasis on the aspects relevant to the implementation of the QDT test method for evacuated tube solar collectors.

Table 1: Conditions and variability required for each test variable specified by the standard ISO-9806.

Variable	SST		QDT	
	Condition	Variability	Condition	Variability
Global solar irradiance G_t (W/m^2)	>700	±50	-	-
Diffuse fraction f_d (%)	<30	-	-	-
Incident angle θ (°)	<20	-	-	-
Inlet temperature ϑ_i (°C)	-	±0.1	-	±1
Outlet temperature ϑ_o (°C)	-	±0.4	-	-
Ambient temperature ϑ_a (°C)	-	±1.5	-	-
Wind velocity parallel to the collector u (m/s)	3±1	±1.0	<4	-
Mass flow rate $\dot{m}$ (kg/(s m^2))	0.02	±1 %	0.02	±2 %

2.4.1. Quasi dynamic testing method

For the QDT method, all parameters are determined by a single test, which involves performing at least one measurement sequence for each type of day, with each day type corresponding to a specific measurement sequence defined by the standard. The main objective of these day types is to operate the collector under various working conditions, such as different temperature differences and sky conditions. The total number of sequences required depends on the local climatic conditions and the time of year when the test is carried out. Each type of day must last at least 3 hours and may consist of several non-consecutive sub-sequences, each lasting at least 30 minutes. The conditions that the day types must meet in order to comply with the standard are described below:

- Day type 1: this sequence should be conducted with the fluid temperature kept as close as possible to the ambient temperature. The measurements should be carried out mostly under clear sky conditions. Additionally, the angle of incidence should vary within a defined range to ensure ample variability for the IAM for direct irradiance. This range should encompass incident angles exceeding 60° and extend

to angles where the difference in the IAM for beam irradiance does not exceed 2 % from the value at normal incidence. This sequence contributes to the determination of the parameters related to the optical efficiency of the collector; $\eta_{0,b}$, K_b and K_d.

- Day type 2: during this measurement sequence, the collector should operate under conditions of varying cloudiness, and it can be conducted at any operating temperature. The high degree of variability in solar irradiance in these sequences contributes to the determination of the thermal capacity of the collector. To ensure an accurate determination of this parameter, the time derivative of the mean temperature of the fluid, $d\vartheta_m/dt$, must exceed the threshold value of $\pm 0.005\,^{\circ}\mathrm{C/s}$. In addition, the measurement at low diffuse fraction also contributes to the determination of the IAM for the diffuse solar irradiance; K_d.

- Day type 3: in this sequence the collector must operate with an intermediate inlet temperature and the measurements must include clear sky conditions. At least two intermediate temperatures are needed (i.e., $(\vartheta_m - \vartheta_a)$ equal to 20 and 40 °C).

- Day type 4: in this sequence the collector must operate with a high inlet temperature and the measurements must include clear sky conditions (i.e., $(\vartheta_m - \vartheta_a)$ equal to 60 °C). The day type sequences 3 and 4 contribute to determining the thermal loss factors; a_1 and a_2.

To ensure that the experimental data set contains sufficient variability and different working conditions are achieved, the standard recommends the generation of the following diagnostic plots: 1) $(\vartheta_m - \vartheta_a)$ as a function of G; 2) G_{bt} as a function of θ; 3) G_{dt} as a function of G; and 4) $(\vartheta_m - \vartheta_a)$ as a function of u (the ambient air speed). These plots must be compared with the typical plots in the standard and should show a significant degree of similarity.

To improve the reliability of results, the following guidelines for ETC-HP testing are outlined, taking into account the specific characteristics of this technology. An effective approach for day type 1 would involve obtaining two measurement sequences: one with $\theta_L = 0^{\circ}$ and θ_T varied from 0° up to angles exceeding 60°, and the converse for the second sequence (i.e., θ_L varied from 0° up to angles exceeding 60° and $\theta_T = 0^{\circ}$). This decoupling of variables simplifies the determination of the functions K_{bL} and K_{bT}. In QAiST (2012), it is recommended to carry out these tests using an automatic solar tracker: in the first sequence, the tracker is fixed to the equator, and it follows the Sun's height, while in the second sequence, the tracker's horizontal inclination is fixed, and it tracks the Sun's azimuth. If an automatic solar tracker is not available (fixed or manually-operated support), the procedure described in Zambolin & Del Col (2012) can be followed. In this case, the collector support is fixed to the equator, and various measurement sequences are taken with different horizontal inclinations.

For this study, an intermediate procedure was adopted: in the initial sequence, the solar tracker's azimuth

was aligned North (as it is located in the Southern Hemisphere), while the horizontal inclination was set at 45° ($\theta_L < 20°$, $\theta_T = 0$–$70°$). In the second sequence, the tracker was adjusted to track the Sun's azimuthal position ($\theta_L = 0$–$50°$, $\theta_T = 0°$), and the horizontal inclination was fixed at 30°. These selections of horizontal inclinations were not arbitrary but meticulously chosen for the specific location and moment of the year to ensure that $\theta_L < 20°$ was attained in the first sequence and $\theta_L = 0$–$50°$ in the second sequence, encompassing the most substantial achievable variation during the test's time of execution.

Regarding day type 2, the requirement of $\pm 0.005\,°C/s$ poses a challenge for ETC collectors due to the specific characteristics of the technology, such as slow thermal response and low temperature difference between the inlet and outlet. To address this issue, we recommend that this test is performed at a low temperature to maximise temperature variation (although even with this approach it may still be difficult to meet the requirement).

For day type 4, while a temperature difference of $(\vartheta_m - \vartheta_a) = 60\,°C$ may be suitable for many collectors, it may not be sufficient for tube collectors due to their low thermal loss coefficient. This can make the identification of the parameter a_2 difficult. In this respect, it is recommended to run this type of day with the highest possible temperature difference. Subsequently, the intermediate temperatures corresponding to day type 3 should be chosen so that the separation between all test temperatures is as uniform as possible.

In addition, two important points are highlighted regarding the installation of these collectors before the tests are carried out. Firstly, the back of the collector should be shielded from any solar radiation that may be reflected from the ground and/or adjacent surfaces. This type of collector is susceptible to this back solar radiation, which can affect the results, even if the surfaces have a low reflectivity. Secondly, it is important that the tubes of the collector are well aligned, that is, the structure of the collector should be squared and aligned with the test bench, otherwise erroneous results may be obtained in the IAM (small misalignment in flat collectors are not a problem as their IAM is uniaxial).

2.4.2. Steady state testing method

In the case of the SST method, parameter identification involves three independent tests: (i) the performance test, where the parameters $\eta_{0,hem}$, a_1 and a_2 are determined; (ii) the incident angle modifier test, where K_{hem} is determined; and (iii) the effective thermal capacity test, where the parameter a_5 is determined. The first test is well documented and extensively discussed in several references (Rojas et al., 2008) and therefore a detailed description is not necessary.

For the second test (IAM determination), the same procedure as for day 1 of the QDT test was followed, but the experimental data were processed according to the standard for this method. For each angle of incidence, the experimental IAM value was determined using Eq. (4), assuming steady state conditions ($d\vartheta_m/dt \approx 0$),

$$K_{hem}(\theta) = \frac{\dot{Q}_u/A_G + a_1\,(\vartheta_m - \vartheta_a) + a_2\,(\vartheta_m - \vartheta_a)^2}{\eta_{0,hem}\,G_t}. \tag{6}$$

The final value of the IAM for a given angle of incidence was calculated as the average of two measurements: one before and one after solar noon (symmetrical), to account for transient effects.

The effective thermal capacity test was carried out in accordance with section 25.2 of the ISO-9806 (2017) standard, taking into account the second-order correction for thermal losses, i.e. the a_2 coefficient. At the beginning of the test, the inlet temperature was set equal to the ambient temperature and the collector was covered with a reflective blanket to reach steady state. The cover was then removed and the collector was allowed to reach a new steady state point, which differed from the initial one due to the effect of solar irradiance. The effective thermal capacity was determined by integrating Eq. (4) over the period between the two steady state operating points, assuming normal incidence ($K_{hem} \approx 1$),

$$a_5 = \frac{\int_{t_1}^{t_2} \left[\eta_{0,hem} G_t - a_1 \left(\vartheta_m - \vartheta_a\right) - a_2 \left(\vartheta_m - \vartheta_a\right)^2 - \dot{Q}_u / A_G\right] \, dt}{\vartheta_{m2} - \vartheta_{m1}}. \tag{7}$$

All these SST stages were done as standard as possible, following closely the ISO-9806 (2017), so they act as a baseline reference to compare with the QDT method's results under the proposed framework.

2.5. Parameter identification algorithm for QDT

There are two parameter identification procedures (Fischer et al., 2004): (i) the finite difference time derivative approximation and (ii) the dynamic parameter identification. In both cases, the mean square error of the useful power is used as the objective function to be minimised. The first method is the most commonly used and the one used in this study. It involves the approximation of the time derivative of the mean temperature of the fluid using finite differences, as follows:

$$\frac{d\vartheta_m}{dt} \cong \frac{\vartheta_m(t + \Delta t) - \vartheta_m(t)}{\Delta t}. \tag{8}$$

where Δt is the data averaging time, $\vartheta_m(t)$ and $\vartheta_m(t + \Delta t)$ correspond to the average temperature of the fluid at the beginning and end of the time interval Δt. The term $d\vartheta_m/dt$ is then an additional independent variable within the regression algorithm. The time interval Δt corresponds to the averaging time of the experimental data.

The implementation of the MLR (Multi Linear Regression) method is widely used in the literature for flat plate collectors because the regression problem can be expressed in linear form (Perers, 1997). However, when dealing with ETC collectors, the problem becomes nonlinear due to the characteristics of the IAM. Some studies have proposed to deal with this nonlinearity by using the MLR method in an iterative way (Hofer et al., 2015). In this study, we opt for the direct implementation and propose the use of a constrained nonlinear regression algorithm. Although this method is more challenging to implement, it is a more appropriate approach to deal with the nonlinearity of the problem. In addition, once implemented, it does not require iteration or manual parameter substitution, which simplifies its use and reduces the risk of error.

The nonlinear regression algorithm used in this work is known as the two-metric projection method (Bertsekas, 1999). The projection is used to incorporate the constraints and ensure that the parameters converge to physically possible values. This iterative algorithm starts with an assumed vector of characteristic parameters, denoted p_0. The useful power produced by the collector is then linearised around this initial operating point, as shown in Eq. (9), to simplify the implementation of the method.

$$\dot{Q}_u^*(p) \approx \dot{Q}_u^*(p_0) + J(p_0)\,(p - p_0)\,, \tag{9}$$

The Jacobian $J(p_0)$ represents the derivatives of the function $\dot{Q}_u^*(p)$ with respect to the characteristic parameters, evaluated at the point p_0. The function $\dot{Q}_u^*(p)$ corresponds to the useful power calculated with Eq. (9). The entries of $J(p_0)$ can be estimated numerically using centred finite differences,

$$J(p_0)_{i,j} = \frac{\partial \dot{Q}_u^*(t_i, p_0)}{\partial p_j} = \frac{\dot{Q}_u^*(t_i, p_0 + \delta p_j) - \dot{Q}_u^*(t_i, p_0 - \delta p_j)}{2\delta p_j}. \tag{10}$$

For δp_j, the value suggested by Bates & Watts (1988) was used, that is, $\delta p_j = \sqrt{\epsilon} p_j$, where ϵ is the epsilon machine. Then, the parameter's vector in the next step is calculated as follows,

$$\hat{p} = \text{Proy}\left\{p_0 + S\,J(p_0)^\top \left(\dot{Q}_u - \dot{Q}_u^*(p_0)\right)\right\}, \tag{11}$$

where $\dot{Q}_u$ is the experimentally observed useful power produced by the collector, the matrix S is an approximation to the Hessian of the useful power function, and Proy{} is the projection function over the range of physically possible parameter values. Experimental errors can cause some parameters to take on values that are inconsistent with their physical meaning. To address this problem, certain constraints have been imposed: $a_2 \geq 0$ and $K_{bL} \leq 1$, which are box-type constraints. For a deeper understanding of these parameters and the rationale behind these constraints, the reader can refer to Duffie & Beckman (1991) and Theunissen & Beckman (1985). The latter gives an estimate of the IAM for tubular collectors using ray tracing and shows, among other things, that $K_{bL} \leq 1$.

The matrix S is first set to $\left[J(p_0)^\top J(p_0)\right]^{-1}$, which is an approximation of the Hessian matrix of the function $\dot{Q}_u^*(p)$. Then, when a constraint is active, the corresponding row and column in the matrix S are set to zero, except for the element on the diagonal, which is set to one. The implementation of the projection function in this case is straightforward. If one of the parameters exceeds the defined limits, it is assigned the closest limit value (e.g. if $a_2 < 0$, then a_2 is set to 0). The iteration process continues until the difference in the parameter vector p between one iteration and the next becomes negligible (less than a certain tolerance, set to 0.1 % is this work).

A drawback of this algorithm is that it may converge to a local minimum instead of the global minimum. To address this issue, the procedure is iterated with 10 different randomly generated initial points (p_0). In cases where the algorithm converges to different solutions, the solution with the smallest mean square error (representing the global minimum) is selected. The linearisation approach is used to estimate parameter uncertainties, as shown in Hofer et al. (2015); Rodríguez-Muñoz et al. (2021b).

3. Test facilities and experimental data

In this section, the test setup and the measurements taken for parameter identification are described.

3.1. Test facilities and collectors

The tests were carried out at the Solar Heater Test Bench (Banco de Ensayos de Calentadores Solares - BECS) of the Solar Energy Laboratory (Laboratorio de Energía Solar - LES, http://les.edu.uy/) of the University of the Republic (Udelar), located in Salto, Uruguay (latitude=31.28° S, longitude=57.92° W). This test facility was designed by researchers from this laboratory, based on existing facilities from the National Renewable Energy Centre (Centro Nacional de Energías Renovables - CENER) in Spain. This installation, including the thermo-hydraulic system, measurement instruments, and data acquisition systems, is described in detail in Rodríguez-Muñoz et al. (2021b).

It should be noted that recently, this testing capacity participated in a Latin American Laboratory Intercomparison organised by PTB (Physikalisch-Technische Bundesanstalt), the German Metrology Institute, and supported by Solar und Wärmetechnik Stuttgart (SWS, Germany), where it obtained the highest rating in most of the test variables and received only two minor observations regarding secondary variables, which were already addressed by the laboratory (Fischer, 2020).

For this study, two evacuated tube solar thermal collectors with heat pipes were considered, designated ETC-HP-1 and ETC-HP-2, with gross areas A_G of 1.79 m^2 and 1.55 m^2, respectively. The gross area corresponds to the maximum projected area of the complete collector, excluding any integral means of mounting and connecting fluid piping, as specified in ISO-9488 (2022). Both collectors were mounted on a mobile tracker with a manually adjustable horizontal tilt and an azimuth that could be adjusted either manually or automatically at 2-minute intervals. Figure 1 shows the assembly of the ETC-HP-1 collector in the test facility as an example. In this figure, the black cover behind the collector, which is used to prevent solar radiation reflection from the ground, can be seen. The tracker was configured during the tests according to the procedures described in Subsection 2.4. ETC-HP-1 was tested from 18 August to 4 October 2021, while ETC-HP-2 was tested from 3 September to 30 September 2022.

The design of the collectors is standardized, so they share several similarities. They both utilize borosilicate tubes with an outer diameter of 59 mm and a length of 1.80 m. Additionally, both collectors are equipped with heat pipes featuring metal cylindrical fin absorber. For a better understanding of the different evacuated collector technologies, particularly the one used in this work, please refer to Kumar et al. (2021). The heat pipes measure 168.7 cm in length, with 163 cm designated for the condenser section and 5.7 cm for the evaporator section. The diameters of the condenser and evaporator in both collectors are 14 mm and 8 mm, respectively.

The main difference between ETC-HP-1 and ETC-HP-2 lies in the number of tubes and their spacing. The ETC-HP-1 consists of 8 tubes, spaced 52 mm apart, while the ETC-HP-2 has 10 tubes with a smaller

Figure 1: Assembly of the collector ETC-HP-1 on the solar tracker of the test bench.

spacing of 18 mm between them. The larger spacing of ETC-HP-1 is due to its design for use with compound parabolic concentrators (CPCs), although in this case, it is used without them. The difference in spacing gives rise to different IAMs, which makes them of interest for the evaluation of the proposals presented in this article (novel IAM for QDT method and improved parameter conversion for SST method).

3.2. Data set description

The tests were carried out according to the ISO-9806 (2017) standard. During the tests, a wind speed of 3 m/s (spatial average) was maintained using fans. In addition, the mass flow rate was set to 2.00 kg/min for ETC-HP-1 and 1.90 kg/min for ETC-HP-2 due to the different collector gross area, in accordance with ISO-9806 (2017), 0.02 kg/(s m^2) approximately. From the tests carried out, 6 different measurement sequences were obtained for each collector using the QDT method. Table 2 summarises the main characteristics of the measurement sequences for each collector. The table shows the date of each test, the inlet temperature ϑ_i (average, and maximum variability between brackets), the flow rate $\dot{m}$ (average and maximum variability, the latter in percent), the average temperature difference $\vartheta_m - \vartheta_a$, the diffuse fraction $f_d = G_{dh}/G_h$ (range of variation) and the transverse and longitudinal angles of incidence (range of variation). All sequences meet the temperature and flow rate stability requirements at the collector inlet as specified in the ISO-9806 (2017) standard for the QDT method (variability less than ± 1 °C and 2 % of the mean, respectively). Appendix A shows the required figure checks according to the standard for the ETC-HP-1 collector as an example. The plots for ETC-HP-2 were omitted because they are very similar to those for ETC-HP-1 and do not provide any additional information.

Table 2: Description of the measurement sequences conducted for the QDT method on each collector.

Collector	Sec.	Date	Hour	Dur.	ϑ_i (°C)	$\dot{m}$ (kg/min)	$\vartheta_m - \vartheta_a$ (°C)	f_d	θ_L (°)	θ_T (°)
ETC-HP-1	1a	30/08/2021	08:05-17:55	09:50	27.1(0.49)	1.984(1.19)	4.3	0.09-0.32	0-13	0-72
	1b	04/10/2021	07:35-17:40	10:05	20.2(0.48)	1.987(0.34)	3.4	0.07-0.14	0-46	0
	2a	28/08/2021	11:25-14:25	03:00	22.2(0.15)	1.985(1.14)	2.2	0.25-0.95	0-5	0-24
	3a	18/08/2021	11:25-14:25	03:00	53.3(0.19)	1.964(1.02)	27.3	0.22-0.26	0-4	0
	3b	11/09/2021	11:25-14:25	03:00	64.6(0.18)	1.953(1.08)	46.2	0.07-0.37	0-10	0-25
	4a	27/08/2021	11:25-14:25	03:00	89.6(0.14)	1.922(1.03)	72.0	0.10-0.12	0-4	0
ETC-HP-2	1a	07/09/2022	07:50-17:15	09:25	22.9(0.49)	1.885(0.56)	3.0	0.12-0.26	0-8	0-72
	1b	27/09/2022	08:05-17:15	09:10	24.9(0.20)	1.887(0.62)	2.6	0.10-0.13	0-40	0
	2a	30/09/2022	11:30-14:30	03:00	23.0(0.16)	1.887(0.52)	2.5	0.17-0.99	0-18	0
	3a	04/09/2022	12:50-15:50	03:00	45.9(0.11)	1.873(0.28)	29.0	0.10-0.10	0-12	0
	3b	05/09/2022	12:50-15:50	03:00	66.9(0.17)	1.853(0.46)	47.0	0.09-0.10	0-12	0
	4a	03/09/2022	12:50-15:50	03:00	88.5(0.15)	1.828(0.77)	72.4	0.09-0.09	0-12	0

The SST method used the same data set, but it is subject to the specific processing procedures for this method, identifying the sub-sequences or data points that meet the measurement requirements shown in Table 1. Sequences 1a, 3a, 3b and 4a were used for the performance test, representing data under clear sky conditions and around solar noon (low angle of incidence). Sequences 1a and 1b were used to determine the IAM, and an additional test of the effective thermal capacity was performed by covering and uncovering the collector as described in section Subsection 2.4.2.

4. Results

This section presents and discusses the main scientific results of this work. Subsection 4.1 validates the novel IAM model for the QDT method by comparison with the SST method, and provides a detailed analysis of the discrepancies between the test methods. In this context, Subsection 4.2 shows the effect of these discrepancies on the useful power produced by the collector. Subsection 4.3 illustrates the dependence of QDT results on the averaging time of the experimental data and reveals the optimal value that improves the reliability of the results for the QDT methodology. Finally, Subsection 4.4 proposes and evaluates an alternative method to convert SST parameters to QDT.

4.1. Validation of the novel IAM model and comparison between test methods

Table 3 shows the coefficients of the thermal models from Eq. (1) for each test method and their respective typical uncertainty. The same IAM model is used for both test methodologies. Also, the proposed non-linear

fit strategy based on the two-metric projection is used for the QDT. It should be noted that the parameters are referred to the gross area of the collectors, as required by the test standard. For this reason, the optical efficiency is relatively low compared if the absorption area is used as a reference. The values of the nodes for the angle of incidence modifier are reported every 10 degrees, where K_{bL} for $\theta_L > 40°$ and K_{bT} for $\theta_T = 80°$ are interpolated values, as commonly done for these angle values. For the QDT method, the characteristic parameters were determined for three different averaging times: 1, 5, and 10 minutes. The 10-minute averages were used for Table 3, as they minimize the difference with the results from the SST methodology (which will be further discussed in Subsection 4.3).

Table 3: Characteristic parameters of the tested collectors obtained through SST and QDT methodologies.

Collector	ETC-HP-1				ETC-HP-2			
Method	SST		QDT		SST		QDT	
	Value	Uncer.	Value	Uncer.	Value	Uncer.	Value	Uncer.
$\eta_{0,hem}$	0.274	±0.002	n.c	n.c	0.371	±0.003	n.c	n.c
$\eta_{0,b}$	0.274	n.c	0.262	±0.001	0.371	n.c	0.367	±0.003
K_d	1.013	n.c	1.257	±0.023	1.007	n.c	1.181	±0.033
a_1	1.211	±0.041	1.255	±0.029	1.682	±0.060	1.686	±0.044
a_2	0	0	0	0	0	0	0	0
$a_5 \times 1000$	122.3	±1.1	65.0	±4.0	207.6	±1.0	126.0	±4.0
$\theta_L \backslash \theta_T$	K_{bL}	K_{bT}	K_{bL}	K_{bT}	K_{bL}	K_{bT}	K_{bL}	K_{bT}
0	1,00	1,00	1.00	1.00	1,00	1,00	1.00	1.00
10	0,98	0,98	1.00	1.02	0,99	1,01	0.98	1.01
20	0,98	1,03	1.00	1.10	0,99	1,07	1.00	1.07
30	0,98	1,12	1.00	1.15	1,00	1,15	1.00	1.20
40	0,94	1,25	1.00	1.33	0,97	1,29	0.93	1.39
50	0,75	1,46	0.78	1.56	0,77	1,40	0.74	1.58
60	0,57	1,76	0.59	2.08	0,58	1,44	0.56	1.57
70	0,38	1,62	0.39	2.35	0,39	1,18	0.37	1.68
80	0,19	0,81	0.20	1.18	0,19	0,59	0.19	0.84
90	0	0	0	0	0	0	0	0

For all parameters, a t-statistic exceeding 3 was acquired, indicating statistical significance, except for the parameter a_2, which therefore had to be held constant at 0. In most instances, the disparities between values obtained from either method were below 10%, except for parameters K_{bT} for $\theta_T > 50°$, K_d, and a_5, which are elaborated upon in subsequent sections. It is important to highlight that despite these variations, the obtained values are consistent with those reported in other literature for collectors of the same technology (Osório & Carvalho, 2014; Zambolin & Del Col, 2012). This validates the implementation of the novel IAM

model.

It is noted that in (Rodríguez-Muñoz et al., 2021b) the performance of this model has already been compared with that of other models (Souka & Safwat, 1966; Perers, 1997; Kalogirou, 2004; ISO-9806, 2017), and its superiority has been demonstrated for flat plate collectors. In the aforementioned work, two independent data sets of a flat plate collector are used: one to adjust the parameters of the models and another to evaluate their performance using metrics such as root mean square error and mean bias. In this sense, the novel model shows better performance over the entire range of incidence angles, indicating superior accuracy. IAM models typically extend from those used for flat plate collectors to tube collectors; therefore, we are confident that the superiority of the proposed model remains in the context of ETC collectors.

Next, the differences obtained in the parameters K_{bT} for $\theta_T > 50°$, K_d, and a_5 are discussed in greater detail, aiming to guide future research in the area and thereby improve testing standards in general, especially for this type of technology. Some of these differences are partially addressed in the following sections.

In the case of $K_{bT}(\theta_T > 50°)$, the differences between the SST and QDT methods increase with the angle of incidence and range from 9 % to 45 %. These differences can be attributed to two main factors. First, as the angle of incidence increases, the useful power produced by the collector decreases, leading to higher relative uncertainty and variability in the IAM determination. Second, the SST method does not distinguish between direct and diffuse solar irradiance, but works with global solar irradiance, and the determined IAM (K_{hem}) refers to the latter. Since the SST test is performed under clear sky conditions (low diffuse fraction, less than 30 %), the standard assumes $K_{hem} = K_b$. This suggests that the IAM obtained by the QDT should be a more reliable estimate, as it incorporates the separate modeling of direct and diffuse solar irradiance.

Regarding the parameter K_d, the difference is about 18 % for both collectors, and in both cases the value of K_d estimated by the SST method is lower than the one determined experimentally by the QDT method. This discrepancy has also been reported in other publications for both flat plate collectors and evacuated tube collectors Kovács et al. (2011); Osório & Carvalho (2014); Rodríguez-Muñoz et al. (2021b) (note that Osório & Carvalho (2014) does not report the value of K_d for the SST method, but it can be estimated by integrating the values of K_{hem} using Eq. (5)). We attribute the discrepancy in K_d to two reasons derived from the assumptions underlying Eq. (5): 1) $K_{hem} = K_b$, and 2) the isotropic behavior of the diffuse solar irradiance. The first assumption was discussed in the previous section. The second assumption is valid under cloudy sky conditions, but not under partly cloudy and clear sky conditions, as shown in Brunger & Hooper (1993); Rodríguez-Muñoz et al. (2021c). The IAM test for the SST method is performed under clear sky conditions and requires measurements throughout the day if performed with a fixed tracker (with varying solar altitude throughout the day), so neither of these assumptions is fully satisfied during the test. On the other hand, the value of K_d in the QDT method is determined directly from the experimental data, taking into account the anisotropic effects of diffuse solar irradiance and the varying sun positions during the test. This creates a clear contrast in the treatment of K_d between the two test methods. In an effort to

improve the compatibility between the two methods, in Subsection 4.4 we propose an alternative method for converting SST and QDT parameters, taking into account the diffuse fraction during the IAM test of the SST method, which provides parameters more similar to those of the QDT method.

Finally, for the parameter a_5 (effective thermal capacity per unit of gross area), differences of 40 % and 89 % were found, with the value obtained by the SST method being higher. This behavior was also observed previously by Osório & Carvalho (2014). Moreover, the obtained values seem high if we consider the physical composition of the collectors. If we weigh the mass and specific heat of the materials that make up the collectors (according to section 25.4 of ISO-9806 (2017)), we obtain a_5 values of 4080 J/°Cm^2 and 5459 J/°Cm^2 for collectors ETC-HP-1 and ETC-HP-2, respectively. The significant difference from these values raises doubts about the reliability of the test methods for determining the thermal capacity of this type of collectors. This is not the case for flat plate collectors, where similar thermal capacity values are obtained using different test methods or estimates (Osório & Carvalho, 2014; Rodríguez-Muñoz et al., 2021b). In addition, it is worth mentioning that in most calculations of the energy produced by the collectors, steady-state conditions are assumed, which makes the value of the thermal capacity less important. However, in the QDT method, the determination of the parameters is global, i.e. all parameters are determined at the same time, so an error in the determination of a_5 could lead to errors in the determination of the other parameters. For this reason, improving the test methods for determining a_5 is relevant future work.

4.2. Useful power under standard reporting conditions

In addition to the results presented in the previous section, the useful power produced by the collector was calculated for each case using Eq. (1), assuming normal incidence and steady-state conditions, for different temperature and sky conditions. The Standard Reporting Conditions (SRC) specified in the ISO-9806 (2017) standard were used for the different sky conditions. The results are shown in Table 4 together with the temperature and cloudiness conditions defined by the standard.

For blue sky conditions, the difference in useful power is not very significant; between 1 and 2 % for collector ETC-HP-1 and less than 2 % for collector ETC-HP-2. However, the differences become more noticeable as cloudiness increases, reaching values between 4 % and 8 % for hazy sky and between 15 % and 39 % for grey sky conditions. Moreover, in all cases, the differences increase with the temperature difference. This difference is mainly attributed to the variation in the incidence angle modifier for diffuse irradiance, K_d. The impact of these differences on annual simulations will depend on the climate considered and the proportion of clear, partly cloudy, and overcast days. For instance, if the proportions of these days were equally distributed, differences ranging from 4 % and 11 % would be expected (average of the differences in Table 4, weighted by solar irradiance). It is anticipated that in arid and temperate climates, the difference will be much smaller due to the prevalence of clear and partly cloudy days over overcast days. This analysis shows the expected discrepancies in the useful power estimation due to different parameters' determination

Table 4: Useful power produced by the collectors tested under standard reporting conditions. Calculations are done assuming normal incidence and steady-state conditions.

Collector	$\vartheta_m - \vartheta_a$ (°C)	Blue Sky $G_{bt} = 850\,\mathrm{W/m^2}$ $G_{dt} = 150\,\mathrm{W/m^2}$			Hazy Sky $G_{bt} = 440\,\mathrm{W/m^2}$ $G_{dt} = 260\,\mathrm{W/m^2}$			Gray Sky $G_{bt} = 0\,\mathrm{W/m^2}$ $G_{dt} = 400\,\mathrm{W/m^2}$		
		SST	QDT	Diff	SST	QDT	Diff	SST	QDT	Diff
ETC-HP-1	0	274	272	1 %	192	201	−4 %	111	132	−17 %
	20	260	247	1 %	168	176	−4 %	87	107	−21 %
	40	250	222	2 %	144	151	−5 %	62	82	−27 %
	60	226	197	2 %	120	126	−5 %	38	56	−39 %
ETC-HP-2	0	371	377	−1 %	260	274	−5 %	149	173	−15 %
	20	338	343	−2 %	227	240	−6 %	116	140	−19 %
	40	304	310	−2 %	193	207	−7 %	82	106	−25 %
	60	270	276	−2 %	159	173	−8 %	49	72	−39 %

with the SST and QDT methodologies.

This study makes it clear that the differences obtained in the estimation of the parameter K_d with each testing method have a significant impact on the prediction of the useful energy of the collectors. Therefore, improving the estimation of this parameter constitutes an aspect to be enhanced in the standard. In this regard, in Subsection 4.4, an improved method is proposed to estimate the parameter K_d using the SST method, which partially reduces the differences with the QDT method.

4.3. Impact of the averaging time of experimental data on QDT method

In a previous study (Rodríguez-Muñoz, 2021), the effect of averaging time in the quasi-dynamic test of flat plate collectors was investigated. The results showed that most of the parameters remained almost constant regardless of the averaging time, with the exception of the parameter a_5. The value of this parameter showed an increasing trend with averaging time, reaching a stable value close to that obtained by the SST method after approximately 5 minutes of averaging. In addition, it was observed that the uncertainty of the parameters also increased with longer averaging times. Based on these results, it was concluded that an averaging time of 5 minutes was the most appropriate for this particular technology. However, this issue has not yet been analyzed for evacuated tube solar collectors with heat pipes.

Table 5 presents the parameter values for the collectors obtained with three different averaging times: 1, 5 and 10 minutes. The behavior of the parameters can be divided into three different groups. The first group includes parameters such as $\eta_{0,b}$, K_d, a_1, $K_{bT}(\theta_T \leq 50°)$, and $K_{bL}(\theta_L \leq 50°)$. As the averaging time increases, the values of these parameters tend to approach the corresponding values obtained by the SST method. The second group includes the parameters $K_{bT}(\theta_T > 50°)$ and $K_{bL}(\theta_L > 50°)$. In this case, the

values deviate further from the corresponding SST values as the averaging time increases. The third and final group consists only of the parameter a_5, which shows a continuous increase with the averaging time and does not seem to stabilize within the analyzed time interval. However, it remains consistently below the SST value (although, as explained before, this value may not be an appropriate reference for this type of collector). Similar to the findings for flat plate collectors, the uncertainty of the parameters also increases with longer averaging times for evacuated tube collectors.

Table 5: Characteristic parameters according to the QDT method for different averaging times.

Collector	ETC-HP-1						ETC-HP-2					
Method	1 minute		5 minute		10 minute		1 minute		5 minute		10 minute	
	Value	Uncer.	Value	Uncer.	Value	Uncer.	Value	Uncer.	Value	Uncer.	Value	Uncer.
$\eta_{0,b}$	0.258	±0.001	0.260	±0.0012	0.262	±0.001	0.350	±0.003	0.365	±0.003	0.367	±0.003
K_d	1.350	±0.013	1.306	±0.022	1.257	±0.023	1.479	±0.032	1.215	±0.038	1.181	±0.033
a_1	1.246	±0.016	1.244	±0.027	1.255	±0.029	1.452	±0.040	1.616	±0.051	1.686	±0.044
a_2	0.00	0	0.00	0	0.00	0	0.00	0.00	0.00	0.00	0.00	0.00
$a_5 \times 1000$	4	±0.4	46	±2.0	65	±4.0	14	±0.9	108	±3.0	126	±4.0
$\theta_L \backslash \theta_T$	K_{bL}	K_{bT}	K_{bL}	K_{bT}	K_{bL}	K_{bT}	K_{bL}	K_{bT}	K_{bL}	K_{bT}	K_{bL}	K_{bT}
0	1.00	1.00	1.00	1.00	1.00	1.00	1.00	1.00	1.00	1.00	1.00	1.00
10	1.00	0.98	1.00	1.01	1.00	1.02	0.93	1.05	0.97	1.02	0.98	1.01
20	1.00	1.08	1.00	1.09	1.00	1.10	0.80	1.13	0.98	1.11	1.00	1.07
30	1.00	1.16	1.00	1.14	1.00	1.15	1.00	1.21	1.00	1.20	1.00	1.20
40	1.00	1.33	1.00	1.34	1.00	1.33	0.99	1.40	1.00	1.39	0.93	1.39
50	0.95	1.60	0.80	1.56	0.78	1.56	0.80	1.55	0.80	1.56	0.74	1.58
60	0.71	2.07	0.60	2.10	0.59	2.08	0.60	1.59	0.60	1.60	0.56	1.57
70	0.47	2.12	0.40	2.22	0.39	2.35	0.40	1.48	0.40	1.51	0.37	1.68
80	0.24	1.06	0.20	1.11	0.2	1.18	0.2	0.74	0.2	0.76	0.19	0.84
90	0	0	0	0	0	0	0	0	0	0	0	0

Considering that the parameters in the first group have a more substantial impact on the calculation of useful energy (under steady-state conditions, as is typically assumed), it can be concluded that an averaging time of 10 minutes is the most suitable in this case.

However, it is important to acknowledge that the significant variability of results with averaging time is a drawback of the QDT method. Therefore, improving this aspect is an area for future work. A possible alternative could be the adoption of dynamic identification algorithms, which have been successfully implemented in transient testing of other technologies and have shown advantages in modeling the transient effects of collectors (Spirkl et al., 1997; Hofer et al., 2015; Fahr et al., 2018; Rodríguez-Muñoz et al., 2021a). The use of dynamic algorithms is an interesting alternative to overcome some of the limitations associated

with the current quasi-dynamic testing approach and to achieve more consistent and reliable results over different averaging times.

4.4. Enhanced parameter conversion procedure SST to QDT

As mentioned earlier, the parameter conversion between SST and QDT methods assumes the hypothesis that $K_{hem} = K_b$. However, this assumption may lead to differences in the estimation of the IAM between the SST and QDT methods, especially at low solar positions when the angle of incidence on the collector's plane is high, such as during sunrise and sunset. In this section, an alternative method is proposed to perform this conversion, taking into consideration the diffuse fraction during the test, and providing values more similar to those obtained through the QDT methodology.

Let's begin by considering Eq. (3), from which we can express the incidence angle modifier for direct irradiance, K_b, as follows,

$$K_b = \frac{\frac{\eta_{0,hem}}{\eta_{0,b}} K_{hem} - K_d \; f_d}{1 - f_d}. \tag{12}$$

Using this equation, it would be possible to calculate K_b from the measurements of K_{hem} under steady-state conditions. However, to do this, we need to know the diffuse fraction during the test and the values of the parameters $\eta_{0,hem}$, $\eta_{0,b}$, and K_d. While the diffuse irradiance is measured during the SST test, obtaining the values of $\eta_{0,b}$ and K_d poses a challenge as they are determined from K_b.

The alternative method proposed in this work involves an iterative process to determine K_b, $\eta_{0,b}$, and K_d. The procedure is described as follows. Firstly, we assume initial values for $\eta_{0,b}$ and K_d (initial seed). Next, we calculate K_b using Eq. (12), and subsequently, we recalculate the parameters $\eta_{0,b}$ and K_d. The initial seed values can be taken from the assumption that $K_{hem} = K_b$. The iterative process continues until the difference between the input and output parameters is less than a certain tolerance. This iterative approach helps refine the parameter values and provides a method to convert parameters between the SST and QDT methodologies, accounting for the influence of the diffuse fraction during the test.

Table 6 shows the results of the proposed procedure for the collectors ETC-HP-1 and ETC-HP-2 and compares them with the standard conversion method and the QDT results. The following trend can be observed: the proposed method produces lower IAM values when $K_b < K_d$ and higher values when $K_b > K_d$. The differences increase with higher separation between K_b and K_d and higher diffuse fraction. When compared with the results of the QDT method, it is observed that the proposed method gives more similar results, going from differences between 9 % and 45 % to differences between 8 % and 26 %. The increase in similarity occurs at high angles of incidence. The same happens with the parameters $\eta_{0,b}$ and K_d, for which the difference between the test methods is reduced. It is also observed that with the new set of parameters $\eta_{0,b}$ and K_d the difference in the useful power values under standard reporting conditions is reduced, between 1 % and 7 % percentage points depending on the temperature difference.

Table 6: Comparison of the standard procedure for conversion of SST to QDT parameters with the proposed procedure.

Collector	ETC-HP-1						ETC-HP-2					
Method	standard conversion		proposed conversion		QDT		standard conversion		proposed conversion		QDT	
$\eta_{0,b}$	0.274		0.272		0.262		0.371		0.369		0.376	
K_d	1.013		1.041		1.257		1.007		1.039		1.255	
$\theta_L \backslash \theta_T$	K_{bL}	K_{bT}	K_{bL}	K_{bT}	K_{bL}	K_{bT}	K_{bL}	K_{bT}	K_{bL}	K_{bT}	K_{bL}	K_{bT}
0	1,00	1,00	1,00	1,00	1.00	1.00	1,00	1,00	1,00	1,00	1.00	1.00
10	0,98	0,98	0,98	0,97	1.00	1.02	0,99	1,01	1,00	1,01	0.98	1.01
20	0,98	1,03	0,97	1,03	1.00	1.10	0,99	1,07	1,00	1,08	1.00	1.07
30	0,98	1,12	0,97	1,13	1.00	1.15	1,00	1,15	1,00	1,18	1.00	1.20
40	0,94	1,25	0,93	1,29	1.00	1.33	0,97	1,29	0,97	1,34	0.93	1.39
50	0,75	1,46	0,72	1,54	0.78	1.56	0,77	1,40	0,78	1,48	0.74	1.58
60	0,57	1,76	0,56	1,93	0.59	2.08	0,58	1,44	0,58	1,54	0.56	1.57
70	0,38	1,62	0,37	1,87	0.39	2.35	0,39	1,18	0,39	1,27	0.37	1.68
80	0,19	0,81	0,19	0,94	0.20	1.18	0,19	0,59	0,19	0,64	0.19	0.84
90	0	0	0	0	0	0	0	0	0	0	0	0

5. Conclusions

The thermal performance test procedures for evacuated tube solar collectors with heat pipes have been analyzed using two different test methods: SST and QDT (ISO-9806, 2017). The experimental estimation of the IAM of the ETC-HP technology was improved by proposing modifications to both test methods, and two solar collectors of this type were considered to evaluate these modifications.

A novel IAM model for the QDT method was presented and validated against the SST results. This model was originally developed for flat plate collectors, and in this case its superiority over other models has already been demonstrated (Rodríguez-Muñoz et al., 2021b). This work further highlights the versatility of application of this model, as it is applicable to both uniaxial and biaxial IAM collectors. The versatility and superior performance of this model make it suitable for use as a general model in testing standards.

The role of the data averaging time in the QDT test was also analyzed, and variability in the results was observed. Based on the comparison with the SST test results, it was concluded that an averaging time of 10 minutes is the most suitable choice for this methodology. We recognize this variability as a drawback of the QDT method, and consequently, the improvement of this aspect represents an area for future research. As mentioned in the previous section, an alternative approach could involve the utilization of dynamic identification algorithms, which have demonstrated advantages in modeling the transient effects of various collector types (Spirkl et al., 1997; Hofer et al., 2015; Fahr et al., 2018; Rodríguez-Muñoz et al., 2021a).

Finally, to improve compatibility between testing methodologies, an alternative parameter conversion procedure from SST to QDT was proposed. The main differences between the testing methods were found in the incidence angle modifiers and the effective thermal capacity. The proposed method specifically addresses the incidence angle modifiers difference. It incorporates the diffuse fraction in the data processing of the IAM SST method, leading to improved results, especially for high angles of incidence where the diffuse radiation influence increase. The application of this method reduces the K_d differences between QDT and SST from 9 % and 45 % to differences between 8 % and 26 %, depending on the angle of incidence. Higher reductions are observed for larger incidence angles. Although this work introduces improved methods and analysis for setting parameters based on experimental evidence, it is important to note that this proposal only partially resolves the SST-QDT differences, and further research is necessary in this area.

Regarding future studies, in addition to the aforementioned differences regarding the IAM, significant disparities were observed in the estimation of the effective thermal capacity per unit area (a_5). The values obtained from both testing methods appear to be unusually high considering the physical composition of the collectors. The methodology proposed here leads to a_5 QDT estimations closer to their real value, as lower and more plausible values were found. Addressing and improving the determination of this parameter represents another area for future research, especially in the QDT method, where all parameters are determined simultaneously. Further studies are also needed, taking into account different collector types, to confirm the advantages of the proposed approach and to demonstrate its general applicability across different technologies.

Acknowledgments

The authors would like to thank the Ministerio de Industria, Energía y Minería (MIEM, Uruguay), especially its Dirección Nacional de Energía (DNE), the Fideicomiso Uruguayo de Ahorro y Eficiencia Energética (Fudaee, Uruguay) and the Corporación Nacional para el Desarrollo (CND, Uruguay), for having provided financial and logistical support for the development of the BECS facility and for having promoted this project with local capacities. The authors are also grateful to the PTB of Germany for promoting and financing the inter-laboratory on efficiency test of solar collectors, which has given us technical certainty about our local testing capabilities. The authors acknowledge partial financial support from CSIC Research Group Program, Universidad de la República, Uruguay.

Appendix A. Tests checks according to the ISO 9806:2017

Figure A.1 shows the graphs suggested by the standard to assess the variability of the operating conditions of the measurement set, where each data point (blue) corresponds to a 10 minute average. The data shown correspond to the ETC-HP-1 collector. The plots for ETC-HP-2 were omitted because they are very similar

to those for ETC-HP-1 and do not provide any additional information. In Figure A.1a, clear sky and cloudy conditions can be distinguished, with clear sky values showing a more consistent pattern. The red line with a slope of 1 ($G_t = G_{dt}$) in this figure is used for basic quality control; the G_{dt} and G_t measurements should be below the red line, since $G_{dt} \leq G_t$. Figure A.1b shows the different inlet temperatures, while Figure A.1c shows the variability in the angle of incidence. Negative and positive values in the latter graph correspond to measurements taken before and after solar noon, respectively. Finally, Figure A.1d shows the variability of the wind speed parallel to the plane of the collector. Although certain wind speed values exceed the upper limit specified in the standard (as shown in Table 1), it is well known that the thermal performance of this type of collector (double cover with vacuum between them) is not significantly affected by wind speed (Zambolin & Del Col, 2012). Therefore, these occasional high wind speeds are not expected to have a significant impact on the results.

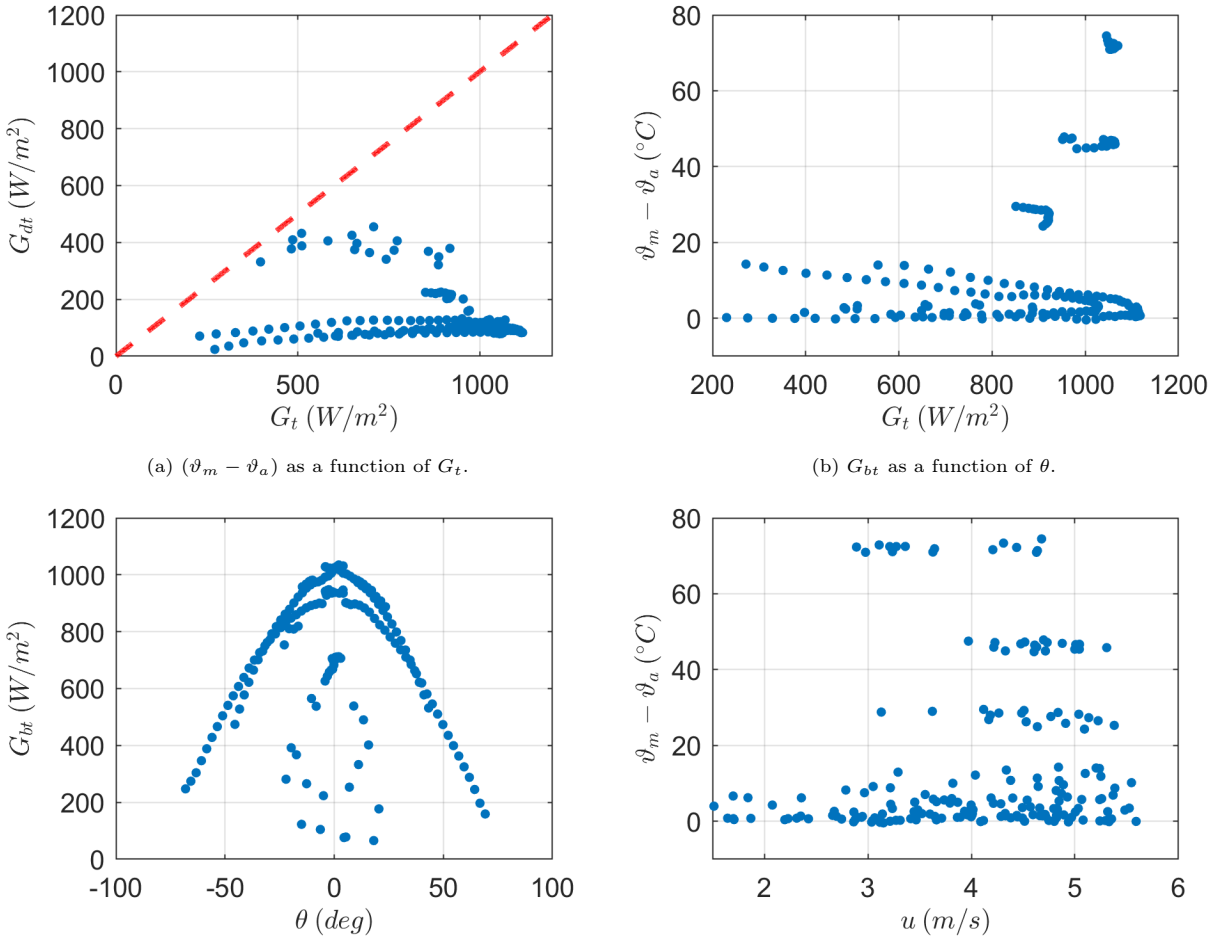

(a) $(\vartheta_m - \vartheta_a)$ as a function of G_t.

(b) G_{bt} as a function of θ.

(c) G_{dt} as a function of G_t.

(d) $(\vartheta_m - \vartheta_a)$ as function of u.

Figure A.1: Data set used for the parameter identification of the ETC-HP-1 collector, following the standard recommendations.

Appendix B. Data and software availability

To facilitate the reproduction of QDT tests for ETC collectors, a Matlab program is provided with the implementation of this algorithm, which can be downloaded here. Although initially developed for ETC collectors, the program has broader applicability and allows the identification of parameters for low-temperature collectors with uniaxial or biaxial IAM. The program employs a constrained nonlinear regression algorithm to calculate and report the values of the characteristic parameters, along with their typical uncertainties and t-statistics (the ratio between the parameter value and its uncertainty). For parameter a_2, it is possible to set the upper and lower limit arbitrarily, which allows setting the parameter to zero if a positive value is obtained with a t-statistic less than 3 (in this case, both limits must be set to zero). However, note that the program does not verify the quality of the experimental data set or compliance with the requirements of the ISO-9806 (2017) standard, which should be ensured prior to utilization. Nevertheless, it does provide the recommended graphs to assess the variability of the data set. The software is provided with the two experimental data sets used in this work.

References

ASHRAE-93 (2014). *Methods of Testing to Determine the Thermal Performance of Solar Collectorss*. Standard American Society of Heating, Refrigerating and Air-Conditioning Engineers USA.

Bates, D. M., & Watts, D. G. (1988). *Nonlinear regression analysis and its applications*. John Wiley & Sons.

Bertsekas, D. (1999). *Nonlinear Programming*. Athena Scientific.

Brunger, A. P., & Hooper, F. C. (1993). Anisotropic sky radiance model based on narrow field of view measurements of shortwave radiance. *Solar Energy*, *51*, 53 – 64. doi:https://doi.org/10.1016/0038-092X(93)90042-M.

Duffie, J. A., & Beckman, W. A. (1991). *Solar engineering of thermal processes*. John Wiley & Sons.

EN-12975 (2022). *Solar collectors - General requirements*. Standard European Committee for Standardisation Belgium.

Fahr, S., Gumbel, U., Zirkel-Hofer, A., & Kramer, K. (2018). In situ characterization of thermal collectors in field installations. In *Proceedings of EuroSun*. doi:0.18086/eurosun2018.12.01.

Fischer, S. (2020). *Quality Infrastructure for Energy Efficiency and Renewable Energy in Latin America and the Caribbean, Report # 95309*. Report Intituto Metrológico Aleman - PTB.

Fischer, S., Heidemann, W., Müller-Steinhagen, H., Perers, B., Bergquist, P., & Hellström, B. (2004). Collector test method under quasi-dynamic conditions according to the european standard en 12975-2. *Solar Energy*, *76*, 117 – 123. doi:https://doi.org/10.1016/j.solener.2003.07.021.

Fischer, S., Lüpfert, E., & Müller-Steinhagen, H. (2006). Efficiency testing of parabolic trough collectors using the quasi-dynamic test procedure according to the european standard en 12975. In *SolarPACES 13th symposium on concentrating solar power and chemical energy technologies*.

Hofer, A., Büchner, D., Kramer, K., Fahr, S., Heimsath, A., Platzer, W., & Scholl, S. (2015). Comparison of two different (quasi-) dynamic testing methods for the performance evaluation of a linear fresnel process heat collector. *Energy Procedia*, *69*, 84–95. doi:https://doi.org/10.1016/j.egypro.2015.03.011. International Conference on Concentrating Solar Power and Chemical Energy Systems, SolarPACES 2014.

ISO-9488 (2022). *Solar energy — Vocabulary*. Standard International Organization of Standarization Switzerland.

ISO-9806 (2017). *Solar Energy – Solar thermal collectors – Test methods*. Standard International Organization of Standarization Switzerland.

García de Jalón, A., Sallaberry, F., Olano, X., , Mateu, E., Astiz, R., Ezcurra, M., & Ramíres, L. (2011). Comprarison of thermal efficiency curves of solar collectors tested in outdoor conditions. In *Proceedings of ISES World Congress 2011*.

Janotte, N., Meiser, S., Krüger, D., Lüpfert, E., Pitz-Paal, R., Fischer, S., & Müller-Steinhagen, H. (2009). Quasi-dynamic analysis of thermal performance of parabolic trough collectors. In *SolarPACES 2009 Conference Proceedings*.

Kalogirou, S. A. (2004). Solar thermal collectors and applications. *Progress in Energy and Combustion Science*, *30*, 231 – 295. doi:https://doi.org/10.1016/j.pecs.2004.02.001.

Kong, W., Perers, B., Fan, J., Furbo, S., & Bava, F. (2015). A new laplace transformation method for dynamic testing of solar collectors. *Renewable Energy*, *75*, 448–458. URL: https://www.sciencedirect.com/science/article/pii/S0960148114006533. doi:https://doi.org/10.1016/j.renene.2014.10.026.

Kong, W., Wang, Z., Fan, J., Bacher, P., Perers, B., Chen, Z., & Furbo, S. (2012). An improved dynamic test method for solar collectors. *Solar Energy*, *86*, 1838 – 1848. doi:https://doi.org/10.1016/j.solener.2012.03.002.

Kovács, P., Pettersson, U., Persson, M., Perers, B., & Fischer, S. (2011). Improving the accurancy in performance prediction for new collector desings. In *Proceedings of Solar World Congress*.

Kratzenberg, M., Beyer, H., & Colle, S. (2006). Uncertainty calculation applied to different regression methods in the quasi-dynamic collector test. *Solar Energy*, *80*, 1453 – 1462. doi:https://doi.org/10.1016/j.solener.2006.03.010.

Kumar, A., Said, Z., & Bellos, E. (2021). An up-to-date review on evacuated tube solar collectors. *Journal of Thermal Analysis and Calorimetry*, *145*, 2873–2889.

McIntire, W. R. (1982). Factored approximations for biaxial incident angle modifiers. *Solar Energy*, *29*, 315 – 322. doi:https://doi.org/10.1016/0038-092X(82)90246-8.

Osório, T., & Carvalho, M. J. (2014). Testing of solar thermal collectors under transient conditions. *Solar Energy*, *104*, 71 – 81. doi:https://doi.org/10.1016/j.solener.2014.01.048. Solar heating and cooling.

Perers, B. (1997). An improved dynamic solar collector test method for determination of non-linear optical and thermal characteristics with multiple regression. *Solar Energy*, *59*, 163 – 178. doi:https://doi.org/10.1016/S0038-092X(97)00147-3.

QAiST (2012). *Performance testing of evacuated tubular collectors*. Report Quality Assurance in Solar heating and cooling Technology.

Rodríguez-Muñoz, J. M. (2021). *Ensayos de desempeño térmico de colectores solares de placa plana*. Thesis Universidad de la República (Uruguay). Facultad de Ingeniería. doi:10.13140/RG.2.2.23050.18881.

Rodríguez-Muñoz, J. M., Bove, I., & Alonso-Suárez., R. (2021a). A detailed dynamic parameter identification procedure for quasi-dynamic testing of solar thermal collectors. In *Proceedings of Solar World Congress*. doi:doi:10.18086/swc.2021.25.01.

Rodríguez-Muñoz, J. M., Bove, I., & Alonso-Suárez, R. (2021b). Novel incident angle modifier model for quasi-dynamic testing of flat plate solar thermal collectors. *Solar Energy*, *224*, 112–124. doi:https://doi.org/10.1016/j.solener.2021.05.026.

Rodríguez-Muñoz, J. M., Monetta, A., Alonso-Suárez, R., Bove, I., & Abal, G. (2021c). Correction methods for shadow-band diffuse irradiance measurements: assessing the impact of local adaptation. *Renewable Energy*, *178*, 830–844. doi:https://doi.org/10.1016/j.renene.2021.06.102.

Rodríguez-Muñoz, J. M., Monetta, A., Bove, I., & Alonso-Suárez, R. (2020). Ensayo cuasi-dinámico de colectores solares de placa plana en uruguay de acuerdo a la norma iso 9806:2017. *ENERLAC. Revista de energía de Latinoamérica y el Caribe*, *4*, 10–26.

Rojas, D., Beermann, J., Klein, S., & Reindl, D. (2008). Thermal performance testing of flat-plate collectors. *Solar Energy*, *82*, 746 – 757. doi:https://doi.org/10.1016/j.solener.2008.02.001.

Sallaberry, F., García de Jalón, A., Olano, X., Mateu, E., Erice, R., & Ramirez, L. (2011). Bi-axial incidence angle modifier

using quasi-dynamic test for asymmetrical solar collector using dummy variables. In *ESTEC congress, Marseille (France)*.

Souka, A., & Safwat, H. (1966). Determination of the optimum orientations for the double-exposure, flat-plate collector and its reflectors. *Solar Energy*, *10*, 170 – 174. doi:https://doi.org/10.1016/0038-092X(66)90004-1.

Spirkl, W., Muschaweck, J., Kronthaler, P., Scholkopf, W., & Spehr, J. (1997). In situ characterization of solar flat plate collectors under intermittent operation. *Solar Energy*, *61*, 147–152.

Theunissen, P.-H., & Beckman, W. (1985). Solar transmittance characteristics of evacuated tubular collectors with diffuse back reflectors. *Solar Energy*, *35*, 311–320. doi:https://doi.org/10.1016/0038-092X(85)90139-2.

Xu, L., Wang, Z., Li, X., Yuan, G., Sun, F., & Lei, D. (2013). Dynamic test model for the transient thermal performance of parabolic trough solar collectors. *Solar Energy*, *95*, 65–78. URL: https://www.sciencedirect.com/science/article/pii/S0038092X13002089. doi:https://doi.org/10.1016/j.solener.2013.05.017.

Xu, L., Wang, Z., Yuan, G., Li, X., & Ruan, Y. (2012). A new dynamic test method for thermal performance of all-glass evacuated solar air collectors. *Solar Energy*, *86*, 1222–1231. URL: https://www.sciencedirect.com/science/article/pii/S0038092X1200031X. doi:https://doi.org/10.1016/j.solener.2012.01.015.

Zambolin, E., & Del Col, D. (2012). An improved procedure for the experimental characterization of optical efficiency in evacuated tube solar collectors. *Renewable Energy*, *43*, 37 – 46. doi:https://doi.org/10.1016/j.renene.2011.11.011.

4.3. Paper 3

On the choice of the parameter identification procedure in quasi-dynamic testing of low-temperature solar collectors

J. M. Rodríguez-Muñoz[a,*], I. Bove[b], R. Alonso-Suárez[a,b], P. A. Galione[c]

[a] *Laboratorio de Energía Solar, Departamento de Física del Litoral, CENUR Litoral Norte, Universidad de la República*
[b] *Laboratorio de Energía Solar, Instituto de Física, Facultad de Ingeniería, Universidad de la República*
[c] *Laboratorio de Energía Solar, Instituto de Ingeniería Mecánica y Producción Industrial, Facultad de Ingeniería, Universidad de la República*

Abstract

The ISO 9806:2017 standard is widely used to characterize the thermal performance of solar collectors. It permits two test methods: Steady State Testing (SST) and Quasi-Dynamic Testing (QDT). While SST requires high stability and clear sky conditions, which limit its application, QDT offers more flexibility in sky conditions. In contrast, the QDT method adds complexity due to the handling of transient phenomena during data processing. There are two approaches to parameter identification in QDT: multilinear regression (MLR) and dynamic parameter identification (DPI). MLR, the most common tool, faces challenges with certain collector types and its results depend on the data averaging time. DPI, while more complex, has the potential to overcome MLR's shortcomings. Which of these two methods is most suitable for testing low-temperature solar collectors in a broad sense is an issue that has not yet been addressed. This work provides evidence that the DPI procedure is more convenient than the MLR procedure, especially for evacuated tube collectors with heat pipes. Specifically, it is shown that DPI produces more reliable test results and provides more accurate estimates of useful power, and it exhibits less variability with respect to data averaging time, demonstrating its improved robustness.

Keywords: Solar thermal collector, dynamic parameter identification, transient model, ISO 9806 standard.

1. Introduction

The ISO 9806:2017 [1] is the most widely used standard for characterizing the thermal performance of solar collectors. It establishes a general thermal model that can be used for a wide variety of technologies: flat plate, evacuated tube, concentrating, etc., both for water and air solar heating systems. Although there are other standards such as ASHRAE-93 [2], they have a high degree of similarity, making them essentially equivalent to each other [3]. The ISO 9806:2017 standard includes two test procedures: Steady State Testing (SST), which requires a high degree of system stability (including flow rate, inlet temperature,

*Corresp. author: J. M. Rodríguez-Muñoz, jrodrigue@fing.edu.uy

List of Symbols

$\dot{m}$	Mass flow rate, $\mathrm{kg\,s^{-1}}$.	f_d	Diffuse fraction, G_{dt}/G_t.
$\dot{Q}_u$	Useful power produced by the collector, W.	G_{bt}	Direct solar irradiance on collector plane, $\mathrm{Wm^{-2}}$.
$\eta_{0,b}$	collector peak efficiency referred to direct solar irradiance.	G_{dt}	Diffuse solar irradiance on collector plane, $\mathrm{Wm^{-2}}$.
$\eta_{0,hem}$	collector peak efficiency referred to global solar irradiance.	G_t	Global solar irradiance on collector plane, $\mathrm{Wm^{-2}}$.
θ	Incidence angle.	K_b	Incidence angle modifier for direct solar irradiance.
θ_L	Longitudinal angle of incidence.	K_d	incidence angle modifier for diffuse solar irradiance.
θ_T	Transversal angle of incidence.	K_{bL}	Incidence angle modifier in the longitudinal plane.
ϑ_a	Ambient air temperature, °C.	K_{bT}	Incidence angle modifier in the transversal plane.
ϑ_i	Collector inlet temperature, °C.	K_{hem}	Incidence angle modifier for global solar irradiance.
ϑ_m	Mean temperature of heat transfer fluid, °C.	q	Volumetric flow rate, $\mathrm{L\,min^{-1}}$.
ϑ_o	Collector outlet temperature, °C.	u	Surrounding air speed, $\mathrm{m\,s^{-1}}$.
a_1	Heat loss coefficient, $\mathrm{W/m^2K}$.		
a_2	Temperature dependence of the heat loss coefficient, $\mathrm{W/m^2K^2}$.		
a_5	Effective thermal capacity, $\mathrm{J/Km^2}$.		
A_G	Gross area of collector, $\mathrm{m^2}$.		

solar irradiance, wind speed, etc.), and Quasi-Dynamic Testing (QDT), where stability conditions are more flexible. Numerous publications have demonstrated the equivalence between these methods, using the current ISO 9806:2017 standard for flat plate collectors (FPC) [4] and evacuated tube collectors (ETC) [5], as well as the European standard EN 12975 for the same technologies, FPC [6] and ETC [7]. The latest version of this standard has become a requirements standard from now on, referring to ISO 9806. This work focuses on the QDT method, specifically for water heating systems, considering the two main solar collector technologies: flat plate and evacuated tube. Next, a brief background on the QDT methodology is provided.

1.1. State of the art

The SST methodology requires strict control of test variables, particularly solar irradiance stability. As a result, outdoor testing must adhere to strict clear-sky conditions, limiting the viability of testing in regions with variable cloud conditions. In contrast, the less common QDT methodology allows for collector operation under a variety of sky conditions - clear, partly cloudy, and completely cloudy. This flexibility makes quasi-dynamic testing more suitable for climates with variable cloudiness, resulting in shorter testing times and increased testing capacity for outdoor laboratories, as shown for temperate climate zones in Europe [7] and Latin America [8]. However, data processing for the QDT method becomes more complex

due to the management of transient collector behavior and the separation modeling of direct and diffuse solar irradiance.

There are two different approaches to determining the parameters of the models in the QDT methodology [6], which differ in how they handle transient phenomena. The first method involves approximating the time derivative using finite differences and treating it as an independent variable in a regression algorithm, commonly known as multi-linear regression (MLR). The second method is to perform a dynamic simulation coupled with a non-linear regression algorithm (Dynamic Parameter Identification, DPI). While DPI offers advantages over the MLR method, its implementation is more challenging. The study by Muschaweck and Spirkl [9] represents one of the early precedents for this procedure for FPC. The thermodynamic model used in this work was later improved by Bosanac [10], becoming more similar to the current thermal model suggested by ISO 9806:2017 for this type of collector. Fischer et al. [11] demonstrated the equivalence between these two methods for four different flat plate collectors. The equivalence for evacuated tube collectors has not been addressed yet.

The MLR method is the most widely used tool due to its simplicity and has been implemented in a variety of technologies. In addition to the FPC and ETC collectors already mentioned, there are also precedents for their application to uncovered collectors [7], parabolic trough collectors [12] and Fresnel concentrators [13]. However, it has some disadvantages, which are summarized below. First, MLR results depends of averaging time used for experimental data [14]. Although a 30-second averaging time is suggested by the standard, it is well known that small averaging time duration can create difficulties in the parameter identification process. Typically, data averaging times of 5 to 10 minutes are used, producing results similar to those of the SST method. The specific data averaging time that provides the best results, closest to SST parameter values, depends on the collector technology. Second, while this methodology is widely used in the context of flat plate collectors, some difficulties have been reported when trying to extend this methodology to evacuated tube collectors with heat pipes [15]. These types of collectors have a much larger time constant compared to other technologies, and the MLR method has difficulty in accurately describing the temperature variations at the collector outlet. This makes it difficult to determine some of the characteristic parameters, especially those related to the incident angle modifier. Finally, the MLR method must limit temperature variations at the collector inlet. This is not a problem in QDT testing because the standard itself imposes a limit on the variability, but it becomes an issue in the context of in-situ testing [14].

The DPI procedure has the potential to overcome the disadvantages of the MLR method. In this regard, DPI allows the use of test data with high temporal resolution, e.g. 10 seconds, as shown in [13], as well as a 5-minute average, as shown in [10]. Therefore, this procedure appears to be more robust in handling different data averaging times. On the other hand, DPI provides greater flexibility regarding the thermodynamic model of the collector [11], allowing the use of more sophisticated models. For example, it allows the use of multi-nodal models, which have been shown to be suitable for in-situ testing and are able

to handle significant variations in fluid temperature at the collector inlet [14]. Finally, it is worth noting that the combination of multi-node models and high temporal resolution test data allows a more accurate reproduction of the real collector dynamics, improving the modeling of transient phenomena and resulting in shorter test times [13].

The disadvantage of the DPI procedure is that its implementation requires the use of more complex mathematical tools. While some implementations are available for the kind of collector used in this work, they often rely on closed-code or paid programs [14], making replication difficult. Furthermore, the implementation of this method for evacuated tube collectors has not yet been reported in the literature, compromising the generality of the method, which represents another limitation of this approach.

1.2. Article's contribution

The main objective of this work is to demonstrate that the DPI procedure is the better choice for QDT testing of low-temperature solar collectors.

It is observed that critical aspects of the QDT method are significantly improved through this procedure, especially for evacuated tubes. To achieve this objective, a specific implementation of the DPI procedure for both types of collectors is presented and experimentally validated against SST results and compared to QDT-MLR results. Specifically, the test data from a Flat Plate Collector (FPC) and an Evacuated Tube Collector with Heat Pipes (ETC-HP) are considered. This work represents the first case of implementation of the DPI procedure for ETC-HP collectors. Thus, it represents a significant progress in demonstrating the generality of the DPI procedure, that is, its application to different technologies.

The advantage of the DPI procedure demonstrated in this work are the following. First, through sensitivity analysis and comparison with MLR results, it is shown that the DPI procedure has less variability in terms of data averaging time. While for the MLR method this variable (data averaging time) has to be set specifically for each type of collector, in the DPI procedure this variable can be set within a wide range without compromising the results. The ability of the DPI procedure to work with data of high temporal resolution is demonstrated, showing the superiority of this procedure over the MLR in terms of parameter uncertainty and the consequent precision of the useful power estimation. Furthermore, it is shown that DPI reduces the problems associated with the determination of the IAM in the case of ETC technology. It provides more reliable results and allows to reduce the test duration by shortening the sequences related to the IAM determination.

Finally, to address one of the major drawbacks of the DPI procedure, a free and explained computational code is provided. This not only facilitates the replication of this work, but also aims to broaden the application of the DPI procedure to test laboratories worldwide. The availability of such free and open algorithms is an important foundation for future research in the field of solar collector testing, which has not been provided in previous related work.

1.3. Article's outline

This article is organized as follows. In the following section, Section 2, we describe the thermodynamic model proposed by the ISO 9806:2017 standard for low-temperature glazed solar collectors, along with the specific DPI algorithm implemented in this work. In Section 3, we provide detailed information about the test platform, the collectors tested and the measurements performed. In Section 4, we present the results obtained using the DPI procedure and compare them with SST and QDT-MLR results, thus providing experimental validation for the proposed DPI procedure. This section also highlights the advantages of the DPI procedure over the MLR and discusses the findings. Finally, Section 5 summarizes the main conclusions.

2. Methodology

This section describes the thermodynamic model used for the QDT methodology, the test procedure, and the dynamic parameter identification algorithm introduced in this work.

2.1. Thermodynamic model and parameters

The thermodynamic model used by the quasi-dynamic method in the ISO 9806:2017 standard is quite general and applicable to different solar collector technologies. The standard provides guidelines for using the model in each case, specifying the terms that can be omitted from the general equation based on the technology of the solar collector being tested. The proposed model for low-temperature glazed collectors is shown in Eq. (1):

$$\frac{\dot{Q}_u}{A_G} = \eta_{0,b}\left[K_b\left(\theta\right)\ G_{bt} + K_d\ G_{dt}\right] - a_1\left(\vartheta_m - \vartheta_a\right) - a_2\left(\vartheta_m - \vartheta_a\right)^2 - a_5\frac{d\vartheta_m}{dt}, \tag{1}$$

where $\dot{Q}_u$ is the useful power produced by the collector (i.e. delivered to the heat transfer fluid), G_{bt} and G_{dt} are the direct and diffuse solar irradiance on the collector plane, respectively, ϑ_m is the average temperature of the fluid passing through the collector (it is calculated as the average of the inlet and outlet temperatures, assuming a linear temperature variation along the collector), ϑ_a is the ambient temperature, and the set of parameters p that characterize the thermal behavior of the collector are: $\eta_{0,b}$, K_b, K_d, a_1, a_2 and a_5. The first parameter is the optical efficiency of the collector at normal incidence referred to direct solar irradiance, a_1 and a_2 are the thermal loss factors, a_5 is the effective thermal capacity divided by the gross collector area (A_G), and K_b and K_d are the incident angle modifiers (IAM – Incident Angle Modifier) with respect to direct and diffuse solar irradiance, respectively.

All parameters are constant except the IAM associated to the direct solar irradiance, K_b, which varies with the angle of incidence, θ. For this function we use the model of [4], originally designed for flat plate collectors and then extended to evacuated tube collectors in [5]. Thus, it is a general model applicable to different technologies (uniaxial and biaxial IAM). This model involves dividing the incident angle range into

smaller intervals and using a piecewise linear function within each interval. For example, with a 10° interval, the adjustable parameters would be $K_b(10°), K_b(20°), \ldots, K_b(80°)$, where $K_b(\theta_i)$ is the K_b value at angle θ_i. It is set that $K_b(0°) = 1$ and $K_b(90°) = 0$. This approach outperforms other models over a wide range of incidence angles as shown in [4].

In the case of evacuated tube collectors, K_b is a function of two angles of incidence, θ_L and θ_T, corresponding to angles projected onto two perpendicular planes. We use the simplification of [16], factorizing the IAM into two different functions: $K_b = K_{bL} \times K_{bT}$. Here, K_{bL} denotes K_b computed at $(\theta_L, 0)$, and K_{bT} denotes K_b computed at $(0, \theta_T)$. In this case, the discretization process was applied to both K_{bL} and K_{bT}.

2.2. Test procedure

In the QDT method, parameter identification involves a single test that requires the execution of at least one measurement sequence for each designated day type. Each day type corresponds to a specific measurement sequence defined by the standard. The total number of sequences required will depend on local climatic conditions and the timing of the test. Each day type should last a minimum of 3 hours and may consist of several non-consecutive sub-sequences, each lasting a minimum of 30 minutes. There are four different day types, each with specific conditions as described in the following paragraph.

Day type 1 requires running sequences where the fluid temperature is close to the ambient temperature, primarily under clear sky conditions. The angle of incidence is varied within a specified range to provide sufficient variability for the K_b function. Day Type 2 involves measurements under varying cloud cover conditions. Day Type 3 requires the collector to operate at an intermediate inlet temperature, at least two different temperatures are required, and Day Type 4 requires a high inlet temperature sequence. Both day types 3 and 4 must include clear sky measurements. Guidelines for improving the clarity of parameter identification for ETC-HP technology are outlined in [5, 15].

To ensure that the experimental data set contains sufficient variability for accurate parameter identification, the standard recommends generating the following plots: 1) $(\vartheta_m - \vartheta_a)$ as a function of G; 2) G_{bt} as a function of θ; 3) G_{dt} as a function of G; and 4) $(\vartheta_m - \vartheta_a)$ as a function of wind velocity parallel to the collector area, u. These plots should be compared to the typical plots of the standard and show a significant degree of similarity. Variability in this work is ensured in accordance with the ISO 9806:2017 standard.

Although this work focuses primarily on the QDT method, the SST method is also implemented and presented in Section 4 as a baseline and reference. The SST method is well known and described in numerous references, such as [7], and therefore its detailed explanation is omitted.

2.3. Parameter identification algorithm for QDT methodology

There are two parameter identification procedures for the QDT method [6]: (i) the finite difference approximation of the time derivative and (ii) dynamic parameter identification. In both cases, the afore-

mentioned thermodynamic model is used and the mean squared error of the useful power serves as the objective function for minimization:

$$E_c(p) = \frac{1}{M} \sum_{i=1}^{M} \left[\dot{Q}_u(t_i) - \dot{Q}_u^*(t_i, p) \right]^2, \tag{2}$$

where $\dot{Q}_u(t_i)$ represents the useful power produced by the collector at time t_i (experimental measurement), $\dot{Q}_u^*(t_i, p)$ is the model estimate of useful power at the same time, and M is the number of measurements. Note that the mean squared error is a function of the parameters, i.e., $E_c = E_c(p)$. The goal of the regression algorithm is to find the parameter set $\hat{p}$ that minimizes the function $E_c(p)$.

Regarding the regression algorithm, in this study the Two-Metric Projection method has been implemented for both parameter identification procedures [17]. This algorithm is iterative, non-linear and constrained, and its versatility is highlighted, being suitable for different collector technologies. Furthermore, its constraints ensure convergence to physically plausible values. To reduce the algorithm's susceptibility to local minima, the procedure is iterated with 10 different randomly generated starting points, and the solution with the smallest mean square error is selected. Parameter uncertainties are estimated using a linearization approach [13]. Detailed information on this algorithm can be found in [5].

The parameter identification procedures, MLR and DPI, differ in how they estimate $\dot{Q}_u^*$. In particular, the procedures differ in their approach to transient effects, which is discussed in detail in the following subsections. In both cases, averages of the variables involved should be taken every certain time interval.

2.3.1. Approximation of derivative by finite difference (MLR)

The essence of this method is a finite difference approximation of the time derivative of the mean temperature of the fluid, as follows:

$$\frac{d\vartheta_m}{dt} \cong \frac{\vartheta_m(t + \Delta t) - \vartheta_m(t)}{\Delta t}. \tag{3}$$

where Δt is the data averaging time, $\vartheta_m(t)$ and $\vartheta_m(t + \Delta t)$ are, respectively, the experimental average temperature of the fluid at the beginning and at the end of the time interval Δt. The estimated useful power produced by the collector, $\dot{Q}_u^*$, is estimated using Eq. (1) in combination with Eq. (3). Subsequently, the term $d\vartheta_m/dt$ serves as an additional independent variable in the regression algorithm, along with the other measured variables on the right side of Eq. (1): ϑ_i, ϑ_a, θ, G_b, and G_d, averaged over Δt.

Note that in this procedure, the regression algorithm can be either linear or non-linear, depending on the collector technology. In the case of flat plate collectors, the thermodynamic model can be expressed linearly in terms of the parameters. Thus, the regression problems can be reduced to a simple Multi-Linear Regression (MLR) algorithm. Since the first implementations of this procedure were applied to flat plate collectors [18], this procedure is commonly known as MLR. However, as mentioned before, for the generality of this work, a non-linear algorithm has been chosen.

This procedure is applicable to different collector technologies and is widely used as mentioned above, mainly due to its simplicity of implementation. In particular, we highlight the previous work of [5], a study that provides a computational program for parameter identification using the QDT methodology through the MLR procedure. This program is intended for general use with low temperature glazed solar collectors.

2.3.2. Dynamic parameter identification (DPI)

This procedure differs from the previous one in that it requires a dynamic simulation of the collector. Specifically, the estimation of the mean fluid temperature, ϑ_m^*, is obtained by solving the differential equation provided by Eq. (1) based on the input variables and a set of characteristic parameters p. Once this equation is solved, $\dot{Q}_u^*$ is estimated as follows,

$$\dot{Q}_u^* = 2\ \dot{m}\ c_p\ \left(\vartheta_m^* - \vartheta_i\right), \tag{4}$$

where $\dot{m}$ and ϑ_i correspond to the experimental measurements of mass flow rate and fluid temperature at the collector inlet, respectively. To distinguish experimental measurements from estimates, an asterisk notation is used. Variables with an asterisk (e.g., $\dot{Q}_u^*$) represent estimates, while those without it correspond to experimental measurements.

The input variables correspond to measurements of the relevant variables in the collector modeling: ϑ_a, θ, G_b, and G_d, which are added to the previously mentioned ϑ_i and $\dot{m}$. These input variables are time-dependent functions (averaged over Δt), but remain constant during each iteration of the regression algorithm, while the characteristic parameters of the collector vary in each iteration.

In this work, the differential equation is solved numerically with the procedure that is explained below. To do this, Eq. (1) is first combined with Eq. (4) and conveniently rewritten as follows:

$$\frac{d\vartheta_m^*}{dt} = \frac{A_G}{a_5}\left(\eta_{0,b}\left[K_b\left(\theta\right)\ G_{bt} + K_d\ G_{dt}\right] - a_1\left(\vartheta_m^* - \vartheta_a\right) - a_2\left(\vartheta_m^* - \vartheta_a\right)^2 - \frac{2\dot{m}c_p\left(\vartheta_m^* - \vartheta_i\right)}{A_G}\right). \tag{5}$$

Then, the value of ϑ_m^* at a generic time t_i, i.e., $\vartheta_m^*(t_i)$, is determined by integrating Eq. (5) between the times t_{i-1} and t_i, assuming the value of ϑ_m^* at the initial time t_0 is known. This integral is performed using the trapezoidal rule. For simplicity, we will refer to $F(t, \vartheta_m^*)$ as the right-hand side of Eq. (5). This results in:

$$\vartheta_m^*(t_i) = \vartheta_m^*(t_{i-1}) + \frac{\delta t}{2}\left[F\left(t_i, \vartheta_m^*(t_i)\right) + F\left(t_{i-1}, \vartheta_m^*(t_{i-1})\right)\right], \tag{6}$$

where $\delta t = t_{i-1} - t_i$ represents the simulation time step. The Eq. (6) is non-linear with respect to $\vartheta_m^*(t_i)$ and is solved for each time step by a fixed-point iteration. The forward Euler method, which approximates the integral by the area of a rectangle, is used as the initial value for this iteration.

$$\vartheta_m^*(t_i) = \vartheta_m^*(t_{i-1}) + \delta t\ F\left(t_{i-1}, \vartheta_m^*(t_{i-1})\right). \tag{7}$$

The numerical accuracy of the trapezoidal rule method is directly influenced by the chosen simulation time step. In general, the numerical error decreases with decreasing simulation time step. Higher values

of the simulation time step can lead to convergence problems in the regression algorithm, as shown in [19]. In the present work, the simulation time step is decoupled from the data averaging time. This solves the aforementioned convergence problems and allows to reduce the numerical error simply by choosing a simulation time step smaller than the data averaging time of the experimental data. However, the numerical method still requires input variable values at each simulation time step. Consequently, when the simulation time step is smaller than the data averaging time ($\delta t < \Delta t$), the input variables are linearly interpolated. The effects of varying these parameters or using an alternative numerical resolution method are explored in the Section 4.

The numerical solution of the differential equation requires the regression algorithm to be nonlinear. The combination of these factors makes the implementation of this procedure more challenging than the MLR procedure. In this context, there are some precedents for the implementation of this parameter identification procedure for low-temperature collectors [14, 20]. However, all of these implementations rely on closed-source, paid tools, which further complicates reproducibility. Furthermore, these works only demonstrate the implementation of the method for flat plate collectors. While the procedure is theoretically applicable to other types of technologies, similar to MLR, this generalization has not yet been demonstrated nor tested. As mentioned in the introduction, this work aims to further demonstrate the generality of the procedure and improve its reproducibility by providing well-described computational code (see the Data and Software Availability section). This code represents an improvement and continuation of the software provided in [5, 19].

3. Test facilities and experimental data

This section describes the test facilities, the collector tested, and the measurements used to determine the collector parameters.

3.1. Testing facilities and evaluated collectors

The experiments were carried out at the Solar Heater Test Bench (Banco de Ensayos de Calentadores Solares - BECS) located at the Solar Energy Laboratory (Laboratorio de Energía Solar - LES, http://les.edu.uy/) of the University of the Republic (Udelar) in Salto, Uruguay (latitude=−31.28°S, longitude=−57.92°W). This test facility, adapted by researchers at LES, is based on existing facilities at the National Renewable Energy Center (Centro Nacional de Energías Renovables - CENER) in Spain and is described in detail in [4]. It is noteworthy that in 2019 this test facility participated in a laboratory intercomparison at the Latin American regional level, organized by the PTB (Physikalisch-Technische Bundesanstalt), the German metrology institute. It received the highest rating in most of the test variables and received only two minor observations related to the determination of secondary variables, both of which have already been addressed by the laboratory [21].

For this study, the thermal performance of two solar thermal collectors was evaluated: a flat plate collector, denoted as FPC, and an evacuated tube collector with heat pipes, denoted as ETC-HP. The FPC, which serves as the reference collector in the aforementioned interlaboratory comparison, has a gross area of 2.02 m^2 and is made of a copper plate and a selective titanium oxide coating, which contribute to its excellent thermal performance. The ETC-HP has a gross area of 1.55 m^2 and consists of 10 evacuated tubes, each with an outside diameter of 59 mm and a length of 1.80 cm, spaced 18 mm apart. This collector is equipped with heat pipes measuring 168.7 cm in length, with 163 cm as the evaporator section and 5.7 cm as the condenser section. The diameters of the evaporator and condenser are 14 mm and 8 mm, respectively.

The FPC was tested from April 30 to May 15, 2021, and the ETC-HP was tested from September 3 to September 30, 2022. Both collectors were mounted on a mobile tracker with a manually adjustable horizontal tilt and an azimuth that could be adjusted either manually or automatically at 2-minute intervals.

3.2. Data set description

The tests were conducted in accordance with the ISO 9806:2017 standard. Throughout the experiments, a spatial average wind speed of 3 m/s was maintained using blowers. In addition, the flow rates were set to 2.40 L/min for the FPC and 1.90 L/min for the ETC-HP, following the standard recommendation. Five different measurement sequences were obtained for the FPC and six different sequences for the ETC-HP (due to its complex IAM) using the QDT method. The main characteristics of these measurement sequences for each collector are summarized in Table 1.

Table 1: Description of the measurement sequences performed on each collector for the QDT method.

Collector	Sec.	Date	Hour	ϑ_i (°C)	q (L/min)	$\vartheta_m - \vartheta_a$ (°C)	f_d	θ (°)	θ_L (°)	θ_T (°)
FPC	1a	04/30/2021	08:15-17:35	20.1(0.55)	2.388(0.89)	7.3	0.08-0.35	0-69	-	-
	2a	11/05/2021	09:35-12:45	16.1(0.17)	2.388(1.87)	3.5	0.06-0.95	0-44	-	-
	3a	08/05/2021	12:45-15:55	42.5(0.13)	2.388(1.01)	26.9	0.07-0.09	0-44	-	-
	3b	12/05/2021	12:45-15:55	61.8(0.10)	2.391(1.04)	45.9	0.07-0.11	0-44	-	-
	4a	15/05/2021	09:35-12:55	82.9(0.25)	2.389(0.83)	67.1	0.08-0.09	0-44	-	-
ETC-HP	1a	07/09/2022	07:51-17:15	22.9(0.49)	1.889(0.56)	3.0	0.12-0.26	-	0-8	0-72
	1b	27/09/2022	08:05-17:15	24.9(0.20)	1.892(0.62)	2.6	0.10-0.13	-	0-40	0
	2a	30/09/2022	11:15-14:30	23.0(0.16)	1.892(0.52)	2.5	0.17-0.99	-	0-18	0
	3a	04/09/2022	12:35-15:50	45.9(0.11)	1.892(0.28)	29.0	0.10-0.10	-	0-12	0
	3b	05/09/2022	12:35-15:50	66.9(0.17)	1.891(0.46)	47.0	0.09-0.10	-	0-12	0
	4a	03/09/2022	12:35-15:50	88.5(0.15)	1.892(0.77)	72.4	0.09-0.09	-	0-12	0

The table contains information about the test date, inlet temperature ϑ_i (mean and maximum variability), flow rate q (mean and maximum variability), mean temperature difference $\vartheta_m - \vartheta_a$, diffuse fraction

$f_d = G_{dh}/G_h$ (range of variation), angle of incidence and transverse and longitudinal angles of incidence (range of variation). All sequences meet the collector inlet temperature and flow stability requirements of the standard for the QDT method; variability is less than $\pm 1\,°C$ and $2\,\%$ of the mean, respectively.

The SST method used the same data set, but underwent different processing procedures to identify the subsequences or data points that met the specific measurement requirements of that method.

4. Results

In this section, we present and discuss the results of the two test methods, SST and QDT, as well as the two parameter identification procedures for the QDT method: MLR and DPI, both with the non-linear optimization method. Subsection 4.1 validates the DPI algorithm presented in this work and provides an analysis of the discrepancies between these test methods, especially for ETC-HP. In the following subsection (Subsection 4.2), we show the advantages of the DPI procedure over MLR, demonstrating its superiority for solar collector testing.

4.1. DPI algorithm validation

Table 2 shows the values of the parameters of the thermal models described in Eq. (1) for each test method, together with the typical P67 uncertainty of the parameters. For all the parameters, a t-statistic greater than 3 (ratio between the parameter value and its uncertainty) was obtained, indicating statistical significance, except for the parameter a_2, which had to be kept constant at zero in some cases, in accordance with the test standard. Node values for the IAM are reported at 10 degree intervals, where $K_b(80°)$ for FPC and $K_{bL}(\theta_L > 40°)$ and $K_{bT}(80°)$ for ETC-HP correspond to interpolated data, as is usually done for these high angle values.

For the QDT method and both parameter identification procedures, parameters were determined at four different data averaging times: 30 seconds, 1, 5, and 10 minutes. In the case of the MLR method, 5-minute averages were used for FPC and 10-minute averages were used for ETC-HP. This choice of data averaging time minimizes the deviation from the results obtained with the SST method, as demonstrated in previous studies [5, 8]. For the DPI procedure, although there are minimal changes in parameters with different data averaging times (as shown in the following subsection), we have found that the 30-second average provides the best option. In addition, a simulation time step of 30 seconds was chosen for the numerical simulation in the DPI algorithm.

The results of the SST and QDT-MLR have been previously presented and discussed in [5, 8] for FPC and ETC, respectively. The only difference in this study is the use of different test data for FPC. Considering the previous testing of this type of collector [7], both test methods have a relatively high degree of agreement. The main differences occurred in the parameters a_5, K_d for both collectors and in the parameter $K_b(\theta \geq 70°)$ for ETC-HP.

Table 2: Parameter values and uncertainty for each collector obtained using the different test methods and parameter identification procedures. Data not applicable is indicated by N/A.

Collector	FPC						ETC-HP					
Testing method	SST (10 minutes)		QDT-MLR (5 minutes)		QDT-DPI (30 second)		SST (10 minutes)		QDT-MLR (10 minutes)		QDT-DPI (30 second)	
Parameters	Value	Uncer.	Value	Uncer.	Value	Uncer.	Value	Uncer.	Value	Uncer.	Value	Uncer.
$\eta_{0,b}$	0.726	N/A	0.718	±0.0018	0.72	±0.0009	0.371	N/A	0.367	±0.0027	0.365	±0.0003
K_d	0.905	N/A	0.973	±0.005	0.941	±0.004	1.007	N/A	1.181	±0.033	1.237	±0.003
a_1	4.499	±0.0186	4.311	±0.041	4.331	±0.02	1.682	±0.06	1.686	±0.044	1.677	±0.004
a_2	0	N/A	0.001	±0.0006	0.001	±0.0003	0	N/A	0	N/A	0	N/A
$a_5 \times 1000$	11.0	±0.6	11.4	±0.3	12.7	±0.2	207.6	±1	126	±4	168	±0.7
θ	K_b		K_b		K_b		K_{bL}	K_{bT}	K_{bL}	K_{bT}	K_{bL}	K_{bT}
0	1		1		1		1	1	1	1	1	1
10	1.00		0.99		0.99		0.99	1.01	0.98	1.01	0.98	1.00
20	1.00		0.99		0.99		0.99	1.07	1.00	1.07	1.00	1.09
30	1.00		0.99		0.98		1.00	1.15	1.00	1.20	1.00	1.18
40	1.00		0.98		0.98		0.97	1.29	0.93	1.39	1.00	1.36
50	0.97		0.94		0.94		0.77	1.40	0.74	1.58	0.80	1.57
60	0.90		0.86		0.87		0.58	1.44	0.56	1.57	0.60	1.56
70	0.72		0.74		0.68		0.39	1.18	0.37	1.68	0.40	1.75
80	0.36		0.37		0.34		0.19	0.59	0.19	0.84	0.20	0.88
90	0		0		0		0	0	0	0	0	0

In the case of QDT-DPI, the results of both collectors show small differences compared to QDT-MLR. Again, the largest differences are observed in the parameters a_5, K_d and $K_b(\theta \geq 70°)$, but the discrepancies are smaller than those observed in SST vs. QDT-MLR. Regarding the differences observed in the parameters K_d and $K_b(\theta \geq 70°)$, it does not seem to be a clear trend that one algorithm gives better results than the other. The same applies to a_5 for the FPC collector. However, in the case of a_5 for the ETC-HP collector, the DPI algorithm gives values closer to those of the SST method, suggesting a better modeling of the transient effects of the collectors.

It is important to note that the determination of the a_5 value by the SST method follows the procedure described in section 25.2 of the ISO 9806:2017 standard. This involves operating the covered collector in a steady state, uncovering it and waiting for it to reach a new steady state. The a_5 value is obtained by integrating the thermodynamic model between these two operating points. However, taking into account the mass and specific heat of ETC-HP materials, according to section 25.4 of the ISO 9806:2017, a_5 values of 5459 J/°Cm^2 were obtained, which are significantly lower than the previous SST and QDT values in Table 2.

One interpretation of this difference could be that the procedure in section 25.4 of the ISO 9806:2017 does not take into account the phase change within the heat pipe. This oversight may slow down the temperature changes at the collector outlet, resulting in an effective thermal capacity greater than predicted by this method (section 24.5 of the ISO 9806:2017). In other words, a_5 from QDT and SST takes these effects into account, resulting in lower values for this parameter. It is imperative to deepen this analysis and the interpretation of the a_5 parameter for this type of collector, which represents future work.

Despite the observations mentioned in the previous paragraph, we conclude that the DPI algorithm presented in this paper has been successfully validated for both collectors and provides equivalent results to SST and QDT-MLR. Although MLR and DPI give equivalent results when their optimal data averaging time is considered, the latter has some advantages that are discussed in the following subsection.

4.2. Superiority of the DPI procedure

This subsection shows the advantages of the DPI procedure over the MLR. Subsection 4.2.1 shows the robustness of DPI with respect to data averaging time, which results in lower parameter variability, and also presents its ability to provide more accurate estimates of useful power and the consequent reduction in parameter uncertainty. Subsection 4.2.2 shows that the DPI procedure yields more reliable IAM results, showing greater robustness to experimental data and the possibility of reducing test duration.

4.2.1. Robustness against data averaging time

In this subsection, the robustness of the parameter identification procedures with respect to the data averaging time is evaluated. For this comparison, parameter values for both collectors were determined using the QDT method with different averaging times: 30 seconds, 1, 5 and 10 minutes. While 30 seconds is the value suggested by the standard, 1 and 10 minutes are the typical values used in the literature. The 1 minute time base was chosen as an intermediate value between 30 seconds and 5 minutes, which also reduces the number of samples to be treated computationally. Both MLR and DPI procedures were used for parameter identification. The results are summarized in Table 3. For each parameter, the mean value and the maximum variability are presented, taking into account the different data averaging times mentioned above. The maximum variability for each parameter was calculated as the difference between the maximum and minimum values and then expressed as a percentage of the average. At the end of the table, the average of the maximum variability for all parameters is shown. For simplicity, the table presents the a_{50} factor instead of a_1 and a_2, as it represents the overall thermal loss factor at a temperature difference of 50 K. This factor is calculated as $a_{50} = a_1 + 50 \times a_2$. Additionally, the K_b values at 0° and 90° are omitted since they are fixed by physical constraints.

In most cases, the average values of the parameters show small differences with respect to the optimal values of the table Table 2, so the parameter specification procedures differ mainly in the maximum

Table 3: Average values and maximum variability of the parameters for each collector obtained by the QDT method and each parameter identification procedure, MLR and DPI, taking into account different data averaging times: 30 seconds, 1, 5 and 10 minutes.

Collector	FPC				ETC-HP							
Method	QDT-MLR		QDT-DPI		QDT-MLR				QDT-DPI			
Parameters	Ave.	Var.	Ave.	Var.	Ave.		Var.		Ave.		Var.	
$\eta_{0,b}$	0.718	0.8 %	0.719	0.4 %	0.358		5.3 %		0.365		0.3 %	
K_d	0.969	6.8 %	0.965	3.5 %	1.352		26 %		1.234		2.3 %	
a_{50}	4.359	1.6 %	4.385	0.9 %	1.549		16 %		1.659		6.0 %	
$a_5 \times 1000$	9.9	42.4 %	11.7	14.5 %	62.6		196 %		163		8.0 %	
θ	K_b	K_b	K_b	K_b	K_{bL}	K_{bT}	K_{bL}	K_{bT}	K_{bL}	K_{bT}	K_{bL}	K_{bT}
10	0.99	1.0 %	0.99	0.0 %	0.96	1.03	5.2 %	3.9 %	0.98	1.00	0.0 %	1.0 %
20	0.99	0.0 %	0.99	0.0 %	0.91	1.10	22 %	5.4 %	1.00	1.09	0.0 %	0.0 %
30	0.99	0.0 %	0.99	1.0 %	1.00	1.21	0.0 %	0.8 %	1.00	1.18	0.0 %	0.0 %
40	0.98	0.0 %	0.98	0.0 %	0.98	1.39	7.1 %	0.7 %	1.00	1.36	0.0 %	0.0 %
50	0.94	4.3 %	0.94	0.0 %	0.79	1.56	7.6 %	2.6 %	0.80	1.57	0.0 %	0.6 %
60	0.86	1.2 %	0.87	1.2 %	0.59	1.59	6.8 %	1.9 %	0.60	1.56	0.0 %	0.6 %
70	0.73	6.8 %	0.70	5.7 %	0.39	1.55	7.6 %	13 %	0.40	1.77	0.0 %	4.5 %
80	0.37	5.4 %	0.35	5.7 %	0.20	0.78	5.1 %	13 %	0.20	0.89	0.0 %	4.5 %
Var. all	-	5.9 %	-	2.8 %	-		17.2 %		-		1.6 %	

variability.

Regarding the MLR procedure, the results show a considerable variability with respect to the data averaging time, which is in line with previous findings [14] for FPC. This variability is particularly pronounced in the case of the ETC-HP, with many parameters showing values greater than 10 %. To obtain accurate parameter values, a data averaging time equal to or greater than 5 minutes (approximately) is required. However, the specific data averaging time that gives the best results, closest to the SST parameter values, depends on the collector technology. Consequently, this variable (data averaging time) must be set specifically for each collector type, which is a clear disadvantage of this procedure. The optimal data averaging time has been found in previous studies [5, 22] and corresponds to 5 minutes and 10 minutes for FPC and ETC-HP, respectively.

To further understand and clarify the above results, the mean squared error of the useful power was also calculated for each case and the results are shown in Figure 1. This error is expressed as a percentage of the average useful power for each collector, being 504 $\mathrm{W/m^2}$ and 326 $\mathrm{W/m^2}$ for FPC and ETC respectively. This figure shows a clear trend: the mean squared power error for the MLR procedure decreases with data averaging time. This trend illustrates why it is necessary to work with relatively long averaging times in the

case of the MLR procedure; this procedure has difficulty modeling the transient effects of the collectors at low data averaging times, resulting in high errors. One explanation for this is that since $d\vartheta_m/dt$ is estimated using finite differences, i.e. $d\vartheta_m/dt \approx \Delta\vartheta_m/\Delta t$, the relative error in this variable is inversely proportional to the experimental temperature differences $\Delta\vartheta_m$ [22]. At low data averaging times, the differences $\Delta\vartheta_m$ are small and therefore the relative error of the associated independent variable is high, which naturally introduces error into the modeling and explains the behavior shown in Figure 1.

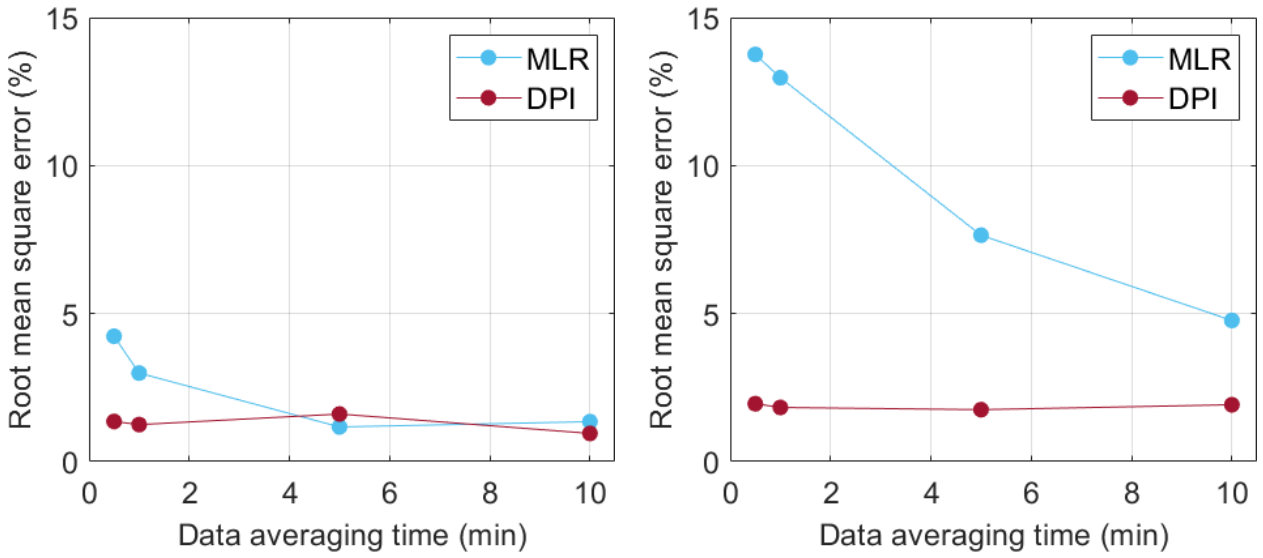

(a) FPC.

(b) ETC.

Figure 1: Root mean square error of useful power as a function of data averaging time for both collectors and parameter identification procedures of the QDT methodology. This error is expressed as a percentage of the average useful power for each collector, which is 504 $\mathrm{W/m^2}$ and 326 $\mathrm{W/m^2}$ for FPC and ETC, respectively.

The DPI procedure, Table 3, also shows a significant reduction in parameter variability compared to the MLR procedure. In particular, this behavior is accentuated in the case of the ETC-HP collector, with a reduction in the variability of almost all the parameters. This makes the method less dependent on data averaging time and more robust than the MLR procedure. Figure 1 shows a clear trend for the DPI procedure that, in contrast to the MLR procedure, the mean squared error is approximately constant and independent of the data averaging time.

In addition, Figure 1 allows a depth comparison between MLR and DPI. In the case of the FPC collector, it can be seen that the MLR and DPI procedures have similar errors for data averaging times greater than 5 minutes. However, for data averaging times less than or equal to 1 minute, the DPI procedure provides more accurate estimates, i.e., the root mean square error is lower. In the case of the ETC collector, the DPI procedure provides more accurate estimates over the entire range of data averaging times analyzed. In conclusion, the superiority of the DPI procedure over the MLR method is particularly evident at low

averaging times (30 seconds and 1 minute) for both FPC and ETC.

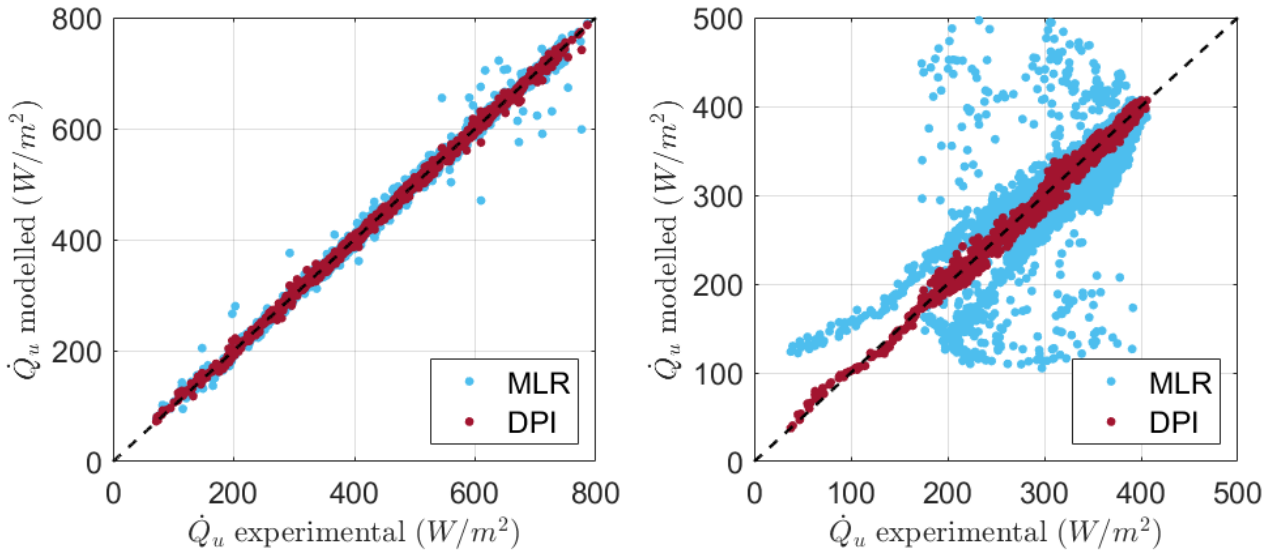

(a) FPC.

(b) ETC.

Figure 2: Scatter plots of useful power for both collectors and parameter identification procedures of the QDT method. Data correspond to 30 seconds of data averaging.

Complementing the previous paragraph, Figure 2 shows the scatter plots of the useful power for each collector and parameter identification method for a data averaging time of 30 seconds. This figure further highlights the fact that the DPI procedure has a lower mean square error, as shown by the lower dispersion of these figures. In particular, for the ETC-HP collector, these differences are more pronounced, clearly showing the advantages of the DPI procedure for this specific technology. Consequently, for this collector, the parameter uncertainty estimated by the DPI procedure at this data averaging time is an order of magnitude lower than that estimated by the MLR method at its optimal data averaging time (10 minutes), as shown in Table 2.

It is important to note that although the study carried out in this section focuses on the effect of data averaging time on parameter values, this variable also affects the assessment of experimental data quality, i.e. the verification of compliance with the requirements of the standard. Some measured variables, in particular wind speed, vary significantly with averaging time, potentially complying with the standard in some cases but not in others. As the collectors in this work are covered, wind speed does not play a significant role in the thermal modeling and power output. Although there can be minor deviations from the wind speed requirements in the analysis, they do not significantly affect the results. However, this should be investigated in more detail when applying the DPI tool to uncovered collectors, which represents future work.

4.2.2. Improving the reliability of IAM estimation

In this subsection it is shown that the DPI procedure yields more reliable IAM results, especially for the ETC-HP technology, overcoming one of the main drawbacks of the MLR procedure. This is due to its improved transient modeling, which provides robustness to experimental data. Specifically, we evaluate the feasibility of using data sequences for day type 1 that are not symmetric with respect to solar noon, which is a requirement of the standard that results in higher testing times. Thus, the elimination of this requirement allows for a reduction in test times by shortening the measurement sequences associated with day type 1.

To achieve this, each day type 1 measurement sequence from Table 1 was split into two segments, distinguishing whether the data were taken before or after solar noon. Separate training datasets were then created sharing the day type 2, 3, and 4 sequences, but being difference in the previously generated day type 1 sub-sequences. Two different datasets were created for the FPC collector and four for the ETC-HP collector. The next step was to identify the parameter values of the collectors using the different data sets. In each case, the optimal data averaging time was used for each collector and parameter identification procedure. After parameter identification, the average of each parameter was calculated based on the results obtained from the different data sets. The maximum variability for each parameter was calculated as the difference between the maximum and minimum values and then expressed as a percentage of the average parameter value. The results of this analysis for each collector and parameter identification procedure are presented in Table 4. At the end of the table, the average of the maximum variability for all tests are shown, considering all parameters and the K_b values.

In the case of the FPC collector, it is observed that the average values of the parameters are close to the optimal values in Table 2, and the maximum variability is relatively small in both cases, MLR and DPI, being slightly lower in the case of DPI. Therefore, for this particular type of collector, it is possible to use measurement sequences for day type 1 that are not symmetrical with respect to solar noon in both cases (MLR and DPI). However, it is noted than the DPI provide better results, specially for the a_5 parameter and the K_b values for the higher incident angles.

On the other hand, a different behavior is observed in the case of the ETC-HP collector. In the case of the MLR procedure, it is observed that the average values of some parameters differ from their optimal values, but the differences are small. This is particularly the case for the IAM values for large angles of incidence. In addition to these differences, a significant maximum variability is also observed, reaching up to 18 % in some cases. For this reason, it is not advisable to use asymmetric measurements for day type 1 in the MLR procedure. On the contrary, in the case of the DPI procedure, it is observed that the average values of the parameters are close to the optimal values and the maximum variability is relatively small. Therefore, in the case of DPI, it is possible to use asymmetric measurements for day type 1. This makes DPI a more versatile and reliable method, since its results do not depend on the type of collector.

Table 4: Average values and maximum variability of the parameters for each collector obtained by the QDT method and by each parameter identification procedure, MLR and DPI, considering different data sets.

Collector	FPC				ETC-HP							
Method	QDT-MLR		QDT-DPI		QDT-MLR				QDT-DPI			
Parameters	Ave.	Var.	Ave.	Var.	Ave.		Var.		Ave.		Var.	
$\eta_{0,b}$	0.719	0.1 %	0.721	0.0 %	0.365		1.4 %		0.363		0.6 %	
K_d	0.971	0.0 %	0.938	0.0 %	1.202		2.6 %		1.251		1.4 %	
a_{50}	4.418	0.1 %	4.404	0.1 %	1.621		5.3 %		1.637		2.2 %	
$a_5 \times 1000$	11.7	2.6 %	13.0	0.8 %	122		9.1 %		161		8.7 %	
θ	K_b	K_b	K_b	K_b	K_{bL}	K_{bT}	K_{bL}	K_{bT}	K_{bL}	K_{bT}	K_{bL}	K_{bT}
10	0.99	0.0 %	0.99	0.0 %	0.97	1.03	0.0 %	0.0 %	1.00	1.01	0.0 %	1.0 %
20	0.99	0.0 %	0.99	0.0 %	0.99	1.08	0.0 %	4.9 %	0.98	1.09	0.0 %	0.9 %
30	0.99	0.0 %	0.99	0.0 %	1.00	1.21	1.0 %	3.7 %	1.00	1.19	0.0 %	0.8 %
40	0.99	1.0 %	0.98	0.0 %	0.93	1.40	0.0 %	9.9 %	1.00	1.37	0.0 %	0.7 %
50	0.95	1.1 %	0.95	0.0 %	0.75	1.59	15 %	6.4 %	0.80	1.57	0.0 %	1.9 %
60	0.86	3.5 %	0.87	3.5 %	0.56	1.57	15 %	7 %	0.60	1.55	0.0 %	7.1 %
70	0.65	22 %	0.63	13 %	0.37	1.66	16 %	18 %	0.40	1.74	0.0 %	6.3 %
80	0.33	22 %	0.32	16 %	0.19	0.83	16 %	10 %	0.20	0.87	0.0 %	6.9 %
Var. all	-	4.3 %	-	2.7 %	-		8.4 %		-		1.7 %	
Var. K_b	-	6.1 %	-	4.0 %	-		9.3 %		-		1.6 %	

It should be noted that although the data corresponding to day type 1 are mostly clear skies and could in principle be considered quasi-stationary, significant variations in IAM and solar irradiance levels occur near sunrise and sunset, causing significant transients in the collectors. For this reason, the standard requires that the measurement sequences associated with this type of day be symmetrical with respect to solar noon; this compensates for these effects and improves the reliability of the results, but at the cost of longer test times. The removal of this requirement increases the demands on the parameter identification procedure, and the accurate identification of the IAM for high angles of incidence will depend on the approach used to deal with such transients. In this regard, the results obtained in this section are due to the fact that the DPI procedure has a better ability to model transient effects than the MLR procedure.

Finally, it is important to note that in all cases (collectors and averaging times), a simulation time step of 30 seconds was used for the numerical simulation in the DPI algorithm. Since this variable must be specified by the tester, different values were studied to evaluate its impact on the results. This analysis demonstrated that the results and conclusions presented in this paper remain consistent as long as the interval is kept below 1 minute. Reducing the interval below 30 seconds did not significantly improve parameter estimation but did slow down program execution. Therefore, a simulation time step of 30 seconds is recommended, as it

proved suitable for both collectors, ensuring modeling accuracy compared to MLR while maintaining efficient program execution. Additionally, different numerical solution algorithms for the differential equations (e.g., forward Euler, backward Euler, multipass methods) and various interpolation schemes for the experimental data were tested, with no significant differences observed in the results.

5. Conclusions

In this work, a DPI procedure has been presented for QDT testing of low temperature glazed solar collectors. The algorithm's results were compared with the SST and QDT-MLR methods using two solar collectors of this type: an FPC and an ETC-HP. This work represents the first precedent of the implementation of the DPI procedure for the ETC collector. By comparison with the SST reference, the proposed DPI procedure was validated. This work represents progress in demonstrating the generality of the general procedure, that is, its applicability to different collector technologies.

Although the MLR and DPI procedures provided similar parameter values for their optimal data averaging times, the latter procedure was demonstrated in this work to have significant advantages in terms of reliability of results. In this regard, a sensitivity analysis of the data averaging time was performed, which revealed the large variability of the results of the MLR procedure, especially in the case of the ETC-HP collectors. This highlights the particular challenges of the MLR procedure for this type of collector. It also shows the need for this procedure to work with data averaging times longer than 5 minutes to ensure the reliability of the results, which is in line with previous work. For averaging times less than 5 minutes, the root mean square error of the useful power increases significantly, introducing uncertainty in the process and in the final parameter values. The specific data averaging time that gives the best results, closest to the SST parameter values, but depends on the collector technology.

In contrast, the DPI procedure shows much lower variability with respect to data averaging time, and the mean square error of the useful power remains stable over a wide range of data averaging times considered. The greatest reduction in parameter variability and mean square error is observed in the case of the ETC-HP, indicating that DPI is a better option for this particular technology. The fact that the characteristic parameter values do not depend on the averaging time makes the DPI procedure more robust. However, we recommend using averaging times for the DPI procedure that are less than or equal to 1 minute; this ensures the advantages of this method over the MLR for both types of collectors in terms of precision of useful power estimates and reduction of parameter uncertainty.

Another advantage of the DPI procedure that has been demonstrated is that it provides more reliable results for the IAM, especially with respect to the nodal values of this function at high angles of incidence. In addition, the DPI procedure was demonstrated to enable the use of asymmetric measurement sequences with respect to solar noon for day type 1, which is currently required by the test regulations. Removing

this requirement from the standard would allow for reduced test times by shortening the measurement sequences dedicated to Day Type 1. This also suggests that the DPI procedure is a better alternative for testing collectors with asymmetric IAM, i.e. collectors whose IAM is not symmetrical with respect to the longitudinal and/or transverse plane.

A drawback of DPI procedures is that their implementation requires more complex mathematical tools. Although some literature describes implementations of this procedure, they are often based on closed code or paid programs, which pose challenges for replication. To address this limitation, a freely available and documented computational code is provided to facilitate the replication of this work and to broaden the application of the DPI procedure across different testing laboratories worldwide.

Acknowledgments

The authors would like to thank the Ministerio de Industria, Energía y Minería (MIEM, Uruguay), especially its Dirección Nacional de Energía (DNE), the Fideicomiso Uruguayo de Ahorro y Eficiencia Energética (Fudaee, Uruguay) and the Corporación Nacional para el Desarrollo (CND, Uruguay), for having provided financial and logistical support for the development of the BECS facility and for having promoted this project with local capacities. The authors are also grateful to the PTB of Germany for promoting and financing the inter-laboratory on efficiency test of solar collectors, which has given us technical certainty about our local testing capabilities. The authors acknowledges financial support from the CSIC Group's Program, Universidad de la República, Uruguay.

Appendix A. Data and software availability

To facilitate the reproduction of DPI procedure tests for FPC and ETC collectors, a Matlab program implementing this algorithm is provided and can be downloaded: http://les.edu.uy/RDpub/PITool_STCT_v2-program.rar. This program is intended for general use with low-temperature collectors with covers, with uniaxial or biaxial IAM, and represents a second version of the program provided in [5]. The program calculates and reports the values of the characteristic parameters, together with their uncertainties and t-statistics (the ratio between the parameter value and its uncertainty). For the parameter a_2, it is possible to set arbitrary upper and lower limits, so that the parameter can be set to zero if a positive value is obtained with a t-statistic less than 3 (in this case, both limits must be set to zero). Note, however, that the program does not check the quality of the experimental data set or its compliance with the requirements of the ISO 9806:2017 standard, which should be ensured by the practitioner before using it. However, it does provide the recommended graphs to assess the variability of the data set. The software is provided with the two experimental data sets used in this work.

References

[1] ISO-9806, Solar energy – solar thermal collectors – test methods, Standard, International Organization of Standarization, Switzerland (2017).

[2] ASHRAE-93, Methods of testing to determine the thermal performance of solar collectors, Standard, American Society of Heating, Refrigerating and Air-Conditioning Engineers, USA (2014).

[3] D. Rojas, J. Beermann, S. Klein, D. Reindl, Thermal performance testing of flat-plate collectors, Solar Energy 82 (8) (2008) 746 – 757. doi:https://doi.org/10.1016/j.solener.2008.02.001.

[4] J. M. Rodríguez-Muñoz, I. Bove, R. Alonso-Suárez, Novel incident angle modifier model for quasi-dynamic testing of flat plate solar thermal collectors, Solar Energy 224 (2021) 112–124. doi:https://doi.org/10.1016/j.solener.2021.05.026.

[5] J. M. Rodríguez-Muñoz, I. Bove, R. Alonso-Suárez, Improving the experimental estimation of the incident angle modifier of evacuated tube solar collectors with heat pipes, Renewable Energy 235 (2024) 121240. doi:https://doi.org/10.1016/j.renene.2024.121240.
URL https://www.sciencedirect.com/science/article/pii/S0960148124013089

[6] S. Fischer, W. Heidemann, H. Müller-Steinhagen, B. Perers, P. Bergquist, B. Hellström, Collector test method under quasi-dynamic conditions according to the european standard en 12975-2, Solar Energy 76 (1) (2004) 117 – 123. doi:https://doi.org/10.1016/j.solener.2003.07.021.

[7] T. Osório, M. J. Carvalho, Testing of solar thermal collectors under transient conditions, Solar Energy 104 (2014) 71 – 81, solar heating and cooling. doi:https://doi.org/10.1016/j.solener.2014.01.048.

[8] J. M. Rodríguez-Muñoz, A. Monetta, I. Bove, R. Alonso-Suárez, Ensayo cuasi-dinámico de colectores solares de placa plana en uruguay de acuerdo a la norma iso 9806:2017, ENERLAC. Revista de energía de Latinoamérica y el Caribe 4 (2) (2020) 10–26.

[9] J. Muschaweck, W. Spirkl, Dynamic solar collector performance testing, Solar Energy Materials and Solar Cells 30 (2) (1993) 95 – 105. doi:https://doi.org/10.1016/0927-0248(93)90011-Q.

[10] M. Bosanac, A. Brunotte, W. Spirkl, R. Sizmann, The use of parameter identification for flat-plate collector testing under non-stationary conditions, Renewable Energy 4 (2) (1994) 217–222.

[11] S. Fischer, W. Heidemann, H. Müller-Steinhagen, B. Perers, Collector parameter identification-iterative methods versus multiple linear regression, in: ISES Solar World Congress, International Solar Energy Society (ISES,, 2003, pp. 14–19.

[12] N. Janotte, S. Meiser, D. Krüger, E. Lüpfert, R. Pitz-Paal, S. Fischer, H. Müller-Steinhagen, Quasi-dynamic analysis of thermal performance of parabolic trough collectors, in: SolarPACES 2009 Conference Proceedings, 2009.

[13] A. Hofer, D. Büchner, K. Kramer, S. Fahr, A. Heimsath, W. Platzer, S. Scholl, Comparison of two different (quasi-) dynamic testing methods for the performance evaluation of a linear fresnel process heat collector, Energy Procedia 69 (2015) 84–95, international Conference on Concentrating Solar Power and Chemical Energy Systems, SolarPACES 2014. doi:https://doi.org/10.1016/j.egypro.2015.03.011.

[14] S. Fahr, U. Gumbel, A. Zirkel-Hofer, K. Kramer, In situ characterization of thermal collectors in field installations, in: Proceedings of EuroSun, 2018. doi:0.18086/eurosun2018.12.01.

[15] QAiST, Performance testing of evacuated tubular collectors, Report, Quality Assurance in Solar heating and cooling Technology (2012).

[16] W. R. McIntire, Factored approximations for biaxial incident angle modifiers, Solar Energy 29 (4) (1982) 315 – 322. doi:https://doi.org/10.1016/0038-092X(82)90246-8.

[17] D. Bertsekas, Nonlinear Programming, Athena Scientific, 1999.

[18] B. Perers, An improved dynamic solar collector test method for determination of non-linear optical and thermal characteristics with multiple regression, Solar Energy 59 (4) (1997) 163 – 178. doi:https://doi.org/10.1016/S0038-092X(97)00147-3.

[19] J. M. Rodríguez-Muñoz, I. Bove, R. Alonso-Suárez., A detailed dynamic parameter identification procedure for quasi-dynamic testing of solar thermal collectors, in: Proceedings of Solar World Congress, 2021. doi:doi:10.18086/swc.2021.25.01.

[20] W. Spirkl, J. Muschaweck, P. Kronthaler, W. Scholkopf, J. Spehr, In situ characterization of solar flat plate collectors under intermittent operation, Solar Energy 61 (3) (1997) 147–152.

[21] S. Fischer, Quality infrastructure for energy efficiency and renewable energy in latin america and the caribbean, report # 95309, Report, Intituto Metrológico Aleman - PTB (2020).

[22] J. M. Rodríguez-Muñoz, Ensayos de desempeño térmico de colectores solares de placa plana, Thesis, Universidad de la República (Uruguay). Facultad de Ingeniería. (2021). doi:10.13140/RG.2.2.23050.18881.

4.4. Paper 4

Experimental characterization of the diffuse incident angle modifier of solar thermal collectors: improving consistency between test methods

J. M. Rodríguez-Muñoz[a,*], I. Bove[b], R. Alonso-Suárez[a,b]

[a] *Laboratorio de Energía Solar, Departamento de Física del Litoral, CENUR Litoral Norte, Universidad de la República*
[b] *Laboratorio de Energía Solar, Instituto de Física, Facultad de Ingeniería, Universidad de la República*

Abstract

Diffuse solar irradiance is essential for modeling solar energy conversion devices, especially solar thermal collectors. The globally accepted ISO 9806:2017 standard defines a thermodynamic model and two test methods to determine its parameters, the steady-state test (SST) and the quasi-dynamic test (QDT). Although both methods are generally considered equivalent, discrepancies between the values of the diffuse incident angle modifier (IAM) have been reported, representing an area for improvement. This study advances the experimental characterization of diffuse IAM, specifically improving the compatibility between SST and QDT methods. Using the ISO 9806:2017 model as a baseline, two alternative diffuse IAM models are introduced and experimentally evaluated with data from a flat plate collector and an evacuated tube collector, covering different technologies. Model 1 extends the SST diffuse IAM model to QDT and treats diffuse irradiance in a global manner, while Model 2 treats diffuse irradiance from sky and ground separately, requiring an additional solar measurement. The evaluation shows that both proposed models improve the consistency between test methods. As the performance differences between these two new models are minimal, Model 1 is the recommended option as its implementation is simpler.

Keywords: Solar thermal collector, diffuse incident angle modifier, ground albedo, ISO 9806 standard.

1. Introduction

Diffuse solar irradiance is important for modeling solar devices such as solar thermal collectors. In mid-latitude temperate climates, around 1/3 of the annual global horizontal irradiation is diffuse [1]. The widely accepted international ISO 9806:2017 standard [2] offers a thermodynamic model to estimate useful power from solar thermal collectors and includes two testing methods to determine its parameters: Steady State Testing (SST) and Quasi-Dynamic Testing (QDT). Although other standards exist, such as ASHRAE-93 [3], they are highly similar, essentially making them equivalent to each other [4].

*Corresp. author: J. M. Rodríguez-Muñoz, jrodrigue@fing.edu.uy

List of Symbols

$\dot{Q}_u$	Useful power produced by the collector, W.
$\eta_{0,b}$	collector peak efficiency referred to direct solar irradiance.
$\eta_{0,hem}$	collector peak efficiency referred to global solar irradiance.
θ	Incidence angle.
θ_L	Longitudinal angle of incidence.
θ_T	Transversal angle of incidence.
ϑ_a	Ambient air temperature, °C.
ϑ_i	Collector inlet temperature, °C.
ϑ_m	Mean temperature of heat transfer fluid, °C.
ϑ_o	Collector outlet temperature, °C..
a_1	Heat loss coefficient, $\mathrm{W/m^2K}$.
a_2	Temperature dependence of the heat loss coefficient, $\mathrm{W/m^2K^2}$.
a_5	Effective thermal capacity, $\mathrm{J/Km^2}$.
A_G	Gross area of collector, $\mathrm{m^2}$.
f_d	Diffuse fraction, G_{dt}/G_t.
G_{bt}	Direct solar irradiance on collector plane, $\mathrm{Wm^{-2}}$.
G_b	Direct normal solar irradiance, $\mathrm{Wm^{-2}}$.
G_{dg}	Diffuse solar irradiance on the collector plane reflected by the ground, $\mathrm{Wm^{-2}}$.
G_{dh}	Diffuse solar irradiance on horizontal plane, $\mathrm{Wm^{-2}}$.
G_{ds}	Diffuse solar irradiance on collector plane from the sky, $\mathrm{Wm^{-2}}$.
G_{dt}	Diffuse solar irradiance on collector plane, $\mathrm{Wm^{-2}}$.
G_h	Global solar irradiance on horizontal plane, $\mathrm{Wm^{-2}}$.
G_t	Global solar irradiance on collector plane, $\mathrm{Wm^{-2}}$.
K_b	Incidence angle modifier for direct solar irradiance.
K_d	incidence angle modifier for diffuse solar irradiance.
K_{bL}	Incidence angle modifier in the longitudinal plane.
K_{bT}	Incidence angle modifier in the transversal plane.
K_{dg}	incidence angle modifier for diffuse solar irradiance reflected by the ground.
K_{ds}	incidence angle modifier for diffuse solar irradiance from the sky.
K_{hem}	Incidence angle modifier for global solar irradiance.
q	Volumetric flow rate, $\mathrm{L\,min^{-1}}$.
u	Surrounding air speed, $\mathrm{m\,s^{-1}}$.

The Incidence Angle Modifier (IAM) is an important part of the above-mentioned thermodynamic model that takes into account the variation of the optical efficiency with the angle of incidence and the environmental conditions. This modeling is addressed with two parameters, one for each component of the solar irradiance, direct and diffuse, namely K_b and K_d, respectively. The importance of direct-diffuse modeling disaggregation in energy performance calculations has been demonstrated in Ref. [5]. In our previous work, an improved direct IAM model (K_b) was proposed, originally developed for flat plate collectors [6] and then extended to evacuated tube collectors [7]. This model shows better performance than the other available models and is suitable for general use; it can be applied to collectors with uniaxial or biaxial IAM. This study builds on these previous efforts and focuses specifically on the other part of IAM modeling: the improvement of the diffuse IAM (K_d). As in the previous work, the ISO 9806:2017 standard model is used as a baseline.

In both test methods of ISO 9806:2017 (SST and QDT), diffuse solar irradiance is modeled globally by a single parameter, K_d, which remains constant for a given collector. Although this is the most usual approach, it should be noted that it does not distinguish, for example, the different contributions to the diffuse irradiance from the sky by atmospheric scattering and from the surroundings by reflection, nor their different directionality. The two test methods differ in the way this global diffuse parameter is estimated. In the SST method, K_d is derived indirectly from K_b, the latter being determined experimentally through a specific sub-test. Specifically, to estimate K_d in the SST framework, the previously determined K_b function is integrated and weighted over the solid angle seen by the collector, assuming an isotropic distribution of diffuse solar irradiance. In the QDT method, the parameter K_d is determined directly from experimental data, addressing some anisotropic effects in the solar irradiance distribution. This creates a clear contrast in the treatment of K_d between the two test methods, which has led to discrepancies between them [7–10], i.e. the values of K_d obtained by one method and the other show differences. In the case of flat plate collectors, the differences are small, on the order of 5 %, so the useful power estimated by both methods is similar [11]. In contrast, for evacuated tube collectors, the differences are significant and increase with diffusion fraction and temperature differences, reaching 39 % in the worst case [7].

To reduce these differences, Rodríguez-Muñoz et al. [7] propose an improved parameter conversion procedure from SST to QDT that incorporates the diffuse solar irradiance measurements into the standard procedure. This procedure has been implemented for two different ETC-HP collectors, and the advantages over the standard procedure have been demonstrated. It reduces the differences between SST and QDT in the parameters related to the optical efficiency, in particular the K_d parameter. However, the reduction in differences is partial and further research is needed to improve the consistency between test methods. This motivates the present work, which focuses on improving the modeling and consistency of the K_d parameter within the ISO 9806:2017 framework. Although alternative approaches exist, for various reasons, these approaches have not been incorporated into the testing standards, as will be discussed in the following paragraphs.

One of the alternative approaches to modeling K_d in the QDT method is derived from the work of Bosanac et al. [12]. In this work, experiments with a flat plate collector were performed using in-situ measurements. Although the procedure and model used are not exactly those of the standard, the methodology is similar to that of the QDT method. Specifically, this author proposes modeling K_d based on K_b, similar to the SST method; K_b is integrated and weighted over the solid angle seen by the collector, globally, without distinguishing between that from the sky and that reflected from the ground. The implementation of this model in the standard QDT method may allow greater consistency with the SST method. However, this has not yet been tested. Another research gap is that other types of collectors, such as evacuated tubes, have not yet been tested. Finally, the main disadvantage is that the parameter identification process is more complex and requires a non-linear regression algorithm.

Another alternative is proposed by Carvalho et al. [13], who suggest modifying the SST method by calculating K_d separately, using two different parameters instead of one. One parameter accounts for diffuse radiation from the sky, while the other accounts for ground-reflected radiation. This author introduces a calculation procedure for these new parameters, similar to the SST method, but with customized integration limits for each case. This model has been experimentally evaluated for both a flat plate collector and an evacuated tube collector, demonstrating the advantages of this approach [5]. However, the model has not been implemented in the QDT method. It is important to mention that Carvalho et al.'s model was originally proposed by Brandemuehl and Beckman [14] and later adopted in various textbooks in the field of solar energy [15]. This author has contributed to the integration of the model into the standard and has gone further to demonstrate its applicability to different solar collector technologies and orientations.

Finally, the work of Hess and Hanby [16] is highlighted. Continuing the work of Carvalho et al., it incorporates an anisotropic distribution in the calculation procedure of the parameter associated with the diffuse solar irradiance from the sky [17], introducing precision as well as computational complexity. This work illustrates the advantages of this model over previous models at moderate operating temperatures for a flat plate collector with reflectors through numerical analysis. However, at low operating temperatures and/or traditional flat collectors, no advantages appear. In line with these results, in Ref. [18] the diffuse solar transmittance of a common flat glazing was analyzed and the anisotropic model of Hess and Hanby was adapted and compared with the traditional isotropic assumption. Both models were evaluated with experimental data for two different glass orientations. The results show that the anisotropic model is superior to the isotropic model, but the differences are very small and do not compensate for the additional computational complexity of the anisotropic model. For this reason, in the context of the present work, the anisotropy of the diffuse solar irradiance from the sky is considered as a second-order effect.

1.1. Article's contribution

The main objective of this work is to advance in the experimental characterization of the diffuse IAM (K_d), improving the compatibility between thermal performance test methods. In this sense, two alternative models (Model 1 and Model 2) are proposed to address this problem.

These models are based on the models of Bosanac et al. and Carvalho et al. and seek to fill the research gap of these previous works. Specifically, the integration of these models into the ISO 9806:2017 framework is detailed for both SST and QDT test methods, and their applicability is experimentally demonstrated using test data from two solar collectors: a flat plate collector (FPC) and an evacuated tube collector with heat pipes (ETC-HP). These collectors have very different IAM characteristics so that the results can be easily extrapolated to a wide range of collectors. The advantages and disadvantages of each approach are identified, and guidelines for improving the test standard are proposed.

The first model (Model 1) extends the K_d modeling of the SST methodology to QDT. Although this

model was originally proposed by Bosanac et al. for FPC, in this work we show its applicability to the standard QDT method and demonstrate its applicability to ETC technology. In the second model (Model 2), we propose a separate modeling of the diffuse irradiance, distinguishing between that coming from the sky and that reflected from the ground, as proposed by Carvalho et al. for the SST method. In this case, unlike the previous study [13], the specific implementation for the QDT method is presented and compared with SST. This model is more accurate in predicting the useful power of the collector. However, it has the disadvantage of requiring an additional measurement of the solar irradiance, i.e. the diffuse solar irradiance reflected by the ground. In this sense, a simple method for estimating this component is proposed, which requires the prior characterization of the albedo of the ground surrounding the test bed. Nevertheless, it is also shown that substantial variations in the albedo estimation do not significantly affect the test results, which is experimentally demonstrated in this work, evidencing the robustness of this method.

With respect to the experimental evaluation of the models, it is shown that both approaches provide more robust results compared to the standard model by improving the consistency between the test methods. It is also shown that although Model 2 outperforms Model 1, the differences are small, making it difficult to compensate for the additional cost of implementing an additional solar irradiance measure. Therefore, we consider that Model 1 is the best option for improving the test standard. In addition, it is also shown that this model can be used to characterize a specific collector, and then Model 2 can be used to estimate its energy production in a long-term simulation, for a specific site and usage conditions, taking full advantage of each model.

Furthermore, the improved parameter conversion from SST to QDT proposed in Ref. [7] has been extended and evaluated in combination with the diffuse IAM models considered in this work. This approach further improves the consistency between the test methods, especially in the case of the ETC-HP collector.

An important drawback of both models is that the parameter identification procedure in the case of the QDT method requires a non-linear regression algorithm, which adds complexity and makes it difficult to replicate. In this context, a free and documented Matlab program is provided to perform the parameter identification, facilitating the reproduction of the QDT method and the integration of the alternative diffuse IAM models into the test standard.

By addressing the above, the following scientific and technical contributions are provided in this work:

- The diffuse IAM models proposed by Bosanac et al. and Carvalho et al. are implemented within the current ISO 9806 framework for both the SST and QDT test methods for the first time, and guidelines are provides for its posterior use in long-term performance simulations.

- The applicability of these models is demonstrated experimentally for two solar collector technologies, FPC and ETC, reducing discrepancies between steady-state and quasi-dynamic test methods, a well recognized problem in the field of solar thermal collector testing.

- A simple and robust method is proposed to measured diffuse solar irradiance reflected from the ground in the framework of QDT method, minimizing the need for additional solar irradiance instruments.
- The improved parameter conversion procedure proposed by Rodríguez-Muñoz et al. [7] is extended, showing that its use, in combination with these diffuse IAM models, further reduces test method discrepancies.
- A free and well-documented MATLAB program is provided for parameter identification, facilitating the reproduction of the QDT method and the integration of the aforementioned models.

1.2. Article's outline

The structure of this work is presented as follows. In the next section, Section 2, the thermodynamic model proposed by the ISO standard is presented for the collector technologies considered in this work, along with the experimental procedure for each test method. This section also shows the integration of the alternative diffuse IAM models into the standard test methods: SST and QDT. Section 3 describes the test platform and the experimental data used in this work, in particular the procedure for obtaining the diffuse solar irradiance reflected by the ground, which is required for the implementation of Model 2. Additionally, this section outlines the methodology used to assess the performance comparison of the alternative diffuse IAM models with respect to the standard model. Section 4 presents the results obtained, and finally, Section 5 summarizes the main conclusions of this work.

2. Thermodynamic model and testing methods

This section describes the thermodynamic model used in the test standard, the procedure for each test method, and provides a detailed description of the alternative diffuse IAM model and its integration into the standard.

2.1. Standard thermodynamic model

The thermodynamic model defined in the ISO 9806:2017 standard is general enough to be applied to different solar collector technologies. The standard also provides guidelines for adapting the model to specific cases, specifying which terms can be omitted from the general equation based on the solar collector technology used. Eq. (1) presents the recommended model for low temperature glazed collectors,

$$\frac{\dot{Q}_u}{A_G} = \eta_{0,b}\left[K_b\left(\theta\right)\ G_{bt} + K_d\ G_{dt}\right] - a_1\left(\vartheta_m - \vartheta_a\right) - a_2\left(\vartheta_m - \vartheta_a\right)^2 - a_5\frac{d\vartheta_m}{dt}, \tag{1}$$

where $\dot{Q}_u$ is the useful power produced by the collector; G_{bt} and G_{dt} are the direct and diffuse solar irradiances on the collector plane, respectively; ϑ_m is the mean temperature of the fluid flowing through the collector (mean between the inlet and outlet temperatures); ϑ_a is the ambient temperature; and the

parameters characterizing the thermal behavior of the collector are $\eta_{0,b}$, K_b, K_d, a_1, a_2 and a_5. The first parameter is the optical efficiency of the collector at normal incidence with respect to direct solar irradiance, a_1 and a_2 are the thermal loss factors, and a_5 is the effective thermal capacity divided by the total collector area (A_G). As introduced earlier, K_b and K_d characterize the IAM with respect to direct and diffuse solar irradiance, respectively.

All parameters remain constant except K_b, which varies as a function of the angle of incidence of the direct beam, θ. In this work, for this function we have used the model proposed in Ref. [6, 7] due to its wide applicability (uniaxial or biaxial IAM) and its superior performance compared to other models available in the scientific literature. This model consists of dividing the incident angle range into smaller intervals and assuming a piecewise linear function within each interval. For example, if a 10° interval is used, the adjustable parameters would be $K_b(10°), K_b(20°), \ldots, K_b(80°)$, where $K_b(\theta_i)$ represents the K_b value at angle θ_i. For all types of collectors, it is mandatory that $K_b(0°) = 1$ and $K_b(90°) = 0$ for the first and last parameters, respectively. In the case of ETC, the standard factorization approach was used [2], i.e. the IAM was expressed as the product of two different functions: one dependent on θ_L and the other dependent on θ_T, denoted as $K_b = K_{bL} \times K_{bT}$. Here K_{bL} is K_b calculated at $(\theta_L, 0)$ and K_{bT} is K_b calculated at $(0, \theta_T)$. The discretization process described above was applied to both the K_{bL} and K_{bT} functions.

The QDT method uses the model directly presented in Eq. (1). The SST method, however, uses a simpler model that treats solar radiation globally. This involves the following substitution,

$$\eta_{0,b}\left[K_b\left(\theta\right)\ G_{bt} + K_d\ G_{dt}\right] = \eta_{0,hem} K_{hem} G_t, \tag{2}$$

leading to the following model,

$$\frac{\dot{Q}_u}{A_G} = \eta_{0,hem} K_{hem} G_t - a_1\left(\vartheta_m - \vartheta_a\right) - a_2\left(\vartheta_m - \vartheta_a\right)^2 - a_5 \frac{d\vartheta_m}{dt}. \tag{3}$$

Here G_t is the global irradiance at the collector plane. The parameters $\eta_{0,hem}$ and K_{hem} correspond to the optical efficiency at normal incidence and the incident angle modifier, both with respect to the global solar irradiance. It is noteworthy that in the SST model, the parameter C is commonly used to characterize the effective thermal capacity of the collector. However, in order to reduce the number of parameters and maintain homogeneity, a_5 was chosen as an alternative. The relationship between C and a_5 is expressed as $a_5 = C/A_G$.

The procedure for estimating QDT parameters from SST parameters (parameter conversions), i.e., estimating $\eta_{0,b}$, K_b, and K_d from $\eta_{0,hem}$ and K_{hem}, is detailed in Annex B of ISO 9806:2017. This procedure is described as follows. First, to estimate K_d, clear sky conditions are assumed, so $K_{hem} = K_b$. Then, K_b is averaged and normalized over the solid angle seen by the collector, assuming an isotropic distribution for

diffuse solar irradiance. That is,

$$K_d = \frac{\int_0^{\pi/2}\int_0^{\pi/2} K_b\left(\theta,\gamma\right)\cos\left(\theta\right)\sin\left(\theta\right)d\theta d\gamma}{\int_0^{\pi/2}\int_0^{\pi/2}\cos\left(\theta\right)\sin\left(\theta\right)d\theta d\gamma}. \tag{4}$$

The standard recommends performing this integral as a summation by discretising the integration domain into intervals of length 10°, an approach used in this study. The parameter $\eta_{0,b}$ is then calculated from Eq. (2) assuming normal incidence and a diffuse fraction of 15 % in the plane of the collector, which is reasonable for SST conditions. That is,

$$\eta_{0,b} = \frac{\eta_{0,hem}}{0.85 + 0.15 \times K_d}. \tag{5}$$

2.2. Test procedure

This section describes the data collection procedure for each test method. It should be noted that in each case the test variables must meet certain stability requirements, as specified in the respective test standard and summarized in various works, such as Ref. [4]. This work can be consulted if the reader is interested in a deeper study of these requirements.

2.2.1. Quasi dynamic testing method

In the QDT method, parameter identification is performed by a single test, which requires the execution of at least one measurement sequence for each day type. Each day type corresponds to a specific measurement sequence as defined in the standard. The total number of sequences required depends on the local climatic conditions and the timing of the test. Each day type must be at least 3 hours in duration and may consist of several non-consecutive sub-sequences of at least 30 minutes each. There are four different day types, and the conditions that must be met for each are detailed in the following paragraph.

Day type 1 focuses on running sequences where the fluid temperature is close to the ambient temperature, emphasizing clear sky conditions. The angle of incidence varies within a specified range, providing sufficient variability for K_b function. Day type 2 involves measurements under varying cloud conditions at any operating temperature. Day type 3 requires the collector to operate at an intermediate inlet temperature, with measurements including clear sky conditions at two different intermediate temperatures. Day type 4 requires a high inlet temperature sequence, including clear sky measurements.

To ensure that the experimental data set contains sufficient variability for accurate parameter identification, the standard recommends that the following plots be generated: 1) $(\vartheta_m - \vartheta_a)$ as a function of G; 2) G_{bt} as a function of θ; 3) G_{dt} as a function of G; and 4) $(\vartheta_m - \vartheta_a)$ as a function of u. These plots must be compared to the typical plots of the standard and should show a significant degree of similarity.

2.2.2. Steady state testing method

In the SST method, parameter determination involves three distinct tests: (i) a performance test to determine the parameters $\eta_{0,hem}$, a_1, and a_2; (ii) an incident angle modifier test to determine K_{hem}; and (iii) an effective thermal capacity test to determine the parameter a_5. The first test is extensively documented and discussed in several references [4], so a detailed description is omitted here.

For the second test (IAM determination), we followed the same procedure as for day type 1 of the QDT test, but the experimental data were processed according to the SST methodology. For each angle of incidence, the experimental IAM value was determined using Eq. (3). The final IAM value for a given angle of incidence was calculated as the average between two measurements: one before and one after solar noon (symmetrical), taking into account transient effects (a fixed tracker was used for this test).

Both the current and previous tests; performance and IAM, must be conducted under steady-state conditions, ensuring that $d\vartheta_m/dt \approx 0$. Once these tests are complete, the parameter conversion procedure described in the previous section must be performed.

The effective thermal capacity test was conducted following section 25.2 of the ISO 9806:2017 standard, considering the second-order adjustment in thermal losses, i.e., the a_2 coefficient. At the beginning of the test, the inlet temperature was set equal to the ambient temperature, and the collector was covered with a reflective blanket to reach a steady state. Subsequently, the cover was removed, and the collector was allowed to reach a new steady-state point, which differed from the initial one due to the effect of solar irradiance. The effective thermal capacity was determined by integrating Eq. (3) over the time period between the two stationary operating points.

2.3. Diffuse incident angle modifier

In this study, two alternative models for K_d are considered, referred to as Model 1 and Model 2, in addition to the standard model (Model 0) which serves as the baseline. For Model 0, the parameter K_d is computed using Eq. (4) within the SST method, following the procedure outlined above. In the QDT method, however, this parameter is derived directly from the experimental data.

In Model 1, the procedure for estimating K_d in the SST method remains unchanged, and this model is extended to QDT. In other words, Eq. (4) is incorporated into Eq. (2), so that K_d is no longer fitted directly from the data. Instead, it depends directly on the nodal values of K_b, which are determined along with the rest of the parameters in the parameter identification algorithm. This change improves the overall consistency between the test methods because both models treat K_d in the same manner and, for a given collector, the parameter K_d corresponds to a constant value.

Model 2 differs from the previous models in the way it treats diffuse solar irradiance. While both Model 0 and Model 1 treat diffuse solar irradiance globally, Model 2 makes a distinction between diffuse solar irradiance coming from the sky and that reflected from the ground, with a parameter for each component:

K_{ds} and K_{dg}, respectively. The calculations for these parameters are given below,

$$K_{ds} = \frac{\int_0^{\pi/2}\int_0^{\zeta} K_b(\theta,\gamma)\cos(\theta)\sin(\theta)d\theta d\gamma + \int_{\pi/2}^{\pi}\int_0^{\pi/2} K_b(\theta,\gamma)\cos(\theta)\sin(\theta)d\theta d\gamma}{\int_0^{\pi/2}\int_0^{\zeta}\cos(\theta)\sin(\theta)d\theta d\gamma + \int_{\pi/2}^{\pi}\int_0^{\pi/2}\cos(\theta)\sin(\theta)d\theta d\gamma}, \tag{6}$$

$$K_{dg} = \frac{\int_0^{\pi/2}\int_{\zeta}^{\pi/2} K_b(\theta,\gamma)\cos(\theta)\sin(\theta)d\theta d\gamma}{\int_0^{\pi/2}\int_{\zeta}^{\pi/2}\cos(\theta)\sin(\theta)d\theta d\gamma}. \tag{7}$$

Here, β corresponds to the horizontal tilt of the collector, and $\zeta = \arctan\left[(-\tan\beta\cos\gamma)^{-1}\right]$. In this case, for a given collector, the parameters K_{ds} and K_{dg} vary as a function of the horizontal tilt of the collector. These expressions assume symmetry with respect to the longitudinal plane of the collectors.

Two observations are made about these equations. The first observation is that in the original paper by Carvalho et al., these integrals were expressed in a different coordinate system. In this paper, the choice has been made to use the same coordinate system as ISO 9806:2017, θ and γ, thus maintaining greater homogeneity and consistency with the standard, and facilitating model integration. The second observation is that in the case of collectors with biaxial K_b, for example, evacuated tube collectors, the function K_b is written in terms of the angles θ_L and θ_T, as already mentioned. Therefore, to perform the integrals, these angles must be expressed in terms of θ and γ. These relations are provided in the ISO 9806:2017 standard.

Finally, below is an explanation of how Model 2 is incorporated into the thermodynamic model of the standard and into the SST and QDT test methods. In the case of the thermodynamic model, Eqs. (6) and (7) are incorporated directly into the model of Eq. (1) by the following substitution,

$$K_d\ G_{dt} = K_{ds}\ G_{ds} + K_{dg}\ G_{dg}, \tag{8}$$

leading to the following model,

$$\frac{\dot{Q}_u}{A_G} = \eta_{0,b}\left[K_b(\theta)\ G_{bt} + K_{ds}\ G_{ds} + K_{dg}\ G_{dg}\right] - a_1(\vartheta_m - \vartheta_a) - a_2(\vartheta_m - \vartheta_a)^2 - a_5\frac{d\vartheta_m}{dt}, \tag{9}$$

where G_{ds} and G_{dg} are the diffuse solar irradiance at the collector plane, coming from the sky and reflected from the ground, respectively.

In both test methods, the integration of this model takes place at the data processing level. In the case of the SST method, the parameter conversion procedure changes and now requires the estimation of the parameters $\eta_{0,b}$, K_b, K_{ds} and K_{dg} (new thermodynamic model) from $\eta_{0,hem}$ and K_{hem}. The procedure is described as follows. First, to estimate K_d, clear sky conditions are assumed, so $K_{hem} = K_b$, as before. Then the parameters K_{ds} and K_{dg} are calculated using Eqs. (6) and (7). Finally, the parameter $\eta_{0,b}$ is estimated as follows,

$$\eta_{0,b} = \frac{\eta_{0,hem}}{0.85 + 0.12 \times K_{ds} + 0.03 \times K_{dg}}. \tag{10}$$

This equation results from combining Eq. (5) and Eq. (8). In addition, it was assumed that 15 % accounts for diffuse solar irradiance, distributed as 12 % from the sky and 3 % reflected from the ground, a reasonable hypothesis for clear sky conditions and low reflective ground.

2.4. Parameter identification algorithm for QDT

Regarding the parameter identification algorithm for the QDT method, there are two options [11], which differ in how they treat transient phenomena. The first method involves approximating the time derivative using finite differences and treating it as an independent variable in a regression algorithm commonly known as multi-linear regression (MLR). Its name derives from its use in the context of flat-plate collector testing [19]. The second method is to perform a dynamic simulation coupled with a non-linear regression algorithm (Dynamic Parameter Identification, DPI). Although its implementation is more challenging, it offers significant advantages as it better handles the transient effects of solar collectors, both under standard test conditions and in situ conditions as demonstrated in Refs. [20, 21]. As a result, it provides more reliable parameter estimations. . This method is particularly suitable for ETC-HP technology, as experimentally demonstrated in Ref. [18], technology addressed in the present work.

In this work, the DPI procedure was used, as it provides more reliable results and therefore offers a better framework for comparing diffuse IAM models. Given the difficulty of its implementation, a Matlab program for parameter identification is provided here, which represents a continuation and improvement of the code provided in Ref. [18]. This program facilitates the implementation and reproduction of the QDT methodology and the integration of the alternative diffuse IAM models in the test standard.

The program also reports uncertainty values for performance parameters (i.e., all parameters except those related to the beam IAM) using the linearization approach, which is simple and provides reliable results [20]. However, this method can only estimate uncertainty for parameters that represent input variables within the regression algorithm. Since the parameters of the proposed diffuse IAM models are not adjustable themselves but are instead calculated from the beam IAM, it is not possible to assign uncertainty to them. Other uncertainty estimation methods exist for the DPI approach, such as bootstrapping and Monte Carlo methods [22, 23], which allow estimation of the uncertainty of these parameters. However, these methods are more complex, computationally intensive, and do not provide additional insights for the specific objective of diffuse IAM modeling, and were therefore not considered in this work. Nevertheless, this remains a topic for future work.

3. Experimental data and methodology

This section provides a description of the test facilities, in particular, the diffuse solar irradiance measurements that are central to this work. It also describes the collectors considered, the experimental data, and the methodology used to assess the performance of the alternative diffuse IAM models.

3.1. Test facilities

The experiments were carried out at the Solar Heater Test Bench (Banco de Ensayos de Calentadores Solares - BECS) located at the Solar Energy Laboratory (Laboratorio de Energía Solar - LES, http://les.

edu.uy/) of the University of the Republic in the city of Salto, Uruguay (latitude=31.28° S, longitude=57.92° W). This test bench, originally designed by LES researchers, is based on existing facilities of the Spanish National Renewable Energy Center (Centro Nacional de Energías Renovables - CENER). Notably, this test facility recently participated in a Latin American laboratory intercomparison organized by the PTB (Physikalisch-Technische Bundesanstalt), Germany's national metrology institute. It received the highest ratings in most of the test variables and only had two minor observations regarding the determination of secondary variables, both of which were already addressed by the laboratory [24].

The thermo-hydraulic installation and the data acquisition system are described in detail in Ref. [6], so they will not be reproduced here. However, we provide a description of the instrumentation dedicated to solar irradiance measurements, with particular emphasis on diffuse solar irradiance, a crucial aspect of this study.

In this regard, the facility is equipped with three Kipp & Zonen CMP10 pyranometers. These pyranometers measure global solar irradiance in the collector plane (G_t), as global and diffuse solar irradiance in the horizontal plane (G_h and G_{dh}, respectively). All pyranometers used are spectrally flat and classified as class A according to the ISO 9060:2018 standard [25]. They are calibrated annually at LES with the ISO 9847:2023 standard [26] against a Kipp & Zonen CMP22 secondary standard traceable to the World Radiometric Reference at the World Radiation Center in Davos, Switzerland. The diffuse irradiance measurement is mounted with a shadow band, so the raw measurements must be corrected. For this correction, the expression given in Ref. [27] has been used, which is significantly better than the correction suggested by the manufacturer [28].

Parameter identification in the SST method requires the measurement of global solar irradiance at the collector plane for the diffuse IAM models analyzed. However, the QDT method requires separate estimation of its direct and diffuse components. Therefore, the following information is provided on how each component was estimated at the collector plane.

The direct solar irradiance G_{bt} at the collector plane was estimated from G_h and G_{dh} using the following procedure. First, the direct normal irradiance (DNI, G_b) was calculated using the closure relation $G_h = G_b \cos\theta_z + G_{dh}$, where $\cos\theta_z$ is the cosine of the solar zenith angle. Then G_{bt} was calculated from the DNI by multiplying it by the cosine of the angle of incidence, θ. The diffuse solar irradiance G_{dt} at the collector plane was estimated from G_t and G_{bt}, simply by the difference, i.e. $G_{dt} = G_t - G_{bt}$. This diffuse measurement includes both the diffuse irradiance from the sky and the diffuse irradiance reflected from the ground (G_{ds} and G_{dg}, respectively) and is sufficient for the implementation of Models 0 and 1.

For the implementation of Model 2, however, it is necessary to estimate G_{ds} and G_{dg} separately. The diffuse irradiance G_{dg} in the collector plane reflected by the ground is estimated from G_h as follows: $G_{dg} = \rho_g\,(1 - \cos\beta)\,G_h/2$. This equation assumes that the ground behaves as a perfect diffuse and isotropic reflector, where ρ_g is the albedo of the ground. Finally, G_{ds} is estimated by difference, $G_{ds} = G_{dt} - G_{dg}$.

With respect to the albedo of the ground, there are two options. The first and more accurate option is to add an albedometer in front of the test platform. This instrument consists of two global pyranometers positioned horizontally, one facing down to measure the solar radiation reflected by the ground. The albedo is then obtained as the ratio of the two measurements. Ideally, these measurements should be synchronized with those of the tested collector to provide albedo values specific to the sky conditions at the time of the test at the specific site. This has the disadvantage of requiring an additional radiometer. The second option is to perform a long asynchronous measurement campaign; one year would be optimal to capture the annual variability of albedo, and use this data to fit an empirical model. This model can then be used to estimate the albedo at the time of the test using the solar irradiance measurements on the horizontal plane mentioned above. This option is less accurate but does not require an additional radiometer at the time of the test.

The second approach was used in this work. In this sense, six empirical albedo models were fitted in Ref. [29] using measurements from the albedometer shown in Figure 1, which is located in front of the collector test platform. For simplicity, the simplest model was used, which results from assuming a constant value for the ground albedo; $\rho_g = 0.2190$, independent of sky conditions. In addition, a sensitivity analysis was conducted to evaluate the impact of varying albedo values on the results. It was found that deviations of $\pm$ 20 % in albedo lead to only $\pm$ 1 % variations in the parameter identification of the collectors, confirming the robustness of the proposed procedure.

Figure 1: Experimental setup to measure the albedo of the ground surrounding the test bench (both instruments on the right; the others are for inclined solar irradiance, not used in this study).

3.2. Experimental data and methodology for assessing diffuse IAM models

In this study, we used test data from two different solar thermal collectors: a Flat Plate Collector, referred to as FPC, and an Evacuated Tube Collector with Heat Pipes, referred as ETC-HP. The FPC served as the reference collector in a previously mentioned inter-laboratory comparison. These collectors and the experimental data set used in this study are identical to those used in Ref. [30]. For this reason, some general details of the tests are given below, but specific details can be found in the aforementioned article.

Testing for the FPC took place from April 30 to May 15, 2021, while the ETC-HP was tested from September 3 to September 30, 2022. All tests followed the ISO 9806:2017 standard. Throughout the experiments, a spatial average wind speed of 3 m/s was maintained using air blowers. In addition, flow rates were set at 2.40 L/min for the FPC and 1.90 L/min for the ETC-HP. Five different measurement sequences were obtained for the FPC and six different sequences for the ETC-HP (due to its complex IAM) using the QDT method. The SST methodology used the same data, but subjected it to different processing procedures to identify the sub-sequences or data points that met the specific requirements of that method.

The methodology used to assess the performance of diffuse IAM models is described as follows. The experimental data previously describe were used to determine the parameters of the thermodynamic model introduced in Eq. (1) for both FPC and ETC-HP collectors, considering the various diffuse IAM models (Model 0, 1 and 2) and associated testing methods (SST and QDT).

The comparison between models was carried out in three steps. First, the parameter values were directly compared (when applicable), with particular attention to the differences arising from the testing methodologies adopted for each diffuse IAM model. Since not all models are directly comparable on a parameter-by-parameter basis, the second step involved calculating the useful energy produced by each collector under the reporting conditions defined in the standard. This approach enables a more comprehensive comparison by capturing the combined effect of all model parameters under varying operating conditions.

Finally, the enhanced parameter conversion from SST to QDT, previously proposed by the authors [7], was evaluated alongside the alternative IAM models to further improve the consistency and reliability of the testing procedures. In particular, this work presents the extension of the enhanced parameter conversion procedure from SST to QDT to Model 2, while the extension for Model 1 was already introduced in previous work.

4. Results

This section presents and discusses the results obtained using the methodology described above. First, Subsection 4.1 shows the fitting results of the different diffuse IAM models along with the corresponding discussion. Next, Subsection 4.2 compares the performance of these models by presenting the useful power

produced by each collector under the reporting conditions defined in the standard. The benefits of the new proposals are highlighted, particularly the improved agreement between the steady-state and quasi-dynamic methods achieved with the new modeling. Finally, Subsection 4.3 presents the results of the enhanced parameter conversion procedure from SST to QDT for all models, which show that combining it with alternative diffuse IAM models further reduces discrepancies between testing methods.

4.1. Models' parameters comparison

Models are implemented and evaluated under the SST and QDT procedures for both collector types. Table 1 and Table 2 show the parameter values of the thermodynamic models from Eq. (1) for FPC and ETC-HP, respectively. Uncertainty is reported only when mandatory according to the standard (i.e., for performance parameters: all parameters except those related to the beam IAM), to simplify the tables. Additionally, uncertainty cannot be reported when a parameter is fixed by the regression algorithm (e.g., when the second-order loss coefficient is set to zero). Moreover, it is not possible to provide uncertainty for the diffuse IAM parameters of the proposed model due to limitations of the method used, as discussed in Subsection 2.4.

The values of the nodes for the angle of incidence modifier are reported every 10 degrees at the bottom part of each table. It is noted that K_{bL} for $\theta_L > 40°$ and K_{bT} for $\theta_T = 80°$ correspond to interpolated data. For all parameters, a t-statistic greater than 3 was obtained, indicating statistical significance, except for the parameter a_2, which therefore had to be kept constant at 0. A data averaging time of 10 minutes was used for the SST method, and a data averaging time of 1 minute was used for the QDT method. In addition, the numerical simulation time step in the dynamic parameter identification algorithm of the QDT was set to 30 seconds, effectively balancing the benefits of the algorithm and its execution time [30].

It is worth noting that, in all cases, the final value of the mean square error (used as the objective function in the parameter identification process) is approximately 2-3 % relative to the mean useful power. This indicates that, for the specific dataset used in this study, the models exhibit a comparable level of accuracy.

For better interpretation of the results, the parameters are divided into two sets. The first set includes the parameters $\eta_{0,b}$, a_1, a_2, a_5, and K_b, while the second set consists of the parameters associated with the diffuse IAM: K_d, K_{ds} and K_{dg}, whenever applicable.

The parameters of the *first set* do not change significantly when considering different models of diffuse IAM within the SST framework. This is due to the fact that in this test method, the determination of the parameters involves a certain degree of independence; the parameters are determined by three independent subtests. On the other hand, in the QDT method, the determination of the parameters is global, i.e., all the parameters are determined simultaneously. Therefore, in this case (QDT), some variation in the parameter values is expected when considering different models of diffuse IAM. However, these variations are minimal,

Table 1: Characteristic parameters of the FPC for each diffuse IAM model and test method. N/A indicates not applicable.

Model	Model 0				Model 1				Model 2			
Test	SST		QDT		SST		QDT		SST		QDT	
method	Value	Uncer.	Value	Uncer.	Value	Uncer.	Value	Uncer.	Value	Uncer.	Value	Uncer.
$\eta_{0,b}$	0.726	N/A	0.720	±0.001	0.726	N/A	0.722	±0.001	0.727	N/A	0.721	±0.001
a_1	4.499	±0.019	4.331	±0.020	4.499	±0.019	4.342	±0.021	4.499	±0.019	4.340	±0.020
a_2	0	N/A	0.001	±0.0003	0	N/A	0.001	±0.0003	0	N/A	0.001	±0.0003
$a_5 \times 1000$	11.0	±0.6	12.7	±0.1	11.0	±0.6	12.5	±0.1	11.0	±0.6	12.6	±0.1
K_d	0.905	N/A	0.941	±0.004	0.905	N/A	0.895	N/A	–	–	–	–
K_{ds}	–	–	–	–	–	–	–	–	0.933	N/A	0.913	N/A
K_{dg}	–	–	–	–	–	–	–	–	0.744	N/A	0.717	N/A
θ	K_b		K_b		K_b		K_b		K_b		K_b	
0	1.00		1.00		1.00		1.00		1.00		1.00	
10	1.00		0.99		1.00		1.00		1.00		1.00	
20	1.00		0.99		1.00		0.99		1.00		0.99	
30	1.00		0.98		1.00		0.99		1.00		0.99	
40	1.00		0.98		1.00		0.98		1.00		0.98	
50	0.97		0.94		0.97		0.95		0.97		0.95	
60	0.90		0.87		0.88		0.88		0.88		0.88	
70	0.72		0.68		0.68		0.73		0.68		0.71	
80	0.36		0.34		0.34		0.37		0.34		0.35	
90	0		0		0		0		0		0	

in the order of 1 % in most cases. When comparing the test methods between themselves, it can be seen that for most parameters the differences are small, usually below 10 %, except for a_5 and $K_b(\theta \geq 60°)$, where the differences are between about 17 % and 50 %, being larger in the case of ETC-HP. These differences are in line with previous work [10].

Regarding the *second set*, the parameters of Models 0 and 1 are directly comparable, since both consider the diffuse component globally, assuming a constant value for the parameter K_d. Therefore, we will start with the analysis of these models. In the case of the SST method, the parameter K_d is the same in both models, as expected since it is estimated in the same way (see Subsection 2.3). In the case of the QDT method, it is observed that the value of K_d for Model 1 is quite close to that of the SST, while in the case of Model 0 it is not. Specifically, this parameter is overestimated in the QDT by 4 % and 20 % for the FPC and ETC-HP collectors, respectively, a result that is consistent with previous research [7, 9, 10]. This can be explained as follows. Although Models 0 and 1 consider K_d as a constant, the way in which this constant is determined is different in each case. As explained in Subsection 2.3, in the case of Model 0 for QDT,

Table 2: Characteristic parameters of the ETC-HP for each diffuse IAM model and test method. N/A indicates not applicable.

Collector	Model 0				Model 1				Model 2			
Test	SST		QDT		SST		QDT		SST		QDT	
method	Value	Uncer.	Value	Uncer.	Value	Uncer.	Value	Uncer.	Value	Uncer.	Value	Uncer.
$\eta_{0,b}$	0.371	N/A	0.365	±0.0003	0.371	N/A	0.373	±0.0003	0.372	N/A	0.371	±0.0003
a_1	1.682	±0.060	1.678	±0.005	1.682	±0.060	1.703	±0.006	1.68	±0.060	1.693	±0.006
a_2	0	N/A	0	N/A	0	N/A	0	0	0	N/A	0	N/A
$a_5 \times 1000$	207.6	±1.0	167.8	±0.9	207.6	±1.0	172.0	±1.1	207.6	±1.0	170.2	±0.9
K_d	1.007	N/A	1.235	±0.004	1.007	N/A	1.084	N/A	–	–	–	–
K_{ds}	–	–	–	–	–	–	–	–	1.055	N/A	1.131	N/A
K_{dg}	–	–	–	–	–	–	–	–	0.671	N/A	0.775	N/A
$\theta_L \backslash \theta_T$	K_{bL}	K_{bT}	K_{bL}	K_{bT}	K_{bL}	K_{bT}	K_{bL}	K_{bT}	K_{bL}	K_{bT}	K_{bL}	K_{bT}
0	1.00	1.00	1.00	1.00	1.00	1.00	1.00	1.00	1.00	1.00	1.00	1.00
10	0.99	1.01	0.98	1.00	0.99	1.01	0.99	0.99	0.99	1.01	0.99	0.99
20	0.99	1.07	1.00	1.09	0.99	1.07	1.00	1.09	0.99	1.07	1.00	1.09
30	1.00	1.15	1.00	1.18	1.00	1.15	1.00	1.19	1.00	1.15	1.00	1.19
40	0.97	1.29	1.00	1.36	0.97	1.29	1.00	1.36	0.97	1.29	1.00	1.36
50	0.77	1.40	0.80	1.57	0.77	1.40	0.80	1.57	0.77	1.40	0.80	1.57
60	0.58	1.44	0.60	1.56	0.58	1.44	0.60	1.57	0.58	1.44	0.60	1.57
70	0.39	1.18	0.40	1.74	0.39	1.18	0.40	1.77	0.39	1.18	0.40	1.76
80	0.19	0.59	0.2	0.87	0.19	0.59	0.20	0.88	0.19	0.59	0.2	0.88
90	0	0	0	0	0	0	0	0	0	0	0	0

this parameter is fitted to the experimental data, including possible biases in the distribution of the samples with respect to the sky conditions. In the case of Model 1, the K_d parameter is determined by integrating and weighting the K_b function over the solid angle seen by the collector, in the same way as in the SST method; hence, the differences are smaller. In summary, Model 1 provides greater agreement between the SST and QDT test methods.

For Model 2, the parameters of this model are determined separately, as this model treats diffuse solar irradiance differently from Models 0 and 1. This model distinguishes between diffuse solar irradiance coming from the sky and that reflected from the ground, with a parameter for each component, K_{ds} and K_{dg}. The values of the parameters depend on the horizontal tilt of the collector; for a simple comparison, a horizontal tilt of 45° was used. The agreement between the SST and QDT test methods is better than for Model 0, but slightly worse than for Model 1. The main discrepancy is observed in the parameter K_{dg}, and the determination of this parameter is strongly influenced by the nodal values of the K_{bL} function at high angles of incidence, which have greater uncertainty.

As the parameters of Model 2 cannot be directly compared with those of Models 0 and 1, the next section provides a comparative analysis in terms of the useful power produced by the collectors. This will provide a better understanding of the differences between the models.

4.2. Useful power under standard reporting conditions

To complement the results and discussion presented in the previous section, the useful power produced by each collector was calculated for different temperature differences and sky conditions using Eq. (1) for Models 0 and 1, and Eq. (9) for Model 2. In all cases, normal incidence and steady-state conditions were assumed, as specified in the ISO 9806:2017 standard. For the temperature difference, four cases were considered: 0, 20, 40 and 60 K. For the sky conditions, the Standard Reporting Conditions (SRC) specified in the ISO 9806:2017 standard were used, as shown in Table 3. In addition, the evaluation of Model 2 requires the specific values of G_{ds} and G_{dg}. The diffuse solar irradiance reflected by the ground G_{dg} was estimated using Eq. (11), a relationship derived using the isotropic transposition model [15], assuming normal incidence and $G_{dh}/G_h \approx G_{dt}/G_t$.

$$G_{dg} = G_{dt}\,\frac{\rho\,(1-\cos\beta)}{(G_{dt}/G_t)(1+\cos\beta)+\rho\,(1-\cos\beta)}. \tag{11}$$

Then the diffuse solar irradiance from the sky was estimated by the difference, i.e.: $G_{ds} = G_{dt} - G_{dg}$. These expressions were evaluated assuming an albedo of 0.2 and a horizontal tilt of 45°, and their results are shown in the last two columns of Table 3. These values (albedo and tilt) are commonly used in the field of solar thermal testing [15].

Table 3: Standard Reporting Conditions (SRC).

Solar irradiance	G_{bt} (W/m^2)	G_{dt} (W/m^2)	G_{ds} (W/m^2)	G_{dg} (W/m^2)
Blue Sky	850	150	121	29
Hazy Sky	440	260	239	21
Gray Sky	0	400	287	13

The useful power estimates for the different cases are shown in Figure 2 and Figure 3 for FPC and ETC-HP respectively. For a better understanding of these figures, note that each column corresponds to a different diffuse IAM model; Model 0, 1, and 2 from left to right, and each row corresponds to a different sky condition: clear, hazy, and gray sky, from top to bottom. In general, no significant differences are observed for clear sky conditions. However, for hazy and gray sky conditions, the differences between the test methods and the models become evident and tend to increase with the diffuse fraction. In terms of temperature differences, the discrepancy between test methods and models becomes more pronounced at

higher values. These observations are more pronounced for the ETC-HP collector (Figure 3) than for the FPC collector (Figure 2).

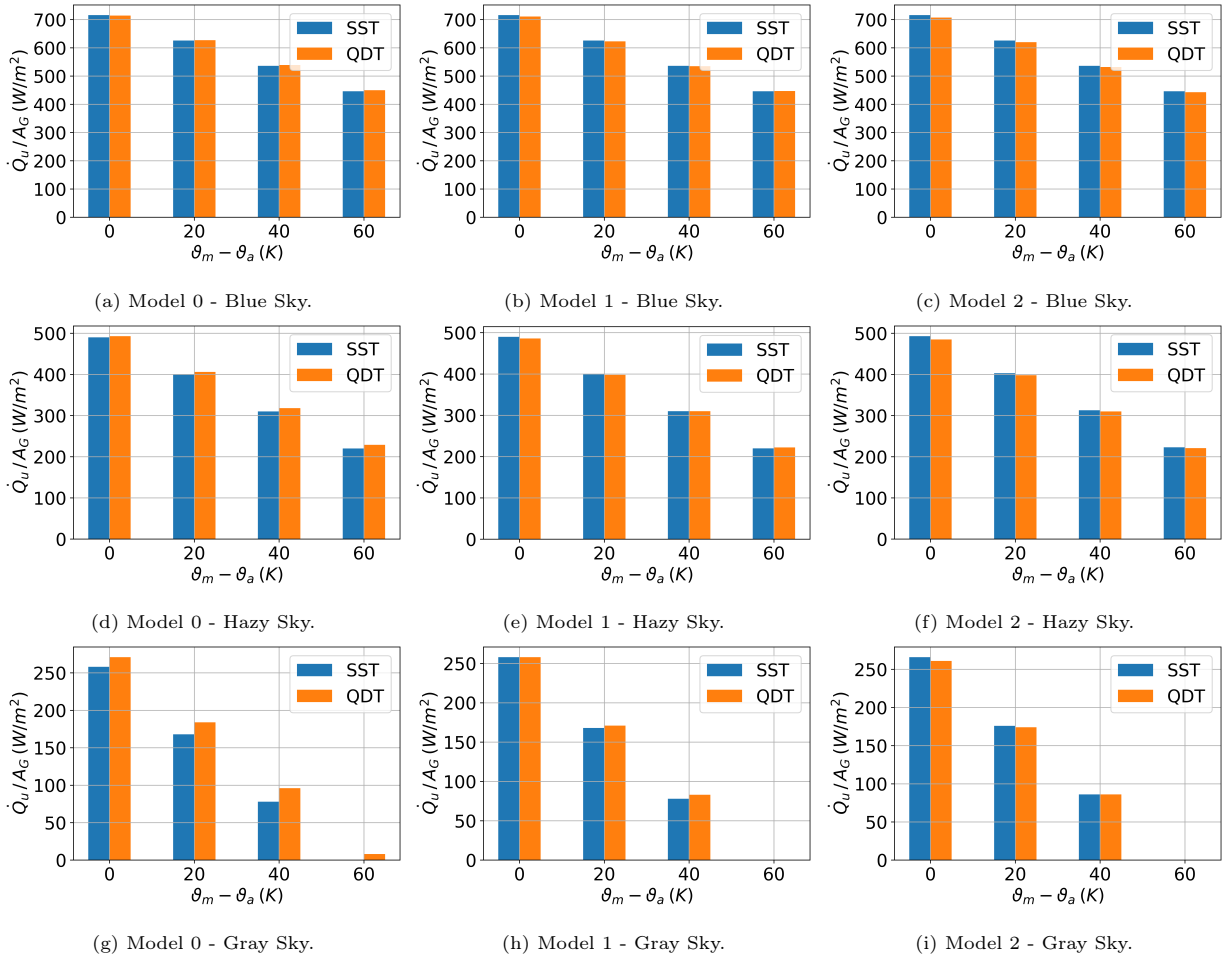

(a) Model 0 - Blue Sky. (b) Model 1 - Blue Sky. (c) Model 2 - Blue Sky.

(d) Model 0 - Hazy Sky. (e) Model 1 - Hazy Sky. (f) Model 2 - Hazy Sky.

(g) Model 0 - Gray Sky. (h) Model 1 - Gray Sky. (i) Model 2 - Gray Sky.

Figure 2: Useful power per gross area unit produced by FPC collector under standard reporting conditions, for each test method and diffuse IAM model.

The following procedure was used to analyze the consistency of the test methods. First, the difference between SST and QDT useful power estimates was calculated for the different sky conditions and temperature differences, and then all the differences were averaged for each diffuse IAM model. Finally, the models were ranked in decreasing order, from the least consistent to the most consistent, i.e. from the largest difference to the smallest average difference. This procedure was done separately for each collector.

For FPC, the models are ordered as follows: Model 0, 2, and 1, with average differences of 3.3 %, 1.6 %, and 0.6 %, respectively. In this case, the difference between the models is small, consistent with Figure 2. For ETC, the models are ordered as follows: Model 0, 1, and 2, with average differences of 16 %, 6.7 %, and 5.2 %, respectively. In this case, the differences are significant, especially for Model 0. Although Model 2 is

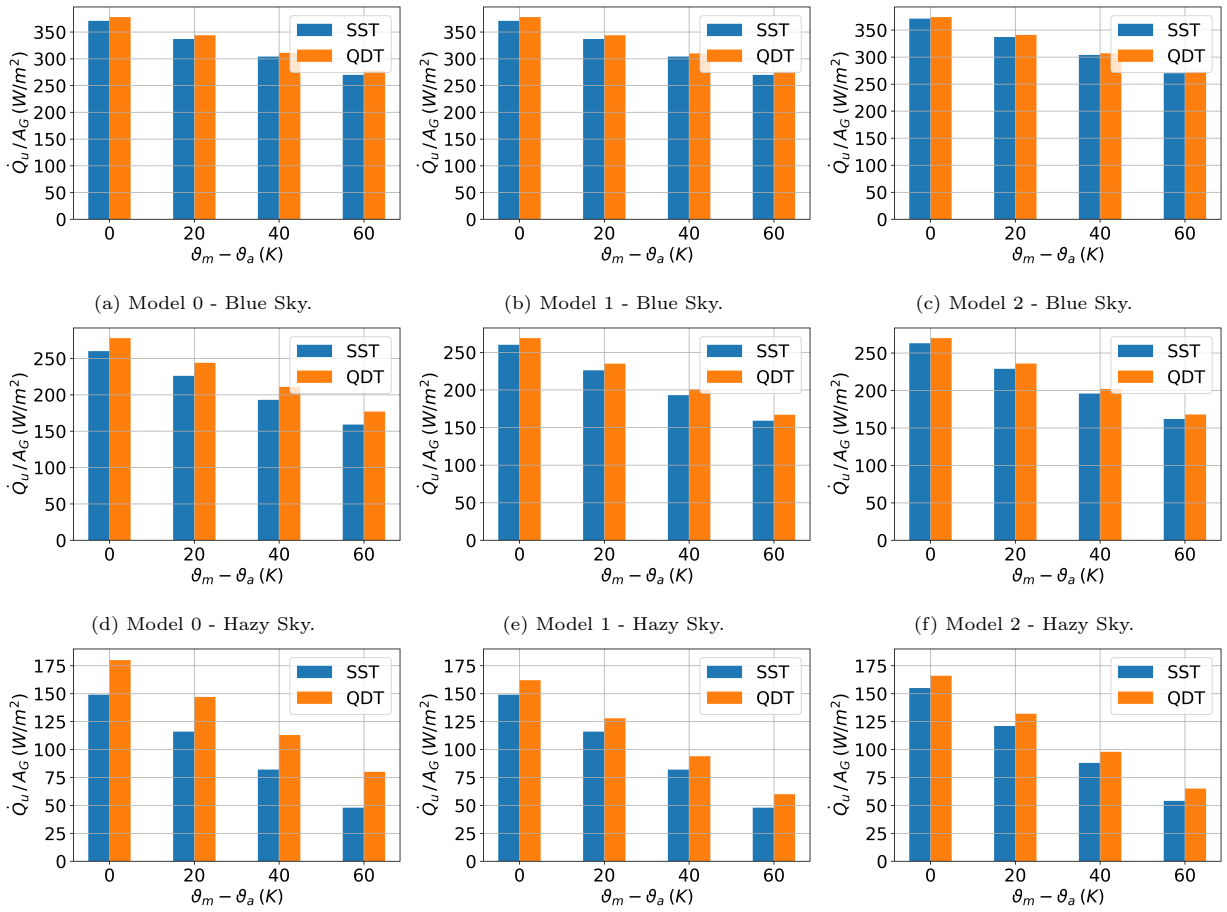

(a) Model 0 - Blue Sky. (b) Model 1 - Blue Sky. (c) Model 2 - Blue Sky.

(d) Model 0 - Hazy Sky. (e) Model 1 - Hazy Sky. (f) Model 2 - Hazy Sky.

(g) Model 0 - Gray Sky. (h) Model 1 - Gray Sky. (i) Model 2 - Gray Sky.

Figure 3: Useful power per gross area unit produced by ETC-HP collector under standard reporting conditions, for each test method and diffuse IAM model.

better than Model 1, the difference between these models is small, as shown in Figure 3. It should also be noted that the percentages above are averages and therefore indicative. They do not reflect the asymmetry of the differences in sky conditions and temperature differences (see Figures 2 and 3). In general, as mentioned above, the differences are much larger for hazy sky conditions and high temperature conditions.

In summary, Models 1 and 2 significantly improve the consistency between test methods compared to Model 0. However, the differences between Models 1 and 2 are small, so considering the additional cost of the additional albedo measurement, we consider Model 1 to be the ideal choice for testing the solar collector technology considered in this work. However, for other technologies, for example those that are particularly sensitive to diffuse solar irradiance [16], Model 2 may be the better choice for testing due to its superior performance, allowing for a better evaluation of design improvements and/or the use of alternative materials.

Furthermore, since the values of K_b obtained during the tests do not change when considering different

models of diffuse IAM (as demonstrated in the previous section), Models 1 and 2 can be used in a complementary way, as described below. Once the parameters have been determined with Model 1 in the context of the normalized tests, it would be possible to use Model 2 to carry out a long-term performance simulation, reconstructing the parameters of this model, i.e. calculating K_{ds} and k_{dg} from Eqs. (6) and (7) respectively, using the previously determined value of K_b with Model 1.

4.3. Enhanced parameter conversion from SST to QDT

In previous work [7], an enhanced parameter conversion procedure from SST to QDT was proposed, in which the procedure was applied to two ETC-HP collectors. It was shown that this procedure is better than that of the standard, since it produces converted IAM values closer to the QDT method. The above work covers Models 0 and 1, as the models are the same for the SST method. This subsection demonstrates the extension of this procedure for Model 2 and both collector types: FPC and ETC-HP.

The standard conversion procedure was described in Section 2. The extended procedure for Models 0 and 1, although detailed in [7], is briefly described below. First, we assume initial values for $\eta_{0,b}$ and K_d (which could be those of the standard conversion). Next, we compute K_b using Eq. (12) (instead of assuming $K_{hem} = K_b$), and then we recompute the parameters $\eta_{0,b}$ and K_d as in the standard case; Eqs. (4) and (5). The iterative process continues until the difference between the input and output parameters is less than a specified tolerance. For Model 2, the process is similar, but it uses Eq. (13) instead of Eq. (12), and Eqs. (6), (7) and (10) instead of Eqs. (4) and (5).

$$K_b = \frac{(\eta_{0,hem}/\eta_{0,b})\ K_{hem}\ G_t - K_d\ G_{dt}}{G_{bt}}. \tag{12}$$

$$K_b = \frac{(\eta_{0,hem}/\eta_{0,b})\ K_{hem} - K_{ds}\ G_{ds} - K_{dg}\ G_{dg}}{G_{bt}}. \tag{13}$$

The results of the standard and improved parameter conversion are shown in Table 4 for both collectors.

In the case of the FPC collector, although the enhanced procedure gives results closer to the QDT, the differences with the standard procedure are minimal. In the case of the ETC-HP collector, the results are much more significant: the improved procedure gives better IAM values (direct and diffuse), i.e. closer to those obtained by the QDT method.

In this context, the useful power values presented in the previous subsection were recalculated for the SST method using the diffuse IAM obtained through the enhanced procedure. For the FPC collector, no significant differences were observed. In contrast, for the ETC-HP collec, the average difference between SST and QDT estimates decreased by approximately 2 to 3 percentage points when considering all sky conditions, and by 5 to 10 percentage points under gray sky conditions. These results confirm that the enhanced procedure effectively reduces discrepancies between SST and QDT, particularly under hazy or overcast conditions.

Table 4: Comparison between standard and enhanced parameter conversion from SST to QDT for both collector and the different diffuse IAM models.

Collector	FPC				ETC-HP							
Model	Model 0 and 1		Model 2		Model 0 and 1				Model 2			
Conversion	Standard	Enhanced	Standard	Enhanced	Standard		Enhanced		Standard		Enhanced	
$\eta_{0,b}$	0.726	0.727	0.727	0.728	0.371		0.369		0.375		0.370	
K_d	0.905	0.896	N/A	N/A	1.007		1.039		N/A		N/A	
K_{ds}	N/A	N/A	0.933	0.925	N/A		N/A		1.055		1.095	
K_{dg}	N/A	N/A	0.744	0.717	N/A		N/A		0.671		0.702	
θ	K_b	K_b	K_b	K_b	K_{bL}	K_{bT}	K_{bL}	K_{bT}	K_{bL}	K_{bT}	K_{bL}	K_{bT}
0	1.00	1.00	1.00	1.00	1.00	1.00	1.00	1.00	1.00	1.00	1.00	1.00
10	1.00	1.00	1.00	1.00	0.99	1.01	1.00	1.01	0.99	1.01	1.00	1.01
20	1.00	1.00	1.00	1.00	0.99	1.07	1.00	1.08	0.99	1.07	1.00	1.08
30	1.00	1.00	1.00	1.00	1.00	1.15	1.00	1.18	1.00	1.15	1.00	1.18
40	1.00	1.00	1.00	1.00	0.97	1.29	0.97	1.34	0.97	1.29	0.97	1.34
50	0.97	0.97	0.97	0.96	0.77	1.40	0.78	1.48	0.77	1.40	0.78	1.48
60	0.90	0.88	0.90	0.87	0.58	1.44	0.58	1.54	0.58	1.44	0.58	1.54
70	0.72	0.68	0.72	0.67	0.39	1.18	0.39	1.27	0.39	1.18	0.39	1.27
80	0.36	0.34	0.36	0.34	0.19	0.59	0.19	0.64	0.19	0.59	0.19	0.63
90	0	0	0	0	0	0	0	0	0	0	0	0

As for the comparison between models, no significant differences were found between Models 1 and 2. This suggests that the enhanced procedure benefits both models similarly, and the conclusions drawn in the previous section regarding their performance remain valid.

5. Conclusions

In this work, two different diffuse IAM models for solar thermal collectors have been integrated into the standard test method of ISO 9806:2017; Model 1 and Model 2. The first model treats the diffuse in a global manner, and the second model distinguishes between the direction, that from the sky and that reflected from the ground, requiring an additional measurement for the latter component. The performance of these models has been evaluated and compared with the standard model, which serves as a baseline, using test data from two different solar collectors: a Flat Plate Collector (FPC) and an Evacuated Tube Collector with Heat Pipe (ETC-HP). The evaluation was performed using both ISO 9806:2017 test methods: steady-state (SST) and quasi-dynamic (QDT).

First, the parameter values of each collector and diffuse IAM model were identified. The results showed

that all the parameter values, except those related to the diffuse IAM, are very similar and independent of the diffuse IAM chosen. On the other hand, in the case of the parameters related to the diffuse IAM, Models 1 and 2 show a much better test method coherence, i.e. the parameter values obtained by the SST and QDT methods are closer.

However, the parameters of Models 1 and 2 cannot be directly compared due to the different way in which the diffuse solar radiation is treated. In this sense, for a better comparison of these models and using the previously determined parameter values, the useful power produced by the collectors was calculated and compared. For the temperature difference, four cases were considered: 0, 20, 40 and 60 K and for the sky conditions, the Standard Reporting Conditions (SRC) specified in the ISO 9806:2017 standard were used. Overall, no significant differences are found under clear sky conditions. However, under hazy and overcast conditions, differences between the test methods and the models become significant. Regarding temperature differences, the differences between test methods and models become more pronounced at higher values. These trends are particularly pronounced for ETC-HP. It is observed that Models 1 and 2 improve the consistency between test methods.

Nevertheless, the differences between Models 1 and 2 are small, so the loss of precision associated with the global modeling of diffuse irradiance does not compensate for the additional measurement for Model 2. Therefore, we consider Model 1 to be the best choice for evaluating the solar collector technology considered in this work. However, for technologies more sensitive to diffuse solar irradiance, Model 2 may be more suitable. Furthermore, as the K_b values obtained during testing remain unchanged across models, they can be used complementarily: first, Model 1 for standardized testing, and then Model 2 for long-term simulations, reconstructing its parameters from those obtained with Model 1.

Furthermore, the improved parameter conversion from SST to QDT proposed by Rodríguez-Muñoz et al. has been extended and evaluated in combination with the diffuse IAM models considered in this work. This procedure improves even more the consistency between the test methods, especially in the case of ETC-HP, providing IAM values (direct and diffuse) that are closer and reducing the differences in the estimated useful power for the collectors. In the case of FPC, although the enhanced procedure gave better results, the difference with the standard procedure was small.

It is important to mention that all tests were carried out with a low albedo soil, as specified by the standard. It is to be expected that the differences between Models 1 and 2 will be more considerable when working with higher albedo soils, e.g. in the framework of in-situ tests. The analysis of more complex terrains represents future work.

Acknowledgments

The authors extend their gratitude to the Ministerio de Industria, Energía y Minería (MIEM, Uruguay), particularly the Dirección Nacional de Energía (DNE), the Fideicomiso Uruguayo de Ahorro y Eficiencia Energética (Fudaee, Uruguay), and the Corporación Nacional para el Desarrollo (CND, Uruguay) for their financial and logistical support in developing the BECS facility and fostering this project with local expertise. Special thanks also go to the PTB of Germany for promoting and funding the interlaboratory test on solar collector efficiency, which provided valuable technical assurance of our local testing capabilities. The authors acknowledge financial support from the CSIC Research Group Program, Universidad de la República, Uruguay.

Appendix A. Data and software availability

To facilitate the application of the QDT method, a MATLAB program with a nonlinear regression algorithm is available for download: https://bit.ly/STCT-Program-V3. This program is designed for general use with low-temperature solar collectors that have covers, supporting both uniaxial and biaxial IAM. It builds on the previous versions of the software provided in [7, 30], making this the third version, which retains the options from the earlier versions. In this version, three models for diffuse IAM (Model 0, 1, and 2, as discussed in this study) are included.

The program calculates and reports the characteristic parameter values along with their uncertainties and t-statistics (the ratio of the parameter value to its uncertainty). For parameter a_2, users can set custom upper and lower limits, allowing it to be fixed at zero if the t-statistic is below 3 (both limits must be set to zero in this case). The software does not verify the quality of the experimental data set or ensure compliance with the ISO 9806:2017 standard, which must be checked beforehand. However, it provides graphs to evaluate data variability. The software also includes the two experimental data sets used in this study.

References

[1] G. Abal, D. Aicardi, R. Alonso-Suárez, A. Laguarda, Performance of empirical models for diffuse fraction in uruguay, Solar Energy 141 (2017) 166 – 181. doi:https://doi.org/10.1016/j.solener.2016.11.030.

[2] ISO-9806, Solar energy – solar thermal collectors – test methods, Standard, International Organization of Standarization, Switzerland (2017).

[3] ASHRAE-93, Methods of testing to determine the thermal performance of solar collectorss, Standard, American Society of Heating, Refrigerating and Air-Conditioning Engineers, USA (2014).

[4] D. Rojas, J. Beermann, S. Klein, D. Reindl, Thermal performance testing of flat-plate collectors, Solar Energy 82 (8) (2008) 746 – 757. doi:https://doi.org/10.1016/j.solener.2008.02.001.

[5] P. Horta, M. J. Carvalho, M. C. Pereira, W. Carbajal, Long-term performance calculations based on steady-state efficiency test results: Analysis of optical effects affecting beam, diffuse and reflected radiation, Solar Energy 82 (11) (2008) 1076–1082. doi:https://doi.org/10.1016/j.solener.2008.01.004.

[6] J. M. Rodríguez-Muñoz, I. Bove, R. Alonso-Suárez, Novel incident angle modifier model for quasi-dynamic testing of flat plate solar thermal collectors, Solar Energy 224 (2021) 112–124. doi:https://doi.org/10.1016/j.solener.2021.05.026.

[7] J. M. Rodríguez-Muñoz, I. Bove, R. Alonso-Suárez, Improving the experimental estimation of the incident angle modifier of evacuated tube solar collectors with heat pipes, Renewable Energy 235 (2024) 121240. doi:https://doi.org/10.1016/j.renene.2024.121240.

[8] P. Kovács, U. Pettersson, M. Persson, B. Perers, S. Fischer, Improving the accuracy in performance prediction for new collector designs, in: Proceedings of Solar World Congress, 2011.

[9] E. Zambolin, D. Del Col, An improved procedure for the experimental characterization of optical efficiency in evacuated tube solar collectors, Renewable Energy 43 (2012) 37 – 46. doi:https://doi.org/10.1016/j.renene.2011.11.011.

[10] T. Osório, M. J. Carvalho, Testing of solar thermal collectors under transient conditions, Solar Energy 104 (2014) 71 – 81, solar heating and cooling. doi:https://doi.org/10.1016/j.solener.2014.01.048.

[11] S. Fischer, W. Heidemann, H. Müller-Steinhagen, B. Perers, P. Bergquist, B. Hellström, Collector test method under quasi-dynamic conditions according to the european standard en 12975-2, Solar Energy 76 (1) (2004) 117 – 123. doi:https://doi.org/10.1016/j.solener.2003.07.021.

[12] M. Bosanac, A. Brunotte, W. Spirkl, R. Sizmann, The use of parameter identification for flat-plate collector testing under non-stationary conditions, Renewable Energy 4 (2) (1994) 217–222.

[13] M. J. Carvalho, P. Horta, J. F. Mendes, M. C. Pereira, W. M. Carbajal, Incidence angle modifiers: A general approach for energy calculations, in: D. Y. Goswami, Y. Zhao (Eds.), Proceedings of ISES World Congress 2007 (Vol. I – Vol. V), Springer Berlin Heidelberg, Berlin, Heidelberg, 2009, pp. 608–612.

[14] M. Brandemuehl, W. Beckman, Transmission of diffuse radiation through cpc and flat plate collector glazings, Solar Energy 24 (5) (1980) 511–513. doi:https://doi.org/10.1016/0038-092X(80)90320-5.

[15] J. Duffie, W. Beckman, Solar Engineering of Thermal Processes, 3rd Edition, Wiley and Sons, Inc., Hoboken, New Jersey, 2006.

[16] S. Hess, V. I. Hanby, Collector simulation model with dynamic incidence angle modifier for anisotropic diffuse irradiance, Energy Procedia 48 (2014) 87–96, proceedings of the 2nd International Conference on Solar Heating and Cooling for Buildings and Industry (SHC 2013). doi:https://doi.org/10.1016/j.egypro.2014.02.011.

[17] A. P. Brunger, F. C. Hooper, Anisotropic sky radiance model based on narrow field of view measurements of shortwave radiance, Solar Energy 51 (1) (1993) 53 – 64. doi:https://doi.org/10.1016/0038-092X(93)90042-M.

[18] J. M. Rodríguez-Muñoz, G. Vitale, I. Bove, G. Abal, Directional anisotropy of diffuse solar irradiance: impact assessment on the solar transmittance of common glazings, Building Simulation Conference Proceedings 18 (2023) 3832–3839.

[19] B. Perers, An improved dynamic solar collector test method for determination of non-linear optical and thermal characteristics with multiple regression, Solar Energy 59 (4) (1997) 163 – 178. doi:https://doi.org/10.1016/S0038-092X(97)00147-3.

[20] A. Hofer, D. Büchner, K. Kramer, S. Fahr, A. Heimsath, W. Platzer, S. Scholl, Comparison of two different (quasi-) dynamic testing methods for the performance evaluation of a linear fresnel process heat collector, Energy Procedia 69 (2015) 84–95, international Conference on Concentrating Solar Power and Chemical Energy Systems, SolarPACES 2014. doi:https://doi.org/10.1016/j.egypro.2015.03.011.

[21] S. Fahr, U. Gumbel, A. Zirkel-Hofer, K. Kramer, In situ characterization of thermal collectors in field installations, in: Proceedings of EuroSun, 2018. doi:0.18086/eurosun2018.12.01.

[22] A. Zirkel-Hofer, S. Perry, K. Kramer, A. Heimsath, S. Scholl, W. Platzer, Confidence interval computation method for

dynamic performance evaluations of solar thermal collectors, Solar Energy 162 (2018) 585–596. doi:https://doi.org/10.1016/j.solener.2018.01.041.
URL https://www.sciencedirect.com/science/article/pii/S0038092X18300628

[23] J. C. Rodrigues, J. Facão, M. J. Carvalho, Parameter identification and uncertainty evaluation in quasi-dynamic test of solar thermal collectors with monte carlo method, Renewable Energy 236 (2024) 121403. doi:https://doi.org/10.1016/j.renene.2024.121403.
URL https://www.sciencedirect.com/science/article/pii/S096014812401471X

[24] S. Fischer, Quality infrastructure for energy efficiency and renewable energy in latin america and the caribbean, report # 95309, Report, Intituto Metrológico Aleman - PTB (2020).

[25] ISO-9060, Solar energy — specification and classification of instruments for measuring hemispherical solar and direct solar radiation, Standard, International Organization of Standarization, Switzerland (2018).

[26] ISO-9847, Solar energy – calibration of field pyranometers by comparison to a reference pyranometer, Standard, International Organization of Standarization, Switzerland (1992).

[27] J. M. Rodríguez-Muñoz, A. Monetta, R. Alonso-Suárez, I. Bove, G. Abal, Correction methods for shadow-band diffuse irradiance measurements: assessing the impact of local adaptation, Renewable Energy 178 (2021) 830–844. doi:https://doi.org/10.1016/j.renene.2021.06.102.

[28] A. J. Drummond, On the measurement of sky radiation, Archiv für Meteorologie, Geophysik und Bioklimatologie, Serie B 7 (1956) 413 – 436. doi:https://doi.org/10.1007/BF02242969.

[29] J. M. Rodríguez-Muñoz, R. Alonso-Suárez, I. Bove, G. Abal, Evaluación de seis modelos empíricos para estimar albedo del suelo en la pampa húmeda, Avances en Energías Renovables y Medio Ambiente-AVERMA 26 (2022) 357–368.

[30] J. M. Rodríguez-Muñoz, I. Bove, R. Alonso-Suárez, P. Galione, On the choice of the parameter identification procedure in quasi-dynamic testing of low-temperature solar collectors, Renewable Energy 247 (2025) 122931. doi:https://doi.org/10.1016/j.renene.2025.122931.

References

Almeida, P., Carvalho, M., Amorim, R., Mendes, J., and Lopes, V. (2014). Dynamic testing of systems – use of trnsys as an approach for parameter identification [Solar heating and cooling]. *Solar Energy*, *104*, 60–70. https://doi.org/https://doi.org/10.1016/j.solener.2014.02.010

Amer, E., Nayak, J. K., and Sharma, G. K. (1998a). Transient method for testing flat-plate solar collectors. *Energy Conversion and Management*, *39*, 549–558. https://api.semanticscholar.org/CorpusID:98387773

Amer, E., Jadeja, P., Nayak, J., and Sharma, G. (1998b). Comparison of two dynamic test methods for solar flat-plate collectors. *Energy Conversion and Management*, *39*(3), 285–293. https://doi.org/https://doi.org/10.1016/S0196-8904(96)00199-9

Arnell, N. W., Lowe, J. A., Challinor, A. J., and Osborn, T. J. (2019). Global and regional impacts of climate change at different levels of global temperature increase. *Climatic Change*, *155*, 377–391.

Batlles, F., Olmo, F., and Alados-Arboledas, L. (1995). On shadowband correction methods for diffuse irradiance measurements. *Solar Energy*, *54*(2), 105–114. https://doi.org/https://doi.org/10.1016/0038-092X(94)00115-T

Bosanac, M., Brunotte, A., Spirkl, W., and Sizmann, R. (1994). The use of parameter identification for flat-plate collector testing under non-stationary conditions. *Renewable Energy*, *4*(2), 217–222. https://doi.org/https://doi.org/10.1016/0960-1481(94)90006-X

Carvalho, M. J., Horta, P., Mendes, J. F., Pereira, M. C., and Carbajal, W. M. (2009). Incidence angle modifiers: A general approach for energy calculations. In D. Y. Goswami and Y. Zhao (Eds.), *Proceedings of ises world congress 2007 (vol. i – vol. v)* (pp. 608–612). Springer Berlin Heidelberg.

Chen, X., Wang, Y., and Yang, X. (2023). New biaxial approach to evaluate the optical performance of evacuated tube solar thermal collector. *Energy*, *271*, 126990. https://doi.org/https://doi.org/10.1016/j.energy.2023.126990

Duffie, J., and Beckman, W. (2006). *Solar engineering of thermal processes* (Third). Wiley; Sons, Inc.

Emery, M., and Rogers, B. (1984). On a solar collector thermal performance test method for use in variable conditions. *Solar Energy*, *33*(2), 117–123. https://doi.org/https://doi.org/10.1016/0038-092X(84)90228-7

Fahr, S., Gumbel, U., Zirkel-Hofer, A., and Kramer, K. (2018). In situ characterization of thermal collectors in field installations. *Proceedings of EuroSun*, 1231–1240.

Fahr, S., Tschopp, D., Nielsen, J. E., Kramer, K., and Ohnewein, P. (2019). Review of in situ test methods for solar thermal installations. *Proceedings ISES Solar World Congress, 2019*.

Fischer, S., Heidemann, W., Müller-Steinhagen, H., Perers, B., Bergquist, P., and Hellström, B. (2004). Collector test method under quasi-dynamic conditions according to the european standard en 12975-2. *Solar Energy*, *76*(1), 117–123. https://doi.org/https://doi.org/10.1016/j.solener.2003.07.021

Fischer, S. (2020). *Quality infrastructure for energy efficiency and renewable energy in latin america and the caribbean, report # 95309* (Report). Intituto Metrológico Aleman - PTB.

Fischer, S., Lüpfert, E., and Müller-Steinhagen, H. (2006). Efficiency testing of parabolic trough collectors using the quasi-dynamic test procedure according to the european standard en 12975. *SolarPACES 13th symposium on concentrating solar power and chemical energy technologies*.

Hertel, J. D., Martinez-Moll, V., and Pujol-Nadal, R. (2015). Estimation of the influence of different incidence angle modifier models on the biaxial factorization approach. *Energy Conversion and Management*, *106*, 249–259. https://doi.org/https://doi.org/10.1016/j.enconman.2015.08.082

Hill, J. E., and Streed, E. R. (1976). A method of testing for rating solar collectors based on thermal performance. *Solar Energy*, *18*(5), 421–429. https://doi.org/https://doi.org/10.1016/0038-092X(76)90008-6

Hofer, A., Büchner, D., Kramer, K., Fahr, S., Heimsath, A., Platzer, W., and Scholl, S. (2015). Comparison of two different (quasi-) dynamic testing

methods for the performance evaluation of a linear fresnel process heat collector [International Conference on Concentrating Solar Power and Chemical Energy Systems, SolarPACES 2014]. *Energy Procedia*, *69*, 84–95. https://doi.org/https://doi.org/10.1016/j.egypro.2015.03.011

Hottel, H., and Whillier, A. (1955). Evaluation of flat-plate solar collector performance. *Trans. Conf. Use of Solar Energy; () 3 (Thermal Processes) Part 2*. https://www.osti.gov/biblio/5057828

Hottel, H., and Woertz, B. (1942). Performance of flat-plate solar-heat collectors. *Trans. ASME (Am. Soc. Mech. Eng.); (United States)*, *64*. https://www.osti.gov/biblio/5052689

IEA. (2024). World energy outlook 2024 – analysis.

IEA-SCH. (2024). Solar heat worldwide 2024.

IEA. (2022). The future of heat pumps.

IEA-SHC. (1979). Results and analyses of iea round robin testing.

ISO-9459-5. (2007). *Solar heating – domestic water heating systems – part 5: System performance characterization by means of whole-system tests and computer simulation* (tech. rep.) (Standard, ISO).

ISO-9806. (2017). *Solar energy – solar thermal collectors – test methods* (Standard). International Organization of Standarization. Switzerland.

Janotte, N., Meiser, S., Krüger, D., Lüpfert, E., Pitz-Paal, R., Fischer, S., and Müller-Steinhagen, H. (2009). Quasi-dynamic analysis of thermal performance of parabolic trough collectors. *SolarPACES 2009 Conference Proceedings*.

Kong, W., Perers, B., Fan, J., Furbo, S., and Bava, F. (2015). A new laplace transformation method for dynamic testing of solar collectors. *Renewable Energy*, *75*, 448–458. https://doi.org/https://doi.org/10.1016/j.renene.2014.10.026

Kong, W., Wang, Z., Fan, J., Perers, B., Chen, Z., Furbo, S., and Andersen, E. (2012). Investigation of thermal performance of flat plate and evacuated tubular solar collectors according to a new dynamic test method [1st International Conference on Solar Heating and Coolingfor Buildings and Industry (SHC 2012)]. *Energy Procedia*, *30*, 152–161. https://doi.org/https://doi.org/10.1016/j.egypro.2012.11.019

Kovács, P., Pettersson, U., Persson, M., Perers, B., and Fischer, S. (2011). Improving the accurancy in performance prediction for new collector desings. *Proceedings of Solar World Congress*.

Kratzenberg, M., Beyer, H., and Colle, S. (2006). Uncertainty calculation applied to different regression methods in the quasi-dynamic collector test. *Solar Energy*, *80*(11), 1453–1462. https://doi.org/https://doi.org/10.1016/j.solener.2006.03.010

McIntire, W. R. (1982). Factored approximations for biaxial incident angle modifiers. *Solar Energy*, *29*(4), 315–322. https://doi.org/https://doi.org/10.1016/0038-092X(82)90246-8

MIEM-DNE. (2008). Política energética 2005-2030.

Muschaweck, J., and Spirkl, W. (1993). Dynamic solar collector performance testing. *Solar Energy Materials and Solar Cells*, *30*(2), 95–105. https://doi.org/https://doi.org/10.1016/0927-0248(93)90011-Q

Osório, T., and Carvalho, M. J. (2014). Testing of solar thermal collectors under transient conditions [Solar heating and cooling]. *Solar Energy*, *104*, 71–81. https://doi.org/https://doi.org/10.1016/j.solener.2014.01.048

Perers, B. (1993). Dynamic method for solar collector array testing and evaluation with standard database and simulation programs. *Solar Energy*, *50*(6), 517–526. https://doi.org/https://doi.org/10.1016/0038-092X(93)90114-4

Perers, B. (1997). An improved dynamic solar collector test method for determination of non-linear optical and thermal characteristics with multiple regression [Selected Proceeding of ISES 1995: Solar World Congress. Part IV]. *Solar Energy*, *59*(4), 163–178. https://doi.org/https://doi.org/10.1016/S0038-092X(97)00147-3

Prapas, D., Norton, B., Milonidis, E., and Probert, S. (1988). Response function for solar-energy collectors. *Solar Energy*, *40*(4), 371–383. https://doi.org/https://doi.org/10.1016/0038-092X(88)90010-2

QAiST. (2012). *Performance testing of evacuated tubular collectors* (Report). Quality Assurance in Solar heating and cooling Technology. http://www.estif.org/solarkeymarknew/images/downloads/QAiST/qaist%20d2.1%20r2.1%20performance%20testing%20of%20evacuated%20tubular%20collectors.pdf

Ritchie, H., Rosado, P., and Roser, M. (2020). Breakdown of carbon dioxide, methane and nitrous oxide emissions by sector [https://ourworldindata.org/emissions-by-sector]. *Our World in Data*.

Rodrigues, J. C., Facão, J., and Carvalho, M. J. (2024). Parameter identification and uncertainty evaluation in quasi-dynamic test of solar thermal collectors with monte carlo method. *Renewable Energy*, *236*, 121403. https://doi.org/https://doi.org/10.1016/j.renene.2024.121403

Rodríguez-Muñoz, J. M. (2021). *Ensayos de desempeño térmico de colectores solares de placa plana* (Thesis). Universidad de la República (Uruguay). Facultad de Ingeniería. https://doi.org/10.13140/RG.2.2.23050.18881

Rodríguez-Muñoz, J. M., Bove, I., and Alonso-Suárez., R. (2021a). A detailed dynamic parameter identification procedure for quasi-dynamic testing of solar thermal collectors. *Proceedings of Solar World Congress*. https://doi.org/doi:10.18086/swc.2021.25.01

Rodríguez-Muñoz, J. M., Bove, I., and Alonso-Suárez, R. (2021b). Novel incident angle modifier model for quasi-dynamic testing of flat plate solar thermal collectors. *Solar Energy*, *224*, 112–124. https://doi.org/https://doi.org/10.1016/j.solener.2021.05.026

Rodríguez-Muñoz, J. M., Bove, I., and Alonso-Suárez, R. (2024). Improving the experimental estimation of the incident angle modifier of evacuated tube solar collectors with heat pipes. *Renewable Energy*, *235*, 121240. https://doi.org/https://doi.org/10.1016/j.renene.2024.121240

Rodríguez-Muñoz, J. M., Bove, I., and Alonso-Suárez, R. (2026). Experimental characterization of the diffuse incident angle modifier of solar thermal collectors: Improving consistency between test methods. *Renewable Energy*, *256*, 123912. https://doi.org/https://doi.org/10.1016/j.renene.2025.123912

Rodríguez-Muñoz, J. M., Bove, I., Alonso-Suárez, R., and Galione, P. A. (2025). On the choice of the parameter identification procedure in quasi-dynamic testing of low-temperature solar collectors. *Renewable Energy*, *247*, 122931. https://doi.org/https://doi.org/10.1016/j.renene.2025.122931

Rodríguez-Muñoz, J. M., Monetta, A., Alonso-Suárez, R., Bove, I., and Abal, G. (2021c). Correction methods for shadow-band diffuse irradiance measurements: Assessing the impact of local adaptation. *Renewable Energy*, *178*, 830–844. https://doi.org/https://doi.org/10.1016/j.renene.2021.06.102

Rodríguez-Muñoz, J. M., Monetta, A., Bove, I., and Alonso-Suárez, R. (2020). Ensayo cuasi-dinámico de colectores solares de placa plana en uruguay

de acuerdo a la norma iso 9806:2017. *ENERLAC. Revista de energía de Latinoamérica y el Caribe*, *4*(2), 10–26.

Rodríguez-Muñoz, J. M., Alonso-Suárez, R., Bove, I., and Abal, G. (2023). Evaluación de seis modelos empíricos para estimar albedo del suelo en la pampa húmeda. *Avances en Energías Renovables y Medio Ambiente - AVERMA*, *26*, 357–368. https://portalderevistas.unsa.edu.ar/index.php/averma/article/view/3850

Rogers, B. (1981). A method of collector testing under transient conditions. *Proceedings ISES Solar World Forum, August, Brighton, UK*, *1*, 898–902.

Rojas, D., Beermann, J., Klein, S., and Reindl, D. (2008). Thermal performance testing of flat-plate collectors. *Solar Energy*, *82*(8), 746–757. https://doi.org/https://doi.org/10.1016/j.solener.2008.02.001

Rönnelid, M., Perers, B., and Karlsson, B. (1997). On the factorisation of incidence angle modifiers for cpc collectors [Selected Proceeding of ISES 1995: Solar World Congress. Part IV]. *Solar Energy*, *59*(4), 281–286. https://doi.org/https://doi.org/10.1016/S0038-092X(97)00016-9

Sallaberry, F., García de Jalón, A., Olano, X., Mateu, E., Erice, R., and Ramirez, L. (2011). Bi-axial incidence angle modifier using quasi-dynamic test for asymmetrical solar collector using dummy variables. *ESTEC congress, Marseille (France)*.

Souka, A., and Safwat, H. (1966). Determination of the optimum orientations for the double-exposure, flat-plate collector and its reflectors. *Solar Energy*, *10*(4), 170–174. https://doi.org/https://doi.org/10.1016/0038-092X(66)90004-1

Streed, E. R., Hill, J. E., Thomas, W. C., Dawson, A. G., and Wood, B. D. (1979). Results and analysis of a round robin test program for liquid-heating flat-plate solar collectors. *Solar Energy*, *22*(3), 235–249. https://doi.org/https://doi.org/10.1016/0038-092X(79)90139-7

Tschopp, D., Ohnewein, P., Hausner, R., and Rohringer, C. (2017). In-situ testing of large collector arrays–challenges and methodological framework. *Proceedings of SWC2017/SHC2017, International Solar Energy Society*, 1–10.

Wang, X. A., Xu, Y. F., and Meng, X. (1987). A filter method for transient testing of collector performance. *Solar Energy*, *38*, 125–134. https://api.semanticscholar.org/CorpusID:110863189

Whillier, A. (1953). *Solar energy collection and its utilization for house heating* [Doctoral dissertation, Massachusetts Institute of Technology].

Xu, L. (2009). Research on dynamic test method for thermal performance of solar collectors. *Northeast University, Master'Thesis*.

Xu, L., Wang, Z., Li, X., Yuan, G., Sun, F., and Lei, D. (2013). Dynamic test model for the transient thermal performance of parabolic trough solar collectors. *Solar Energy*, *95*, 65–78. https://doi.org/https://doi.org/10.1016/j.solener.2013.05.017

Zambolin, E., and Del Col, D. (2010). Experimental analysis of thermal performance of flat plate and evacuated tube solar collectors in stationary standard and daily conditions. *Solar Energy*, *84*(8), 1382–1396. https://doi.org/https://doi.org/10.1016/j.solener.2010.04.020

Zambolin, E., and Del Col, D. (2012). An improved procedure for the experimental characterization of optical efficiency in evacuated tube solar collectors. *Renewable Energy*, *43*, 37–46. https://doi.org/https://doi.org/10.1016/j.renene.2011.11.011

Zirkel-Hofer, A., Perry, S., Kramer, K., Heimsath, A., Scholl, S., and Platzer, W. (2018). Confidence interval computation method for dynamic performance evaluations of solar thermal collectors. *Solar Energy*, *162*, 585–596. https://doi.org/https://doi.org/10.1016/j.solener.2018.01.041

APPENDICES

Appendix A

Complementary papers

A.1. Paper 5: Correction methods for shadow-band diffuse irradiance measurements: assessing the impact of local adaptation.

Correction methods for shadow-band diffuse irradiance measurements: assessing the impact of local adaptation

J. M. Rodríguez-Muñoz*, A. Monetta, R. Alonso-Suárez, I. Bove, G. Abal

Laboratorio de Energía Solar, Universidad de la República,
Av. L. Batlle Berres km 508, Salto, Uruguay

Abstract

Shadow-bands are a low cost alternative when a precision solar tracker is not available. Adequate precision may be achieved if the measured diffuse irradiance is corrected to account for the sky portion blocked by the shadow-band. The isotropic sky assumption leads to a systematic under estimation of diffuse irradiance. Several correction methods have been proposed to take into account the anisotropic effects. However, their performance at a given site depends on the dominant local climate. In this work, it is shown that the local adaptation of shadow band correction methods results in a significant improvement in the diffuse irradiance measurement's accuracy. Nine well-known correction methods are implemented and tested (both in their original and locally adapted versions) for the Pampa Húmeda region of southeastern South America. In absence of local adaptation, only one of the pre-existing methods improves the simple isotropic model. All locally adapted versions perform similarly well and outperform significantly the original methods. A new model based on the parametrization of Battle's model is proposed. It provides the best performance compared to all locally adapted pre-existing models, under all-sky and discriminated sky conditions.

Keywords: diffuse irradiance, shadow-band measurement, corrections models, sky anisotropy.

1. Introduction

Diffuse radiation represents a significant part of the Sun's radiation that reaches ground level. In mid-latitude temperate climates about 1/3 of the annual global horizontal irradiation is diffuse (Abal et al., 2017). This part of global irradiance has an important role in modeling the solar energy yield of various solar technologies. It is required in transposition models to estimate the global irradiance on inclined surfaces, the relevant solar input for solar photovoltaic and several thermal applications. Furthermore, knowledge of the global and diffuse irradiances incident on a surface can be used to estimate the Direct Normal Irradiance (DNI), relevant for concentrated solar systems, via the closure relation (Eq. (1)), when measurements of this

*Corresp. author: J. M. Rodríguez-Muñoz, jrodrigue@fing.edu.uy

List of Symbols

δ	Solar declination angle.
ϵ	Sky clearness index (Perez et al., 1990).
ω	Solar hour angle.
ω_s	Sunset solar hour angle.
ϕ	Local latitude angle.
τ_b	Beam transmittance, G_b/G_0.
θ	Zenith or polar angle of sky element.
θ_0	Angle subtended by the shadow-band.
θ_z	Solar zenith angle.
φ	Azimuth angle of sky element.
φ_s	Solar azimuth angle.
b_i	Anisotropy parameters of the Muneer & Zhang model, for $i = 1, 2$.
$d\Omega$	Solid angle for a sky element, $\sin\theta\, d\theta\, d\varphi$.
f	Correction factor for diffuse horizontal irradiance, such that $G_{dc} = f\, G_{du}$.
f_d	Diffuse fraction, G_d/G_h.
G_0	Extraterrestrial solar irradiance (modulated by the orbital factor).
G_b	Direct normal irradiance, Wm^{-2}.
G_d	Diffuse horizontal irradiance, Wm^{-2}.
G_h	Global horizontal irradiance, Wm^{-2}.
G_{0h}	Extraterrestrial horizontal irradiance, $G_0 \cos\theta_z$.
G_{dc}	Corrected diffuse horizontal irradiance, Wm^{-2}.
G_{di}	Diffuse horizontal irradiance intercepted by a shadow-band, Wm^{-2}.
G_{du}	Uncorrected diffuse horizontal irradiance, as measured by a shaded pyranometer, Wm^{-2}.
k_d	Diffuse clearness index, G_d/G_{0h}.
k_t	Clearness index, G_h/G_{0h}.
L_p	Sky angular radiance, $\mathrm{Wm}^{-2}/\mathrm{str}$.
N	Sunshine duration (fractional hours).
N_0	Maximum sunshine duration for a given site and day (fractional hours).
n_r	Relative sunshine duration, N/N_0.
r	Shadow-band radius, m.
S	Fraction of diffuse horizontal irradiance intercepted by a shadow-band, G_{di}/G_d.
w	Shadow-band width, m.

component are not available. For a horizontal surface, it can be stated that

$$G_h = G_b \cos\theta_z + G_d, \tag{1}$$

where θ_z is the solar zenith angle (see the list of symbols for the other definitions). The DNI estimated from this expression can have high uncertainties, specially at low Sun elevations. If no diffuse irradiance measurements are available at a given site, a separation model can be used to estimate the diffuse fraction from normalized global irradiance and other variables (Ridley et al., 2010; Ruiz-Arias et al., 2010; Gueymard & Ruiz-Arias, 2016), at the expense of adding considerable uncertainty even if the separation models are locally adjusted to high-quality data (Abal et al., 2017).

To measure diffuse radiation, beam irradiance must be blocked from the sensor by a shadowing device. This can be done in several forms: a shadow-sphere mounted on a precision solar tracker, a manually adjusted shadow-band, an automatically driven rotating shadow-band (RSR systems) or by a specifically designed fixed shadow-mask with no moving parts (Badosa et al., 2014), among other alternatives. These methods have different accuracy, cost and maintenance requirements (Vignola et al., 2019). The shadow-sphere is the

low uncertainty option when a precision solar tracker is available. A shadow-band is a low-cost alternative which can be potentially accurate if appropriate correction factors are used and it is a frequent choice due to its good balance between cost, maintenance and accuracy.

During a diffuse irradiance measurement, the shadow-band blocks the direct beam from the pyranometer but also shades incoming diffuse irradiance from part of the sky dome. A correction factor, $f = G_d/G_{du}$, must be applied to the uncorrected measurement, $G_{du} = G_d - G_{di}$, in order to account for the blocked diffuse irradiance. The irradiance intercepted by the band, G_{di}, depends on the shadow-band geometry and the diffuse radiance distribution in the sky, which is affected by the cloud's distribution. The correction factor is usually expressed as

$$f = \frac{1}{1-S}, \tag{2}$$

in terms of the fraction of blocked diffuse irradiance, $S = G_{di}/G_d$. The simplest expression for S is obtained by assuming an isotropic distribution of the diffuse radiance in the sky. This calculation was originally done by Drummond (1956) and it results in a correction factor that depends on the geometry of the shadow-band, the solar declination angle and the latitude of the observer. However, the isotropic assumption is known to be inaccurate: Drummond realized that due to anisotropy effects in the sky this correction factor would underestimate the diffuse irradiance and suggested to increment its monthly mean value by 3 to 7% of the measurements average, depending on the predominant cloudiness conditions. Higher underestimations have been reported, for instance, Stanhill (1985) found underestimations between 11 and 27% by working with hourly data from the region of the Dead Sea. Under clear-sky conditions, most anisotropy in the sky radiance distribution comes from the bright circumsolar region. In the presence of clouds, multiple reflection and scattering can produce more complex anisotropy effects which should be taken into account in order to obtain accurate correction factors.

Several sophisticated models that attempt to improve on the isotropic assumption have been proposed. Two broad approaches can be distinguished: (i) proposals based on analytical sky radiance distributions, from which the blocked incident diffuse irradiance can be numerically integrated (Ineichen et al., 1984; Rawlins & Readings, 1986; Siren, 1987; Vartiainen, 1999; Muneer & Zhang, 2001) and (ii) proposals based on empirical methods attempting to model directly a correction factor (Painter, 1981; Kasten et al., 1983; Steven, 1984; LeBaron et al., 1990; Kudish & Ianetz, 1993; Batlles et al., 1995). Several authors have evaluated the accuracy of different correction methods working with data from different climates (Rawlins & Readings, 1986; Batlles et al., 1995; López et al., 2004; Kudish & Evseev, 2008; Sánchez et al., 2012). However, there is no broad consensus as to which is the best correction method and this is to be expected, since the local climate is known to be important in the related diffuse-direct separation problem and there is no universal separation model (Gueymard & Ruiz-Arias, 2016).

The main objectives of this work are to implement and evaluate nine pre-existing diffuse irradiance

correction models and to propose an enhanced correction model, that is optimized for the Pampa Húmeda region. This is a broad area of low homogeneous grasslands in southern South America, including the southern part of Brazil, the eastern part of Argentina and the territory of Uruguay. The climate is temperate, classified as Cfa in the updated Köpen-Geiger scheme (Peel et al., 2007). The models are evaluated both in their original (generic) versions and in locally-adjusted or site-adapted forms working with 5-minute time intervals, in order to include some transient effects. Different types of models are considered, including the isotropic correction, sky radiance based models and phenomenological models. Without local data and studies it is difficult to establish general recommendations for a given site, either for original or locally-adapted models, being this an issue that has not been covered previously in the literature for these kinds of correction models. The evaluation of the generic form of the models is done to identify the best generic method and to quantify the impact of local adaptation in our region's climate. Full information is provided to enable the use of locally adjusted or adapted models in the Pampa Húmeda or in similar temperate climate regions. A new optimized model, which outperforms the pre-existing locally adapted models in this region, is presented. The model is an enhancement of the pre-existing Batlles et al. method, replacing the former sky clearness index for a modified version which takes into account the solar altitude, and achieving a lower bias and dispersion by considering in its formulation an additional independent term and the bins of the Perez et al. (1993) model. In fact, the new proposal achieves lower bias and dispersion, not only under all-sky conditions, but also when discriminated for clear sky, partly cloudy and overcast skies. The comparison shows that the performance of some phenomenological models critically depends on the local adaptation and some sophisticated sky radiance models do not provide a significant performance improvement over the simple isotropic model. Finally, as a contribution on the theoretical side, it is shown that Kasten's equation, used to transfer correction factors between different shadow-band geometries (originally derived for a isotropic sky), is valid for any sky radiance distribution, provided the shadow-band satisfies certain requirements.

This article is organized as follows. In Section 2 the details of the selected correction models are described, including the novel proposal of this work. In Section 3 the data being used is discussed along with the quality filters applied. Section 4 describes the implementation and local adaptation of the models and Section 5 discusses their performance. Finally, in Section 6 the main conclusions are summarized.

2. Shadow-band correction models

Most shadow-band correction models either parametrize the correction factor f or estimate the fraction of diffuse irradiance intercepted by the band, S, to obtain f from Eq. (2). Since $S < 1$ the correction factor will satisfy $f > 1$. This excludes the possibility that the shadow-band increases the diffuse irradiance on the target pyranometer due to reflexion of circumsolar radiation on the internal band surface. Commercial

shadow-bands are usually coated with low-reflectivity black paint to minimize this effect. In this article, we assume that this effect can be neglected and $f \geq 1$.

2.1. General considerations on shadow-band correction factors

2.1.1. Geometrical aspects

The sky angular radiance, $L_p(\theta, \varphi)$, describes the flux of radiant energy per unit solid angle incoming from each sky direction (θ, φ) excluding the direct beam. So that the diffuse irradiance reaching an exposed horizontal sensor is

$$G_d = \int_{-\pi}^{\pi} \int_{0}^{\pi/2} L_p(\theta, \varphi)\, \cos\theta \, d\Omega, \tag{3}$$

with $d\Omega = \sin\theta \, d\theta \, d\varphi$. If the sky radiance is isotropically distributed its value is $L_p^{iso} = G_d/\pi$. An expression for the diffuse irradiance intercepted by the band can be obtained by restricting the integration above to the portion of sky blocked by the shadow-band,

$$G_{di} = \iint_{band} L_p(\theta, \varphi)\, \cos\theta \, d\Omega, \tag{4}$$

where the geometry of the shadow-band defines the integration limits. If the ratio between the band width and its radius is small, $b/r \lesssim 0.2$, the surface integral in Eq. (4) can be approximated by a line-integral along the solar path, using the solar hour angle (ω) as the single variable (Steven & Unsworth, 1980):

$$G_{di} = \theta_0 \cos\delta \int_{-\omega_s}^{\omega_s} L_p(\theta_z, \varphi_s)\, \cos\theta_z \, d\omega, \tag{5}$$

where θ_0 is the angle (radians) subtended by the shadow-band as seen by the pyranometer, φ_s is the solar azimuth and δ is the solar declination. Both solar angles, θ_z and φ_s, depend on the solar declination, the site's latitude (ϕ) and w by the usual expressions describing the solar apparent motion (Iqbal, 1983). The integration limits are defined by the extreme values of the hour angle, which for a horizontal surface are $\omega_s = \pm \arccos(-\tan\phi \, \tan\delta)$. In Eq. (5), the geometry of the shadow-band is expressed by θ_0 and is separated from the influence of the sky condition (the line integral). For a flat shadow-band of negligible thickness,

$$\theta_0 = \frac{b}{r} \cos^2\delta. \tag{6}$$

In order to reduce the seasonal dependence of the correction factor, some commercial shadow-bands use a 'U'-shaped profile. For these bands, $\theta_0 \simeq b/r$ (de Simón-Martín et al., 2016) with an error of less than 2% and an impact of less than 0.5% in the correction factor (Kipp & Zonen , 2004).

2.1.2. Drummond's isotropic model (DR)

As mentioned in the introduction, Drummond used the isotropic assumption to evaluate Eq. (5) analytically (Drummond, 1956; Kipp & Zonen , 2004) and obtained

$$S_0 = \frac{2\theta_0}{\pi} \cos\delta \, I_1, \tag{7}$$

where

$$I_1 = \frac{1}{2}\int_{-\omega_s}^{\omega_s} \cos\theta_z \, d\omega = \cos\phi\cos\delta\sin\omega_s + \omega_s \sin\phi\sin\delta, \tag{8}$$

with θ_0 and ω_s expressed in radians (the notation I_1 follows the work of Muneer & Zhang (2001), Subsection 2.2.1). The isotropic correction factor from Eq. (2) is

$$f_0 = \frac{1}{1-S_0} = \left(1 - \frac{2\theta_0}{\pi}\cos\delta\, I_1\right)^{-1} \tag{9}$$

and it depends on the local latitude, day of year and the geometry of the shadow-band, through θ_0. The dependence of f_0 with the day of year for a given latitude and two shadow-band profiles is shown in Fig. 1. Since this expression does not account for anisotropic effects, such as circumsolar radiation, its utilization leads to a systematic underestimation of the diffuse irradiance, except under complete cloud cover when the isotropic approximation is closely satisfied.

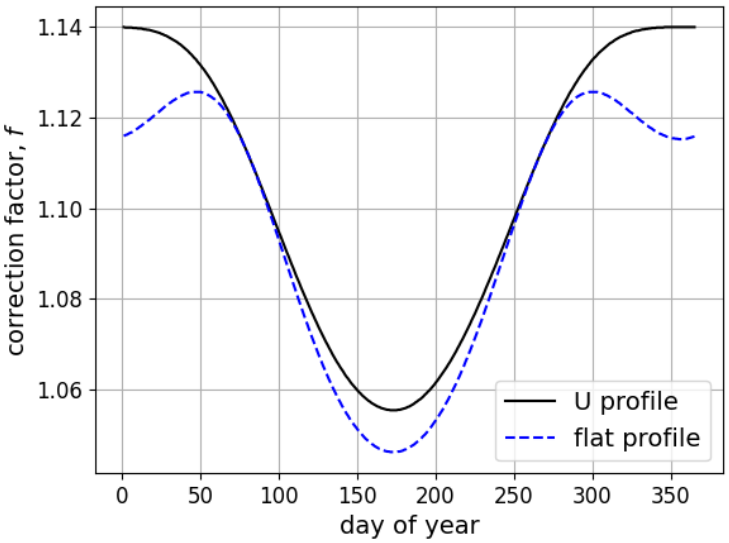

Figure 1: Isotropic correction factor, Eq. (9), for each ordinal day. Latitude is $\phi = -31.28°$ and $b/r = 0.185$.

2.1.3. Transfer of the correction factor to other shadow-bands

The fraction of intercepted diffuse irradiance, Eq. (5), can be written as

$$S = \frac{G_{di}}{G_d} = \theta_0\ \Gamma, \tag{10}$$

where only θ_0 depends on the shadow-band geometry (assumed to satisfy $\theta_0 \lesssim 0.2$) and Γ depends on sky condition and on the Sun's apparent position. It follows that two bands with different geometries, θ_1 and θ_2, will intercept fractions that satisfy $S_1/S_2 = \theta_1/\theta_2$ and the corresponding correction factors will be related

by

$$f_2 = \frac{f_1\theta_1}{f_1\theta_1 + (1-f_1)\,\theta_2}. \tag{11}$$

This useful expression was originally derived by Kasten et al. (1983) for the particular case of isotropic diffuse sky radiance. However, as shown here, it holds valid for an arbitrary sky radiance distribution, provided that two simple conditions are met:

i) Both geometries satisfy $\theta_{1,2} \lesssim 0.20$, so that the approximation in Eq. (5) holds.

ii) That internally reflected diffuse irradiance can be neglected so that Eq. (2) holds and $f \geq 1$.

2.2. Correction models based on assumed sky radiance parametric distributions

2.2.1. Muneer and Zhang (MZ)

As a compromise between a realistic anisotropic distribution and a simplified analytical description that takes into account some anisotropic effects, Muneer & Zhang (2001) use the simple sky radiance distribution from Moon & Spencer (1942),

$$L_p(\theta, \varphi) = L_z \frac{1 + b_i \cos\theta}{1 + b_i}, \tag{12}$$

where L_z is the sky radiance at the zenith ($\theta = 0$) and b_i is a sky radiance distribution index. The index $i = 1, 2$ corresponds to the two half-hemispheres of the sky, depending on the Sun's position. The Sun's half-hemisphere ($i = 1$) is treated separately from the other half-hemisphere ($i = 2$). The original Moon & Spencer proposal is a sky radiance distribution model for overcast sky and Muneer & Zhang extended it to all-sky conditions by introducing a clearness index ($k_t = G_h/G_{0h}$) dependence in the b_i parameters. This parametrization was originally proposed by Muneer (1990) as part of a transport model relating the diffuse irradiance on an inclined surface to the horizontal diffuse irradiance. The relationships between b_i and k_t were fitted by Muneer using data of horizontal and inclined diffuse irradiance from one site to adjust the coefficients and from two sites to validate the model. For cloudy conditions ($k_t \leq 0.2$), $b_1 = b_2 = 1.68$. For other sky conditions ($k_t > 0.2$),

$$b_1 = \frac{3.6 - 10.46\,k_t}{-0.4 + 6.974\,k_t} \qquad \text{and} \qquad b_2 = \frac{1.565 - 0.990\,k_t}{0.957 + 0.660\,k_t}. \tag{13}$$

The integrals in Eqs. (3) and (5) can be evaluated analytically using the radiance distribution from Eq. (12), resulting in expressions for G_d and G_{di},

$$G_d = \frac{\pi L_z}{6}\left[\frac{3 + 2b_1}{1 + b_1} + \frac{3 + 2b_2}{1 + b_2}\right] \tag{14}$$

$$G_{di} = 2\theta_0 \cos\delta\, L_z \left[\frac{I_1 + I_2\, b_1}{1 + b_1}\right], \tag{15}$$

where I_1 is given by Eq. (8) and

$$I_2 = \omega_s \sin^2\phi \sin^2\delta + \frac{\sin\omega_s \sin(2\phi)\sin(2\delta)}{2} + \frac{\cos^2\phi\,\cos^2\delta}{2}\left[\omega_s + \frac{\sin(2\omega_s)}{2}\right].$$

Finally, the S fraction from this model (and the corresponding correction factor f) are obtained as the ratio of Eq. (15) to Eq. (14). Note that the resulting expressions depend on k_t and are independent of the normalization constant L_z.

Although this simple model follows an overcast sky radiance model and has no explicit dependence on the Sun's position (other than treating separately the Sun's position in half-hemispheres), it has been compared to experimental data and found to be an improvement over Drummond's isotropic approximation. In particular, Muneer & Zhang (2001) report that the negative bias of the isotropic correction is reduced from -15.6 W/m^2 to -0.7 W/m^2 under clear-sky conditions ($k_t > 0.6$) while small positive biases are obtained for $k_t \leq 0.6$. Other evaluations show similar improvements over the isotropic model (López et al., 2004; Sánchez et al., 2012).

2.2.2. Vartiainen and Brunger (VB)

Brunger & Hooper (1993a) proposed an expression for the sky radiance that explicitly depends on the Sun's position,

$$L_p(\theta, \varphi) = G_d \left[\frac{a_0 + a_1 \cos\theta + a_2\, e^{-a_3 \psi}}{\pi\,(a_0 + 2a_1/3) + 2a_2\, I(\theta_z)} \right], \tag{16}$$

where $I(\theta_z)$ is such that the sky radiance L_p satisfies Eq. (3),

$$I(\theta_z) = \left[\frac{1 + e^{-a_3 \pi/3}}{1 + a_3^2} \right] \cdot \left[\pi - \left(1 - \frac{2}{\pi a_3} \cdot \frac{1 - e^{-a_3 \pi}}{1 + e^{-a_3 \pi/2}} \right) \times (2\theta_z \sin\theta_z - 0.02\,\pi\, \sin(2\theta_z)) \right]. \tag{17}$$

The first factor in Eq. (17) originally appeared with an erratum, corrected in Brunger & Hooper (1993b). The Sun's position dependence appears through ψ, the angle subtended between a given sky element (θ, φ) and the Sun's position (θ_z, φ_s).

The dependence on the sky conditions is introduced by considering the coefficients a_i as discrete functions of the clearness index k_t and the diffuse fraction, $f_d = G_d/G_h$. This last variable is not known a priory if the diffuse irradiance is measured with a shadow-band. In our implementation we used the isotropic correction factor to estimate f_d from the measured diffuse irradiance, G_{du}. No significant difference was observed when compared to using the reference value of G_d. The coefficients a_i in Eq. (16) are given in Brunger & Hooper (1993a) for a matrix of 9×9 bins in the (k_t, f_d) space. These coefficients were determined by adjusting the model (using non-linear regression) to one year of data from sky scans made in Toronto, Canada (latitude $\phi = 43.67°$). In Vartiainen (1999), this radiance distribution was used to calculate the diffuse irradiance intercepted by a shadow-band performing the numerical integration of Eq. (5). Monthly averaged correction factors were calculated using one year of data for Helsinki, Finland (latitude $\phi = 60°$), and were compared with Drummond's isotropic correction, the all-sky Perez et al. (1993) model (Subsection 2.2.3) and LeBaron et al. (1980) model (Subsection 2.3.3). For that location, Vartiainen found that the LeBaron et al. model produces slightly lower correction factors during summer.

2.2.3. Vartiainen and Perez (VP)

The sky luminance distribution from Perez et al. (1990), used in the all-sky Perez's model for diffuse solar irradiance (Perez et al., 1993), has also been used to calculate the S fraction and its corresponding correction factor (Vartiainen, 1999). In the context of sky illuminance, this model has been shown to outperform several other illuminance models (Perez et al., 1990). With the proper normalization, it can be interpreted as a sky radiance distribution (Gracia et al., 2011),

$$L_p(\theta,\varphi) = C\,(1 + a\,e^{b/\cos\theta}) \cdot (1 + c\,e^{d\psi} + e\cos^2\psi), \tag{18}$$

in terms of the angle ψ. The normalization constant C is determined in terms of G_d, using Eq. (3). Each of the coefficients $(a, b, \ldots e)$ can be related to different aspects of the radiance distribution and depend on the sky condition. As expected, this distribution peaks at the Sun's position ($\psi = 0$) so it captures the circumsolar contribution to diffuse irradiance.

The sky condition is originally modelled in Perez et al. (1990) by a set of two dimensionless parameters: the sky brightness (or diffuse clearness index), $k_d = G_d/G_{0h}$, and the modified sky clearness parameter, ϵ', defined as

$$\epsilon' = 1 + \frac{G_b/G_d}{1 + 1.041\,\theta_z^3}, \tag{19}$$

where θ_z is expressed in radians. When the sky condition is characterized in terms of k_t and f_d, these two parameters (k_d and ϵ') can be obtained as

$$k_d = k_t\,f_d \qquad \text{and} \qquad \epsilon' = 1 + \frac{1/f_d - 1}{\cos\theta_z\,(1 + 1.041\,\theta_z^3)}. \tag{20}$$

The dependence of the sky radiance distribution on the sky condition is given through the vector of coefficients $x = (a, b, c, d, e)$, which satisfy

$$x(\theta_z, k_d, \epsilon') = x_1(\epsilon') + x_2(\epsilon')\,\theta_z + [x_3(\epsilon') + x_4(\epsilon')\,\theta_z]\,k_d. \tag{21}$$

Each of these functions x are analytical in (θ_z, k_d) but are discrete in ϵ', through the x_i values. The sky clearness parameter is grouped in eight bins of increasing sky clearness with boundaries: [1, 1.065, 1.230, 1.500, 1.950, 2.800, 4.500, 6.200, ϵ'_{max}], and the coefficients x_i for each bin are tabulated in Perez et al. (1993). An exception in Eq. (21) occurs for $x = c, d$ in the first bin $\epsilon' \in [1, 1.065)$. For these cases the coefficients are

$$c(\theta_z, k_d, \epsilon') = e^{\{[c_1 + c_2\,\theta_z]k_d\}^{c_3}} - c_4, \tag{22}$$

$$d(\theta_z, k_d, \epsilon') = -e^{[d_1 + d_2\,\theta_z]k_d} + d_3 + d_4\,k_d. \tag{23}$$

The tabulated values $x_i(\epsilon')$ reported in Perez et al. (1993) were obtained from over 1600 sky scans at the Lawrence-Berkeley Laboratory in California between 1985-86. In the same way as in the previous model (VB), in our implementation we used the isotropic correction factor to estimate f_d from the measured diffuse irradiance, G_{du}.

2.2.4. *Comparison of parametric distributions*

In Fig. 2 the four analytical sky radiance distributions (VP, VB, MZ, ISO) are compared for four different sky conditions ranging from clear sky to full overcast. Sky radiances are normalized with the isotropic sky radiance $L_p^{iso} = G_d/\pi$, which therefore appears as a horizontal line. Each panel shows the sky direction along the Sun's meridian, i.e. $\varphi = \varphi_s$ for all θ. The Sun's altitude is fixed and corresponds to an air mass of 1.5 ($\theta_z = 48.2°$). Both VB and VP radiances peak at the Sun's position and these peaks represent the circumsolar contribution to diffuse horizontal irradiance. The VP model under clear skies also shows some horizon brightening. The MZ model shows dependence with the polar angle, increasing towards the horizon under clear skies and decreasing under overcast condition. Under cloudy skies all models approach the isotropic distribution (see Fig. 2d).

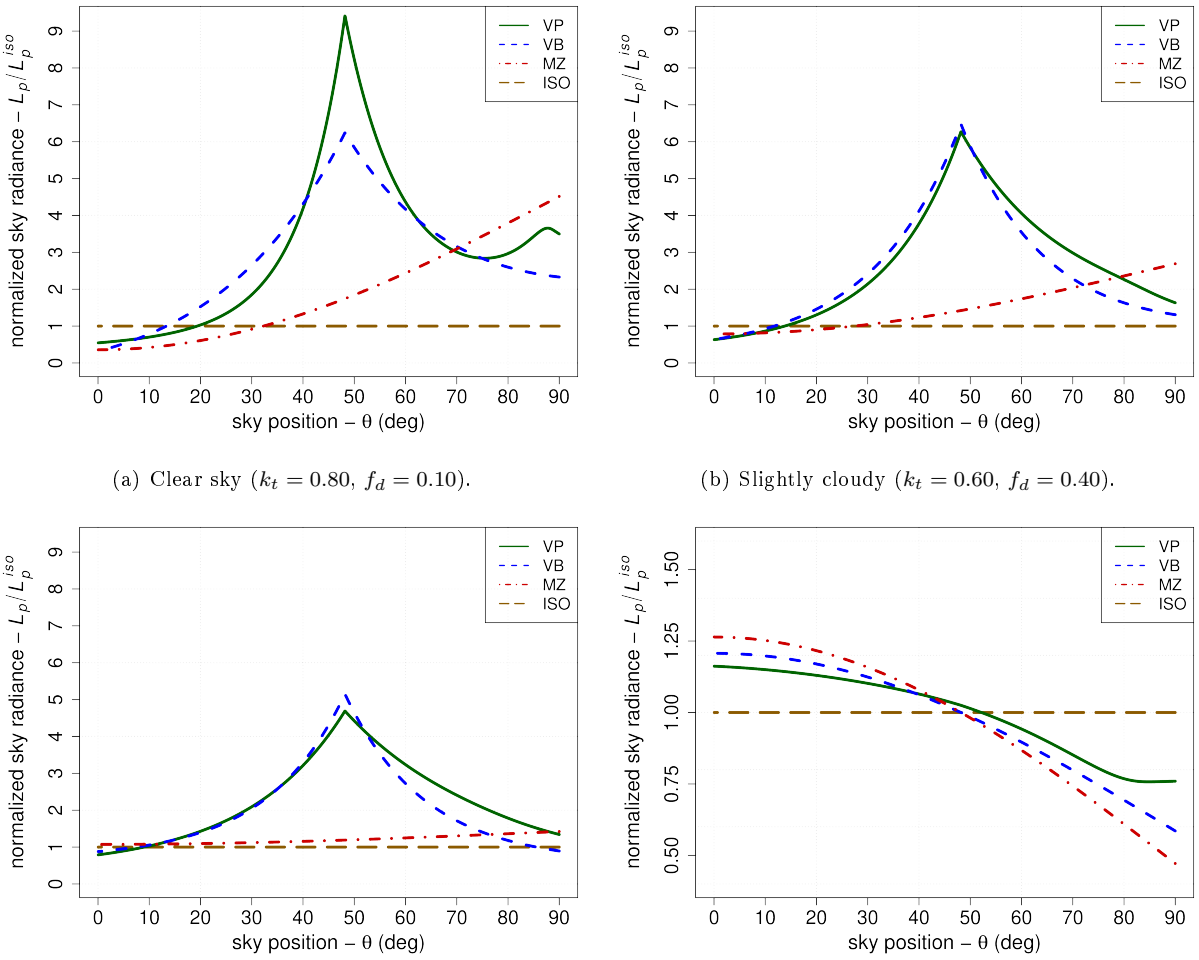

(a) Clear sky ($k_t = 0.80$, $f_d = 0.10$).

(b) Slightly cloudy ($k_t = 0.60$, $f_d = 0.40$).

(c) Partly cloudy ($k_t = 0.40$, $f_d = 0.85$).

(d) Overcast ($k_t = 0.05$, $f_d = 1.00$).

Figure 2: Relative sky radiance (normalized by the isotropic radiance) for the three anisotropic models MZ, VB and VP for air mass 1.5 ($\theta_z = 48.2°$) along the Sun's meridian ($\varphi = \varphi_s$). Note that the y-axis has been modified for figure (d).

2.3. Phenomenological correction models

Working with sky radiance distributions is not straightforward, as it involves (except for the simplified MZ model) the numerical evaluation of double integrals and the use of LUT (look-up-tables) *for each data point*. Phenomenological models skip the sky radiance modeling and aim to obtain the correction factor directly. Five widely used phenomenological models are considered and a new proposal is described, optimized in this work for the region of interest.

2.3.1. Kasten et al. (KA)

In Kasten et al. (1983) the correction factor is parametrized as

$$f = A + B\left(\frac{k_{du}}{k_t}\right)^3 + C\,\delta + \frac{D}{\ln(1/\tau_{bu})}, \tag{24}$$

where $k_{du} = G_{du}/G_{0h}$ and $\tau_{bu} = G_{bu}/G_0$ are the diffuse clearness index and the beam transmittance of the uncorrected solar irradiance components, respectively. These dimensionless variables satisfy $\tau_{bu} = k_t - k_{du}$, so the beam transmittance is derived from k_t and k_{du}, restricted to $\tau_{bu} \geq 0$.

The constants of Eq. (24) were determined by Kasten et al. from less than one year of hourly data for Hamburg, Germany, using a plane shadow-band with $b/r = 0.169$. A pyranometer under a shade-disk device mounted on a solar tracker was used as the reference measurement and the reported values were $A = 1.161$, $B = -0.112$, $C = 0.0009$ and $D = -0.0246$.

2.3.2. Steven et al. (ST)

Steven (1984) proposed an all-sky method that takes into account the anisotropy due to the circumsolar region. The fraction of diffuse irradiance blocked by the shadow-band is expressed as $S = q\ S_0$, where S_0 corresponds to the isotropic case. The anisotropic correction q is parametrized as

$$q = 1 - C\,\xi + \frac{C}{I_1}, \tag{25}$$

where I_1 is given by Eq. (8), ξ is a constant related to the angular width of the circumsolar region ($\xi = 0.60$ rad is the value used in Steven (1984)), and C is related to the relevance of the anisotropic effects. It is expressed as a function of the relative sunshine hours for the day, $n_r = N/N_0$, as measured by a Campbell-Stokes heliograph,

$$C(n_r) = \frac{C_0\, n_r}{1 - \xi\, C_0\,(1 - n_r)}. \tag{26}$$

Anisotropic effects are less relevant for cloudy days ($n_r = 0$), and for a clear day ($n_r = 1$) this expression reduces to C_0, which is given as $C_0 = 1.01$ in Steven (1984). In sum, in order to allow for particular local climatic conditions, this model can be considered to depend on two adjustable constants (C_0 and ξ) and on the relative sunshine duration for the day, n_r.

2.3.3. LeBaron et al. (LB)

LeBaron et al. (1990) develop a Look Up Table (LUT) model for the correction factor f. Two years of hourly data from two sites in the U.S. (Albany, NY, and Bluefield, WV) were used to define the model in terms of four variables. One of them is the isotropic correction factor, $f_0 = 1/(1-S_0)$, with S_0 from Eq. (7). The solar zenith angle, θ_z, is the second variable. The other two are the diffuse clearness index k_d and the sky clearness parameter without the solar zenith angle correction,

$$\epsilon = 1 + \frac{G_b}{G_d}. \tag{27}$$

The parameters k_d and ϵ are calculated using the uncorrected diffuse and beam irradiances, G_{du} and G_{bu}, which satisfy the closure relation, Eq. (1). Each parameter is binned in four categories with the boundaries shown in Table 1, resulting in a LUT with $4^4 = 256$ combinations. $f_{0,max}$ and ϵ_{max} are the maximum experimental values for these variables. The correction factors tabulated in LeBaron et al. (1990) vary between 0.935 and 1.248, with the values lower than unity indicating that some reflection from the inner part of the shadow-band was incident on the pyranometer.

index	variable / category	**1**	**2**	**3**	**4**	
i	θ_z (^{o})	0	35	50	60	90
j	f_0	1.000	1.068	1.100	1.132	$f_{0,max}$
k	ϵ	1.000	1.253	2.134	5.980	ϵ_{max}
l	k_d	0.000	0.120	0.200	0.300	1.000

Table 1: Boundaries for the four categories of the LB model. The index column refers to the notation in LeBaron et al. (1990).

LeBaron et al. (1990) validate this model with independent data sets for both sites and show that it improves the isotropic correction factor, especially under partly clear skies when diffuse irradiance tends to be high and anisotropy effects are most important.

2.3.4. Batlles et al. (BA, BB)

Batlles et al. (1995) builds on LeBaron et al. model by considering the same four parameters and replacing the LUT with two alternative linear parametrizations for the correction factor.

The first proposal (named BA here) parametrizes f as

$$f = a\, f_0 + b\, \ln(k_d) + c\, \ln(\epsilon) + d\, e^{-1/\cos\theta_z}, \tag{28}$$

with a, b, c, d empirical constants fitted to the data. The authors note that the sky clearness parameter ϵ is

one the most relevant predictors and propose a refined version (BB) with four categories in ϵ,

$$f = \begin{cases} a_1\, f_0 + b_1\, \ln(k_d) + d_1\, e^{-1/\cos\theta_z} & \epsilon \leq 3.5 \\ a_2\, f_0 + b_2\, \ln(k_d) + d_2\, e^{-1/\cos\theta_z} & 3.5 < \epsilon \leq 8 \\ a_3\, f_0 + b_3\, \ln(k_d) & 8 < \epsilon \leq 11 \\ a_4\, f_0 + b_4\, \ln(k_d) & \epsilon > 11. \end{cases} \tag{29}$$

Batlles et al. (1995) fit the coefficients in Eqs. (28) and (29) using three years of data for Madrid (hourly) and for Almeria (5-min) in Spain, based on Eppley shadow-bands with $b/r \approx 0.24$. A third of the data set was reserved for the validation of both models. As for the previous models, the parameters k_d and ϵ in BA and BB models are calculated using the uncorrected diffuse and beam irradiances, G_{du} and G_{bu}.

2.3.5. New proposal (NP)

After analyzing the performance of the BB method with different ϵ bin structures, a large variability between the first and last bins in Eq. (29) was observed. We consider a new linear model inspired in Eq. (28), with the addition of a constant (which reduces the mean bias) and with eight bins in ϵ', to allow a fit to each sky condition, similar to the VP model. The use of the modified sky clearness parameter in eight bins is found to improve performance (this parameter is also calculated using the uncorrected diffuse irradiance). The new proposal can be summarized as,

$$f = a_i\, f_0 + b_i\, \ln(k_d) + c_i\, \ln(\epsilon') + d_i\, e^{(-1/\cos\theta_z)} + e_i, \tag{30}$$

for ϵ' in the eight bins ($i = 1, \ldots 8$) as defined in Perez et al. (1993). Boundaries in ϵ' for these categories and the locally adjusted coefficients can be found in Table A.7.

3. Data and quality control

3.1. Data set description

A data set for a one year period (2019-2020) was generated at the Solar Energy Laboratory, located in a semi-rural environment at Salto, Uruguay (latitude $\phi = -31.27°$, longitude $\psi = -57.88°$, altitude $h = 59$ m above sea level). As mentioned in the introduction, the site is representative of a broad region in south-eastern South America, known as Pampa Húmeda, with a temperate climate designated Cfa in the updated Köppen-Geiger classification (Peel et al., 2007).

A Kipp & Zonen CM-121B shadow-band was used to measure the uncorrected diffuse irradiance, G_{du}. It has a U-shape profile with $b/r = 0.185$ (Kipp & Zonen , 2004). The reference global and diffuse horizontal measurements were obtained with two Kipp & Zonen CMP10 pyranometers (spectrally flat, Class A according to the ISO 9060:2018 standard). The pyranometer used to measure the reference diffuse irradiance was

behind a standard shading-sphere assembly mounted on a SOLYS2 precision solar tracker. A Kipp & Zonen CHP1 pyrheliometer, mounted on the same tracker, was used to measure the DNI (used in this work for quality-check only). All these instruments were last calibrated in July 2018 according to the relevant ISO standard by the Solar Energy Laboratory (Abal et al., 2018) against a secondary standard (Kipp & Zonen CMP22) which provides traceability to the World Radiometric Reference.

Measurements were recorded at 1-minute time resolution between May 2019 and June 2020 and later integrated to 5-min intervals. This resulted in a 5-min data set with 57990 records of the reference variables (G_h, G_d, G_b) and 51881 records of the shadow-band variable G_{du}. The data set is restricted to diurnal records ($\cos\theta_z > 0$) and then processed for quality control using 10 filters, applied independently. The original data set includes a little bit more than one year data to compensate seasonal unbalances found after filtering. Each season is adequately represented in the final data set.

3.2. Quality control

Quality control is extremely important when trying to evaluate small effects from the data. The correction factors are not large (representing corrections under 15%) and the differences between them are much smaller, so a careful quality control procedure is required in order to remove potentially erroneous or atypical data records from the data set.

The set of quality-control procedures is based on the BSRN (Baseline Solar Radiation Network) recommended filters (McArthur, 2005) using local coefficients. These are supplemented with a few additional criteria, adopted after inspection of the data in the dimensionless (k_t, f_d) and (k_t, τ_b) spaces.

The quality filtering procedure is summarized in Table 2 and Fig. 3. Three BSRN filters (F1 to F3 in Table 2) apply an upper bound to the measured irradiances, G, as

$$G \leq G_0\, p\, (\cos\theta_z)^a + c, \tag{31}$$

where p, a and c are parameters which can be locally derived for each filter from F1 to F3 by inspection of each tested variable (G_h, G_d, G_b). Filter F4 sets a minimum solar altitude, $\alpha_s > 10°$ or $\cos\theta_z > 0.174$, discarding low-altitude measurements which are affected by larger cosine errors. Filter F5 tests that the three reference irradiance components satisfy the closure relation of Eq. (1) with a tolerance of 8% of the G_h average, to allow for experimental error. This filter is only applied if $G_h > 50$ W/m^2, as indicated in the BSRN guidelines. Filter F6 tests for $f_d \leq 1.03$, allowing a 3% tolerance for experimental error in the reference diffuse fraction measurement. Filter F7 removes points of low k_t and low f_d, mostly associated with very low-irradiance measurements under heavy overcast conditions. Filter F8 is the upper bound $k_t < 1$, which excludes a few short-lived over irradiance events, rarely found in the 5-min records. Filter F9 tests for consistency between the uncorrected diffuse irradiance G_{du} and the reference value G_d: the experimental correction factor $f_e = G_d/G_{du}$ is required to be within $1 \leq f_e \leq 1.5\, f_0$ (internal reflections

in the CM-121B shadow-band can be neglected). The lower limit proved to be useful to discard misaligned shadow-band data. The upper limit of $1.5\,f_0$ was determined by visual inspection of the f_e/f_0 histogram and only discards a few outliers. Finally, filter F10, inspired in the SERI-QC procedure (Maxwell et al., 1993), tests for anomalous clear-sky data, requiring $\tau_b < k_t - k_{d,min}$, with $k_{d,min} = 0.06$ determined from inspection of the (k_t, τ_b) diagram. Filters F2, F6 and F7 were applied also to the isotropically corrected diffuse horizontal measurement, G_{dc}, and are indicated in Table 2 as F2B, F6B and F7B, respectively. After the filtering procedure, about 1/3 of the data is discarded and a clean data set with 36939 5-min records satisfying all filters is obtained.

filter	condition	variables	input	output	% discarded
F1	Eq. (31)	G_h	56950	56926	0.04
F2	Eq. (31)	G_d	56918	56877	0.07
F2B	Eq. (31)	G_{dc}^{iso}	51881	50571	2.53
F3	Eq. (31)	G_b	54336	54336	0.00
F4	$\cos\theta_z > 0.174$	all	57990	49738	14.23
F5	Eq. (1)	G_h, G_d, G_b	54335	53097	2.28
F6	$f_d < 1.03$	G_h, G_d	56918	55472	2.54
F6B	$f_{dc}^{iso} < 1.03$	G_h, G_{dc}^{iso}	51881	43826	15.53
F7	$k_t < 0.20$ & $f_d > 0.80$	G_h, G_d	54336	54104	0.43
F7B	$k_t < 0.20$ & $f_{dc}^{iso} > 0.80$	G_h, G_d^{iso}	50890	50768	0.24
F8	$k_t < 1$	G_h	56950	56860	0.16
F9	$1 \le f_e < 1.5\,f_0$	G_d, G_{dc}^{iso}	51880	45181	12.91
F10	$\tau_b < k_t - 0.06$	G_b, G_h	54336	54104	0.43
all		all	57990	36939	36.3

Table 2: Details of the filtering process applied on diurnal data records.

In addition, the ST model requires daily sunshine duration data (defined by the WMO as the period of time in a day during which $G_b > 120$ W/m^2). This variable is highly correlated with the average daily global solar irradiation. We use a series of sunshine duration measured by a Campbell-Stokes heliograph recorded at the National Agronomic Research Institute (INIA) site at Salto Grande, located 3 km away from the site of our irradiance measurements.

4. Methodology

4.1. Model implementation and local adaptation

The nine pre-existing correction models described in Section 2 were implemented and tested, both in their original and locally adapted versions. The assessment of the original versions, i.e. using the published

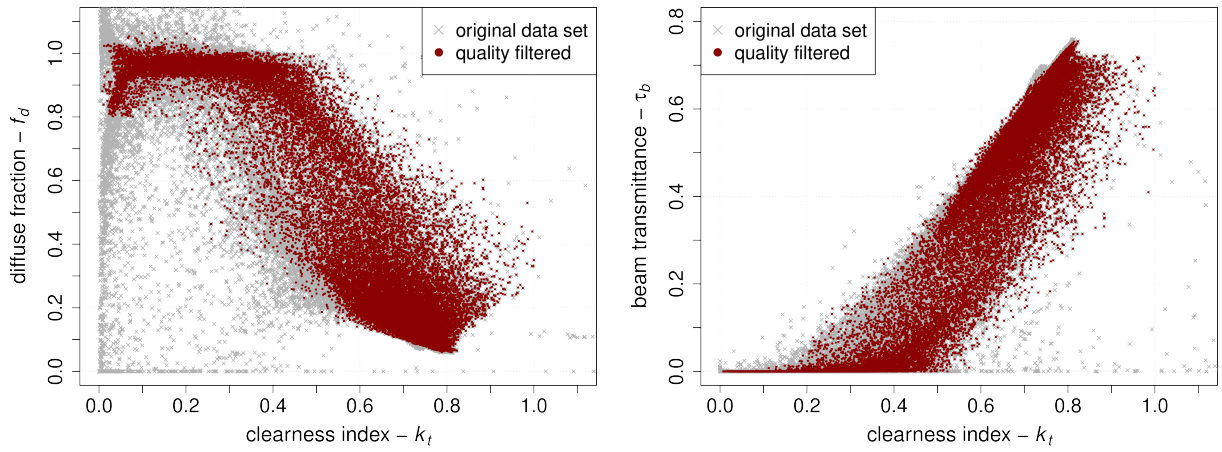

(a) f_d vs k_t diagram.

(b) τ_b vs k_t diagram.

Figure 3: Results of the data quality control procedure represented in two dimensionless spaces (Maxwell et al., 1993). The original data is plotted as gray crosses and the quality filtered data as red circles.

coefficients of the original models, allows to evaluate the baseline uncertainties in the target region when used as a generic (or universal) correction model. The local adaptation of these methods enhances their performance and provides either new local coefficients or locally adjusted correction factors. It also provides an adequate comparison context for the novel proposal of this work, which is obviously only tested with local adaptation.

4.1.1. Original models' implementation

The sky radiance models VB and VP are implemented via numerical integration of Eqs. (3) and (5) using the corresponding sky radiance function. In the case of the MZ model, the sky radiance L_p is implemented analytically (Subsection 2.2.1). For the phenomenological models KA, BA and BB, the Kasten's formula (Eq. (11)) was used to transfer the correction factors to the particular model band geometry to the CM-121B shadow-band used in this work. For the LB model this transfer could not be applied because the geometry of the LB shadow-band was not provided in LeBaron et al. (1990). The ST model is applicable to different shadow-band geometries by simply using the correct θ_0 value in the isotropic fraction S_0, Eq. (7). Drummond's isotropic correction function (DR) is also tested and it provides a baseline for the corrections.

4.1.2. Local adaptation

For local adaptation, models are separated into two categories as follows:

i) Those whose coefficients can be locally adjusted by using the shadow-band and reference diffuse measurements (KA, ST, LB, BA, BB and NP).

ii) Those whose coefficients can not be locally adjusted, either because the diffuse irradiance information is not enough to perform the adjustment, or because the model has too many or no parameters to tune (DR, MZ, VB and VP).

The phenomenological models discussed in Subsection 2.3 belong to type (i). On the other hand, the VB and VP sky-radiance distributions have $4 \times 48 = 192$ and $8 \times 20 = 160$ adjustable coefficients, respectively, and a proper adjustment of these parameters requires directional sky radiance measurements from an sky scanner. Due to this the sky-radiance models (including also the MZ model) belong to type (ii). The DR model is included in this second category as it has no adjustable parameters.

The locally-adjusted versions of type (i) models are obtained from local data using a standard random-sampling and cross-validation procedure. Depending on the model, linear or non-linear multiple regression is used. For type (ii) models, a site-adaptation post-procedure is required. A simple linear site-adaptation function (Polo et al., 2016) is used, so that the corrected diffuse irradiance is

$$G_{dc} = a\,(f\,G_{du}) + b, \tag{32}$$

where a and b are the slope and intercept of the linear fit, respectively, found by standard linear regression. This site-adaptation allows for a fair comparison between all locally-adjusted models. Both the site-adaptation and the local fits were performed by random sampling and cross-validation, using 60% of the data for local adaptation and 40% for validation. The 60/40 random split was repeated 100 times and the average coefficients and performance indicators are calculated for the ensemble.

The original and locally fitted coefficients for the phenomenological models are provided in the Appendix in Tables A.6 and A.7, and the values of a and b for the site-adapted models are listed in Table 3 below. The intercept (b) is small for all models and the slope correction (a) varies from $\simeq +9\%$ (MZ) to $\simeq -5\%$ (VB). The slope correction for the DR model is consistent with the known 3-4% underestimation from the isotropic approximation.

coef.	**DR**	**MZ**	**VB**	**VP**
a (no unit)	1.0310	1.0908	0.9502	0.9569
b (W/m^2)	1.0300	-3.0251	-1.4992	0.1031

Table 3: Coefficients for the site-adaptation of analytical models, Eq. (32).

4.2. Performance metrics

The performance assessment is done by using three common metrics, namely, the Mean Bias Deviation (MBD), the Root Mean Square Deviation (RMSD) and the Kolmogorov-Smirnov Integral (KSI) (Gueymard,

2014). These quantities are defined as follow,

$$\mathrm{MBD} = \frac{1}{n}\sum_{i=1}^{n}(\hat{y}_i - y_i), \qquad \mathrm{RMSD} = \left[\frac{1}{n}\sum_{i=1}^{n}(\hat{y}_i - y_i)^2\right]^{\frac{1}{2}}, \qquad \mathrm{KSI} = \int_0^{y_m} |F(y) - \hat{F}(y)|\, dy, \tag{33}$$

where y_i stands for the reference value (G_d), $\hat{y}_i$ for the corrected value (G_{dc}), y_m for the maximum in $\{G_d, G_{dc}\}$ and F and $\hat{F}$ are cumulative distributions functions of y_i and $\hat{y}_i$, respectively. This set of indicators has been used successfully in this region to assess the performance of empirical diffuse fraction models (Abal et al., 2017) and satellite based solar assessment models (Laguarda et al., 2020). These metrics have units of W/m^2 but can be expressed in relative terms (rMBD, rRMSD and rKSI) as a percentage of the average reference value, $\bar{G}_d$. Since each of them quantifies a different similarity aspect between the measured and corrected data sets, it is convenient to define a collective performance indicator as,

$$\mathrm{CPI} = \frac{1}{3}\left(|\mathrm{rMBD}| + \mathrm{rRMSD} + \mathrm{rKSI}\right). \tag{34}$$

This global index, which is expressed as a percentage of the average reference value, $\bar{G}_d$, is used as an indicator for overall model performance.

5. Results and discussion

In this section the correction models' performances are discussed, both in their original and locally adapted versions. The coefficients for both versions of each model are provided in Tables A.6 and A.7.

5.1. Original models

The performance results for the nine models with their original coefficients are presented in Table 4. The metrics of Subsection 4.2 were calculated for the all-sky data set and also for three subsets (I, II, III) associated to different sky conditions according to k_t: clear sky, partly cloudy skies and overcast skies. Fig. 4 shows the corresponding nine scatter-plots between the reference diffuse measurement and the shadow-band corrected diffuse measurement, showing in color (online version) the k_t discrimination.

The lowest overall biases are observed for DR (underestimation) and ST model (overestimation). Around half of the models (including DR, which has a well-known negative bias) underestimate the diffuse irradiance. The underestimation of these models is present under the three sky conditions, with the exception of the DR model, which changes its behavior to overestimation under overcast sky. MZ is the only sky radiance-based model that underestimates diffuse irradiance. Most models have biases within ±6%, except for the BA and BB phenomenological models, which show high underestimation biases when used with their original coefficients. For these two models, large underestimation occurs under the three sky conditions, being worst under overcast sky for the BB model and under clear sky for the BA model. This behavior can also be

sky condition	metric (%)	DR	MZ	VB	VP	KA	ST	LB	BA	BB
	rMBD	-2.3	-6.4	6.3	4.4	6.2	1.6	6.3	-21.1	-21.8
all sky	rRMSD	7.3	11.0	10.2	8.4	9.0	6.3	9.6	25.2	28.3
	rKSI	2.5	6.4	6.3	4.4	6.2	1.7	6.3	21.0	21.9
$\bar{G}_d = 143.7$ W/m^2	CPI	**4.0**	7.9	7.6	5.8	7.2	**3.2**	7.4	22.4	24.0
mostly clear sky	rMBD	-2.5	-5.9	6.5	5.0	10.9	2.4	5.6	-19.7	-34.8
($k_t \geq 0.6$)	rRMSD	8.2	11.5	9.3	8.8	13.2	7.2	8.8	22.3	41.0
data count: 22950	rKSI	2.8	5.9	6.5	5.1	10.9	3.0	5.6	19.7	34.8
$\bar{G}_d = 115.7$ W/m^2	CPI	**4.5**	7.7	7.4	6.3	11.7	**4.2**	6.7	20.6	36.9
partly cloudy	rMBD	-2.7	-7.4	5.8	3.5	1.4	0.5	6.6	-17.7	-8.1
($0.2 < k_t < 0.6$)	rRMSD	6.1	9.9	9.5	7.2	3.9	5.0	9.1	20.6	12.9
data count: 10695	rKSI	2.7	7.4	5.8	3.9	1.4	0.7	6.6	17.7	8.3
$\bar{G}_d = 221.2$ W/m^2	CPI	3.8	8.2	7.1	4.9	**2.3**	**2.1**	7.4	18.7	9.8
overcast	rMBD	2.4	-3.1	9.1	6.1	2.8	3.6	9.9	-61.5	-15.0
($k_t \leq 0.2$)	rRMSD	4.3	5.0	13.9	9.2	4.1	5.5	11.3	65.7	16.0
data count: 3285	rKSI	2.4	3.0	9.1	6.1	2.8	3.6	9.9	59.9	15.0
$\bar{G}_d = 87.5$ W/m^2	CPI	**3.1**	3.7	10.7	7.1	**3.2**	4.2	10.4	62.4	15.3

Table 4: Performance indicators for the nine original models, expressed as a percentage of the average reference diffuse irradiance ($\bar{G}_d$). The best performing models in terms of the combined index (CPI) are highlighted in boldface.

observed in the scatter-plots of Fig. 4, panels (g) and (h), especially the large overcast underestimation of the BA model. Most models have an overall rRMSD between 6 and 11%, with the exception of the BA and BB models affected by the large bias deviations already discussed. The lowest rRMSD are observed, again, for the ST and DR models. The rKSI metric orders the models in the same way as the rRMSD, but enhances the differences within values. As a result, the overall CPI metric discriminates the original models roughly into three groups:

(a) The best performing original models (ST and DR).

(b) Middle-range models (VP, KA, LB, VB and MZ) that may be used in the region in its original version but with higher uncertainties than the simple DR model.

(c) Models that should not be used in region without local adjustment (BA and BB).

The sky condition discrimination shows further insights. As shown in the data counts of Table 4, the overall metrics are dominated by the mostly clear sky condition, the prevailing situation in the local climate. The best performing model under clear skies is, consistently, the ST model, followed by the DR model. However, under the highly anisotropic partly cloudy conditions, the first and second models are ST

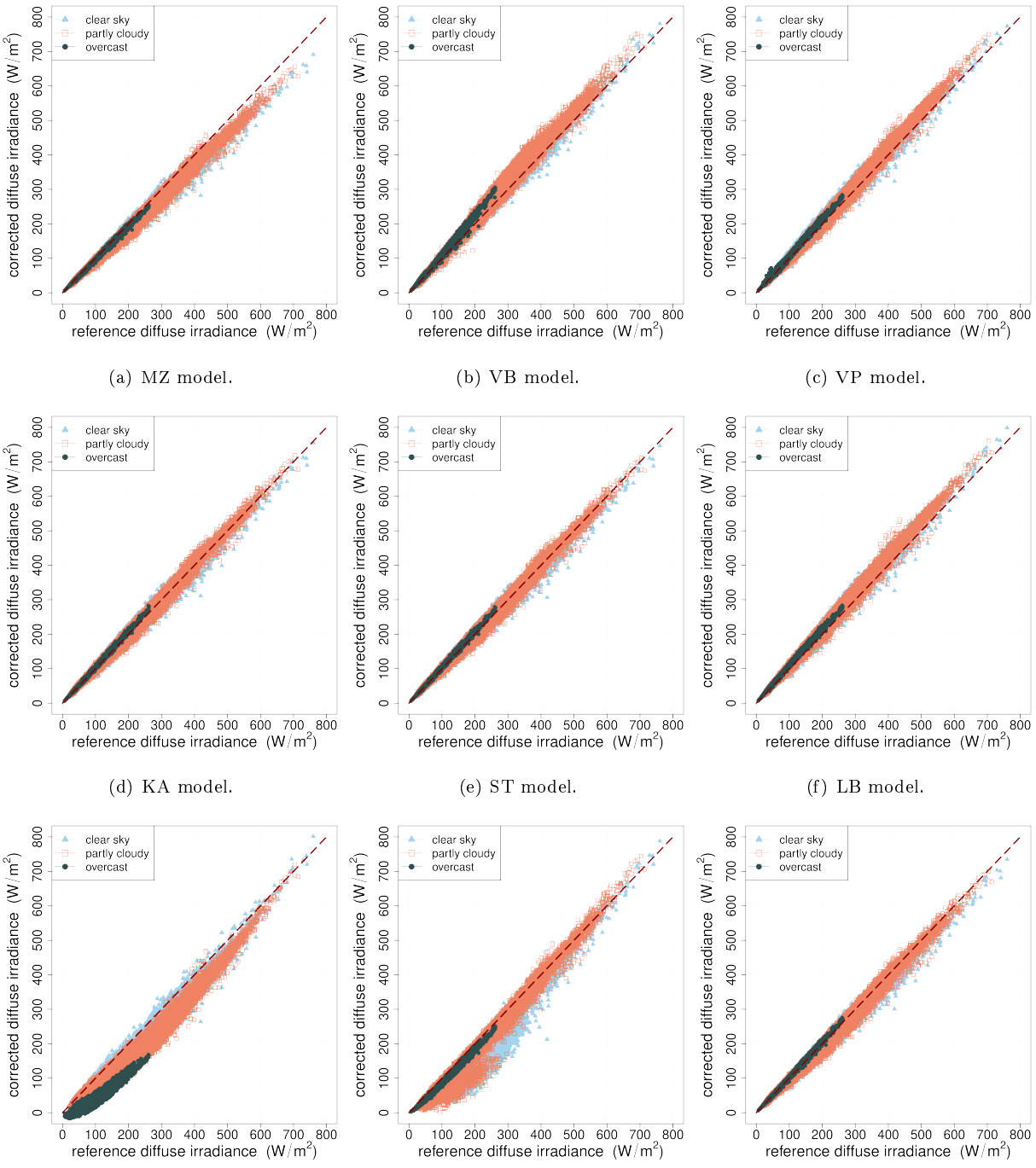

(a) MZ model. (b) VB model. (c) VP model.

(d) KA model. (e) ST model. (f) LB model.

(g) BA model. (h) BB model. (i) Isotropic model (DR).

Figure 4: Scatter-plots between the reference diffuse measurement (G_d) and the corrected shadow-band diffuse measurement (G_{dc}) for the nine pre-existing models with their original coefficients or non site-adapted (color in online version).

and KA, respectively. Furthermore, the KA model is also the second option for overcast condition, very close to the DR model. Of course, the DR model is the best model under overcast conditions, where the isotropic assumption holds better (see Fig. 2 panel (d)). The KA model is indeed a good choice for partly cloudy and overcast conditions and deserves further investigation in other regions. Its overall all-sky performance is not within the best ones because of its poor performance under clear sky, with a high overestimation bias of $\simeq 11\%$. An interestig alternative (not explored in this first article on the subject) is to use a combination of these models for different sky conditions. For instance, for this region, the ST model can be used for mostly clear and partly cloudy skies and the DR model for overcast conditions ($k_t \leq 0.2$). Without local adaptation and in the absence of sunshine hours records, i.e. when only the uncorrected shadow-band measurement is available, the best combination for this region is to use the DR model for clear sky and overcast conditions and the KA model for partly cloudy.

In sum, the ST model is the best generic model to use in the Pampa Húmeda region without local adaptation and it is the only one to outperform the isotropic method. However, it requires daily sunshine duration records and, in the absence of such information, the simple Drummond correction is the best choice, at least for this target region. This claim may be also applicable for other regions and climates, and also the overall performance may be improved by using a models' combination, but all these require specific studies.

5.2. Locally adapted models

The details on the local adaptation of all models have been presented in Subsection 4.1.2. The results for the locally adapted models are presented in Table 5, with the same metrics and sky condition discrimination as the previous analysis for original models. However, in this case, the performance indicators are calculated via the random sampling and cross-validation procedure. The locally adjusted versions perform better and their metrics become closer, with KSI gaining in importance (it can resolve small differences between similar performing models). Overall biases are within $\pm 1\%$, being negligible in most cases, with the exceptions of the ST, KA and LB models. In the rRMSD metric two groups of models are distinguishable, those around 4-5% (KA and NP) and the rest with 6-7%. In this case, the rKSI order (measuring the similarity between cumulative distributions) does not mimic the rRMSD, providing another models' order without distinguishable groups. The scatter-plots of locally adapted models are quite similar, so in this section we will only show the most relevant ones. The full set of scatter-plots are provided in high resolution in the online version of this article.

The new model proposed in this work (NP), inspired in the BA and BB models, is the best performing local model for the target region. It is unbiased and has the lowest overall rRMSD and rKSI, and presents the best overall CPI with a small gap from the other models. These observations holds not only for all-sky conditions, but also for the three sky subsets. Fig. 5 shows the scatter-plot for this model in comparison with the baseline isotropic model. For the NP model, samples for the three sky conditions are centered

sky condition	metric (%)	DR	MZ	VB	VP	KA	ST	LB	BA	BB	NP
	rMBD	0.0	0.0	0.0	0.0	-0.7	0.8	-0.9	-0.1	0.0	0.0
all sky	rRMSD	6.5	6.2	6.9	6.2	4.9	6.2	6.9	6.2	6.3	4.7
	rKSI	0.9	0.6	0.7	1.4	1.2	1.2	1.8	0.8	0.7	0.4
$\bar{G}_d = 143.7$ Wm^{-2}	CPI	2.5	2.3	2.5	2.5	2.3	2.8	2.6	2.4	2.3	**1.7**
mostly clear sky	rMBD	-0.4	0.1	-0.1	0.6	-0.5	1.3	-1.2	-0.5	-0.3	0.0
($k_t \geq 0.6$)	rRMSD	6.9	6.7	6.9	7.1	5.9	6.9	7.5	6.6	6.7	5.8
data count: 22950	rKSI	1.7	1.3	1.7	1.9	1.3	2.6	2.7	1.4	1.2	0.6
$\bar{G}_d = 115.7$ Wm^{-2}	CPI	3.0	2.7	2.9	3.2	2.6	3.6	3.8	2.8	2.8	**2.1**
partly cloudy	rMBD	-0.1	-0.3	-0.1	-0.9	-1.0	0.0	-1.2	0.1	0.1	0.1
($0.2 < k_t < 0.6$)	rRMSD	5.6	5.3	6.2	5.0	3.8	5.0	5.8	5.4	5.5	3.5
data count: 10695	rKSI	1.1	1.0	1.4	1.6	1.2	0.7	1.2	1.1	0.9	0.5
$\bar{G}_d = 221.2$ Wm^{-2}	CPI	2.3	2.2	2.6	2.5	2.0	1.9	2.7	2.2	2.2	**1.3**
overcast	rMBD	4.4	2.3	2.0	1.7	0.9	3.5	4.6	0.9	1.8	-0.3
($k_t \leq 0.2$)	rRMSD	6.6	5.2	8.3	5.7	2.6	5.3	6.4	3.8	4.3	2.8
data count: 3285	rKSI	4.4	2.9	3.2	2.0	1.0	3.5	4.6	1.5	1.9	0.7
$\bar{G}_d = 87.5$ Wm^{-2}	CPI	5.1	3.4	4.5	3.1	1.5	4.1	5.2	2.0	2.6	**1.3**

Table 5: Performance indicators for the ten localized models, expressed as a percentage of the average reference diffuse irradiance ($\bar{G}_d$). The overall mean bias is under ±1% in all cases. The best performing models in terms of the combined index (CPI) are highlighted in boldface.

on the $x = y$ line (dashed-line in red), being essentially unbiased as the corresponding rMBD indicators also show in Table 5. The site-adapted isotropic model, as seen in Fig. 5, shows an overcast overestimation which is partially compensated by a clear sky underestimation. This also happens to several other models in Table 5, i.e. the LB model, to mention the weakest in this sense. The NP model also shows a smaller dispersion of the samples around the $x = y$ line for each sky condition. In fact, it is the lowest dispersion from all models, as shown by the rRMSD metrics in Table 5.

The NP model is an enhancement of the BB and BA models, which are the models that are most impacted by the local adaptation procedure. Comparison of Tables 4 and 5 shows that their performance metrics improve significantly, both under all-sky and discriminated by sky conditions. The scatter-plot of their local versions, Fig. 6, can be easily contrasted with the high deviations observed in the original versions, Fig. 4 panels (g) and (h). However, the NP model improves upon them (both in alignment and dispersion, or rMBD and rRMSD). The radical change in performance due to the local adaptation of these two models is also expected for the NP proposal, so this correction model should not be used in other regions or climates without local adaptation procedure. This also applies for the BB and BA models, as shown.

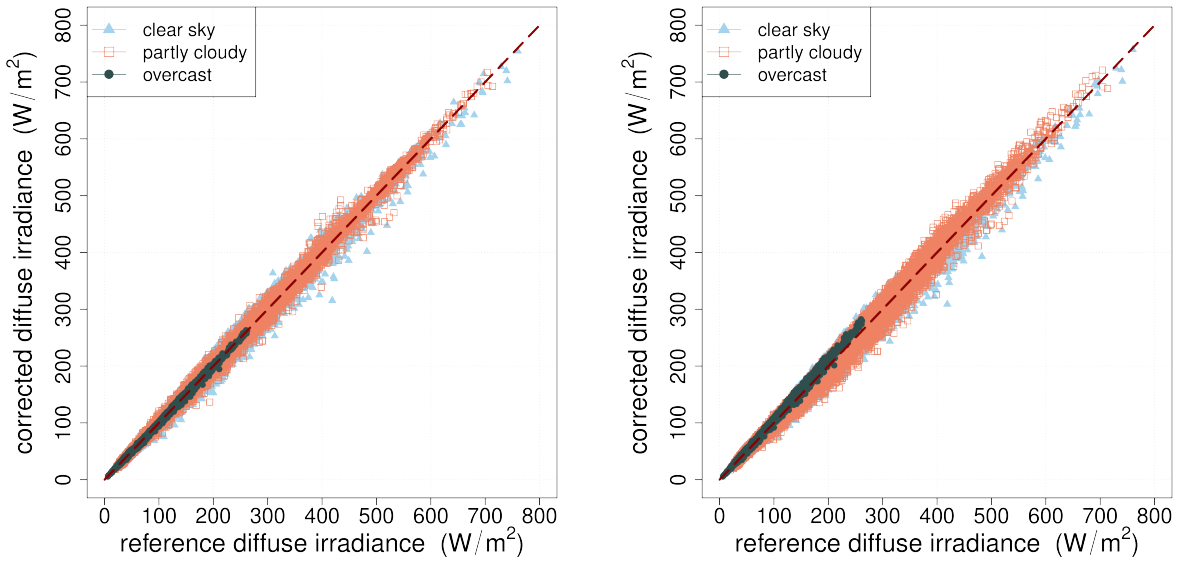

(a) Novel proposal (NP).

(b) Isotropic model (DR).

Figure 5: Scatter-plots between the reference diffuse measurement (G_d) and the corrected shadow-band diffuse measurement (G_{dc}) for the novel model of this work and the baseline isotropic model.

The evaluation of the NP model in other climates is required to test if the enhancements presented in this work imply also a modification of the model's robustness under different climates. In this sense, we provide in http://les.edu.uy/RDpub/JMRM_SBCF_model.zip a matlab program that runs, adjusts and evaluates the novel model based on a local set of data.

When locally adapted, several models are a good choice to use in the region. The second best performing model is the KA model, which presents low dispersion under each sky condition and low overall bias. This model is ranked in the top three positions of CPI both for all-sky and discriminated sky conditions and it has the best rRSMD under overcast sky, narrowly outperforming the NP model for this specific sky condition. Furthermore, the KA model has a good balance between accuracy and simplicity, as it only has 4 adjustable coefficients. By looking at the overall CPI, the BB, BA and MZ models achieve a similar ranking of 2.3-2.4%. The sophisticated VP and VB sky radiance models achieve similar performance than the rest. The unbiased isotropic model (site-adapted DR) is a simple alternative which, once locally adapted, yields similar results as more complicated models and can be considered as a good alternative. Since all localized models perform reasonably well, the selection of the correction model can be based on convenience and on the available information. The ST model, identified as the best generic model to use in the region, does not improve its performance metrics significantly when locally adapted. Its bias is reduced, but the rRMSD and rKSI is only slightly reduced, thus the model results in the worst ranked local version in spite of having the addition sunshine hours information. Consistently, the coefficients of this model do not vary too much between the

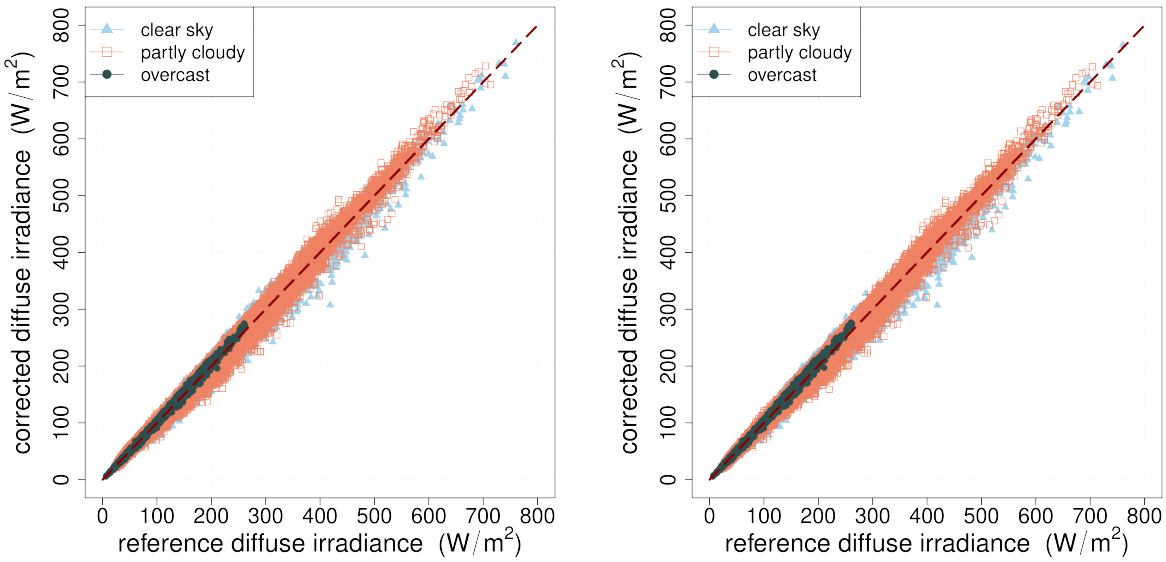

(a) BA model.

(b) BB model.

Figure 6: Scatter-plots between the reference diffuse measurement (G_d) and the corrected shadow-band diffuse measurement (G_{dc}) for the phenomenological models that where most improved by the local adaptation.

original and local versions (see Table A.6).

6. Conclusions

Phenomenological models used in solar resource assessment have different performance under different climates and the necessity and impact of local adaptation is often overlooked in the literature. In this work, an assessment of several shadow-band correction models for diffuse irradiance measurement in the Pampa Húmeda region is reported, both in their original and locally adapted forms, showing the impact of local adaptation on this kind of models. The evaluation includes a novel proposal which outperforms the pre-existing models for this region, even when they are locally adapted.

The best generic (i.e. without local adaptation) model for the Pampa Húmeda is the ST model (Steven, 1984), requiring additional daily sunshine duration information. If only shadow-band measurements are available, the best generic model for the region is the isotropic correction of Drummond (1956) (DR). This implies that the use of more sophisticated correction models without local adaptation, i.e. outside of the region for which they were derived, should be avoided, with the mentioned exception of the ST model. The DR model is known to underestimate diffuse irradiance by a small amount (confirmed by the results from this article) composed by an overestimation under cloudy skies and an underestimation under clear and partially cloudy conditions. A critical dependence of two models from Batlles et al. (1995) (labelled here

as BA and BB) with the local adaptation was found, implying that they should not be used in this region without a previous local adjustment of their coefficients.

Rather than using generic models, it is preferable to use locally adapted versions. However, the work involved in local adaptation varies considerably between models. In this article we calculated the local coefficients and post-processing constants to use in the region for the ten models (including the novel proposal) analyzed, in order to reduce biases and enhance overall performance. Among locally adapted models, the performance differences are quite small and any of them may be used, hence the choice may be based on the user convenience for implementing the model and performing the local adaptation. The best performing model is the novel proposal made here, NP, with negligible bias and a rRMSD under 5%. It has the best performance metrics under all-sky conditions and under discriminated sky conditions (clear, partially cloudy, cloudy). As the model is an enhancement of the pre-existing BB and BA phenomenological models (Batlles et al., 1995), its performance is expected to be strongly dependent on local adaptation and its utilization is not recommended in other climates without the local adjustment, pending further studies to test its robustness under different climates. The local implementation of the NP model has the best performance but it requires to adjust 40 coefficients to local data. With simplicity in consideration, the locally adjusted KA (Kasten et al., 1983) model can be singled out, as it provides an overall low bias and low dispersion under each sky condition and has only four adjustable coefficients. In particular, it was found that the sophisticated sky radiance models do not provide any outstanding feature, nor in overall or sky-discriminated performance, nor in their generic or locally adapted versions, so their utilization is not found to report significant advantages over phenomenological models.

Acknowledgments

The authors acknowledge financial support from Comisión Sectorial de Investigación Científica (CSIC-Grupos), Universidad de la República (Udelar), Uruguay.

Appendix A. Models' coefficients

The values of the local coefficients for the phenomenological models (KA, ST, LE, BA, BB, NP) described in Subsection 2.3 are listed in the tables below. These are included here in order to make the localized versions of the models usable in the broad region (Pampa Húmeda) or in other regions with a similar climate (Cfa). The original coefficients are also reported (except the LB model), for completeness.

model					**Reference**
KA	A	B	C	D	Eq. (24)
original	1.161	-0.112	0.0009	-0.025	Kasten et al. (1983)
local	1.235	-0.191	-0.0362	-0.049	this work
ST	C_0	ξ (rad)			Eq. (25)
original	1.01	0.60			Steven (1984)
local	1.03	0.74			this work
BA	a	b	c	d	Eq. (28)
original	1.245	0.522	0.230	0.322	Batlles et al. (1995)
local	1.085	0.048	0.017	-0.047	this work

Table A.6: Coefficients for original and local versions of models KA, ST, BA.

model								**Reference**
BB	bin	ϵ_1	ϵ_2	a	b		d	Eq. (29)
original	1	1.0	3.5	1.178	0.207	-	0.122	Batlles et al. (1995)
	2	3.5	8.0	1.454	0.655	-	0.476	
	3	8.0	11.0	1.486	0.495	-	0	
	4	11.0	ϵ_{max}	1.384	0.363	-	0	
local	1	1.0	3.5	1.080	0.040	-	-0.043	this work
	2	3.5	8.0	1.007	-0.053	-	0.195	
	3	8.0	11.0	1.024	0.001	-	0	
	4	11.0	ϵ_{max}	1.033	0.013	-	0	
NP	bin	ϵ'_1	ϵ'_2	a	b	c	d	e	Eq. (30)
local	1	1.00	1.065	0.3775	-0.0087	0.6181	0.0919	0.5725	this work
	2	1.065	1.230	0.4151	0.0159	0.4852	-0.0202	0.6007	
	3	1.230	1.500	0.3818	0.0313	0.2051	-0.0477	0.7177	
	4	1.500	1.950	0.0645	-0.0478	0.0625	0.0676	1.0058	
	5	1.950	2.800	-0.1446	-0.1167	-0.0889	0.1531	1.2349	
	6	2.800	4.500	-0.2518	-0.1818	-0.1971	0.2529	1.3465	
	7	4.500	6.200	-0.2305	-0.2245	-0.2643	0.2304	1.3431	
	8	6.200	ϵ'_{max}	0.3101	0.1267	0.0705	-0.0714	0.9491	

Table A.7: Coefficients (original and local) for models BB, NP. The bins for BB are defined by $\epsilon_1 \leq \epsilon < \epsilon_2$. The bins for NP follow the same pattern but in ϵ' (rigth-open intervals) and are adapted from Perez et al. (1993).

$(i,j,1,1)$				$(i,j,1,3)$			
1.051	1.082	1.1298	1.1288	1.051	1.082	1.1286	1.1285
1.051	1.1279	1.1294	1.1283	1.051	1.1276	1.129	1.1292
1.1287	1.1273	1.1273	1.1301	1.1294	1.1279	1.1296	1.1321
1.1279	1.1286	1.1258	1.1353	1.1289	1.1294	1.1296	1.156
$(i,j,2,1)$				$(i,j,2,3)$			
1.051	1.082	1.1282	1.1291	1.051	1.082	1.1278	1.1287
1.051	1.1274	1.1293	1.1283	1.051	1.1276	1.1278	1.1282
1.1292	1.1293	1.1279	1.1321	1.1288	1.1273	1.1282	1.1283
1.1287	1.1287	1.1297	1.1294	1.1289	1.1295	1.1288	1.1286
$(i,j,3,1)$				$(i,j,3,3)$			
1.051	1.082	1.1272	1.1297	1.051	1.082	1.1279	1.1287
1.051	1.082	1.1286	1.156	1.051	1.13	1.1289	1.1274
1.0944	1.082	1.1217	1.133	1.1289	1.1274	1.1292	1.1283
1.1298	1.1261	1.1263	1.128	1.1291	1.129	1.1298	1.1284
$(i,j,4,1)$				$(i,j,4,3)$			
1.051	1.082	1.129	1.1287	1.051	1.082	1.117	1.156
1.1299	1.1286	1.129	1.1289	1.051	1.082	1.117	1.156
1.1287	1.1291	1.1291	1.1292	1.1261	1.1168	1.1328	1.1305
1.1288	1.1287	1.1284	1.1289	1.1293	1.1271	1.1319	1.1281
$(i,j,1,2)$				$(i,j,1,4)$			
1.051	1.082	1.1298	1.1282	1.051	1.082	1.1296	1.1293
1.051	1.1296	1.1293	1.13	1.051	1.1298	1.1284	1.1273
1.1282	1.13	1.128	1.1301	1.1283	1.1254	1.131	1.156
1.1284	1.1289	1.1279	1.1329	1.1312	1.082	1.117	1.156
$(i,j,2,2)$				$(i,j,2,4)$			
1.051	1.082	1.1339	1.1286	1.051	1.082	1.1299	1.1286
1.051	1.1279	1.1296	1.1293	1.1271	1.1294	1.1297	1.1293
1.1229	1.132	1.1293	1.1286	1.1294	1.1288	1.1274	1.1295
1.1289	1.1274	1.1284	1.1301	1.1287	1.1282	1.1279	1.1285
$(i,j,3,2)$				$(i,j,3,4)$			
1.051	1.082	1.1293	1.1286	1.051	1.082	1.1258	1.1277
1.051	1.1284	1.1287	1.1281	1.051	1.1277	1.1278	1.1279
1.1282	1.1292	1.1307	1.1297	1.1279	1.1277	1.1292	1.1305
1.1304	1.1295	1.1283	1.1291	1.1282	1.1267	1.1277	1.1299
$(i,j,4,2)$				$(i,j,4,4)$			
1.051	1.082	1.1286	1.1289	1.051	1.082	1.117	1.156
1.1275	1.1282	1.1293	1.1298	1.051	1.082	1.117	1.156
1.1288	1.1288	1.1283	1.1287	1.051	1.082	1.117	1.156
1.1289	1.1289	1.129	1.1288	1.1283	1.1065	1.1307	1.1294

Table A.8: LUT with the 256 correction factors for the local LB model, described in Subsection 2.3.3. The bins (i,j,k,l) are defined in Table 1. In each sub-matrix, $i \rightarrow$ columns (1 to 4), $j \rightarrow$ rows (1 to 4). The header of each sub-matrix shows the values of $k \rightarrow \epsilon$ and $l \rightarrow k_d$. The underlined values correspond to empty category that are filled with the mean isotropic correction factor. The corresponding values for the original model can be found, in the same format, in LeBaron et al. (1990).

References

Abal, G., Aicardi, D., Alonso-Suárez, R., & Laguarda, A. (2017). Performance of empirical models for diffuse fraction in uruguay. *Solar Energy*, *141*, 166 – 181. doi:https://doi.org/10.1016/j.solener.2016.11.030.

Abal, G., Monetta, A., & Alonso-Suárez, R. (2018). Outdoor solar radiometer calibration under iso-9847:1992 standard and alternative methods. In *2018 IEEE 9th Power, Instrumentation and Measurement Meeting (EPIM)* (pp. 1–6). doi:10.1109/EPIM.2018.8756376.

Badosa, J., Wood, J., Blanc, P., Long, C. N., Vuilleumier, L., Demengel, D., & Haeffelin, M. (2014). Solar irradiances measured using spn1 radiometers: uncertainties and clues for development. *Atmospheric Measurement Techniques*, *7*, 4267–4283. doi:10.5194/amt-7-4267-2014.

Batlles, F., Olmo, F., & Alados-Arboledas, L. (1995). On shadowband correction methods for diffuse irradiance measurements. *Solar Energy*, *54*, 105 – 114. doi:https://doi.org/10.1016/0038-092X(94)00115-T.

Brunger, A. P., & Hooper, F. C. (1993a). Anisotropic sky radiance model based on narrow field of view measurements of shortwave radiance. *Solar Energy*, *51*, 53 – 64. doi:https://doi.org/10.1016/0038-092X(93)90042-M.

Brunger, A. P., & Hooper, F. C. (1993b). Erratum to anisotropic sky radiance model based on narrow field of view measurements of shortwave radiance. *Solar Energy*, *51*, 523.

Drummond, A. J. (1956). On the measurement of sky radiation. *Archiv für Meteorologie, Geophysik und Bioklimatologie, Serie B*, *7*, 413 – 436. doi:https://doi.org/10.1007/BF02242969.

Gracia, A., Torres, J., Blas], M. D., García, A., & Perez, R. (2011). Comparison of four luminance and radiance angular distribution models for radiance estimation. *Solar Energy*, *85*, 2202 – 2216. doi:https://doi.org/10.1016/j.solener.2011.06.005.

Gueymard, C., & Ruiz-Arias, J. (2016). Extensive worldwide validation and climate sensitivity analysis of direct irradiance predictions from 1-min global irradiance. *Solar Energy*, *128*, 1–30.

Gueymard, C. A. (2014). A review of validation methodologies and statistical performance indicators for modeled solar radiation data: Towards a better bankability of solar projects. *Renewable and Sustainable Energy Reviews*, *39*, 1024 – 1034. doi:https://doi.org/10.1016/j.rser.2014.07.117.

Ineichen, P., Gremaud, J., Guisan, O., & Mermoud, A. (1984). Study of the corrective factor involved when measuring the diffuse solar radiation by use of the ring method. *Solar Energy*, *32*, 585 – 590. doi:https://doi.org/10.1016/0038-092X(84)90133-6.

Iqbal, M. (1983). *An introduction to solar radiation*. Academic Press.

Kasten, F., Dehne, K., & Brettschneider, W. (1983). Improvement of measurement of diffuse solar radiation. In W. Palz (Ed.), *Solar Radiation Data* (pp. 221–225). Dordrecht: Springer Netherlands.

Kipp & Zonen (2004). *CM121 Shadow Ring Instruction Manual*. Instruction Manual Kipp & Zonen B.V. www.kippzonen.com.

Kudish, A., & Ianetz, A. (1993). Analysis of diffuse radiation data for beer sheva: Measured (shadow ring) versus calculated (global-horizontal beam) values. *Solar Energy*, *51*, 495 – 503. doi:https://doi.org/10.1016/0038-092X(93)90134-A.

Kudish, A. I., & Evseev, E. G. (2008). The assessment of four different correction models applied to the diffuse radiation measured with a shadow ring using global and normal beam radiation measurements for beer sheva, israel. *Solar Energy*, *82*, 144 – 156. doi:https://doi.org/10.1016/j.solener.2007.06.006.

Laguarda, A., Giacosa, G., Alonso-Suárez, R., & Abal, G. (2020). Performance of the site-adapted cams database and locally adjusted cloud index models for estimating global solar horizontal irradiation over the pampa húmeda. *Solar Energy*, *199*, 295–307. doi:https://doi.org/10.1016/j.solener.2020.02.005.

LeBaron, B., Michalsky, J., & Perez, R. (1990). A simple procedure for correcting shadowband data for all sky conditions. *Solar Energy*, *44*, 249 – 256. doi:https://doi.org/10.1016/0038-092X(90)90053-F.

LeBaron, B. A., Peterson, W. A., & Dirmhirn, I. (1980). Corrections for diffuse irradiance measured with shadowbands. *Solar Energy*, *25*, 1 – 13. doi:https://doi.org/10.1016/0038-092X(80)90401-6.

López, G., Muneer, T., & Claywell, R. (2004). Assessment of four shadow band correction models using beam normal irradiance data from the united kingdom and israel. *Energy Conversion and Management*, *45*, 1963 – 1979. doi:https://doi.org/10.1016/j.enconman.2003.11.001.

Maxwell, E., Wilcox, S., & Rymes, M. (1993). *Users Manual for SERI QC Software: Assessing the Quality of Solar Radiation Data*. NREL/TP-463-5608 National Renewable Energy Laboratory.

McArthur, L. (2005). *Baseline Surface Radiation Network (BSRN) Operations Manual*. TD-No. 1274, WRCP/WMO World Meteorological Organization (WMO). www.wmo.org.

Moon, P., & Spencer, D. (1942). Illumination from a non-uniform sky. *Illum. Engng.(NY)*, *37*, 707–726.

Muneer, T. (1990). Solar Radiation Model for Europe . *Building Services Engineering Research and Technology*, *11*, 153–163. doi:https://doi.org/10.1177/014362449001100405.

Muneer, T., & Zhang, X. (2001). A New Method for Correcting Shadow Band Diffuse Irradiance Data . *Journal of Solar Energy Engineering*, *124*, 34–43. doi:https://doi.org/10.1115/1.1435647.

Painter, H. (1981). The shade ring correction for diffuse irradiance measurements. *Solar Energy*, *26*, 361 – 363. doi:https://doi.org/10.1016/0038-092X(81)90182-1.

Peel, M. C., Finlayson, B. L., & Mcmahon, T. A. (2007). Updated world map of the köppen-geiger climate classification. *Hydrology and Earth System Sciences Discussions*, *11*, 1633–1644.

Perez, R., Ineichen, P., Seals, R., Michalsky, J., & Stewart, R. (1990). Modeling daylight availability and irradiance components from direct and global irradiance. *Solar Energy*, *44*, 271 – 289. doi:https://doi.org/10.1016/0038-092X(90)90055-H.

Perez, R., Seals, R., & Michalsky, J. (1993). All-weather model for sky luminance distribution—preliminary configuration and validation. *Solar Energy*, *50*, 235 – 245. doi:https://doi.org/10.1016/0038-092X(93)90017-I.

Polo, J., Wilbert, S., Ruiz-Arias, J., Meyer, R., Gueymard, C., Súri, M., Martín, L., Mieslinger, T., Blanc, P., Grant, I., Boland, J., Ineichen, P., Remund, J., Escobar, R., Troccoli, A., Sengupta, M., Nielsen, K., Renne, D., Geuder, N., & Cebecauer, T. (2016). Preliminary survey on site-adaptation techniques for satellite-derived and reanalysis solar radiation datasets. *Solar Energy*, *132*, 25 – 37. doi:https://doi.org/10.1016/j.solener.2016.03.001.

Rawlins, F., & Readings, C. (1986). The shade ring correction for measurements of diffuse irradiance under clear skies. *Solar Energy*, *37*, 407 – 416. doi:https://doi.org/10.1016/0038-092X(86)90031-9.

Ridley, B., Boland, J., & Lauret, P. (2010). Modelling of diffuse solar fraction with multiple predictors. *Renewable Energy*, *35*, 478 – 483. doi:https://doi.org/10.1016/j.renene.2009.07.018.

Ruiz-Arias, J., Alsamamra, H., Tovar-Pescador, J., & Pozo-Vázquez, D. (2010). Proposal of a regressive model for the hourly diffuse solar radiation under all sky conditions. *Energy Conversion and Management*, *51*, 881 – 893. doi:https://doi.org/10.1016/j.enconman.2009.11.024.

de Simón-Martín, M., Díez-Mediavilla, M., & Alonso-Tristán, C. (2016). Shadow-band radiometer measurement of diffuse solar irradiance: Calculation of geometrical and total correction factors. *Solar Energy*, *139*, 85 – 99. doi:https://doi.org/10.1016/j.solener.2016.09.026.

Siren, K. (1987). The shadow band correction for diffuse irradiation based on a two-component sky radiance model. *Solar Energy*, *39*, 433 – 438. doi:https://doi.org/10.1016/S0038-092X(87)80062-2.

Stanhill, G. (1985). Observations of shade-ring corrections for diffuse sky radiation measurements at the dead sea. *Quarterly Journal of the Royal Meteorological Society*, *111*, 1125–1130. doi:10.1002/qj.49711147013.

Steven, M. D. (1984). The anisotropy of diffuse solar radiation determined from shade-ring measurements. *Quarterly Journal of the Royal Meteorological Society*, *110*, 261–270. doi:https://doi.org/10.1002/qj.49711046317.

Steven, M. D., & Unsworth, M. H. (1980). Shade-ring corrections for pyranometer measurements of diffuse solar radiation from

cloudless skies. *Quarterly Journal of the Royal Meteorological Society*, *106*, 865–872. doi:10.1002/qj.49710645015.

Sánchez, G., Serrano, A., Cancillo, M. L., & García, J. A. (2012). Comparison of shadow-ring correction models for diffuse solar irradiance. *Journal of Geophysical Research: Atmospheres*, *117*. doi:10.1029/2011JD017346.

Vartiainen, E. (1999). An anisotropic shadow ring correction method for the horizontal diffuse irradiance measurements. *Renewable Energy*, *17*, 311–317. doi:10.1016/S0960-1481(98)007.

Vignola, F., Michalsky, J., & Stoffel, T. (2019). *Solar and Infrared Radiation Measurements https://www.taylorfrancis.com/books/9781315105130*.

A.2. Paper 6: Evaluation of six empirical models to estimate ground albedo in the Pampa Húmeda.

Tema 7 – Radiación solar y clima

EVALUACIÓN DE SEIS MODELOS EMPÍRICOS PARA ESTIMAR ALBEDO DEL SUELO EN LA PAMPA HÚMEDA

Juan M. Rodríguez Muñoz[1], **Rodrigo Alonso Suárez**[2], **Italo Bove**[2], **Gonzalo Abal**[1,2]

[1]Laboratorio de Energía Solar, Departamento de Física del Litoral, Centro Universitario Regional Litoral Norte, Universidad de la República, Cno. Luis B. Berres, km 508, CP 50000, Salto, Uruguay.

[2]Laboratorio de Energía Solar, Instituto de Física, Facultad de Ingeniería, Universidad de la República, Herrera y Reissig 565, CP 11300, Montevideo, Uruguay.

E-mail: jrodrigue@fing.edu.uy

RESUMEN: Modelar el albedo de suelo es requerido para estimar en forma precisa la radiación que éste refleja, necesaria para los modelos de transposición de irradiancia solar a plano inclinado. Esta componente, de menor incidencia en aplicaciones y suelos comunes, adquiere mayor relevancia en el contexto de la aparición de los paneles fotovoltaicos bifaciales. En este trabajo se ajustan y evalúan seis modelos de albedo utilizando medidas registradas en un predio experimental cuyo suelo y clima es representativo de la Pampa Húmeda sudamericana. Se consideran modelos de tres tipos; constantes, univariados (en función del ángulo cenital) y bivariados (que adicionan la fracción difusa). Los modelos bivariados son de mejor desempeño, superando en términos de rRMSD a los univariados en 16 % y a los constantes en 58 %. Los modelos bivariado y univariado de Tuomiranta et al. (2021) son los recomendados, y el uso de uno u otro depende de la disponibilidad de medidas de irradiancia difusa.

Palabras clave: reflectividad del suelo, irradiancia solar reflejada, panel solar bifacial.

INTRODUCCIÓN

El dimensionamiento de aplicaciones de energía solar requiere estimar la irradiancia solar global sobre superficies de orientación arbitraria. Ésta puede separarse en tres componentes: directa, difusa proveniente de la bóveda celeste y difusa reflejada por superficies cercanas. Para esta última componente los modelos clásicos consideran únicamente la reflexión del suelo, supuesto un reflector difuso hemisférico isotrópico y caracterizado por un albedo constante, ρ_g. Esta hipótesis no introduce un error significativo en tanto la componente reflejada por el suelo represente una pequeña fracción del total incidente sobre la superficie, lo cual se verifica en la mayoría de las aplicaciones. Sin embargo, esto no se cumple en el caso de los paneles fotovoltaicos bifaciales. Estos dispositivos son capaces de generar anualmente hasta un 15 % más de energía comparados con paneles fotovoltaicos convencionales en suelos de albedo típico ($\rho_g \simeq 0.22$) y hasta un 30 % más en suelos altamente reflectivos (Yusufoglu et al., 2014). La capacidad instalada de esta tecnología está aumentando, y se espera que la misma pase a tener un rol dominante en el mercado en el futuro cercano (Kopecek y Libal, 2021). Esto ha motivado el estudio de modelos de albedo más sofisticados que consideren el efecto de la geometría solar, la nubosidad y las características del terreno circundante.

Existen diversos modelos de albedo en la literatura, los cuales se pueden agrupar en tres categorías de complejidad creciente. La primera categoría la integran los modelos que asumen el suelo como un reflector difuso hemisférico isotópico con albedo constante. Estos modelos se diferencian por el criterio utilizado para asignar este valor constante (Liu y Jordan, 1960; Gueymard, 1987; Psiloglou y Kambezidis, 2009). Los modelos en la segunda y tercera categorías introducen cierto comportamiento especular

en la reflexión de la irradiancia solar sobre el suelo. Los modelos de la segunda categoría consideran al albedo como una función univariada del ángulo cenital (Nkemdirim, 1972; Temps y Coulson, 1977; Dickinson, 1983; Psiloglou y Kambezidis, 2009; Tuomiranta et al., 2021) y los de la tercera categoría agregan una dependencia en la fracción difusa (Temps y Coulson, 1977; Gueymard, 1987; Gardner y Nadeau, 1988; Ineichen et al., 1990; Chiodetti et al., 2016; Tuomiranta et al., 2021). Estos últimos modelos requieren medidas de irradiancia global y difusa en plano horizontal, en tanto los de las otras categorías solo requiren de la irradiancia global y son por lo tanto de implementación más sencilla.

El desempeño comparado de varios de estos modelos en diferentes tipos de suelos y regiones climáticas ha sido analizado previamente en la literatura (Ineichen et al., 1990; Psiloglou y Kambezidis, 2009; Tuomiranta et al., 2021). Los primeros estudios recomendaban el uso de un albedo constante y localmente medido (Ineichen et al., 1990). En consecuencia, el uso de un albedo constante elegido según las características del terreno ha sido históricamente la práctica más habitual para estimar la componente reflejada de la irradiancia solar sobre una superficie inclinada. Sin embargo, el trabajo más reciente sugiere otra situación. En Tuomiranta et al. (2021) se comparan 26 modelos de albedo en 26 sitios que abarcan diversos tipos de suelo. Los modelos resultan ordenados de menor a mayor desempeño según su grado de complejidad. En general, se reportan ventajas significativas en el uso de modelos bivariados y, en menor medida, también con los univariados. Además, se alerta sobre los potenciales errores debidos a la utilización de valores constantes de albedo provenientes de bases de datos y se destaca la importancia de la adaptación local de los modelos. En todos los casos es importante el ajuste de los modelos a las condiciones locales típicas. Esto motiva la realización de mediciones in-situ de albedo para determinar que modelo se adapta mejor a las características típicas de la Pampa Húmeda, tanto de suelo como de clima.

El objetivo del presente trabajo es evaluar el desempeño de seis modelos pre-existentes para estimar el albedo de un suelo cubierto mayormente por gramíneas (pasto natural) en un punto representativo de la Pampa Húmeda (Salto, Uruguay). Se determina el modelo de mejor desempeño a nivel local, desde una perspectiva general, así como también por categoría. Los seis modelos analizados son seleccionados tomando los dos de mejor desempeño en las tres categorías consideradas por Tuomiranta et al. (2021), considerando únicamente los suelos de tipo vegetal. Los coeficientes de estos modelos fueron determinados por muestreo aleatorio y validación cruzada utilizando 8 meses de medidas de albedo con calidad controlada que fueron registradas en el Laboratorio de Energía Solar de la Universidad de la República (http://les.edu.uy/). Este trabajo se organiza de la siguiente manera. En la sección siguiente se describen los modelos considerados, el conjunto de datos utilizado, el control de calidad y los indicadores de desempeño utilizados para comparar el desempeño de los modelos. Posteriormente, se presentan y analizan los resultados. Finalmente, en la última sección se sintetizan las principales conclusiones.

METODOLOGÍA

Modelos de albedo

El albedo o reflectancia de una superficie es la fracción de la irradiancia solar global que es reflejada por la misma. El albedo del suelo, supuesto horizontal, se define como,

$$\rho_g = \frac{G_g}{G_h}, \tag{1}$$

donde G_g es la irradiancia reflejada por el suelo (hacia todo el hemisferio) y G_h es la irradiancia solar global sobre un plano horizontal. Este parámetro depende de diversos factores: altura solar, nubosidad, cambios debido al clima local o a la acción propia del hombre (por ejemplo, cambios en el terreno circundante o la altura del pasto debido tareas de mantenimiento). El modelo más simple consiste en asumir un valor constante e independiente de las variables antes mencionadas que caracterice al suelo como un reflector difuso hemisférico isotrópico. El albedo puede obtenerse utilizando valores genéricos para el tipo de suelo provenientes de bases de datos (Liu y Jordan, 1960; Gueymard, 1987) o se puede estimar a partir de medidas experimentales, que es lo recomendado (Ineichen et al., 1990; Tuomiranta et al., 2021).

En este trabajo se obtiene el albedo constante considerando dos tipos de estimativos: la media aritmética y la media geométrica de las medidas de albedo (modelos 1 y 2, respectivamente),

$$\text{modelo 1}: \qquad \rho_g = \frac{1}{n}\sum_{i=1}^{n}\rho_i, \tag{2}$$

$$\text{modelo 2}: \qquad \rho_g = \left(\prod_{i=1}^{n}\rho_i\right)^{1/n}, \tag{3}$$

donde ρ_i representa la i-esima medida de albedo en n medidas. Estos modelos, sin parámetros ajustables, integran la categoría I, y son considerados en Psiloglou y Kambezidis (2009) y Tuomiranta et al. (2021).

Los modelos 3 y 4 de este trabajo corresponden a los propuestos por Nkemdirim (1972) y Tuomiranta et al. (2021), respectivamente, los cuales se muestran en las Ecs. (4) y (5).

$$\text{modelo 3}: \qquad \rho_g = \rho_n \times e^{b_1\theta_z}, \tag{4}$$

$$\text{modelo 4}: \qquad \rho_g = \rho_n \times \frac{1+b_1}{1+b_1\cos\theta_z}. \tag{5}$$

Ambos modelos utilizan funciones univariadas dependientes del ángulo cenital, θ_z, y tienen dos parámetros ajustables: ρ_n y b_1. El primero de estos parámetros corresponde al albedo en incidencia normal ($\theta_z = 0°$), y el segundo controla la variación del albedo con el ángulo cenital. El modelo 4 se basa en el trabajo previo de Dickinson (1983) e implica la restricción: $b_1 \in [0, 2]$, lo cual indica que el albedo es una función creciente con el ángulo cenital. Estos dos modelos integran la categoría II.

El quinto modelo es una extensión del cuarto (Tuomiranta et al., 2021) con tres parámetros ajustables y depende de la nubosidad a través de la fracción difusa f_d (el cociente entre la irradiancia solar difusa y la irradiancia solar global, ambas sobre plano horizontal), utilizada para tratar las reflexiones de la irradiancia solar directa y difusa por separado,

$$\text{modelo 5}: \quad \rho_g = (1-f_d)\times\rho_{bn}\times\frac{1+b_1}{1+b_1\cos\theta_z} + f_d\times\rho_d, \tag{6}$$

donde ρ_{bn}, b_1 y ρ_d son los parámetros ajustables. Los parámetros ρ_{bn} y ρ_d son el albedo para la irradiancia solar directa en incidencia normal y difusa, respectivamente. Se mantiene la restricción $b_1 \in [0, 2]$ y se agrega además la condición $\rho_{bn} \leq \rho_d$. El modelo es de categoría III.

El sexto y último modelo está basado en Gueymard (1987), desarrollado en el contexto de modelos de transposición a plano inclinado, y por tanto no directamente aplicable al caso de superficies horizontales. Al igual que el anterior este modelo es una función del ángulo cenital y la fracción difusa, y Tuomiranta et al. (2021) utilizó una versión de este modelo con seis parámetros de ajuste (ρ_n, b'_1, b'_2, b'_3, f_{af} y f_{ab}),

$$\rho_g = (1-f_d)\times\left[\rho_n + f_{af}\,e^{b'_1+b'_2\theta_z+b'_3\theta_z^2}\right] + f_d\times\left[\rho_n + 0.023\,(f_{af}+f_{ab})\right]. \tag{7}$$

El parámetro ρ_n representa el albedo en incidencia normal en condiciones de isotropía pura. Mayor detalle en relación a la definición de esta magnitud puede encontrarse en Gueymard (1987). Los parámetros b'_1, b'_2, b'_3 describen las variaciones del albedo con el ángulo cenital, y los parámetros f_{af} y f_{ab} describen la magnitud de las reflexiones anteriores y posteriores, respectivamente. Gueymard (1987) siguiere la utilización de $f_{af} = f_{ab} = 1$ para pasto verde, asociado a una terna especifica de parámetros b'_1, b'_2, b'_3. En este trabajo se opta por simplificar la expresión anterior al mínimo número de parámetros necesarios para su ajuste, quedando de la forma:

$$\text{modelo 6}: \quad \rho_g = (1-f_d)\times\left[\rho_n + e^{b_1+b_2\theta_z+b_3\theta_z^2}\right] + f_d\times\rho_d. \tag{8}$$

Con,

$$b_1 = b'_1 + \ln(f_{af}), \quad b_2 = b'_2, \quad b_3 = b'_3, \quad \rho_d = \rho_n + 0.023\,(f_{af}+f_{ab}).$$

El modelo 6 escrito de esta manera tiene una expresión más sencilla que la Ec. (7), una nomenclatura más homogénea con respecto a la de los modelos anteriores y está mejor condicionado para el ajuste matemático de sus coeficientes. El modelo 6 tiene entonces cinco parámetros, ρ_n, b_1, b_2, b_3 y ρ_d, es bivariado y por lo tanto de categoría III.

Datos utilizado y control de calidad

La medidas utilizadas en este trabajo se realizaron en el Laboratorio de Energía Solar (LES) en un entorno semi rural cerca de la ciudad de Salto, Uruguay (Latitud = 31.28 ºS, Longitud=57.92 ºW, Altura = 60 m snm). El LES se ubica en la región climática de la Pampa Húmeda, la cual está clasificada como Cfa (clima templado-cálido, húmedo, con veranos calurosos) según la clasificación actualizada de Köppen-Geiger (Peel et al., 2007). El conjunto de medidas tiene una extensión temporal de aproximadamente ocho meses, desde Agosto de 2021 hasta Marzo 2022, e incluye las siguientes magnitudes: irradiancia solar global en plano horizontal, G_h, irradiancia solar reflejada por el suelo, G_g, irradiancia solar difusa en plano horizontal, G_d, e irradiancia solar en incidencia normal, G_b.

La medida experimental del albedo del suelo, cubierto por pasto natural verde en su gran mayoría, se estimó utilizando la Eq. (1) con las medidas G_g y G_h. Estas medidas se realizaron con piranómetros Kipp & Zonen CMP6 a una altura de 1.6 m respecto al nivel suelo en un soporte especial mostrado en la Fig. 1a. La medida de difusa, utilizada para calcular la fracción difusa $f_d = G_d/G_h$, se realiza con un piranómetro Kipp & Zonen CMP10 ventilado y con el sensor sombreado por una esfera de sombra montada en un sistema de seguimiento de precisión SOLYS2 de Kipp & Zonen (Fig. 1b) equipado con sensor de ajuste fino, equipo que se encuentra a aproximadamente 30 m de la medidas anteriores. La medida de directa en incidencia normal se realizó con un pirheliómetro Kipp & Zonen CHP1 montado sobre el mismo sistema de seguimiento. Esta última medida se utiliza únicamente para los controles de calidad. Todos los piranómetros reciben mantenimiento diario y son calibrados con frecuencia bienal con el estándar secundario del LES, con trazabilidad técnica al patrón primario mundial. Los datos fueron registrados a intervalos de un minuto y fueron integrados a 10 minutos. Se trabajó con esta escala temporal para atenuar el efecto de la separación espacial entre las medidas de albedo y las del SOLYS2, así como también el efecto de fenómenos rápidos de sobre-irradiancia asociados a configuraciones particulares de nubes (Russo et al., 2021).

(a) Medida de albedo, G_h y G_g. *(b) Sistema SOLYS2, G_d y G_b.*

Figura 1: Montaje de los instrumentos de medida.

El conjunto de datos diurnos ($N = 17041$) fue sometido a una serie de filtros de control de calidad basados en las recomendaciones de la Baseline Solar Radiation Network (BSRN; McArthur (2005)). El procedimiento de control de calidad se resume en la Tabla 1 y la Fig. 2. Los cuatro primeros filtros (F1 a F4) imponen límites inferiores y superiores a las medidas de irradiancia solar, G, de la siguiente manera

$$b \leq G \leq G_{sc}\, p\, (\cos\theta_z)^a + c, \tag{9}$$

donde G representa cada componente de la irradiancia solar, G_{sc} corresponde a la constante solar y los parámetros p, a, b y c fueron determinaron localmente para cada filtro por inspección visual de las variables correspondientes. El filtro F5 impone un límite inferior para la altura solar, $\alpha_s > 10°$, lo que descarta las medidas afectadas por errores direccionales significativos (bajas alturas solares). El filtro F6 verifica que G_h, G_d y G_b cumplan la relación de clausura,

$$G_h = G_b \cos\theta_z + G_d, \tag{10}$$

con una tolerancia del 8 % del promedio de G_h. Este filtro se aplica únicamente a las medidas que verifiquen $G_h > 50\,\mathrm{W/m^2}$. El filtro F7 es una cota superior sobre la fracción difusa de modo que $f_d \leq 1.03$, estableciendo una tolerancia del 3 %. El filtro F8 retira los puntos de bajo índice de claridad, $k_t = G_h/G_{h0}$, donde G_{h0} es la irradiancia solar extraterrestre sobre plano horizontal, y baja fracción difusa f_d, asociados mayormente a condiciones de cielo cubierto y baja irradiancia. F9 impone un límite superior holgado para el índice de claridad, $k_t < 1$. F10 verifica la consistencia en las medidas de albedo $0 \leq \rho_g \leq 1$. El filtro F11 retira los datos comprendidos entre el 17 y el 30 de enero de 2022, los cuales se identificaron como datos anormales mediante inspección visual de la serie temporal de las medidas de albedo, probablemente debido a la presencia de pasto muy alto. Finalmente, el filtro F12 consiste en un filtro estadístico, donde para diferentes intervalos del ángulo cenital se eliminan los datos que no cumplen $|\rho_g - \bar{\rho}_g| \leq 3\sigma$, siendo $\bar{\rho}_g$ y σ el promedio y la desviación estándar de las medidas de albedo del intervalo correspondiente. Este filtro se aplico en forma independiente en intervalos de 10° del ángulo cenital y para el cálculo de $\bar{\rho}_g$ y σ se aplicaron los filtros de F1 a F11 en forma previa. Después de este procedimiento de filtrado se descartaron aproximadamente 1/3 de los datos originales, siendo 13 % el descarte geométrico por altura solar (F5). La Tabla 1 muestra las condiciones de cada filtro, las variables que afecta, el número de datos que lo pasan y el porcentaje de descarte. La última fila de esta tabla resume el proceso dando los indicadores de todos los filtros. La Fig. 2a muestra el proceso de filtrado en un diagrama f_d vs k_t y la Fig. 2b muestra el resultado del filtrado en las medidas de albedo. Finalmente, se obtienen 11470 datos a escala 10-minutal que pasan todos los filtros. Este conjunto de datos es el utilizado para entrenar y evaluar los modelos de acuerdo a la metodología que se explica en la siguiente sección.

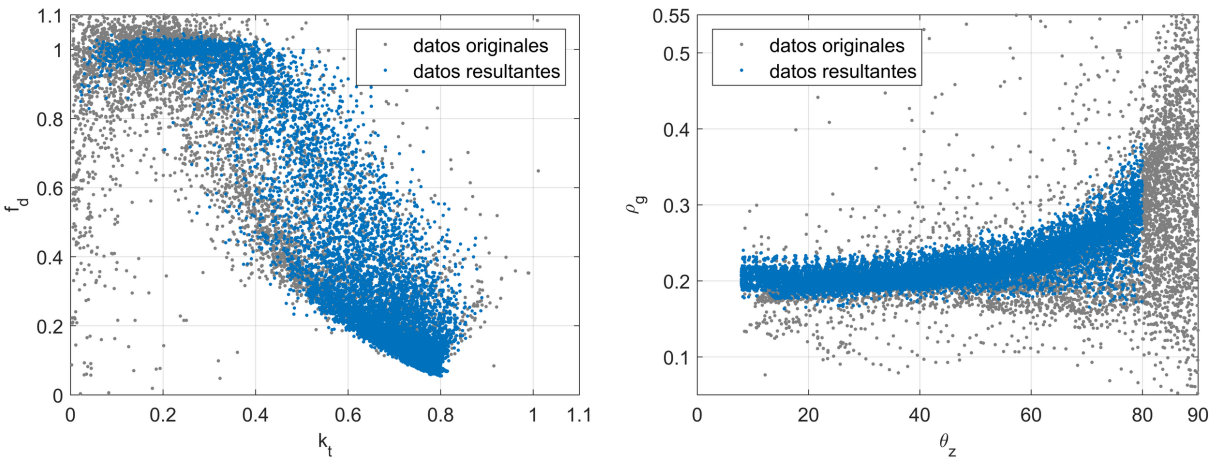

(a) Diagrama f_d vs k_t. *(b) ρ_g como función de θ_z.*

Figura 2: Resultado del procedimiento de filtrado; datos originales en gris y datos resultantes del procedimiento de filtrado en azul (aquellos que pasan todos los filtros).

Tabla 1: Detalle del proceso de filtrado aplicado a las medidas diurnas.

Filtro	**condición**	**variables**	**salida**	**% descartados**
F1	Ec. (9)	G_h	16769	1.6
F2	Ec. (9)	G_d	15981	6.2
F3	Ec. (9)	G_b	16759	1.7
F4	Ec. (9)	G_g	15789	7.4
F5	$\alpha_s > 10°$	todas	14800	13.2
F6	Ec. (10)	G_h, G_d, G_b	16213	4.9
F7	$f_d < 1.03$	G_h, G_d	16299	4.3
F8	$k_t < 0.20$ & $f_d < 0.80$	G_h, G_d	16716	1.9
F9	$k_t < 1$	G_h	16974	0.4
F10	$0 \leq \rho_g \leq 1$	G_g, G_h	16910	0.8
F11	17/01/22-31/01/22	todas	15084	11.5
F12	$\lvert\rho_g - \bar{\rho}_g\rvert \leq 3\sigma$	G_g, G_h	14003	17.9
todos	–	todas	11470	32.7

Indicadores de desempeño

Con el conjunto de datos resultante se ajustaron los coeficientes de los modelos descritos anteriormente. Para los modelos 1 y 2 simplemente se calculó la media aritmética, Ec. (2), y la media geométrica, Ec. (3), del conjunto de medidas de albedo, respectivamente. Para los modelos del 3 al 6 se implementaron algoritmos de regresión (lineal o no lineal según las características de cada modelo) que minimizan el error cuadrático medio, sin imponer ninguna restricción en la optimización.

Los coeficientes de los modelos y los indicadores de desempeño se determinaron mediante muestreo aleatorio y validación cruzada utilizando $60\,\%$ de los datos para entrenamiento y $40\,\%$ para validación. El esquema 60/40 se repitió 1000 veces para asegurar repetibilidad de los resultados, tomándose como resultado final el promedio de los coeficientes y los indicadores.

El desempeño de los modelos se evaluó mediante tres indicadores: el desvío medio (MBD), el desvío cuadrático medio (RMSD) y la integral de Kolmogorov-Smirnov (KSI), los cuales se definen de la siguiente manera,

$$\text{MBD} = \frac{1}{n}\sum_{i=1}^{n}(\hat{y}_i - y_i), \quad \text{RMSD} = \left[\frac{1}{n}\sum_{i=1}^{n}(\hat{y}_i - y_i)^2\right]^{\frac{1}{2}}, \quad \text{KSI} = \int_0^1 |\hat{F}(y) - F(y)|\, dy, \qquad (11)$$

donde y_i corresponde al valor de referencia (medida de albedo), $\hat{y}_i$ corresponde al estimativo del modelo, y F y $\hat{F}$ corresponden a las distribuciones de probabilidad acumulada de y_i e $\hat{y}_i$, respectivamente. Estas

métricas tienen las mismas unidades que la magnitud y_i, es decir, adimensionadas en el caso del albedo. Las mismas pueden ser expresadas en forma relativa (rMBD, rRMSD y rKSI) como porcentaje del valor medio de las medidas, $\bar{\rho}_g$. Los tres indicadores dan información diferente sobre la concordancia entre los modelos y las medidas. El MBD es el sesgo medio de los estimativos, el RMSD es una medida de la dispersión de los desvíos de los estimativos y el KSI una medida de la distancia estadística entre las distribuciones acumuladas de medidas y estimativos.

Es útil definir un indicador que combine los tres indicadores en uno solo (Combined Performance Indicator - CPI),

$$\text{CPI} = \frac{1}{3}\left(|\text{rMBD}| + \text{rRMSD} + \text{rKSI}\right). \tag{12}$$

Un indicador global similar ha sido propuesto en Gueymard (2014). Este conjunto de indicadores ha sido utilizado exitosamente en la evaluación de modelos empíricos de fracción difusa (Abal et al., 2017) y en la evaluación de factores de corrección para medidas de irradiancia solar difusa con banda de sombra (Rodríguez-Muñoz et al., 2021).

RESULTADOS

En la Tabla 2 se muestran los parámetros ajustados localmente de los modelos. Los valores que se muestran en esta tabla corresponden a los promedios de las 1000 ejecuciones del procedimiento de muestro y validación cruzada. También se calcularon las desviaciones estándar de los parámetros, las que resultaron ser al menos 30 veces menor que los promedios, lo cual da cuenta del la robustez de los modelos y del método de ajuste. Los parámetros de los modelos de Tuomiranta et al. (2021) verifican las restricciones $b_1 \in [0, 2]$ y $\rho_{bn} \leq \rho_d$, por lo que se entiende que no es necesario imponer estas restricciones en el procedimiento de ajuste de parámetros.

Tabla 2: Parámetros de los modelos ajustados localmente. Los valores que se muestran corresponden a los promedios de las 1000 ejecuciones del procedimiento de muestro y validación cruzada.

	Parámetros				
Modelo	ρ_n ó ρ_{bn}	b_1	b_2	b_3	ρ_d
#1 Media aritmética	0.2209	-	-	-	-
#2 Media geométrica	0.2192	-	-	-	-
#3 Nkemdirim (1972)	0.1776	0.0046	-	-	-
#4 Tuomiranta et al. (2021)	0.1907	0.6014	-	-	-
#5 Tuomiranta et al. (2021)	0.1835	1.0269	-	-	0.2148
#6 Gueymard (1987)	0.1673	-3.2764	-0.0202	0.0005	0.2146

En la Tabla 3 se muestran los indicadores de desempeño para los seis modelos, como porcentaje del valor medio de la medidas de albedo, $\bar{\rho}_g = 0.2209$. En general todos lo modelos presentan un sesgo medio cercano a cero ($< 1\,\%$). El ordenamiento de los modelos que resulta del rRMSD (de peor a mejor desempeño) es del 1 al 6, y está de acuerdo a su grado de complejidad. El rKSI ordena los modelos de la siguiente manera: 1, 2, 3, 6, 4 y 5, y el CPI de la forma: 1, 2, 3, 4, 6 y 5. En general, se puede ver que el desempeño de los modelos se ordena de menor a mayor según el grado de complejidad de los mismos, es decir, los modelos bivariados son los de mejor desempeño (modelos 5 y 6), seguidos por los univariados

(3 y 4), y por último los modelos constantes (1 y 2), lo que se encuentra en concordancia con el trabajo previo de Tuomiranta et al. (2021). El modelo de mayor desempeño de la categoría III de acuerdo al CPI es el 5 (Tuomiranta et al., 2021), seguido muy cerca por el 6 (Gueymard, 1987). El modelo 6 presenta el menor rRMSD, sin embargo, la mejora en este indicador no logra compensar la diferencia en el rKSI (similitud estadística de las distribuciones). El modelo 5 posee indicadores que son mayores en un $16\,\%$ a los de la categoría II, y un $58\,\%$ a los de la categoría I. El modelo de mayor desempeño de la categoría II es el 4, siendo sensiblemente mejor que el 3 (la diferencia en el CPI es del orden del $20\,\%$). El mejor modelo de la categoría I corresponde a la media aritmética, pero la diferencia con la media geométrica es menor al $3\,\%$.

Tabla 3: Indicadores de desempeño para los seis modelos de albedo, expresados en forma porcentual respecto al valor medio de las medidas, $\bar{\rho}_g = 0.2209$.

	Indicadores de desempeño (%)			
Modelo	**rMBD**	**rRMSD**	**rKSI**	**CPI**
#1 Media aritmética	0.0	13.2	9.9	7.7
#2 Media geométrica	-0.8	13.2	9.7	7.9
#3 Nkemdirim (1972)	-0.4	9.0	3.4	4.3
#4 Tuomiranta et al. (2021)	0.0	8.2	1.9	3.4
#5 Tuomiranta et al. (2021)	0.0	7.9	1.5	3.1
#6 Gueymard (1987)	0.0	7.3	2.2	3.2

Los parámetros y los indicadores del modelo 6 que se muestran en las Tablas 2 y 3 corresponden a su versión simplificada, Ec. (8). También se implementó la versión de 6 parámetros de este modelo, Ec. (7), pero se encontró inestabilidad en la convergencia de los algoritmos de optimización, obteniéndose por tanto una alta dispersión en los coeficientes al ejecutar 1000 veces el procedimiento de ajuste. Además, los indicadores de desempeño no variaban significativamente respecto a la versión utilizada del modelo 6. Por lo tanto, se concluye que el modelo simplificado de 5 parámetros es una mejor alternativa para su ajuste local que la adaptación original de Tuomiranta et al. (2021), en tanto es más sencillo, robusto (menor variabilidad en los parámetros) y posee los mismos indicadores de desempeño.

En la Fig. 3 se muestra la comparativa de las medidas de albedo contra los estimativos de los modelos, en diagramas ρ_g vs θ_z. No hay diferencias significativas entre los modelos 1 y 2 (Fig. 3a, ya que la diferencia entre la media aritmética y geométrica es menor al $1\,\%$. Los modelos 3 y 4 (Fig. 3b) logran describir el comportamiento creciente del albedo con el ángulo cenital en forma general, pero no captan la dispersión de los datos debido a las variaciones en las condiciones de nubosidad. Los modelos 5 y 6 (Fig. 3c y Fig. 3d) logran captar ambos comportamientos; dependencia del ángulo cenital y condiciones de nubosidad, lo que se encuentra en consonancia con los bajos valores de los indicadores de desempeño de estos modelos.

Complementado en análisis anterior, en la Fig. 4 se muestra el rMBD y el rRMSD del mejor modelo de cada categoría (modelos 1, 4 y 5) discriminado por el coseno del ángulo cenital ($\cos\theta_z$) y el índice de claridad. El índice de claridad está correlacionado con la fracción difusa (ver Fig. 2a) y permite distinguir entre las distintas condiciones de cielo. En este sentido, se pueden distinguir tres condiciones diferentes: cielo claro ($k_t > 0.6$), cielo parcialmente nublado ($0.6 \geq k_t \geq 0.2$) y cielo cubierto ($k_t < 0.2$). Los

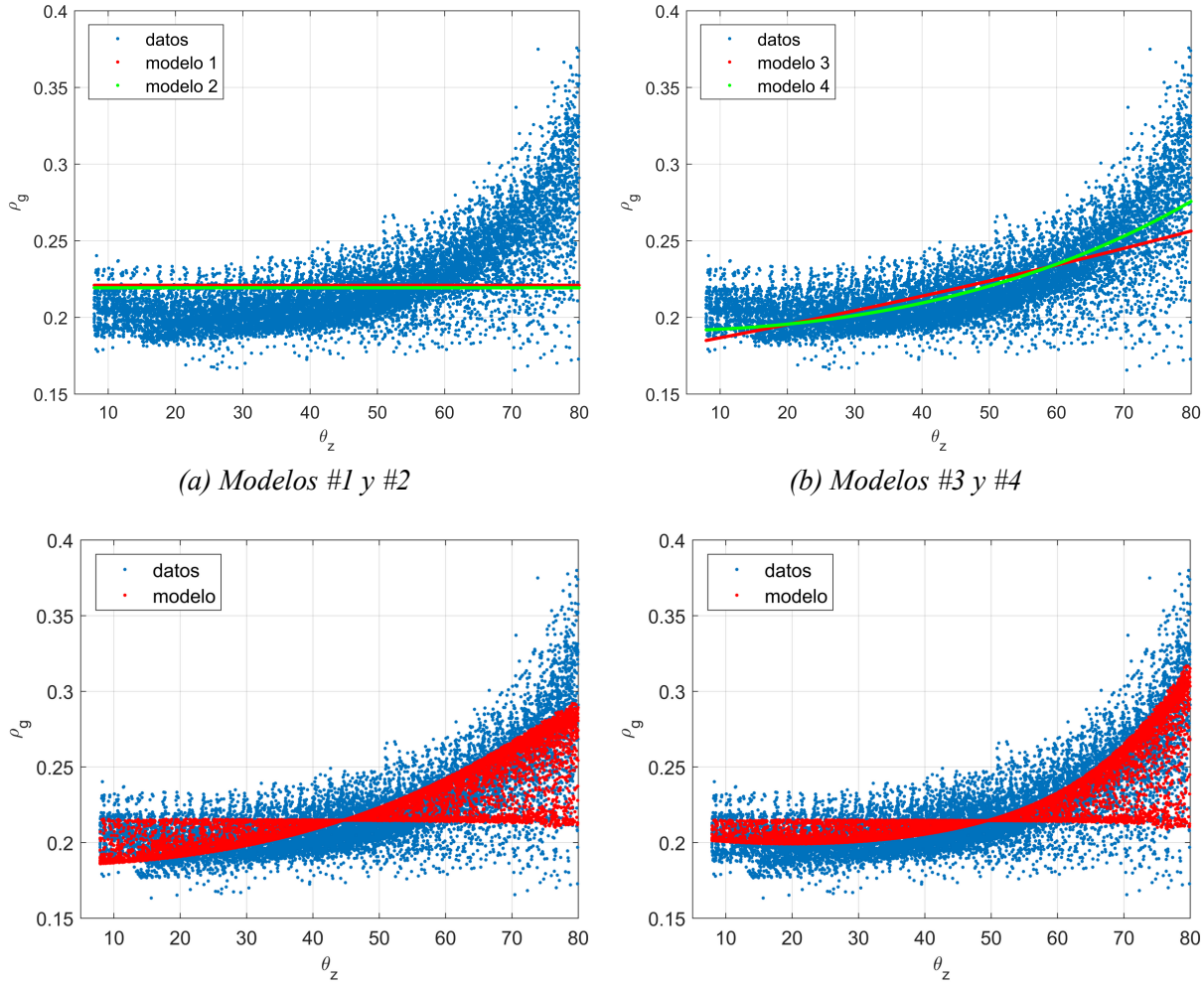

(a) Modelos #1 y #2

(b) Modelos #3 y #4

(c) #5 Tuomiranta et al. (2021)

(d) #6 Gueymard (1987)

Figura 3: Comparativa entre las medidas de albedo y los estimativos de los diferentes modelos.

gráficos respectivos tienen la misma escala de colores, para facilitar la comparación, y satura en algunos casos para tener una visualización adecuada.

En relación al rMBD (Figs. 4a, 4c y 4e), el modelo 1 es el que presenta mayores diferencias, con un comportamiento bastante asimétrico. Este modelo subestima en gran medida en la región de ángulo cenital alto ($\cos\theta_z$ bajo), en particular para condiciones de cielo claro, y sobrestima en la región de ángulo cenital bajo para toda condición de cielo. El rMBD de este modelo en el diagrama discriminado (Fig. 4a) está entre $-38\,\%$ y $+14\,\%$ y su comportamiento es esperable de la inspección de la Fig. 3a. Los modelos 4 y 5 logran reducir considerablemente esta asimetría, especialmente la subestimación, alcanzando valores de rMBD de entre $-15\,\%$ y $+18\,\%$ (modelo 4) y $-14\,\%$ y $+11\,\%$ (modelo 5). El modelo 5 presenta una mejor distribución de los indicadores que el 4, pero la mayor mejoría se produce en la región de ángulos cenitales bajo-medio y condiciones de cielo parcialmente nublado y cubierto ($\cos\theta_z$ entre 0.1 y 0.5 y $k_t < 0.4$). En relación al rRMSD (Figs. 4b, 4d y 4f), los tres modelos presentan peor desempeño en la región ángulo cenital alto, en especial en la región de cielo claro y parcialmente nublado para el modelo 1 (rRMSD $\simeq 40\,\%$), y en la región de cielo parcialmente nublado y cubierto para los modelos 4 y 5 (rRMSD $\simeq 25\,\%$). Se observa una mejora en el desempeño al pasar de los modelos de menor a mayor complejidad, tanto en los valores máximos de rRMSD como en su distribución en este espacio.

A partir de lo expuesto, se concluye que los modelos de la categoría III logran describir de mejor forma las variaciones del albedo con el ángulo cenital y las condiciones de nubosidad. Estos modelos, además

de tener mejores indicadores de desempeño en términos globales (Tabla 3), presentan una distribución de errores más homogénea en el dominio cos θ_z vs. k_t que los modelos de categoría I y II.

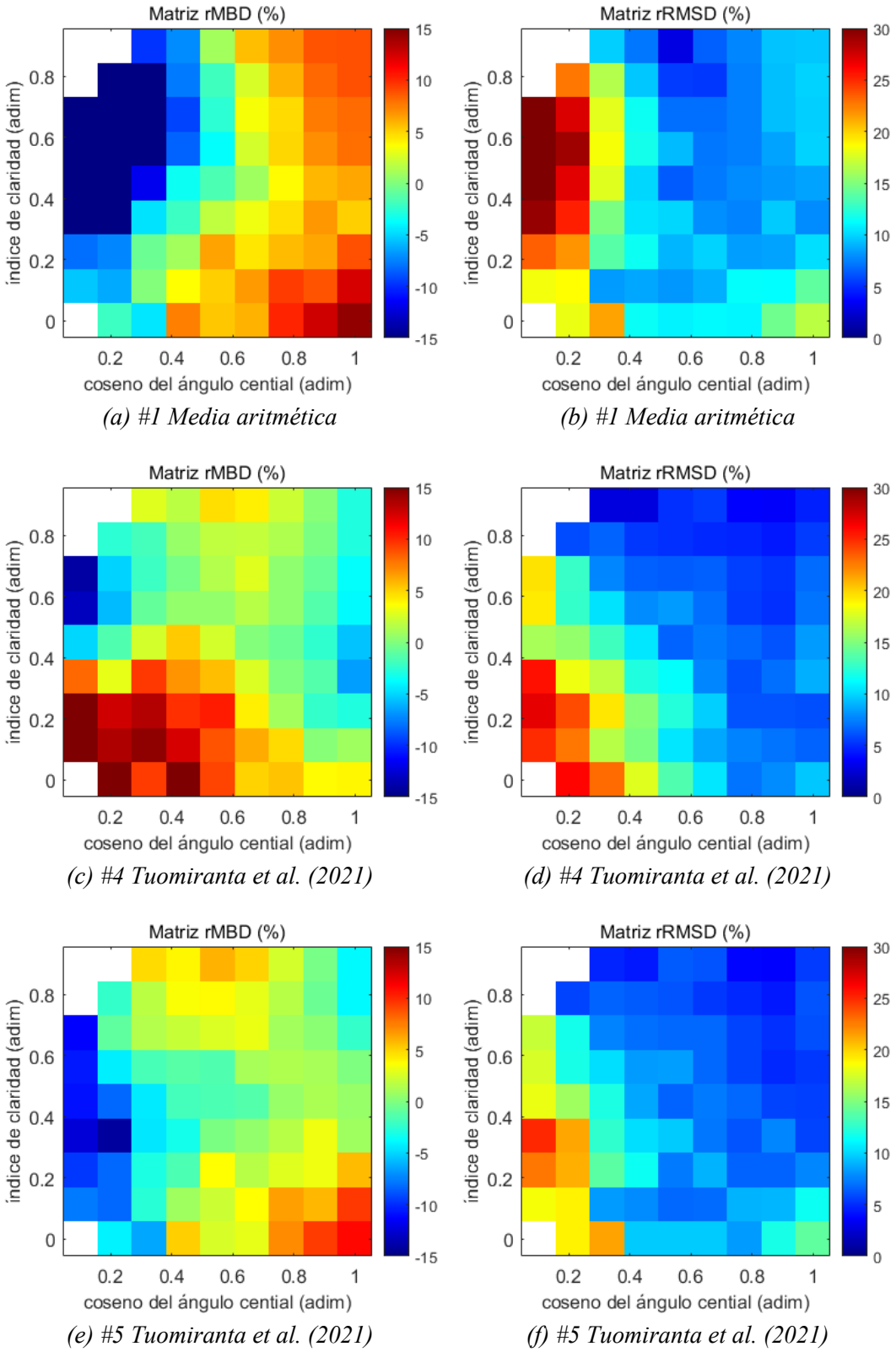

(a) #1 Media aritmética *(b) #1 Media aritmética*

(c) #4 Tuomiranta et al. (2021) *(d) #4 Tuomiranta et al. (2021)*

(e) #5 Tuomiranta et al. (2021) *(f) #5 Tuomiranta et al. (2021)*

Figura 4: Matriz de rMBD y rRMSD para el mejor modelo de cada categoría, expresadas en forma porcentual respecto al valor medio de las medidas, $\bar{\rho}_g = 0.2209$. La escala de las figuras es la misma para facilitar su comparación. Las regiones en blanco indican que no hay datos en dicha condición.

CONCLUSIONES

En este trabajo se evaluó el desempeño de seis modelos pre-existentes para estimar el albedo de un suelo cubierto mayormente por gramíneas (pasto natural) en un punto representativo de la Pampa Húmeda. Los modelos fueron agrupados en tres categorías según la complejidad de los mismos: categoría I (modelos constantes); categoría II (modelos univariados en el ángulo cenital) y categoría III (modelos bivariados en el ángulo cenital y la fracción difusa). Todos los modelos presentaron un rMBD cercano a cero, por lo que el orden de los modelos estuvo dominado por el rRMSD y el rKSI. En este sentido, el ordenamiento dado por el rRMSD y el rKSI fue similar, siendo los modelos de la categoría III los de mejor desempeño, seguidos por los de la categoría II, y por último los de la categoría I, lo que se encuentra en consonancia con el trabajo previo de Tuomiranta et al. (2021) para otras regiones. El modelo de mejor desempeño de la categoría III y a nivel global, es el 5 (Tuomiranta et al., 2021), seguido muy cerca por el 6 (Gueymard, 1987). Este modelo posee indicadores que son mayores en un 16 % a los de la categoría II y un 58 % a los de la categoría I (en promedio), por lo cual se justifica su uso, si la medida de irradiancia difusa esta disponible. El modelo de mejor desempeño de la categoría II es el 4, siendo sensiblemente mejor que el 3, por lo cual es el modelo recomendado si no se cuenta con medidas de irradiancia difusa. El mejor modelo de la categoría I corresponde a la media aritmética, siendo muy pequeña la diferencia con la media geométrica.

Al analizar los indicadores de desempeño discriminados por el coseno del ángulo cenital y el índice de claridad, se observó que el modelo 5, además de presentar los mejores valores de rMBD y rRMSD en términos globales, presenta una mejor distribución de los indicadores en las diferentes condiciones. El modelo 1, si bien presenta un rMBD cercano a cero a nivel global, presenta una gran asimetría en la distribución de su rMBD, sobrestimando en gran medida para ángulos cenitales bajos y sobrestimando en la región de ángulos cenitales altos. En la discriminación de ambas métricas se observa claramente que el aumento de complejidad de los modelos (de la categoría I a la III) mejora su capacidad de modelado del albedo en las diferentes condiciones de altura solar y nubosidad, reduciendo errores en cada región y homogeneizando su comportamiento en este espacio.

A futuro se espera poder extender el trabajo a otros tipos de suelo, en especial aquellos que puede llegar a ser de interés para las instalación de panales fotovoltaicos bifaciales (alta reflectividad y bajo costo). Otro trabajo a futuro consiste en evaluar el impacto que los modelos de la categoría II y III tienen sobre los modelos de transposición para la estimación de irradiancia solar en superficies inclinadas y evaluar el impacto del uso de modelos empíricos de separación de las componentes difusa y directa en los modelos de categoría III, incluyendo su ventaja relativa frente a los modelos de categorías II y I en esta situación.

AGRADECIMIENTOS

Los autores agradecen a la Comisión Sectorial de Investigación Científica (CSIC) de la Universidad de la República por el apoyo financiero a través de su programa de Grupos de I+D.

REFERENCIAS

Abal, G., Aicardi, D., Alonso-Suárez, R., y Laguarda, A. (2017). Performance of empirical models for diffuse fraction in uruguay. *Solar Energy*, 141:166 – 181.

Chiodetti, M., Lindsay, A., Dupeyrat, P., Binesti, D., Lutun, E., Radouane, K., y Mousel, S. (2016). Pv bifacial yield simulation with a variable albedo model. En *Proceedings of the EU PVSEC 2021*.

Dickinson, R. E. (1983). Land surface processes and climate—surface albedos and energy balance. En Saltzman, B., editor, *Theory of Climate*, volumen 25 de *Advances in Geophysics*, pp. 305–353. Elsevier.

Gardner, C. L. y Nadeau, C. (1988). Estimating south slope irradiance in the arctic—a comparison of experimental and modeled values. *Solar Energy*, 41(3):227–240.

Gueymard, C. (1987). An anisotropic solar irradiance model for tilted surfaces and its comparison with

selected engineering algorithms. *Solar Energy*, 38(5):367–386.

Gueymard, C. (2014). A review of validation methodologies and statistical performance indicators for modeled solar radiation data: Towards a better bankability of solar projects. *Renewable and Sustainable Energy Reviews*, 39:1024–1034.

Ineichen, P., Guisan, O., y Perez, R. (1990). Ground-reflected radiation and albedo. *Solar Energy*, 44(4):207–214.

Kopecek, R. y Libal, J. (2021). Bifacial photovoltaics 2021: Status, opportunities and challenges. *Energies*, 14(8).

Liu, B. Y. y Jordan, R. C. (1960). The interrelationship and characteristic distribution of direct, diffuse and total solar radiation. *Solar Energy*, 4(3):1–19.

McArthur, L. (2005). Baseline Surface Radiation Network (BSRN) Operations Manual. Td-no. 1274, wrcp/wmo, World Meteorological Organization (WMO). www.wmo.org.

Nkemdirim, L. C. (1972). A note on the albedo of surfaces. *Journal of Applied Meteorology (1962-1982)*, 11(5):867–874.

Peel, M. C., Finlayson, B. L., y Mcmahon, T. A. (2007). Updated world map of the köppen-geiger climate classification. *Hydrology and Earth System Sciences Discussions*, 11:1633–1644.

Psiloglou, B. y Kambezidis, H. (2009). Estimation of the ground albedo for the athens area, greece. *Journal of Atmospheric and Solar-Terrestrial Physics*, 71(8):943–954.

Rodríguez-Muñoz, J., Monetta, A., Alonso-Suárez, R., Bove, I., y Abal, G. (2021). Correction methods for shadow-band diffuse irradiance measurements: assessing the impact of local adaptation. *Renewable Energy*, 178:830–844.

Russo, P., Laguarda, A., y Abal, G. (2021). Characterization of solar over-irradiance events in uruguay. En *ISES Solar World Congress 2021 Proceedings*, pp. 1–6.

Temps, R. C. y Coulson, K. (1977). Solar radiation incident upon slopes of different orientations. *Solar Energy*, 19(2):179–184.

Tuomiranta, A., Alet, P.-J., Ballif, C., y Ghedira, H. (2021). Worldwide performance evaluation of ground surface reflectance models. *Solar Energy*, 224:1063–1078.

Yusufoglu, U. A., Lee, T. H., Pletzer, T. M., Halm, A., Koduvelikulathu, L. J., Comparotto, C., Kopecek, R., y Kurz, H. (2014). Simulation of energy production by bifacial modules with revision of ground reflection. *Energy Procedia*, 55:389–395. Proceedings of the 4th International Conference on Crystalline Silicon Photovoltaics (SiliconPV 2014).

EVALUATION OF SIX EMPRIRICAL MODELS TO ESTIMATE GROUND ALBEDO IN THE PAMPA HÚMEDA

ABSTRACT: Ground albedo modeling is required for the accurate estimation of ground-reflected radiation, which is needed for solar irradiance transposition models from horizontal to tilted plane. This radiation component represents a small portion of the useful irradiance in typical applications and soils, but it is gaining in relevance due to the recent appearance of bifacial solar panels. In this work, six ground albedo models are adjusted and evaluated by using measurements acquired in an experimental facility whose soil and climate are representative of the broader Pampa Húmeda region of South America. Three types of models are considered; constant models, univariate models of the solar zenith angle and bivariate models that add the diffuse fraction as predictor. Bivariate models are the best performing, overcoming univariate models in 16 % and constant models in 58 % in terms of rRMSD metric. The bivariate and univariate models of Tuomiranta et al. (2021) are recommended, and the choice within them depends on the availability of diffuse irradiance measurements.

Keywords: ground reflectance, reflected solar irradiance, bifacial solar modules.